Development of an Inconel-718 LS-DYNA® Material Model and *MAT_224 Input Parameters

December, 2023

Final report

U.S. Department of Transportation
Federal Aviation Administration

NOTICE

This document is disseminated under the sponsorship of the U.S. Department of Transportation in the interest of information exchange. The U.S. Government assumes no liability for the contents or use thereof. The U.S. Government does not endorse products or manufacturers. Trade or manufacturers' names appear herein solely because they are considered essential to the objective of this report. The findings and conclusions in this report are those of the author(s) and do not necessarily represent the views of the funding agency. This document does not constitute FAA policy. Consult the FAA sponsoring organization listed on the Technical Documentation page as to its use.

This report is available at the Federal Aviation Administration William J. Hughes Technical Center's Full-Text Technical Reports page: actlibrary.tc.faa.gov in Adobe Acrobat portable document format (PDF).

Technical Report Documentation Page

Form DOT F 1700.7 (8-72)   Reproduction of completed page authorized

1. Report No. DOT/FAA/TC-23/68	2. Government Accession No.	3. Recipient's Catalog No.
4. Title and Subtitle Development of an Inconel-718 LS-DYNA® Material Model and *MAT_224 Input Parameters		5. Report Date December 2023
		6. Performing Organization Code
7. Author(s) Stefano Dolci, Kelly Carney, Leyu Wang, Paul Du Bois and Cing-Dao Kan		8. Performing Organization Report No.
9. Performing Organization Name and Address George Mason University Center for Collision Safety and Analysis 4087 University Drive Fairfax, VA 22030 USA		10. Work Unit No. (TRAIS)
		11. Contract or Grant No. 692M151840003
12. Sponsoring Agency Name and Address U.S. Department of Transportation Federal Aviation Administration Air Traffic Organization Operations Planning Office of Aviation Research and Development Washington, DC 20591		13. Type of Report and Period Covered
		14. Sponsoring Agency Code AIR-600

15. Supplementary Notes
The Federal Aviation Administration William J. Hughes Technical Center Aviation Research Division Technical Monitor was Daniel Cordasco.

16. Abstract

In a joint effort by George Mason University, The Ohio State University, NASA John H. Glenn Research Center, and the Federal Aviation Administration (FAA) Aircraft Catastrophic Failure Prevention Program, technology is being advanced to produce predictive impact analysis based on a material's mechanical properties. The team has developed Inconel-718 mechanical property data and the analytical capability that allows for a comprehensive representation of that data in LS-DYNA®, using the *MAT_224 material model. The tabulated input was developed using data from many tests including tension, compression, shear, and many additional stress-states. Both the test data and the modeling also include temperature and strain rate dependencies. This report documents the process of transforming the material test data into a set of *MAT_224 input parameters, including the necessary processing that ensures stable and repeatable results. Verification and validation of the presented models was achieved through comparisons with ballistic impact tests.

17. Key Words Material Model Development, Inconel 718, Adiabatic Shear Band, LS-DYNA®, *MAT_224, engine containment	18. Distribution Statement This document is available to the U.S. public through the National Technical Information Service (NTIS), Springfield, Virginia 22161. This document is also available from the Federal Aviation Administration William J. Hughes Technical Center at actlibrary.tc.faa.gov.		
19. Security Classif. (of this report) Unclassified	20. Security Classif. (of this page) Unclassified	21. No. of Pages 159	19. Security Classif. (of this report) Unclassified

iii

Contents

Figures

ix

Tables

Acronyms

Acronym	Definition
FAA	Federal Aviation Administration
*MAT_024	A piecewise linear plasticity material model in LS-DYNA®
*MAT_224	An elasto-viscoplastic material model in LS-DYNA® with arbitrary stress-strain input curve(s) and strain rate dependency which can be user-defined
AMS	Aerospace Material Specification
C	Celsius
CAD	Computer-Aided Design
DIC	Digital Image Correlation
GPa	Giga Pascal
GMU	George Mason University
In	Inch
JAA	Joint Aviation Authority
K	Kelvin
kg	Kilogram
KN	KiloNewton
Lbf	Pound-force
M	Meter
mg	Milligram
mm	Millimiter
ms	Milliecond
m/s	Meter per second
NASA	National Aeronautics and Space Administration
OSU	The Ohio State University
psi	Pound-force per square inch
RT	Room temperature
s	Second
s^{-1}	Inverse second
SI	International System of Units
Inco 718	Inconel-718
ASB	Adiabatic shear band
TQC	Taylor-Quinney coefficient

Executive summary

In an effort by George Mason University, The Ohio State University (OSU), NASA John H. Glenn Research Center, and the Federal Aviation Administration (FAA) Aircraft Catastrophic Failure Prevention Program, technology has been advanced to produce predictive impact analysis based on a material's mechanical properties. This team has developed Inconel-718 mechanical property data, and the analytical capability that allows for a comprehensive representation of that data in the commercial finite element analysis software LS-DYNA®, using the *MAT_224 material model. The Inconel-718 used was from a single batch of 12.7mm (0.5 inch) rolled plate, which was precipitation hardened.

The tabulated input was developed using data from many Inconel-718 tests including tension, compression, shear, and many additional stress states. The test data and the modeling also include temperature and strain rate dependencies. The test data and the modeling represent both the plasticity and the fracture behavior of the Inconel-718. In the ballistic impact tests, it was determined that the fracture modes were adiabatic shear bands (ASBs). Novel capability was developed to predict ASBs, added to *MAT_224, and documented in separate reports. This report documents the process of transforming the material test data into a set of *MAT_224 input parameters, including the necessary processing that ensures stable and repeatable results. Verification and validation of the presented models was achieved through comparisons with ballistic impact tests.

1 Introduction

Inconel-718 is one of several important metallic materials widely used in aerospace applications, which are more specifically and commonly used in aircraft engines. Traditional metallic constitutive models fell short in their predictions of the plastic and fracture behavior under the range of strain rates and stress-states occurring in dynamic events such as fan blade separation (Kay, 2003; Buyuk, Loikkanen, & Kan, 2008). With the development of *MAT_224, a step towards fully predictive ballistic impact simulations based upon mechanical property data has been made (Emmerling, Altobelli, Carney, & Pereira, 2014). *MAT_224 is an elastic-plastic material with strain rate and temperature dependent stress-strain plasticity, and with stress-state, strain rate, temperature, and element size dependent fracture. It is available in the commercial finite element analysis software LS-DYNA® (Ansys LS-DYNA, 2023). All these material model behaviors can be precisely specified by tabulated input parameters. This report presents the research effort of developing and validating a set of Inconel-718 *MAT_224 tabulated material parameters. Modeling of the rolled 12.7mm (0.5 inch) Inconel-718 plate required utilizing all *MAT_224's stress-state, strain rate, temperature, and element size dependent definition capabilities.

The deformation portion of the material model produced in this effort is based on the results of uniaxial tensile testing conducted on specimens cut from the Inconel plates under plane stress conditions, at varying strain rates and temperatures. Fracture simulation through element erosion is based on Inconel-718 test results under many differing states of stress, which were created by differing test geometries and loading conditions. All of these tests were conducted by The Ohio State University (OSU) (Liutkus, 2014; Ressa A. M., 2015) and documented in an FAA report (Ressa, Liutkus, Seidt, Gilat, & Cordasco, 2023). A test from each rate, temperature, and stress-state condition was simulated and the results were correlated to the test results. Material directional anisotropy and tension compression anisotropy were observed in the tests and were not modeled at this time.

A series of tests, using tool steel projectiles that impact Inconel-718 plates, were performed at NASA Glenn Research Center (Pereira, Revilock, & Ruggeri, 2020). These ballistic impact tests were used to verify and validate the *MAT_224 Inconel-718 models. In the 12.7 mm plate thickness tests where fracture occurred, the dominant failure mode was an adiabatic shear band (ASB). An initial Inconel-718 model was created using an approach that had previously been successful (Haight, Wang, Du Bois, Carney, & Kan, 2016; Park, Carney, Du Bois, Cordasco, & Kan, 2020). However, this initial model did not predict any fracture or rupture at velocities at or near the tested velocities.

A new capability was developed to predict ASBs using practical element sizes, and it was added to *MAT_224. The new capability raises the Taylor-Quinney coefficient (TQC), β, in regions where high shear strain, in combination with a high strain rate, make the formation of an ASB likely. The TQC, β, can now be defined as a function of the ASB initiation shear strain and strain rate, and the element size. These functions can be specified precisely using a multi-dimensional table input. This new capability has been described in previous publications and will not be presented in detail here (Dolci, 2022; Dolci, et al., 2023). Using the tabular β, the modified material model can simulate the appearance of ASB for a variety of practical element sizes.

There remains a degree of uncertainty in the higher temperature, quasi-static behavior of Inconel-718. As a result, two different Inconel-718 input parameter sets are presented, both having been validated using the ballistic impact tests. In addition to the Inconel-718 input parameters using the units presented in this report (millimeter, millisecond, kilogram, kilonewton), the input parameters are also available in SI units (meter, second, kilogram, newton) and in English units (inch, second, lbf/s^2, lbf) (LS-DYNA Aerospace Working Group (AWG), 2023).

2 Methodology

The measured material properties of all metallic alloys, including Inconel-718, can vary significantly. One source of these variations is the manufacturing and post-manufacturing processes involved in plate creation. To maintain consistency, the Inconel-718 material was from a single batch, manufactured by a sole company. As a result, the mechanical property specimens and the ballistic impact specimens were the same material, reducing variations. The material certification sheets can be found in ballistic impact report appendix (Pereira, Revilock, & Ruggeri, 2020).

The 12.7mm (0.5 inch) rolled plate metal Inconel-718 was modeled using *MAT_224 in LS-DYNA®. *MAT_224 uses an isotropic elasto-thermo, visco-plastic constitutive law that defines stress as being dependent on strain, strain rate, and temperature:

$$\sigma_{ij} = \sigma_{ij}\left(\varepsilon_{ij}, \dot{\varepsilon}_{ij}, T\right) \qquad 1$$

where σ_{ij} is stress, $\varepsilon_{(ij)}$ is strain, $\dot{\varepsilon}_{(ij)}$ is the strain rate, and T is the temperature. In the elastic region, the Jaumann rate of the stress tensor, σ_{ij}^{∇}, is a linear function of elastic strain rates:

$$\sigma_{ij}^{\nabla} = \lambda\left(\dot{\varepsilon}_{kk} - \dot{\varepsilon}_{kk}^{p}\right)\delta_{ij} + 2\mu\left(\dot{\varepsilon}_{ij} - \dot{\varepsilon}_{ij}^{p}\right) \qquad 2$$

where $\dot{\varepsilon}_{ij}^p$ are the components of the plastic strain rate tensor and λ and μ are Lamé constants. The Lamé constants are related to the Elastic modulus and the Poisson's ratio as follows:

$$E = \frac{\mu(3\lambda + 2\mu)}{\lambda + \mu} \qquad\qquad 3$$

$$\nu = \frac{\lambda}{2(\lambda + \mu)} \qquad\qquad 4$$

The Elastic modulus of the *MAT_224 Inconel-718 material model will use 210 GPa (Special metals INCONEL Alloy 718).

In the plastic region, the material response is governed by a von Mises-type yield surface in six-dimension stress-space, which can expand and/or contract due to strain hardening, rate effects and thermal softening:

$$\sigma_{vm}(\sigma_{ij}) \le \sigma_y\left(\varepsilon_{ij}^p, \dot{\varepsilon}_{ij}^p, T\right) = \sigma_y\left(\varepsilon_{eff}^p, \dot{\varepsilon}_{eff}^p, T\right) \qquad\qquad 5$$

where σ_{vm} is the Von Mises stress, ε_{eff}^p is the equivalent plastic strain and $\dot{\varepsilon}_{eff}^p$ is the equivalent plastic strain rate. Since *MAT_224 is an isotropic material model, the yield surface's dependency on the plastic strain and plastic strain rate can be expressed as a function of the second invariant of each tensor. Stress-states on the yield surface are plastic, whereas states below the yield surface are elastic. Mathematically these relationships can be expressed as follows:

$$\sigma_{vm}(\sigma_{ij}) - \sigma_y\left(\varepsilon_{eff}^p, \dot{\varepsilon}_{eff}^p, T\right) \le 0$$

$$\dot{\varepsilon}_{eff}^p \ge 0$$

$$\dot{\varepsilon}_{eff}^p \cdot \left(\sigma_{vm}(\sigma_{ij}) - \sigma_y\left(\varepsilon_{eff}^p, \dot{\varepsilon}_{eff}^p, T\right)\right) = 0 \qquad\qquad 6$$

An associated flow rule is used, where the plastic strain increment vector is normal to the yield surface. The plastic strain rates are determined using associated flow, leading to the well-known plastic incompressibility condition typical of metals:

$$\dot{\varepsilon}_{ij}^p = \dot{\varepsilon}_{eff}^p \frac{\partial \sigma_{vm}}{\partial \sigma_{ij}} \Longrightarrow \sum_{k=1}^{3} \dot{\varepsilon}_{kk}^p \equiv 0$$

2.1   Stress strain relationships

A stress-strain relationship that is an accurate representation of a material's true properties is critical to physical simulations. In the extraction of the material's true mechanical properties from test data, several challenges exist that, unless great care is taken, hinder the accuracy of material models. The process that meets these challenges has been documented (Haight, Wang, Du Bois, Carney, & Kan, 2016). In short, stress-strain curves must be created by simulating the mechanical property tests, and by iteration, modifying the input parameters until a precise match to the tests are achieved. Note that in *MAT_224, stress versus plastic strain curves are input. This process was followed, and an accurate Inconel-718 was created.

2.2   Thermal dependency table

The method briefly presented in Section 2.1 is valid for all quasi-static, isothermal, uniaxial tensile tests, independent of the temperature at which they were performed. The quasi-static testing is ideally performed at a low enough strain rate such that the process is isothermal and no thermo-mechanical coupling occurs during the experiment. This is because *MAT_224 requires isothermal stress-strain input curves. Yield curves are created for each temperature at which testing was conducted, and are allocated to that specific temperature. A table of isothermal, temperature-dependent yield curves is assembled. This table can represent the change of material plasticity properties due to changes in temperatures.

2.3   Strain rate dependency table

Strain rate is never constant in a test where there is localization. Although the strain rate is uniform over the sample before necking occurs, the rate increases significantly after the localization of necking begins. Localization is especially early and extreme in the higher strain rate Inconel-718 tests. The strain rate in the region of localization may reach values significantly above the nominal strain rate for the specimen. Since *MAT_224 requires isorate input, the stress-strain curves must be derived from the test data by an iterative simulation process. The measured displacement time history from the test is used as input to the simulation. The simulation must then reproduce the strain rates that occurred in each test, as well as the stresses and strains.

It is not possible to perform tension tests at high strain rates corresponding to rates seen in impacts. So, tension test data must be supplemented with synthetic curves generated using rate sensitivity trends from compression tests. The synthetic curves are created using a combination of information from the compression and tension tests. These synthetic curves are combined with the stress-strain curves derived directly from the tension tests. Additional trial-and-error iterations may be required before the outcome is a close match between the test and the analysis results.

The tension and compression tests were performed by OSU (Liutkus, 2014; Ressa A. M., 2015; Ressa, Liutkus, Seidt, Gilat, & Cordasco, 2023). Examining the stress at 5% strain across all tests, categorized by nominal strain rates, demonstrates the strain rate sensitivity (Figure 1). At any given strain rate, there is a noticeable difference between tension and compression strengths. The strain rate abscissa is plotted on a logarithmic scale.
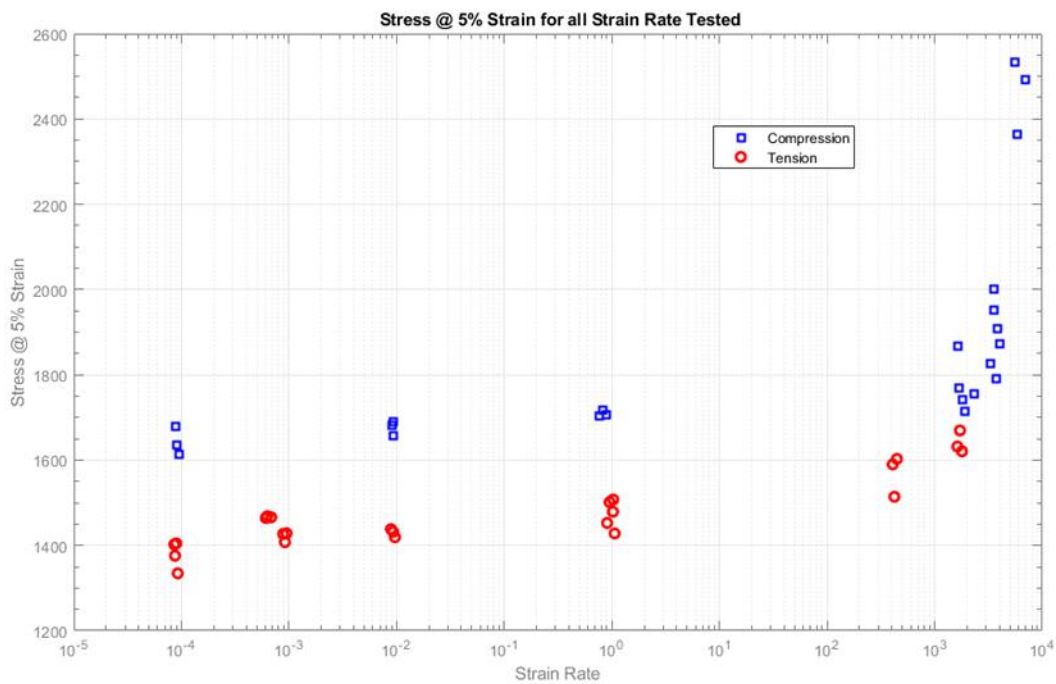
Figure 1. Stress at 5% strain for all strains tested

The strain-rate sensitivity was derived from the compression tests because of the greater strain rate range. The compression tests also have the advantage of having similar test configurations in the varying strain rates. In addition, they maintain a more constant strain rate than the tension tests because of relatively smaller localization. Figure 2 shows the stress at 5% strain of the offset compression and tension tests. The strain rate sensitivity matches the trend seen in many

5

materials, with the yield strength increasing as a logarithmic function of strain rate between rates of $\sim 10^{-4}\ s^{-1}$ and $\sim 10^3 s^{-1}$, and at strain rates greater than $\sim 10^3 s^{-1}$ the stress increases as a linear function of the increase in strain rate. This transition occurs due to a change in the physical processes causing the rate sensitivity (Carney, Pereira, Revilock, & Matheny, 2009).
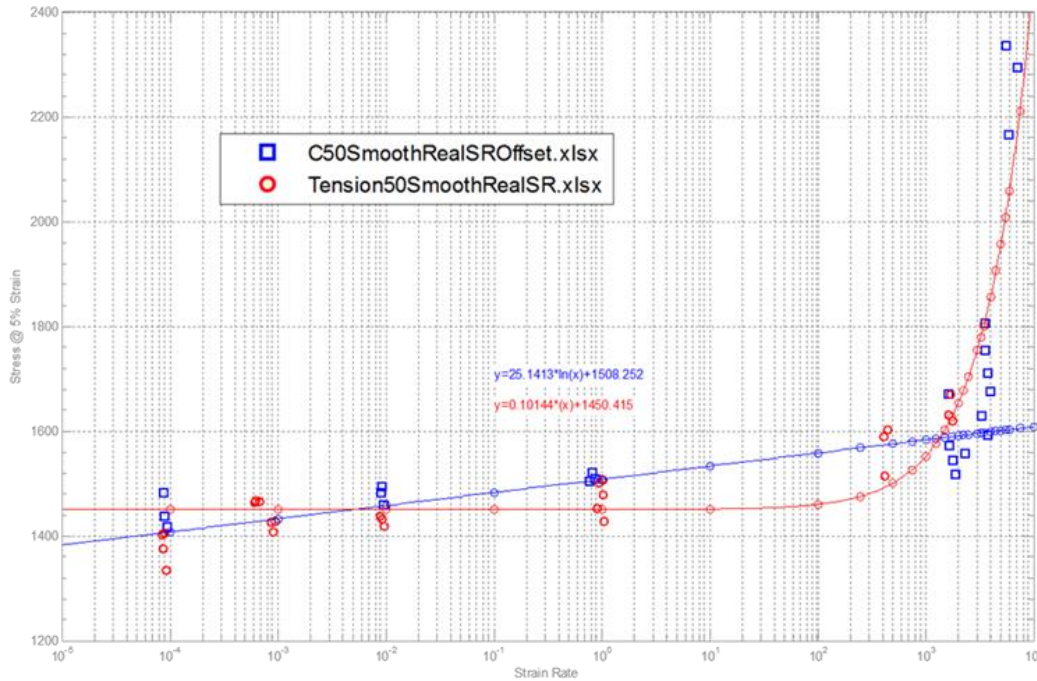
Figure 2. Stress at 5% strain. Separate curve fits for tension and compression

The initial curve fit is (y = 25.1413 ln (x) +1508.252 for the lower strain rates and y = .10144 x + 1450.415 for the higher strain rates) (Figure 2). As mentioned previously, the strain rates are not constant in tension tests, especially those with a nominal strain rate higher than ~10^3 s^{-1}. In addition, the physical processes causing a material's strain rate sensitivity at intermediate rates is transitioning, there is a combination of both the lower and higher rate physics. As a result, the stress-strain behavior for the higher rates cannot be obtained by the same procedure used to create the thermal sensitivity stress-strain curves. The strain rate sensitivity must be established by trial-and-error matching of all the tension test data. The initial sensitivity curve created using the two-separated curve fitting is shown in Figure 3.
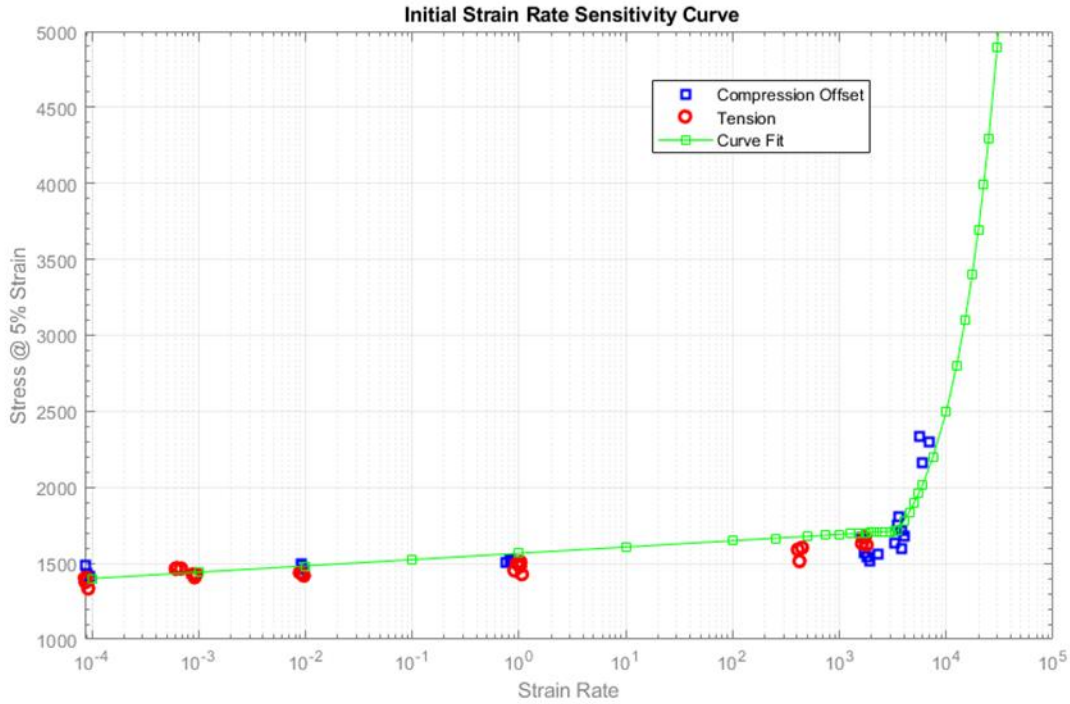
Figure 3. Initial strain rate sensitivity curve

As previously mentioned, the stress-strain input curves required by *MAT_224 must be both isothermal and isorate. The tests at the higher strain rates were neither, making the derivation of isothermal and isorate from these tests difficult. This is another reason why synthetic stress-strain curves are used. The synthetic stress-strain curve generated for the $10\ s^{-1}$ rates was used as the basis for all the higher rate curves. Each curve's stress was translated so that its stress at 5% strain was at the desired value. The synthetic curves at the tested strain rates are shown in Figure 4, with each curve represents the plastic strain vs. stress relationship corresponding to a nominal tested strain rate.
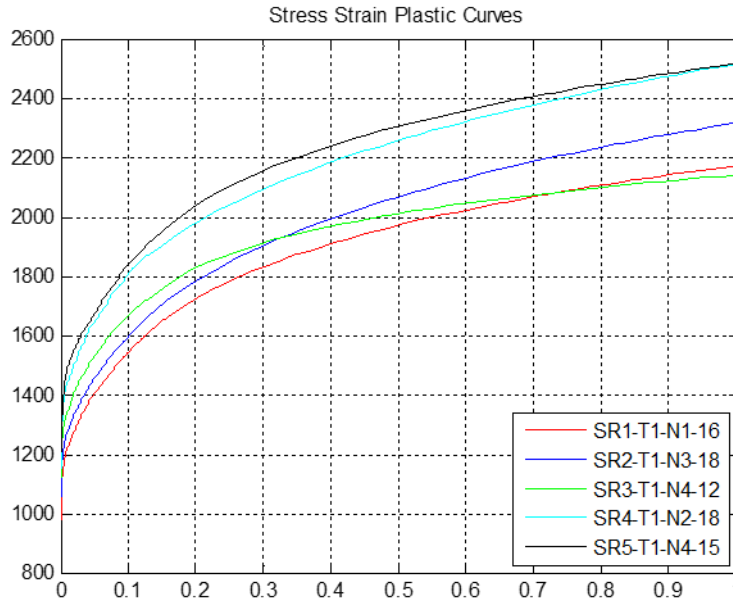
Figure 4. Stress-plastic strain of Inconel-718, varying strain rates

These curves were bundled together as a table for *MAT_224 input (Ansys LS-DYNA, 2023). Additional curves representing intermediate and higher strain rates were created translating the base curve to match the desired stress value at 5% strain. Intermediate curves are created internally by LS-DYNA® through interpolation between user input curves. Unlike material models which use curve-fitting to create an analytical formula for rate sensitivity, this method reads all the input curves and generates an internal yield surface numerically. Given the non-linear strain rate sensitivity, it is recommended that enough intermediate curves are defined to minimize large differences in stress offsets.

2.4   Conversion of plastic work into heat (Taylor-Quinney effect)

In the higher rate tests within the localized region of necking, there is not sufficient time for conduction to carry away the heat generated by the plastic deformation, and so the process is adiabatic. This adiabatic process causes a significant increase in the specimen's temperature locally, and governs the behavior at larger strains. As a result, simulation of the tension tests must consider the amount of energy generated by the plastic work, which is converted into thermal energy and temperature rise. The percentage of plastic work that is converted into thermal energy is defined by the Taylor-Quinney coefficient, typically signified as β. A nominal, constant β value of 0.8 was determined through trial-and-error, and matched the stress-strain test behavior exhibited in the tension tests.

A capability has been added to *MAT_224 that enables the simulation of ASBs in models with practical elements. This capability was realized through adding tabularized β input capability. Through a series of tables β is increased by an order of magnitude when the strain rate is high, and when the shear strain is high. When these conditions are met β is increased, mimicking the temperature rise in ASBs, and allowing the prediction of an ASB (Dolci, 2022; Dolci, et al., 2023). The nominal β value of 0.8 holds for all other conditions.

3 Material model creation by simulation of mechanical property tests

3.1 Test data

The documentation of each test includes time, force, displacement, and strain data. Each test includes test setup data, including exact measured specimen dimensions. DIC imagines at the beginning and at the time of rupture are provided, as well as videos showing the full-field strain in the tests. The tests in Table 1 (Ressa A. M., 2015) are provided by J. Seidt of Ohio State University. These tests are documented in a separate FAA technical report, DOT/FAA/TC-23-52 (Ressa, Liutkus, Seidt, Gilat, & Cordasco, 2023) and were conducted by Liutkus (2014) and Ressa (2015).

Table 1. Test series for 0.5" plate provided by Ohio State University

Test Series	Test Name	Nominal Strain Rate [1/s]	Apparatus	Plate Stock	Specimen geometry	Specimen Orientation	Temp [C]
Tension Strain Rate Dependence	M3-TMT-P4-SG1-O1-SR1-T1-N1	1.00E-04	Instron	0.5"	Flat Dogbone	Rolled	RT
	M3-TMT-P4-SG1-O1-SR1-T1-N2						
	M3-TMT-P4-SG1-O1-SR1-T1-N3						
	M3-TMT-P4-SG1-O1-SR1-T1-N4						
	M3-TMT-P4-SG1-O1-SR2-T1-N1	1.00E-02					
	M3-TMT-P4-SG1-O1-SR2-T1-N2						
	M3-TMT-P4-SG1-O1-SR2-T1-N3						
	M3-TMT-P4-SG1-O1-SR3-T1-N1	1.00E+00					
	M3-TMT-P4-SG1-O1-SR3-T1-N3						
	M3-TMT-P4-SG1-O1-SR3-T1-N4						
	M3-TMT-P4-SG1-O1-SR3-T1-N6						
	M3-TMT-P4-SG1-O1-SR3-T1-N7						
	M3-TMT-P4-SG1-O1-SR4-T1-N2	5.00E+02	SHB				
	M3-TMT-P4-SG1-O1-SR4-T1-N4						
	M3-TMT-P4-SG1-O1-SR4-T1-N5						
	M3-TMT-P4-SG1-O1-SR5-T1-N3	2.00E+03					
	M3-TMT-P4-SG1-O1-SR5-T1-N4						
	M3-TMT-P4-SG1-O1-SR5-T1-N5						

Test Series	Test Name	Nominal Strain Rate [1/s]	Plate Stock	Specimen geometry	Specimen Orientation	Temp [C]
Compression Strain Rate Dependence	M3-TMC-P4-SG1-O1-SR1-T1-N1	1.00E-04	0.5"	Flat Dogbone	Rolled	RT
	M3-TMC-P4-SG1-O1-SR1-T1-N2					
	M3-TMC-P4-SG1-O1-SR1-T1-N3					
	M3-TMC-P4-SG1-O1-SR2-T1-N1	1.00E-02				
	M3-TMC-P4-SG1-O1-SR2-T1-N2					
	M3-TMC-P4-SG1-O1-SR2-T1-N3					

	M3-TMC-P4-SG1-O1-SR3-T1-N1						
	M3-TMC-P4-SG1-O1-SR3-T1-N2	1.00E+00					
	M3-TMC-P4-SG1-O1-SR3-T1-N3						
	M3-TMC-P4-SG1-O1-SR4-T1-N2						
	M3-TMC-P4-SG1-O1-SR4-T1-N3						
	M3-TMC-P4-SG1-O1-SR4-T1-N5	1.00E+03					
	M3-TMC-P4-SG1-O1-SR4-T1-N10						
	M3-TMC-P4-SG1-O1-SR4-T1-N11						
	M3-TMC-P4-SG1-O1-SR5-T1-N1						
	M3-TMC-P4-SG1-O1-SR5-T1-N2						
	M3-TMC-P4-SG1-O1-SR5-T1-N3	2.00E+03					
	M3-TMC-P4-SG1-O1-SR5-T1-N4						
	M3-TMC-P4-SG1-O1-SR5-T1-N5						
	M3-TMC-P4-SG1-O1-SR5-T1-N6						
	M3-TMC-P4-SG1-O1-SR7-T1-N1						
	M3-TMC-P4-SG1-O1-SR7-T1-N2	5.00E+03					
	M3-TMC-P4-SG1-O1-SR7-T1-N3						

Test Series	Test Name	Nominal Strain Rate [1/s]	Apparatus	Plate Stock	Specimen geometry	Specimen Orientation	Temp [C]
Tension Thermal Dependence	M3-TMT-P4-SG1-O1-SR6-T1-N1	1.00E-03	Instron	0.5"	Flat Dogbone	Rolled	RT
	M3-TMT-P4-SG1-O1-SR6-T1-N2						
	M3-TMT-P4-SG1-O1-SR6-T1-N3						
	M3-TMT-P4-SG1-O1-SR6-T1-N4						200
	M3-TMT-P4-SG1-O1-SR6-T1-N1						
	M3-TMT-P4-SG1-O1-SR6-T1-N2						
	M3-TMT-P4-SG1-O1-SR6-T1-N3						400
	M3-TMT-P4-SG1-O1-SR6-T1-N1						
	M3-TMT-P4-SG1-O1-SR6-T1-N3						
	M3-TMT-P4-SG1-O1-SR6-T1-N4						600
	M3-TMT-P4-SG1-O1-SR6-T1-N6						
	M3-TMT-P4-SG1-O1-SR6-T1-N7						
	M3-TMT-P4-SG1-O1-SR6-T1-N2						800
	M3-TMT-P4-SG1-O1-SR6-T1-N4						
	M3-TMT-P4-SG1-O1-SR6-T1-N5						

	M3-TMT-P4-SG1-O1-SR3-T2-N2						
	M3-TMT-P4-SG1-O1-SR3-T2-N3						200
	M3-TMT-P4-SG1-O1-SR3-T2-N4						
	M3-TMT-P4-SG1-O1-SR3-T2-N5						
	M3-TMT-P4-SG1-O1-SR3-T3-N1						
	M3-TMT-P4-SG1-O1-SR3-T3-N2	1.00E+00					400
	M3-TMT-P4-SG1-O1-SR3-T3-N3						
	M3-TMT-P4-SG1-O1-SR3-T4-N1						
	M3-TMT-P4-SG1-O1-SR3-T4-N2						600
	M3-TMT-P4-SG1-O1-SR3-T4-N4						
	M3-TMT-P4-SG1-O1-SR3-T4-N5						
	M3-TMT-P4-SG1-O1-SR3-T1-N1						
	M3-TMT-P4-SG1-O1-SR3-T1-N2						800
	M3-TMT-P4-SG1-O1-SR3-T1-N3						

3.2   Temperature effects

Twenty-nine tests measuring the effect of temperature on the Inconel-718 are listed in the *Tension Thermal Dependence* section of Table 1. Besides the room temperature tests, four additional temperature test sets are available: 200 °C, 400 °C, 600 °C and 800 °C. Each of these test sets contain data at two different strain rates. Simulations of these lower rate tests only used a single input stress-strain curve. This creates an analysis that is insensitive to strain rate. That allows the test displacement to be applied at an artificially high grip speed, which saves computational time.

In the test specimen models, the sample dimensions match the corresponding test specimens precisely. The simulation units are kg, mm, ms, kN, and GPa.

3.2.1 A question of high temperature brittleness in Inconel-718

The series of tests conducted at varying temperatures were conducted at strain rates of both 10^{-3} s^{-1} and 1 s^{-1}. In the tests at conducted at a strain rate of 10^{-3} s^{-1}, at the highest temperature (T5, 800C), the Inconel becomes relatively brittle, with rupture strains of less than 5% (Figure 5).
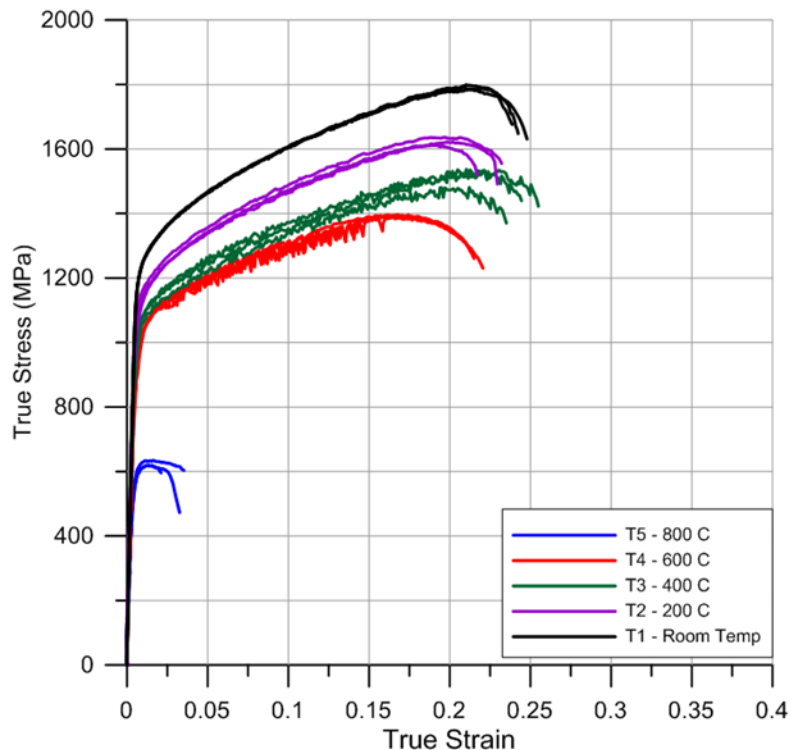

Figure 5. Experimental true stress vs. true strain of tension temperature dependency at strain rate 10^{-3} s^{-1}

1

However, in the test series conducted at a strain rate of 1 s^{-1}, at the highest temperature (T5, 800 °C), the behavior is in no way brittle, with greater ductility and rupture strains of over 30% (Figure 6).
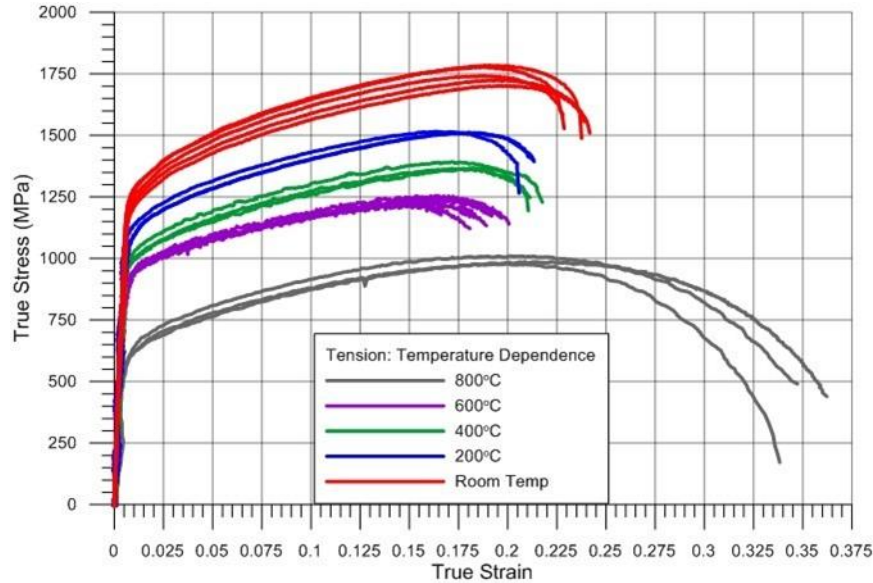

Figure 6. Experimental true stress vs. true strain of tension temperature dependency at strain rate 1 s^{-1}

So, in the 10^{-3} s^{-1} strain rate dataset there is brittle behavior at high temperature (T5 – 800 °C), while in the 1 s^{-1} strain rate dataset there is ductile behavior at the same temperature. There are no known differences in the testing methodology between the testing conducted at 10^{-3} s^{-1} and 1 s^{-1}. In both sets of data, multiple test repeats showed the same behavior. There is no reason to doubt that the noted difference is representative of Inconel-718 behavior. Note that in both strain rate datasets (Figure 5 and Figure 6), starting with the lowest temperature tests, there is a trend of lowering rupture strains with increasing temperature. These general trends towards greater brittleness are similar, until the highest temperature.

The brittle behavior observed in the 10^{-3} s^{-1} is due to recrystallization that can occur at higher temperatures in Inconel-718. This recrystallization leaves the material more brittle. The 10^{-3} s^{-1} strain rate tests are of longer duration; long enough time for the recrystallization to develop. It is possible that the time duration of the 1 s^{-1} tests is short enough that the recrystallization does not have time to develop. Recall that during localization, strain rates increase significantly, and so there is an associated temperature increase. Therefore, it is possible that in the 1 s^{-1} strain rate

tests there is time for recrystallization to occur, but the local temperature rise is high enough to prevent the recrystallization from developing; i.e., the Inconel is annealing.

Because of the noted different high temperature behaviors, and the uncertainty of the cause, two Inconel-718 material sets were developed, V1.1 and V1.2. V1.1 uses the brittle behavior at high temperatures. V1.2 uses the ductile behavior at high temperatures.

3.2.2 Stress strain relationship at room temperature

The three tests conducted at room temperature and a strain rate 10^{-3} s^{-1} are listed in Table 2. Test N2 (M3-TMT-P4-SG1-O1-SR6-T1-N2) was selected to represent this data subset and to undergo further processing. This selection was made using engineering judgment, which was based on data representation, smoothness, and that it was a monotonically increasing curve.

Table 2. Strain rate dependent series data of strain rate = 10^{-3} s^{-1}

Series	Test Name	Plate Stock	Specimen Geometry	Specimen Orientation	Strain Rate (s^{-1})	Temp (°C)
Tension Strain Rate Dependence	M3-TMT-P4-SG1-O1-SR6-T1-N1	0.5	Flat Dogbone	Rolled	1E-3	RT
	M3-TMT-P4-SG1-O1-SR6-T1-N2	0.5	Flat Dogbone	Rolled	1E-3	RT
	M3-TMT-P4-SG1-O1-SR6-T1-N3	0.5	Flat Dogbone	Rolled	1E-3	RT

The engineering stress vs. strain, and the true (logarithmic) stress vs. strain were provided by OSU. The true strain vs. stress curve was smoothed twice by an 18-point moving average. The stress was differentiated with respect to strain in order to determine the tangent modulus curve. The necking point is where the tangent modulus crosses the stress-strain curve. Another smoothing was performed on the tangent modulus curve to make the intersection clearer, as shown in Figure 7. The true stress-strain curve is only retained up till this point; the necking point.
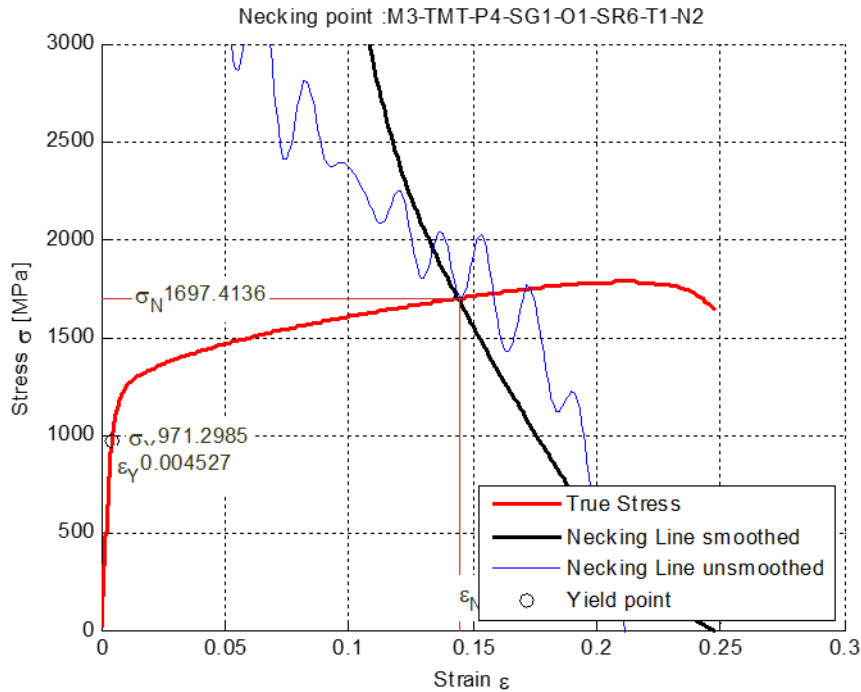
Figure 7. True stress strain relationship and the necking point
of strain rate = 10^{-3} s^{-1} (M3-TMT-P4-SG1-O1-SR6-T1-N2)

Beyond the necking point, 64 curves were generated by exponential extrapolation (Figure 8).
The extrapolation was performed using MATLAB. Each of the generated stress-strain curves
was used in a separate LS-DYNA® *MAT_224 keyword input.

The tension mechanical property test was simulated. The finite element mesh dimensions
matched the test sample's geometry exactly. The DATABASE_CROSS_SECTION option was
used to extract the cross-sectional force at the center of the specimen. A NODOUT file was
written that contained the displacements at two nodal points corresponding to the extensometer
location in the test. The difference in z displacement of these two nodal points gives the
elongation of the simulated extensometer. A cross-plot of this elongation with the cross-sectional
force can be directly compared to the force-displacement curve from the test.

The simulation is performed repeatedly using the extrapolated candidate input curves shown in
Figure 8, until one of them matches the force displacement response of the test. Stress-strain
curve number 24 gives the best match, as shown in Figure 9.
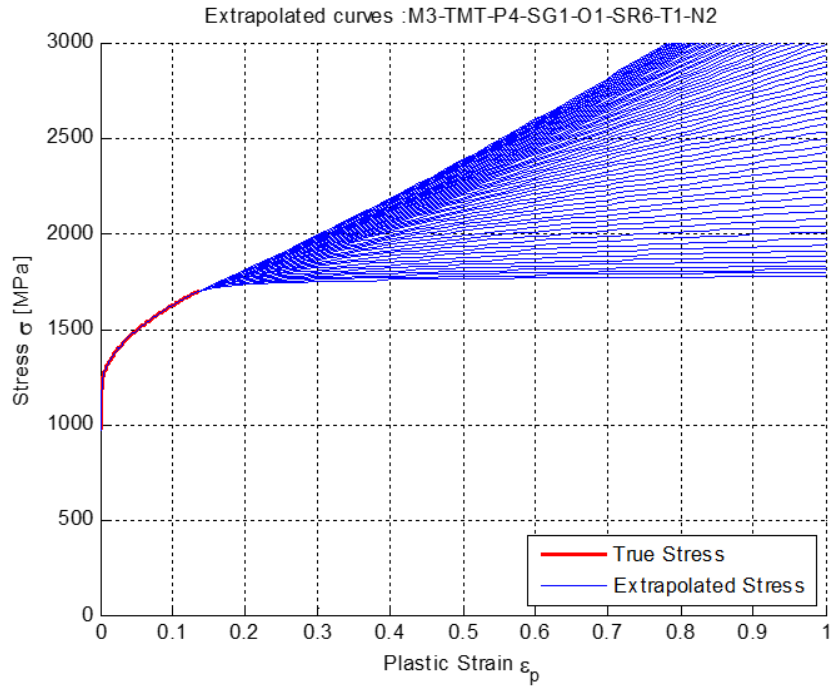
Figure 8. Plastic strain vs. stress relationship of strain rate $= 10^{-3}$ $^{s-1}$ (M3-TMT-P4-SG1-O1-SR6-T1-N2)
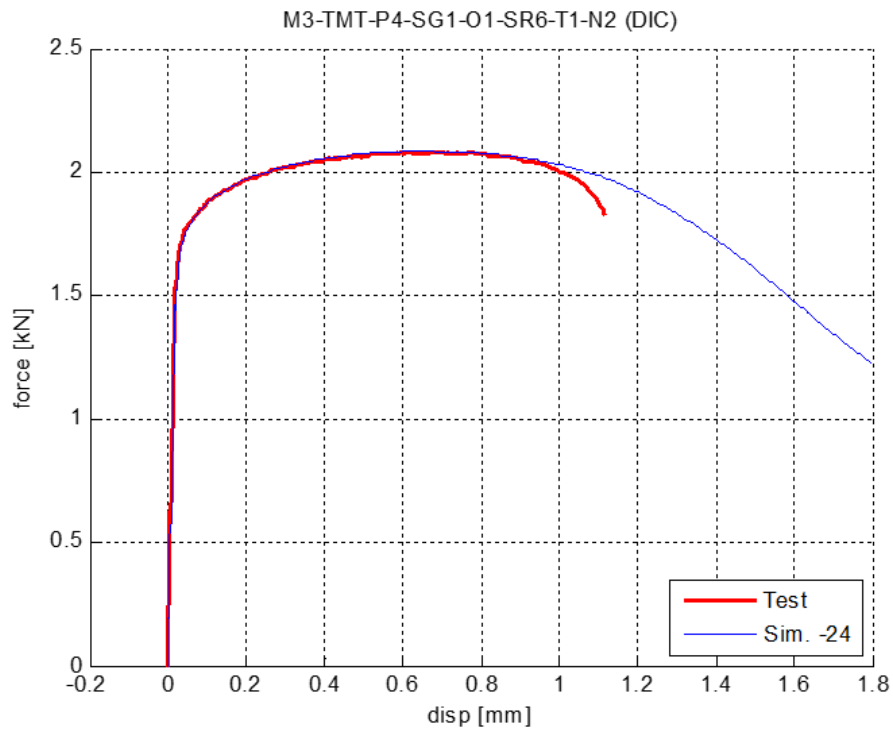

Figure 9. Force displacement result, Curve #24

Figure 10 compares the contour of 1st principal strain from the simulation using curve number 24 to the DIC strain image from the test. The time of both images is immediately before the onset of fracture. The comparison shows a good agreement between the simulation and test.
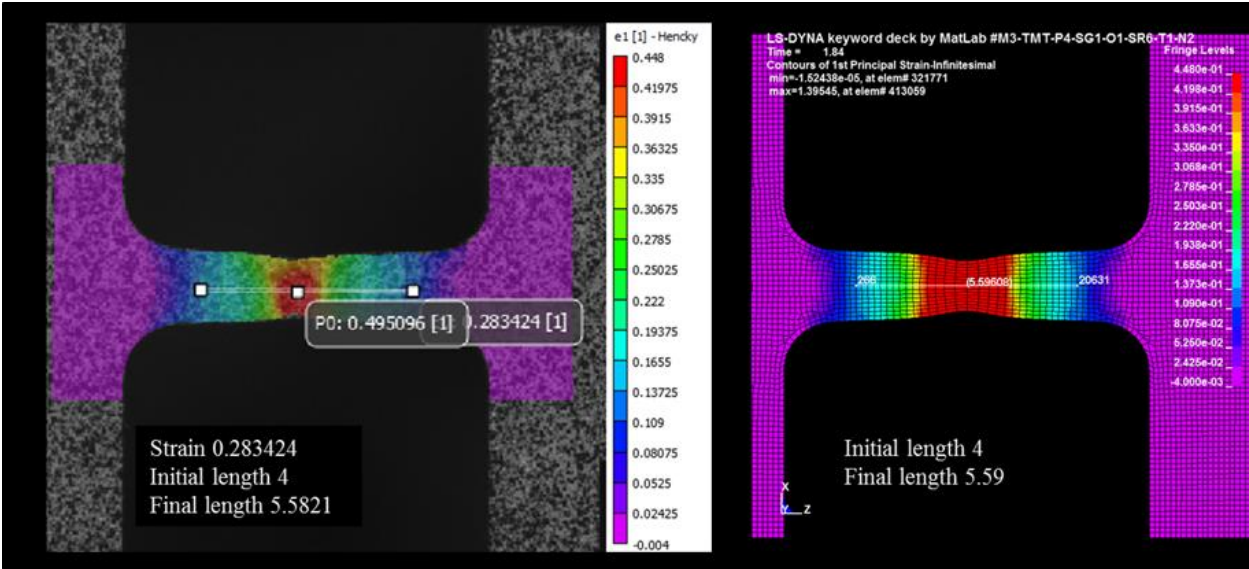

Figure 10. Left: plastic strain DIC image immediately before fracture, Right: 1st principal strain simulation contour immediately before fracture (M3-TMT-P4-SG1-O1-SR6-T1-N2); Strain rate = 10^{-3} s^{-1}

3.2.3 Stress strain relationship at other temperatures

In general, the Inconel-718 stress-strain curves at other, elevated temperatures were generated using the same extrapolation and selection method used in the creation of the room temperature curve, and presented in the previous Section 3.2.2. Isothermal, temperature-dependent stress-strain curves that represent Inconel-718's behavior at 200 °C, 400 °C, 600 °C, and 800 °C were generated. An extra, artificial curve at constant stress zero was added to represent Inconel-718's melting temperature, and aiding numerical stability.

As discussed in Section 3.2.1, the Inconel-718 material sets V1.1 and V1.2 use different stress-strain data at higher temperatures. The V1.1 model was developed using only data from tests provided by OSU (Figure 11). The V1.2 model also includes higher temperature data (1000 C/1273 K, 1100 C/1373 K), obtained from literature (Moretti, 2022), to increase the high temperature accuracy of the model (Figure 12). Additionally, curves for a temperature below what was tested, and two temperatures above what was tested, were added to the stress-strain

6

table in order to limit non-physical extrapolation. One of the higher temperature curves added represented the Inconel-718 melting point.
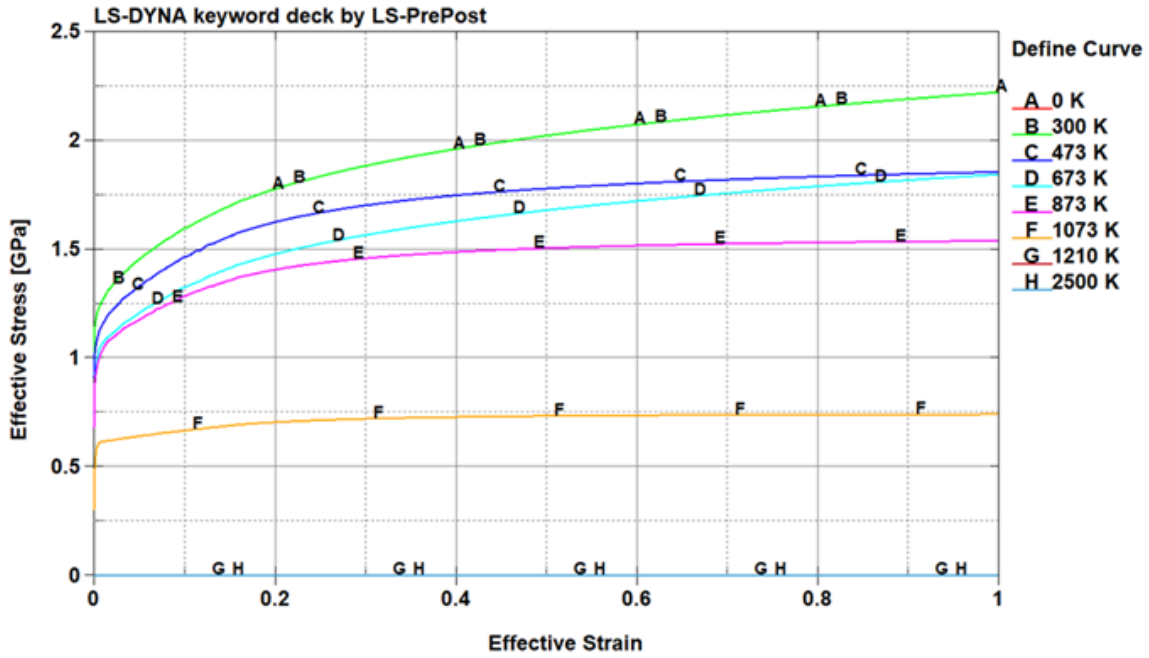

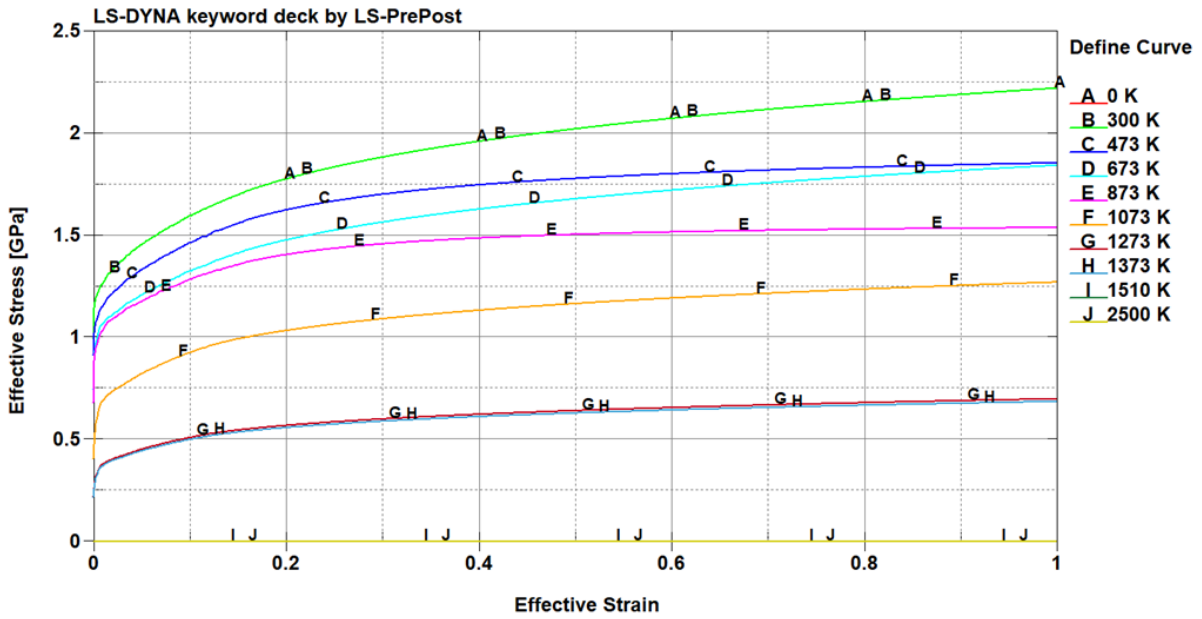Figure 11. V1.1 temperature dependent stress-strain input curves

Figure 12. V1.2 temperature dependent stress-strain input curves

7

The resulting force displacement comparisons of four different temperature tests (200 °C, 400 °C, 600 °C, and 800 °C) at a strain rate of 10^{-3} s^{-1}, and the simulation results using the V1.1 model, are shown next. The comparison between the 200 °C test and the V1.1 simulation is shown in Figure 13.
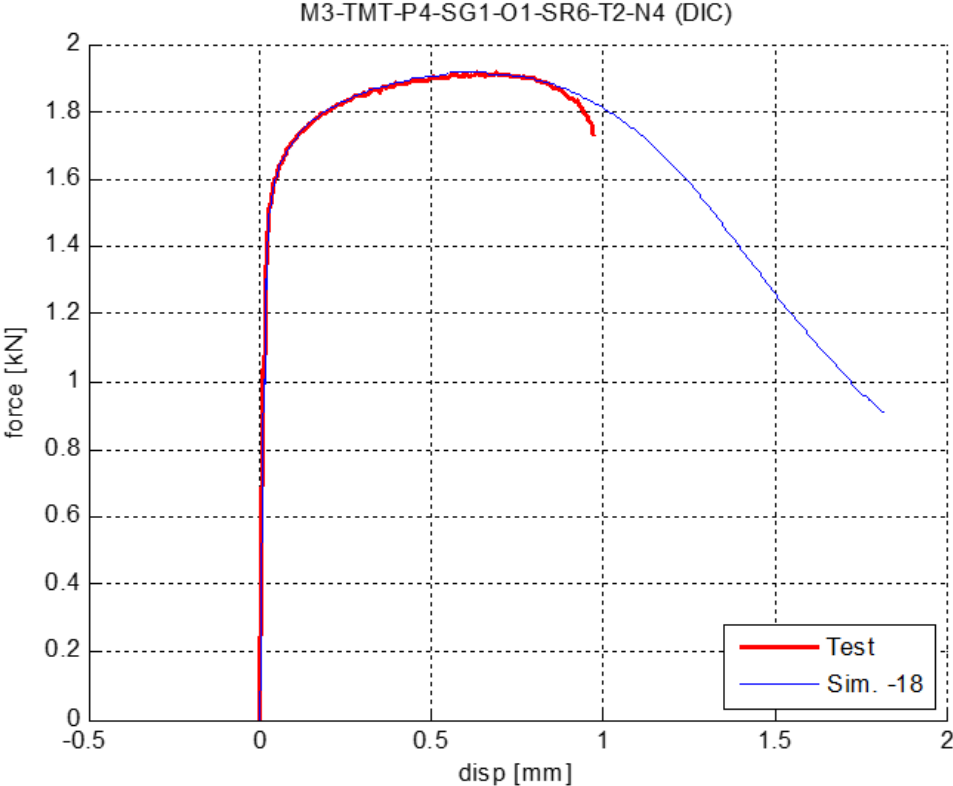
Figure 13. Force displacement comparison at strain rate = 10^{-3} s^{-1}, Temperature = 200 °C

The comparison between the 400 °C test and the V1.1 simulation is shown in Figure 14.
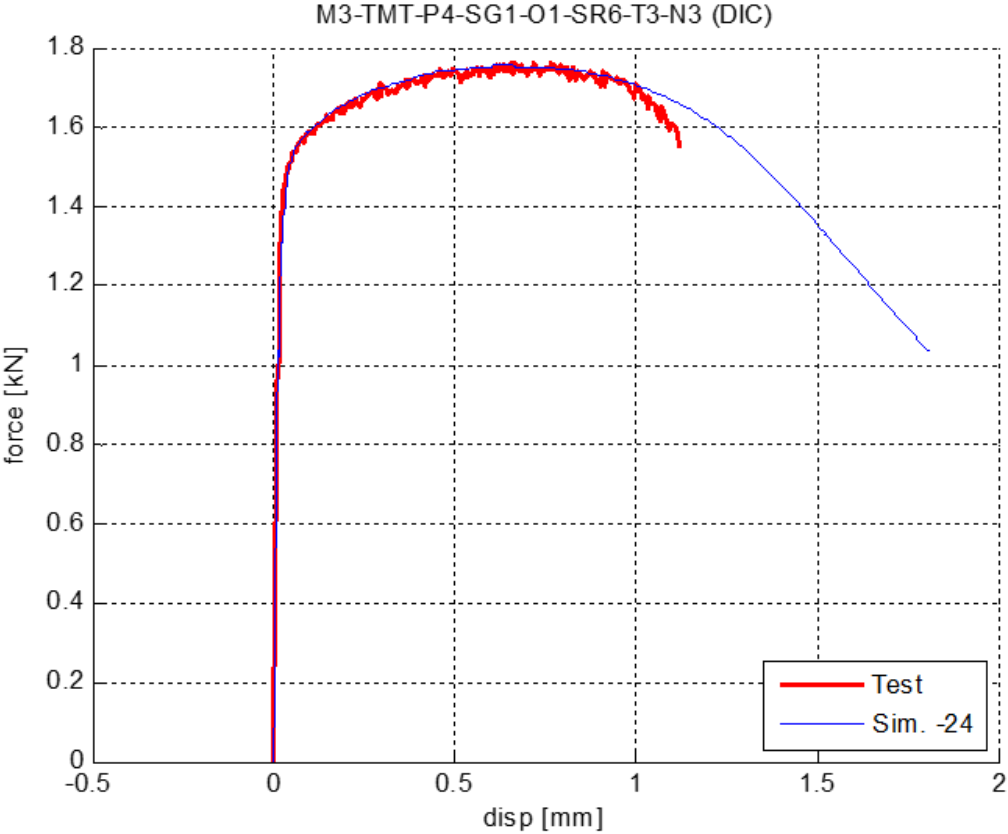
Figure 14. Force displacement comparison at strain rate = 10^{-3} s^{-1}, Temperature = 400 °C

The comparison between the 600 °C test and V1.1 simulation is shown in Figure 15.
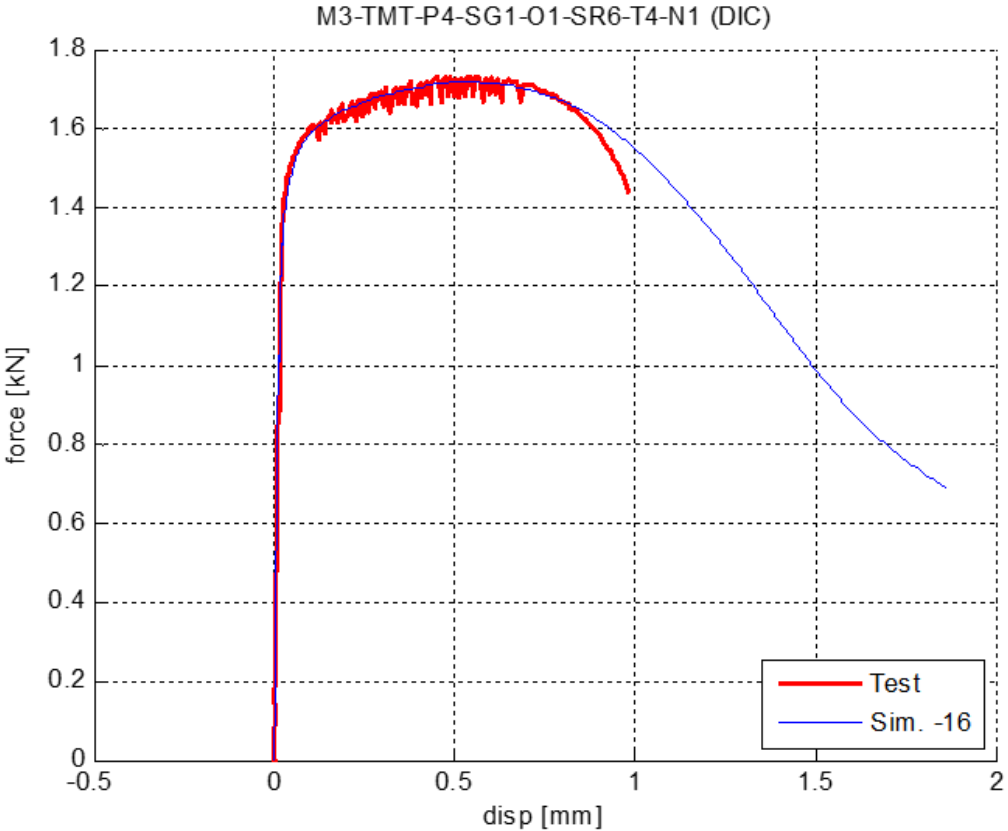
Figure 15. Force displacement comparison at strain rate = 10^{-3} s^{-1}, Temperature = 600 °C

The comparison between the 800 °C test at a strain rate of 10^{-3} s^{-1} and V1.1 simulation is shown in Figure 16.
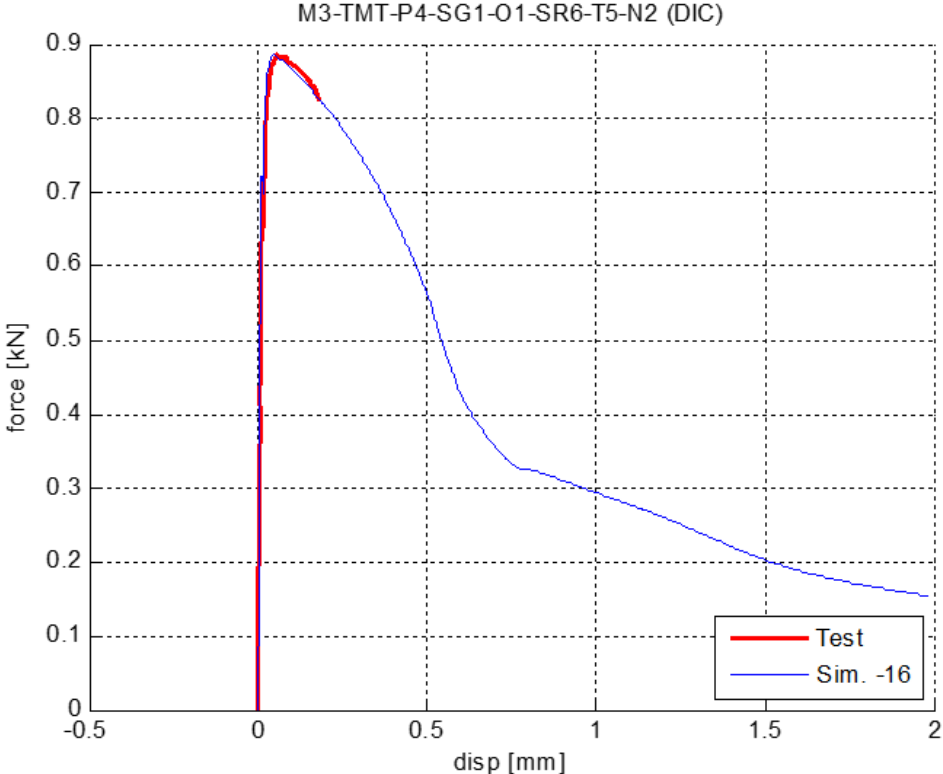
Figure 16. Force displacement comparison at strain rate = 10^{-3} s^{-1}, Temperature = 800 °C

The resulting force displacement comparison of the 800 °C test at a strain rate of 1 s^{-1} and the V1.2 model is shown in Figure 17. The 200 °C, 400 °C, and 600 °C V1.2 simulation results are very similar to V1.1, as are the test results, and these comparisons are not shown in this report.
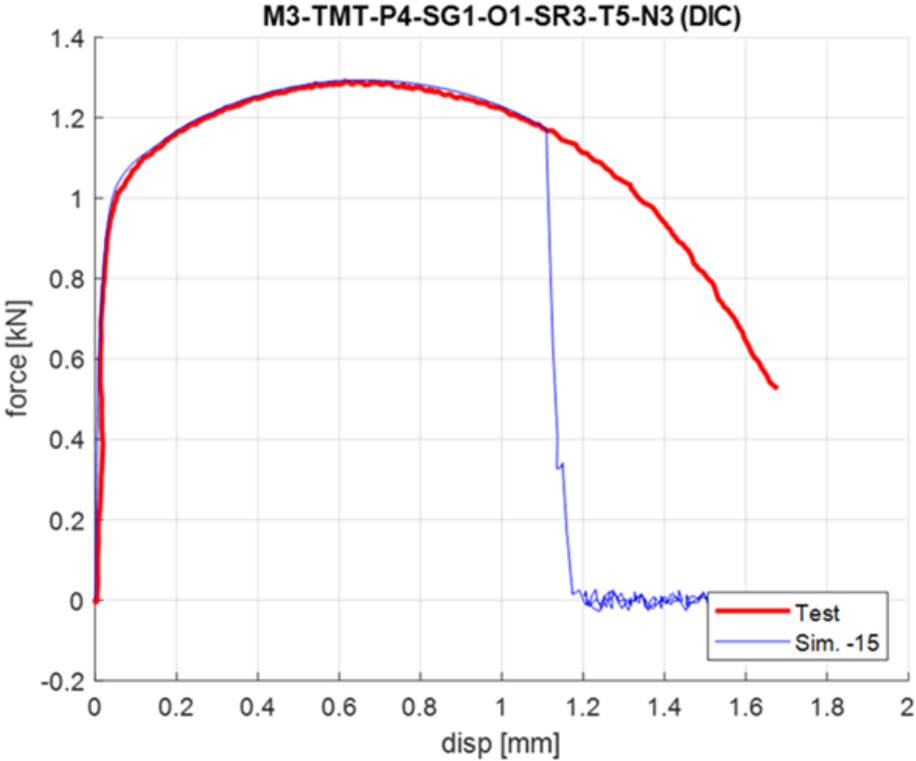
Figure 17. Force displacement comparison at strain rate = 1 s^{-1}, 800 C, V1.2 Inconel-718 model

The 1st principal strain contours of the DIC from the test at 200 °C and the simulation using V1.1, is shown in Figure 18.
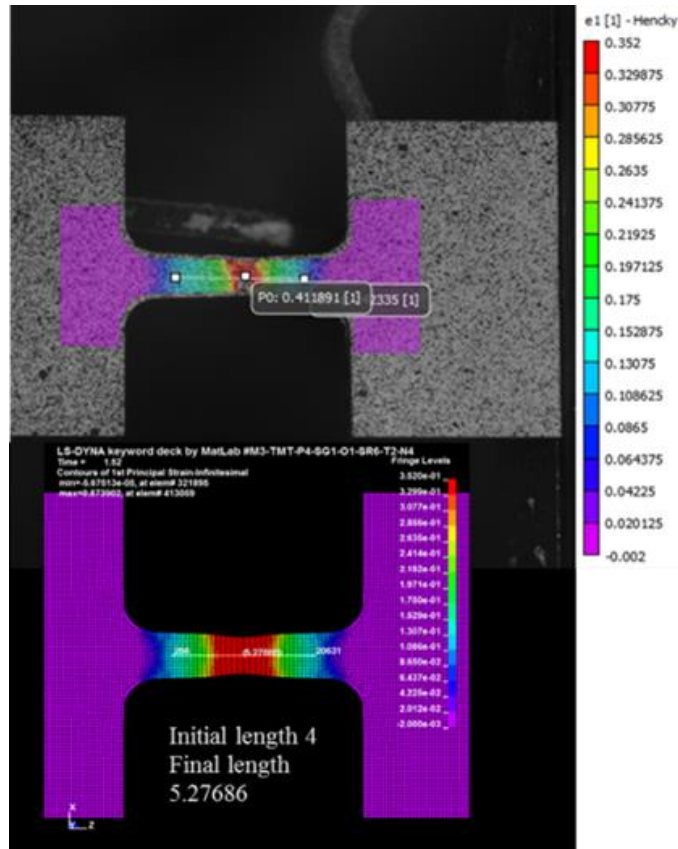
Figure 18. Simulation contour (bottom) and DIC image (top); (M2-TMT-P4-SG1-O1-SR6-T2-N4), Strain rate = 10^{-3} s^{-1}, Temperature = 200 °C

The 1st principal strain contours of the DIC from the test at 400 °C and the simulation using model V1.1 are shown in Figure 19.
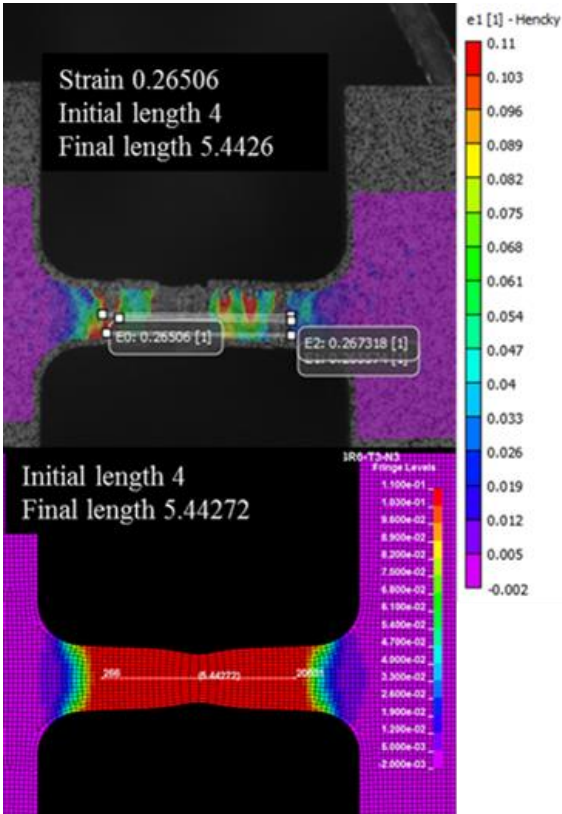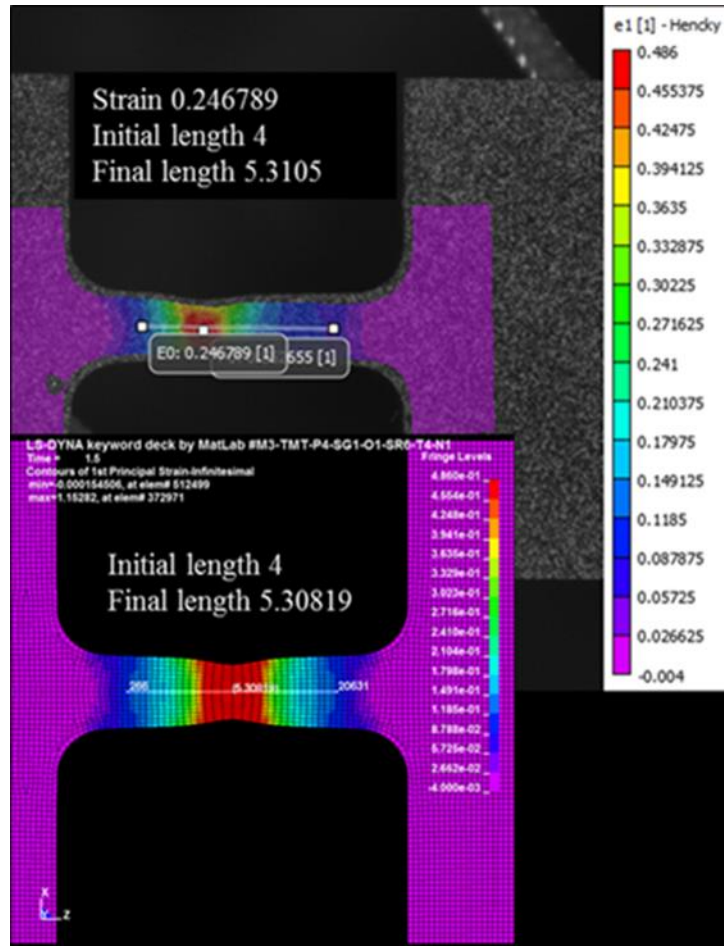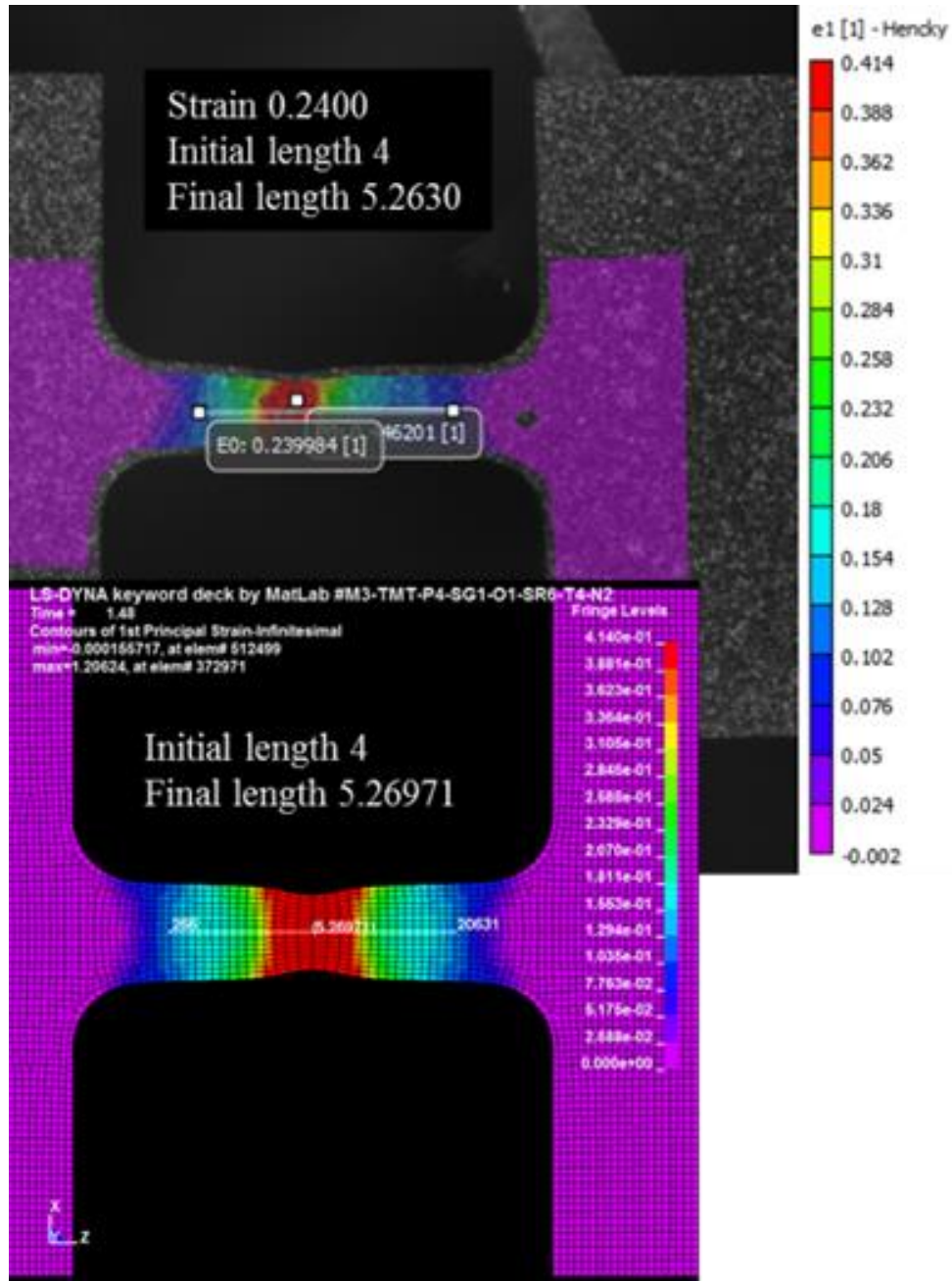

Figure 19. Simulation contour (bottom) and DIC image (top); (M3-TMT-P4-SG1-O1-SR6-T3-N1), Strain rate = 10^{-3} s^{-1}, Temperature = 400 °C

The 1st principal strain contours of the DIC from the test at 600 °C and the simulation using model V1.1 are shown in Figure 20.

Figure 20. Simulation contour (bottom) and DIC image (top) (M3-TMT-P4-SG1-O1-SR6-T4-N1); Strain rate = 10^{-3} s^{-1}, Temperature = 600 °C

The 1st principal strain contours of the DIC from the test at 800 °C and a strain rate of 10^{-3} s^{-1}, and the simulation using model V1.1 are shown in Figure 21.

Figure 21. Simulation contour (bottom) and DIC image (top)
(M3-TMT-P4-SG1-O1-SR6-T5-N2); Strain rate = 10^{-3} s^{-1}, Temperature = 800 °C

The 1st principal strain contours of the DIC from test at 800 °C, and a strain rate of 1 s^{-1}, and the simulation using model V1.2 is shown in Figure 22.
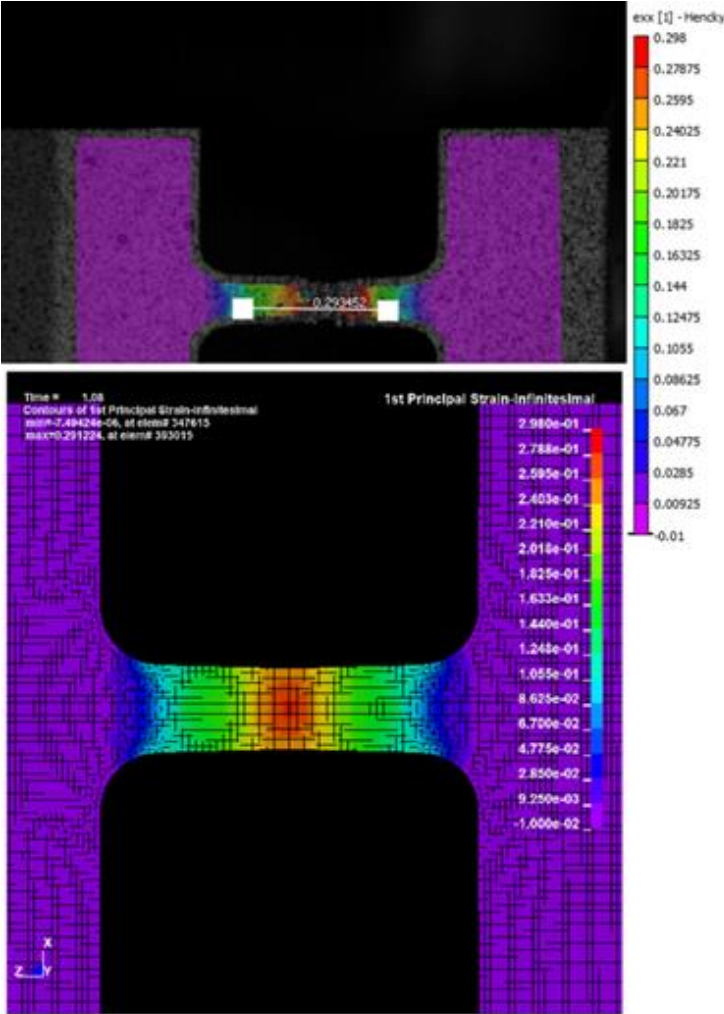
Figure 22. Simulation contour (bottom) and DIC image (top) (M3-TMT-P4-SG1-O1-SR3-T5-N3); Strain rate = 1 s-1; Temperature = 800 °C

All the comparisons of the DIC and simulation strain contours show excellent agreement.

3.3   Stress strain relationship at a single, nominal quasi-static strain rate

The three quasi-static tests conducted at a strain rate of 10^{-4} s^{-1} are listed in Table 3. Test M3-TMT-P4-SG1-O1-SR1-T1-N1 was selected as most representative of the tests at this strain rate. In the lower rate tests, flat dog-bone specimens were pulled at room temperature on the Instron machine. As previously presented in Section 3.2, the simulations presented here were performed with an arbitrary loading speed of 1 m/s, using a single stress-strain curve.

Table 3. Strain rate dependence series data of strain rate = 10^{-4} s^{-1}

Series		Test Name	Plate Stock (in)	Specimen Geometry	Specimen Orientation	Strain Rate (sec^{-1})	Temp (°C)
Tension Strain Rate	Dependence	M3-TMT-P4-SG1-O1-SR1-T1-N1	0.5	Flat Dogbone	Rolled	1.0E-04	RT
		M3-TMT-P4-SG1-O1-SR1-T1-N2	0.5	Flat Dogbone	Rolled	1.0E-04	RT
		M3-TMT-P4-SG1-O1-SR1-T1-N3	0.5	Flat Dogbone	Rolled	1.0E-04	RT

Following the same procedures discussed in Section 3.2.2, the true stress-strain curve was compared to the tangent modulus curve. The intersection between these two curves defines the necking point. The plastic strain at necking was determined to be 0.16332 mm/mm (Figure 23).
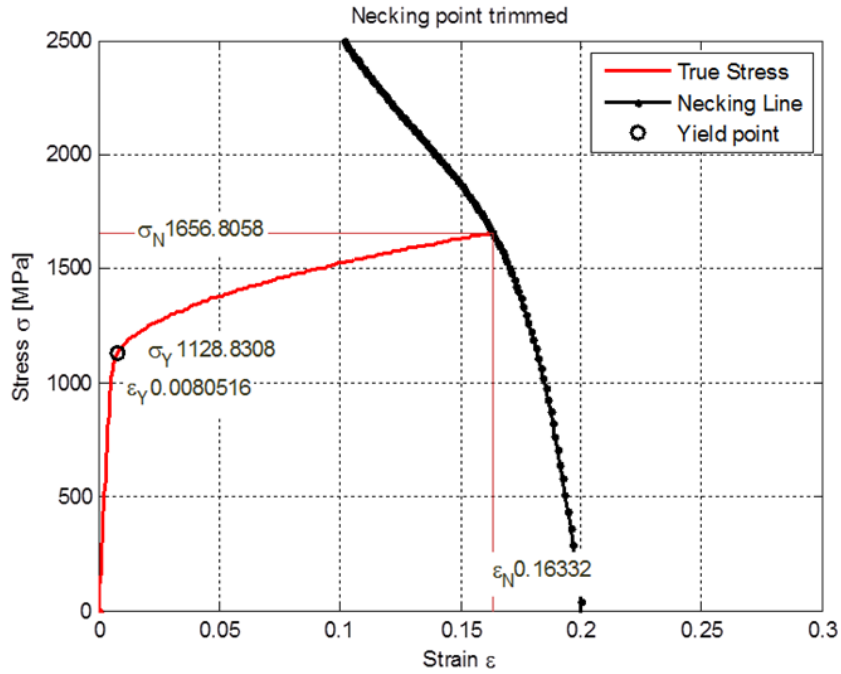
Figure 23. True stress-strain relationship and necking point judgment of strain rate $= 10^{-4}$ s^{-1} tests

A total of 32 trial curves were generated by exponential extrapolation (Figure 24). Each of the generated stress-strain curves were used to create a single curve *MAT_224 keyword input, and was used to perform a simulation of the tensile test.
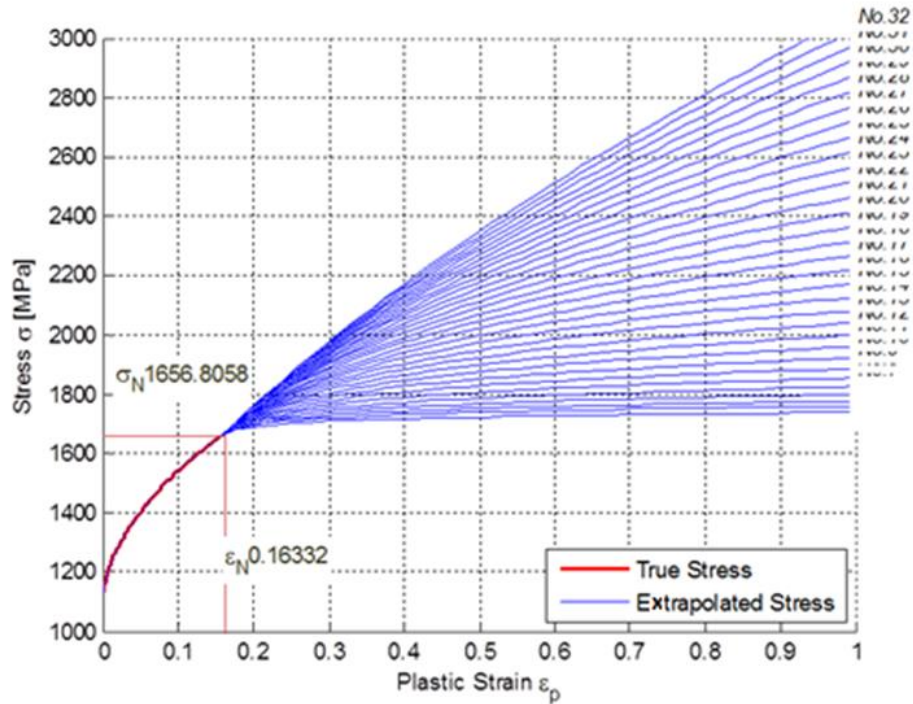
Figure 24. Plastic strain vs. stress extrapolation of strain rate = 10^{-4} s^{-1} (M2-TMT-P4-SG1-O1-SR1-T1-N1)

As described in Section 3.2, a cross-plot of elongation and cross-sectional force is compared to the force-displacement curve from the test. The simulations are repeated using each of the extrapolated candidate input curves, until a match to the test force-displacement curve is found (Figure 25). A simulation contour of 1st principal strain from this simulation is compared to the DIC image from the test at the time immediately before fracture, also with a good agreement (Figure 26).
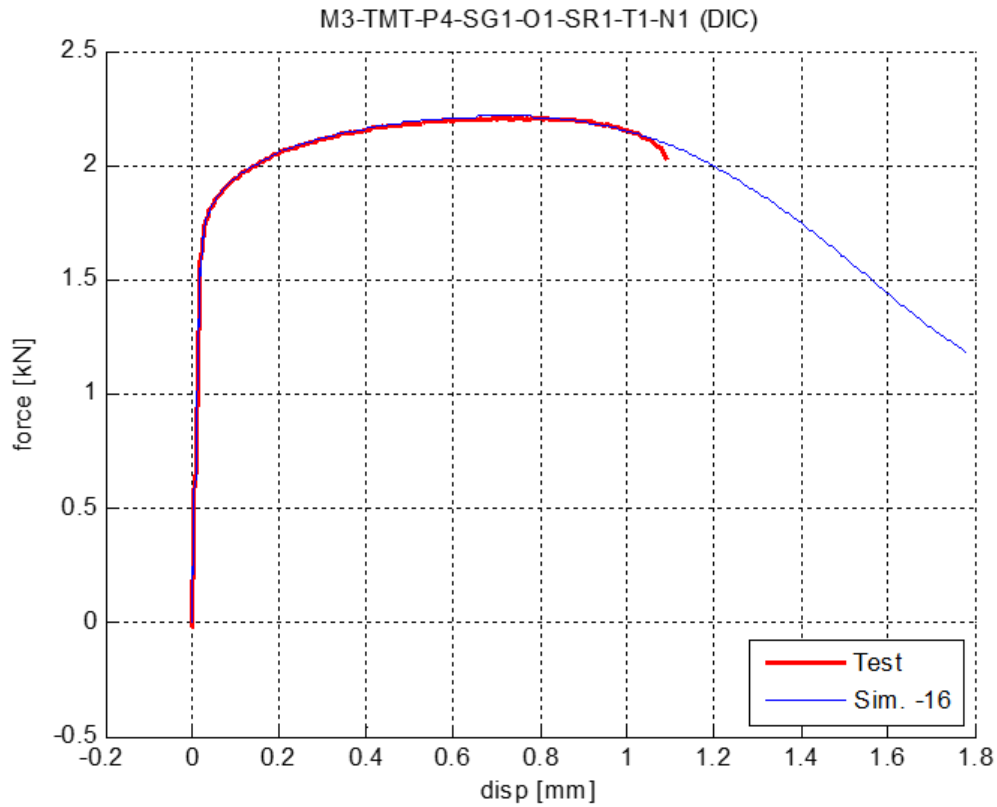
Figure 25. Force displacement result, Curve #16
(TMT-P4-SG1-O1-SR1-T1-N1)
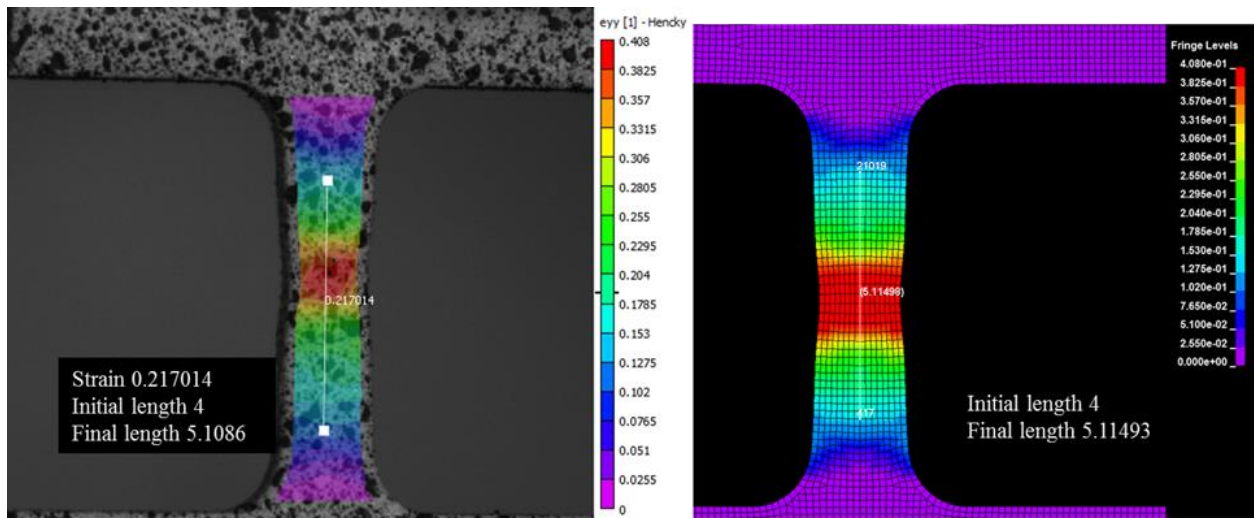
Figure 26. Left: Plastic strain DIC image immediately before fracture.
Right: 1st principal strain simulation contour immediately before fracture
(M3-TMT-P4-SG1-O1-SR1-T1-N1) Strain rate = 10^{-4} s^{-1}

3.4　Stress strain tabulated input of multiple strain rates and temperatures

The high strain rate testing used to create the higher rate Inconel-718 stress-strain curves is commonly referred to as split-Hopkinson (SHB) bar or Kolsky bar tests (Ressa A. M., 2015). This technique differs from lower rate testing in that, rather than a displacement-controlled test, the specimen undergoes impulsive loading. The impulsive loading and smaller test specimen size allow higher strain rates to be reached. A result of the impulsive loading, which affects the analysis, is that the test's nominal strain rate description of the actual, varying strain rate is even more imprecise than in the lower rate tests. Fortunately, the DIC strain measurements precisely give the actual strain rates, varying both spatially and temporally.

The process employed for creating higher rate stress-strain curves from a lower rate stress-strain curve, using the strain rate sensitivity measured in the higher rate tension and compression tests, was introduced in Section 2.3. *MAT_224 input stress-strain curves must be defined both at a constant temperature and at a constant strain rate. Due to this requirement for isorate and isothermal input curves, it is not practical to derive the higher rate input curves from the split-Hopkinson bar tests. Split-Hopkinson bar tests are neither isorate nor the isothermal. The lower rate tests are isothermal, and curves derived from them can be used as a base line for creating synthetic, high strain rate stress-strain curves. The 10^{-4} s^{-1} isothermal stress-strain curve served as the baseline for the Inconel-718 higher strain rate curves. For numerical accuracy, the number of higher rate curves created was more than the number of high strain rate tests.

The higher rate stress-strain curves were initially synthesized by appropriately offsetting the 10^{-4} s^{-1} baseline curve to match the stress at 5% strain of the higher rate responses, following the trend implied by the nominal strain rates. Since the nominal strain rates do not accurately reflect the varying strain rates occurring in a split-Hopkinson bar test, this initial set of curves will not produce simulations that match the higher rate tests. An iterative process is required where both the stress offset and the TQC, β, were varied simultaneously. The iterative process is additionally challenging because of the transitioning rate sensitivity between the logarithmic and linear regions (Section 2.3).

Every split-Hopkinson bar test contains unique information, as the range of strain rates occurring in each of these tests is unique. As a result, each of the 500 s^{-1} and 2000 s^{-1} nominal strain rate (SHP apparatus) tests in the *Tension Strain Rate Dependence* section of Table 1 was simulated multiple times, varying the stress offsets and β, until a satisfactory match to test data from each of the tests was achieved. Thirty-two iterations were performed before the simulation predictions matched all the high strain-rate test data. Force vs. displacement, strain rate vs. strain, and the

strain contours just before fracture, were compared. The initial rate sensitivity curve used to offset the baseline stress-strain curve (labeled KellyV09), and the final strain rate sensitivity curve resulting from the iterative process (labeled 32), are shown in Figure 27.
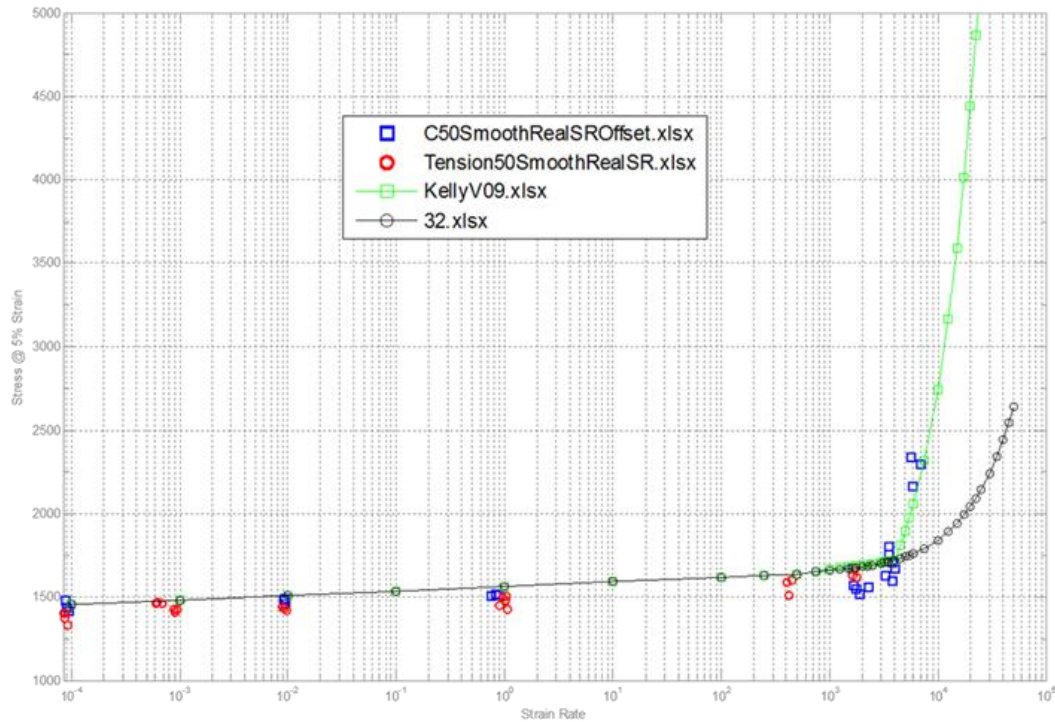

Figure 27. Stress at 5% strain as a function of strain rate; test and synthetic stress-strain curves

The complete table of all stress-strain curves were used in the *MAT_224 input in the split-Hopkinson bar test simulations. These simulations were performed by applying the test displacements taken from DIC as boundary conditions. The fixed end of the split-Hopkinson bar tension tests was not truly fixed, and the applied displacement at the translating boundary was most accurately defined by the DIC measured displacements. Three tests were conducted at the nominal strain rate of $500 \ s^{-1}$. All three of these tests were analyzed and comparisons were made to the physical test results.

Figure 28, Figure 29, and Figure 30 show a comparison of force vs. displacement, strain rate vs. strain, and strain contour plots between the simulation and test M3-TMT-P4-SG1-O1-SR4-T1-N2. With a nominal strain rate of $500 \ s^{-1}$, in the region of localization, the strain rate reached almost $4000 \ s^{-1}$.
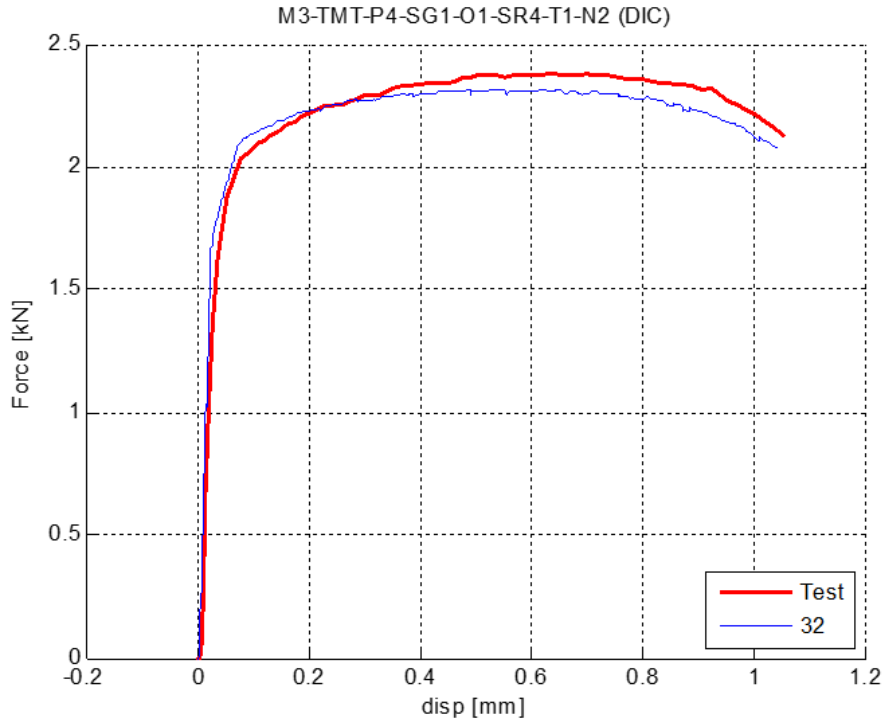
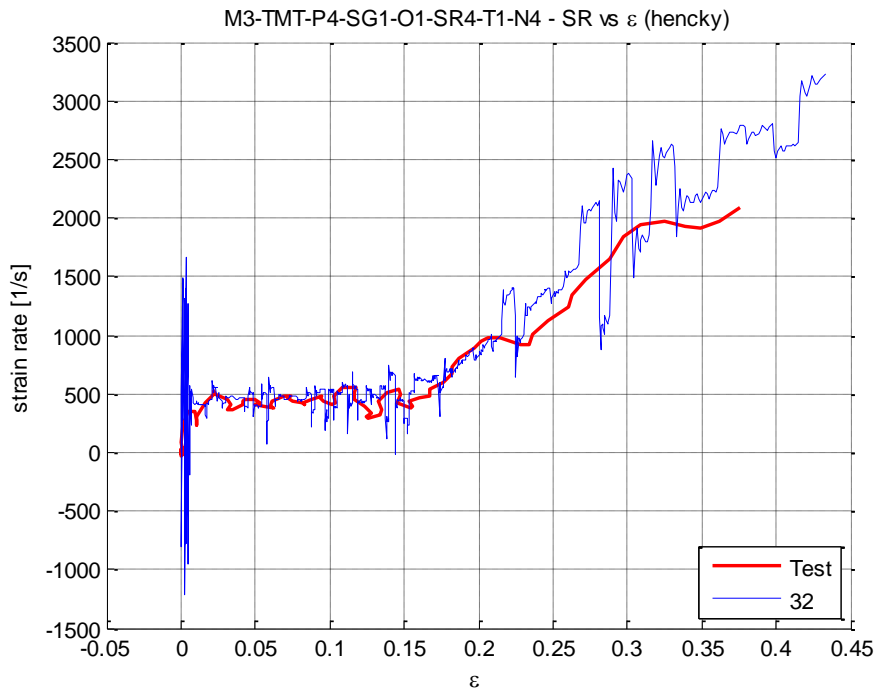Figure 28. Force vs. displacement (M3-TMT-P4-SG1-O1-SR4-T1-N2)
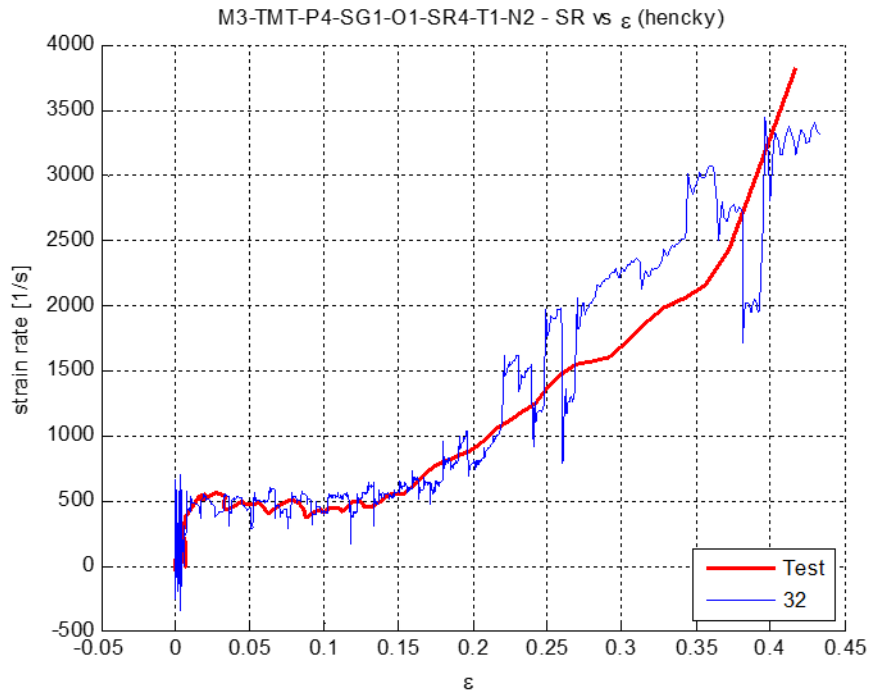
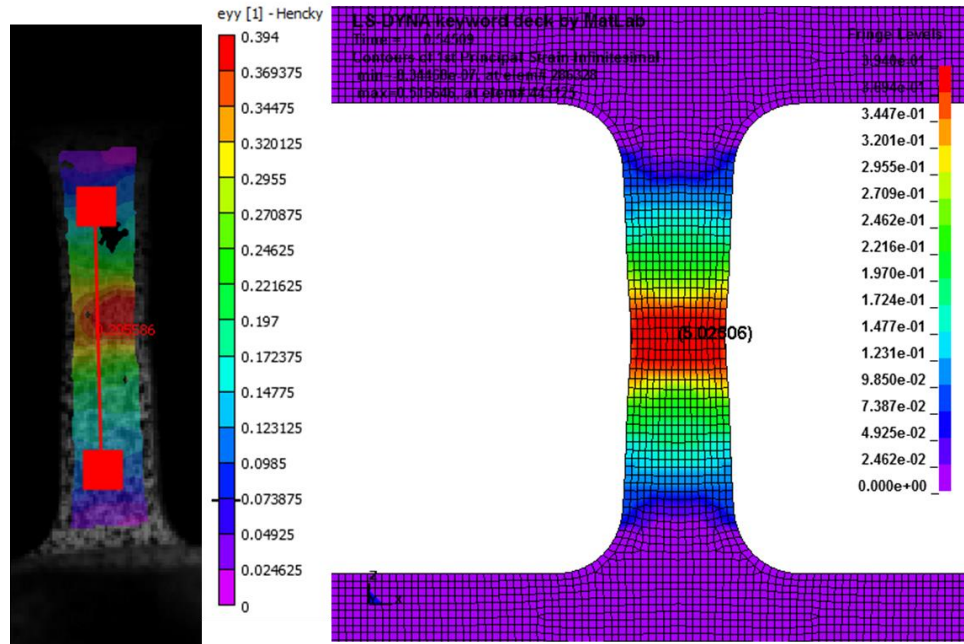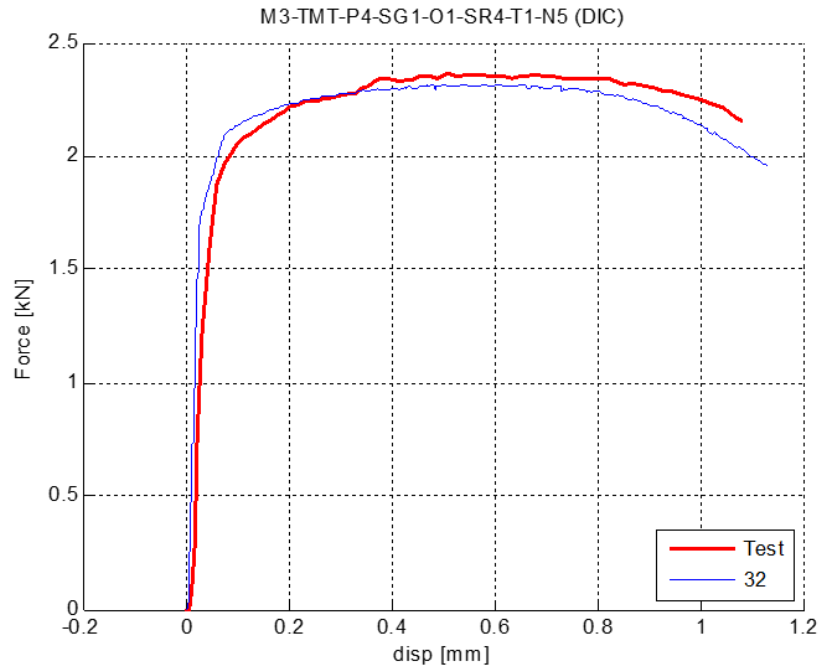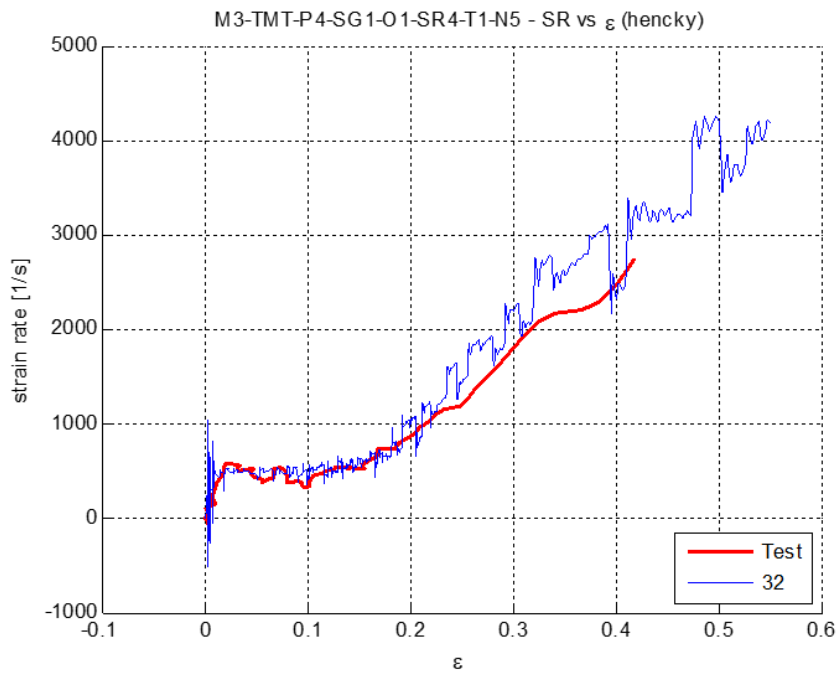Figure 29. Strain rate vs. strain (M3-TMT-P4-SG1-O1-SR4-T1-N2)

24
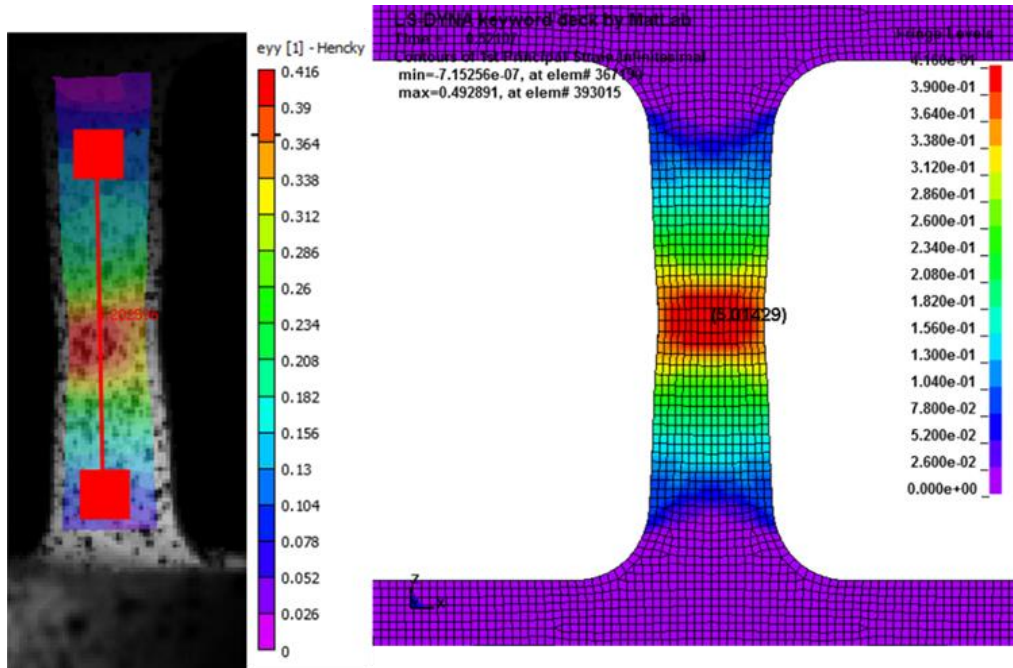
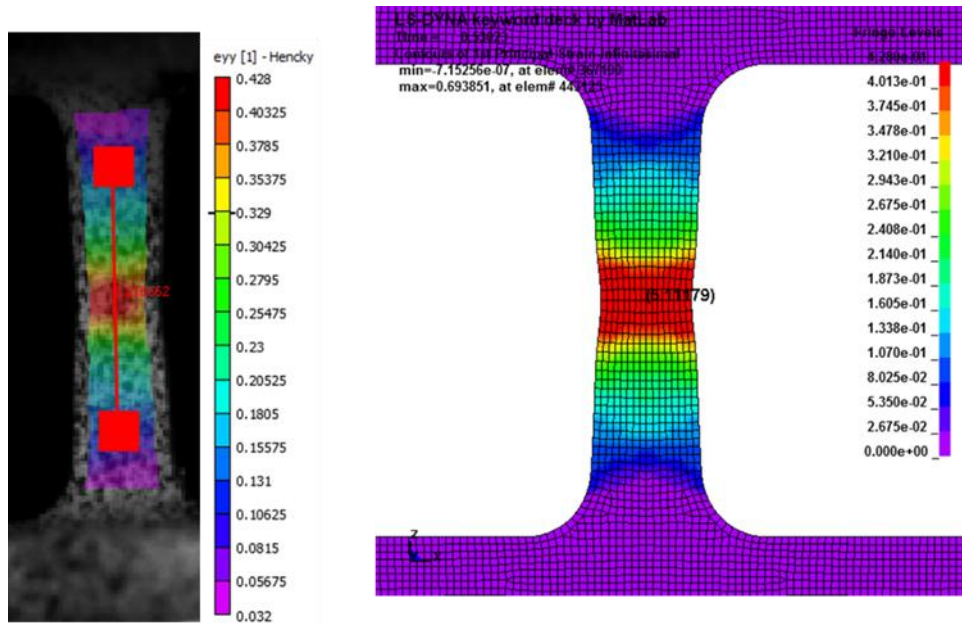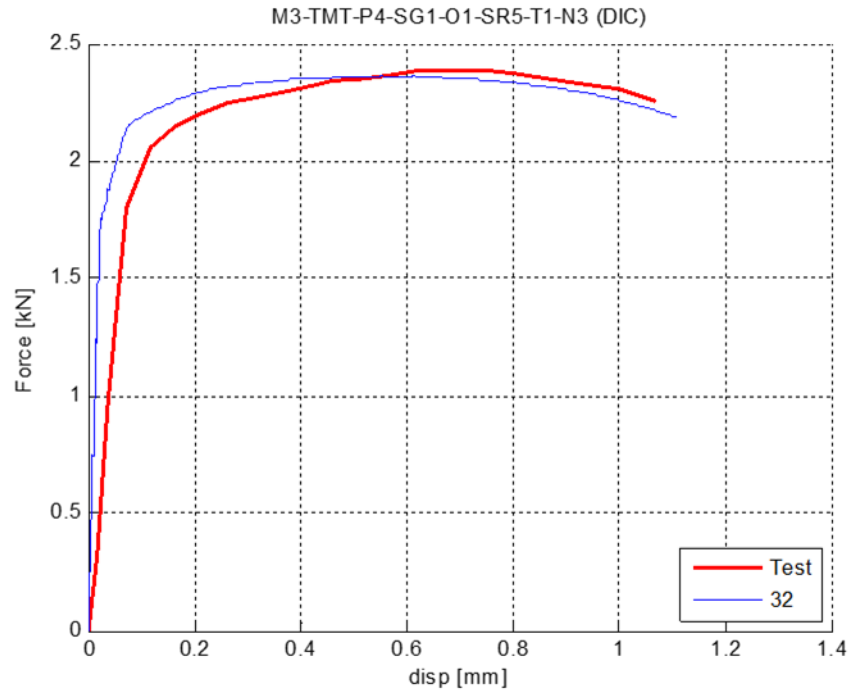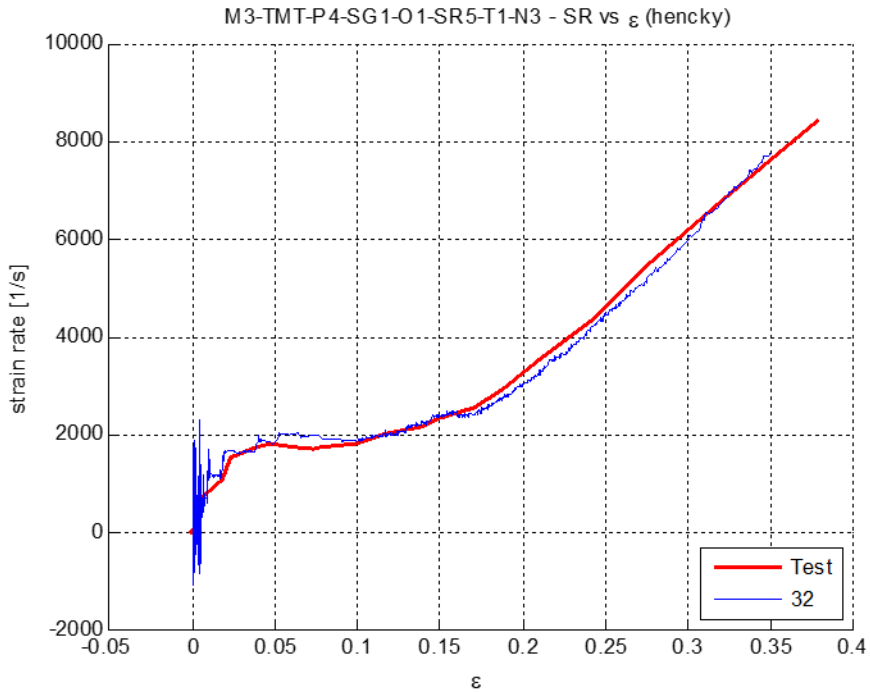Figure 30. Strain contours (M3-TMT-P4-SG1-O1-SR4-T1-N2)

Figure 31, Figure 32, and Figure 33 show a comparison of force vs. displacement, strain rate vs. strain, and strain contour plots between simulation and test M3-TMT-P4-SG1-O1-SR4-T1-N4. With a nominal strain rate of $500\ s^{-1}$, in the region of localization, the strain rate reached approximately $2000\ s^{-1}$.
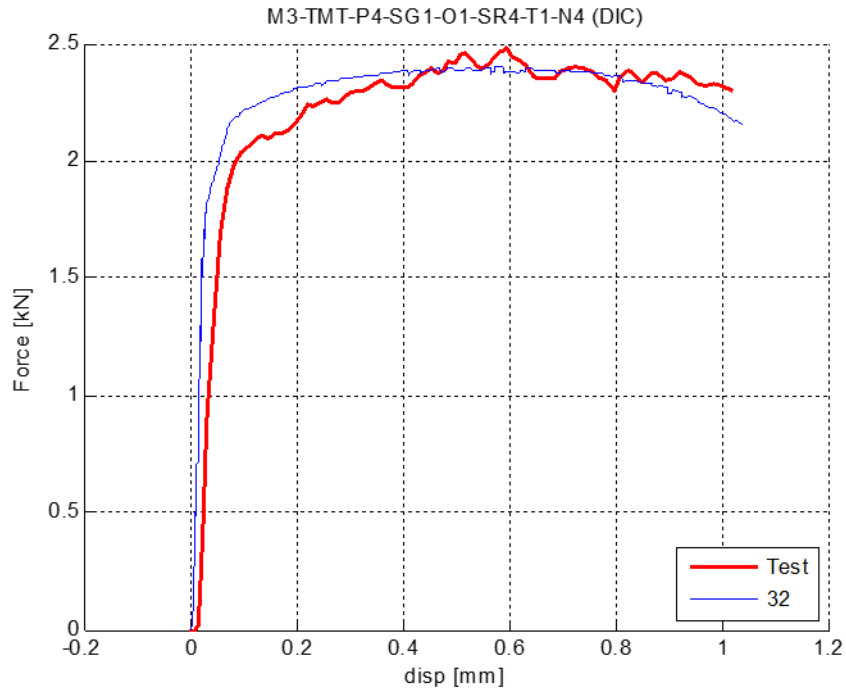
Figure 31. Force vs. displacement (M3-TMT-P4-SG1-O1-SR4-T1-N4)

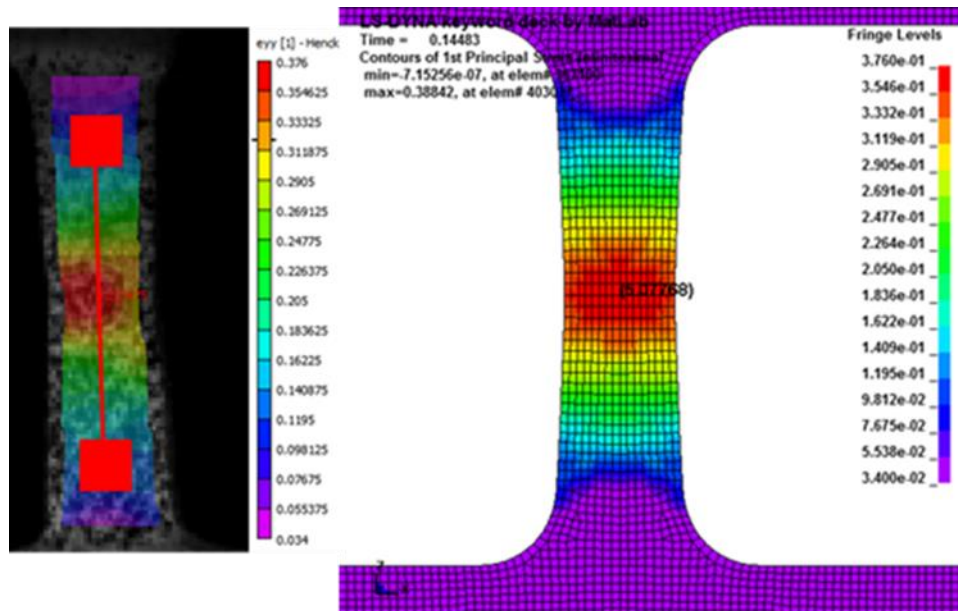Figure 32. Strain rate vs. strain (M3-TMT-P4-SG1-O1-SR4-T1-N4)

Figure 33. Strain contours (M3-TMT-P4-SG1-O1-SR4-T1-N4)

Figure 34, Figure 35, and Figure 36 show a comparison of force vs. displacement, strain rate vs. strain, and strain contour plots between simulation and test M3-TMT-P4-SG1-O1-SR4-T1-N5. In the region of localization, the strain rate reached almost 3000 s^{-1} (500 s^{-1} nominal).
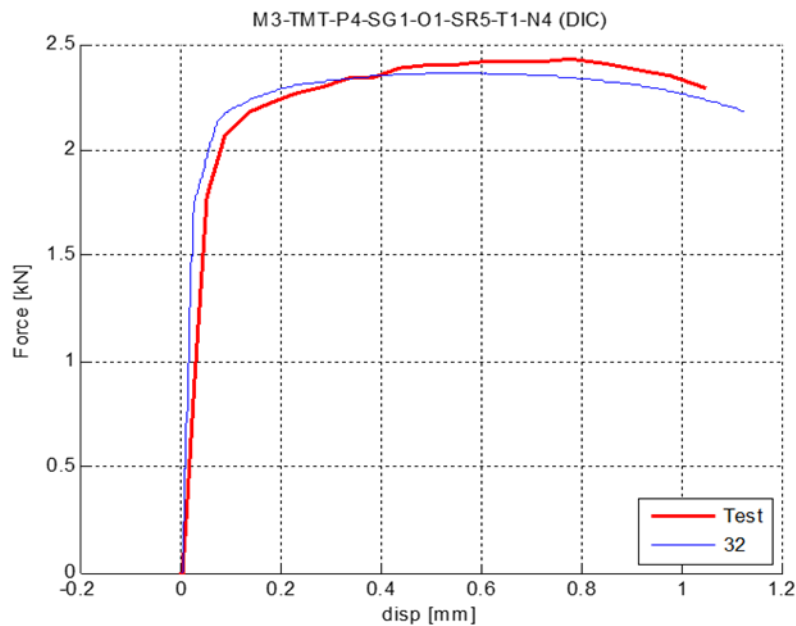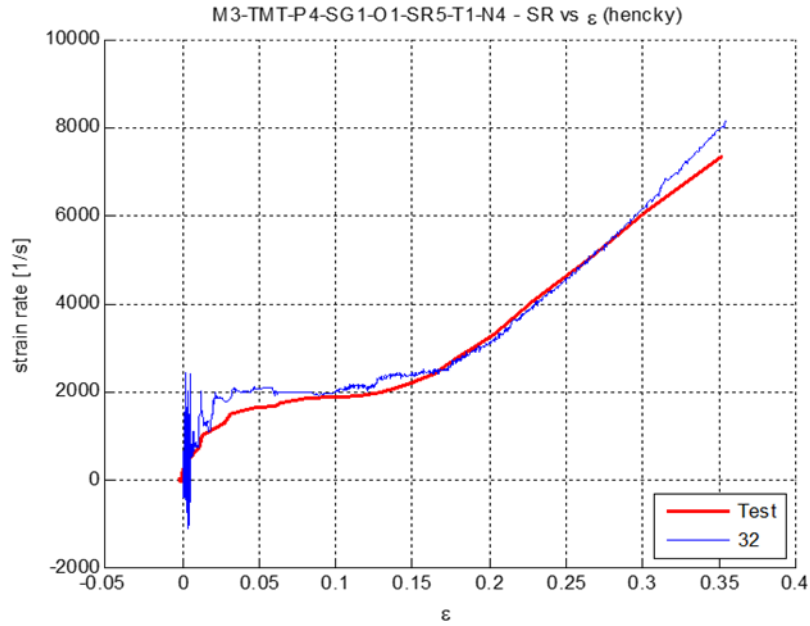
Figure 34. Force vs. displacement (M3-TMT-P4-SG1-O1-SR4-T1-N5)

Figure 35. Strain rate vs. strain (M3-TMT-P4-SG1-O1-SR4-T1-N5)

Figure 36. Strain contours (M3-TMT-P4-SG1-O1-SR4-T1-N5)

Three tests were conducted at the nominal strain rate of 2000 s^{-1}. All three of these tests were analyzed and comparisons were made to the physical test results. Figure 37, Figure 38, and Figure 39 show a comparison of force vs. displacement, strain rate vs. strain, and strain contour plots between simulation and test M3-TMT-P4-SG1-O1-SR5-T1-N3. In the region of localization, the strain rate reached over 8000 s^{-1}.

Figure 37. Force vs. displacement (M3-TMT-P4-SG1-O1-SR5-T1-N3)

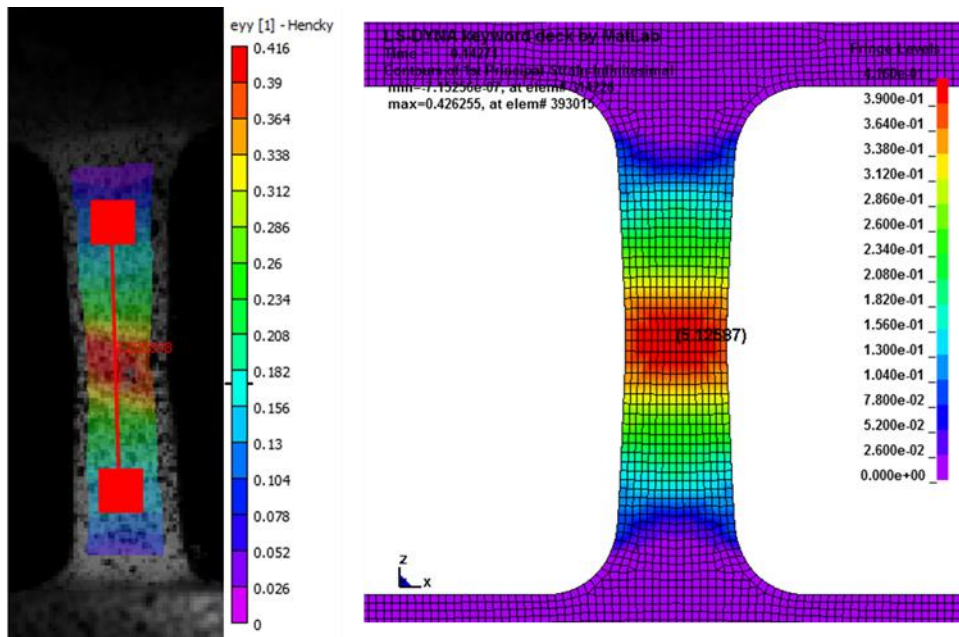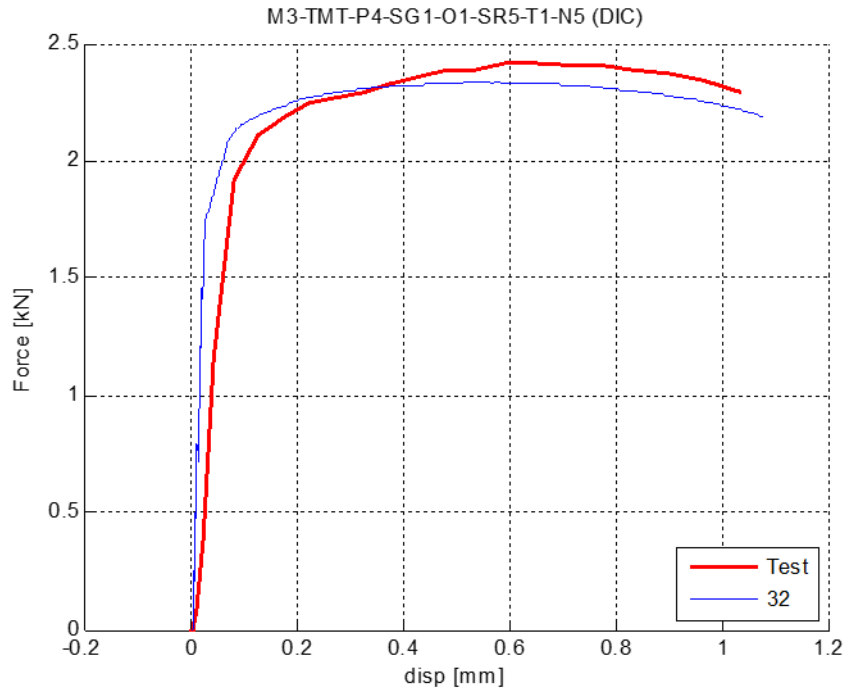Figure 38. Strain rate vs. strain (M3-TMT-P4-SG1-O1-SR5-T1-N3)

Figure 39. Strain contours (M3-TMT-P4-SG1-O1-SR5-T1-N3)

Figure 40, Figure 41, and Figure 42 show a comparison of force vs. displacement, strain rate vs. strain, and strain contour plots between simulation and test M3-TMT-P4-SG1-O1-SR5-T1-N4. With a nominal strain rate of 500 s^{-1} in the region of localization, the strain rate reached over 7000 s^{-1}.

Figure 40. Force vs. Displacement (M3-TMT-P4-SG1-O1-SR5-T1-N4)

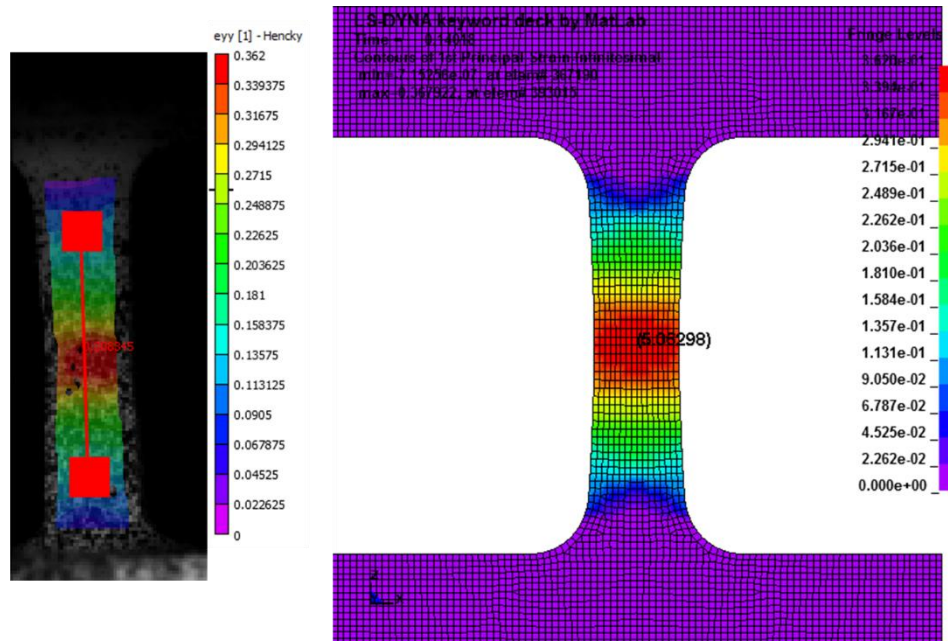Figure 41. Strain rate vs. strain (M3-TMT-P4-SG1-O1-SR5-T1-N4)

Figure 42. Strain contours (M3-TMT-P4-SG1-O1-SR5-T1-N4)

Figure 43, Figure 44, and Figure 45 show a comparison of force vs. displacement, strain rate vs. strain, and strain contour plots between simulation and test M3-TMT-P4-SG1-O1-SR5-T1-N5. With the nominal strain rate of 2000 s^{-1}, in the region of localization the strain rate reached over 8000 s^{-1}.

Figure 43. Force vs. displacement (M3-TMT-P4-SG1-O1-SR5-T1-N5)
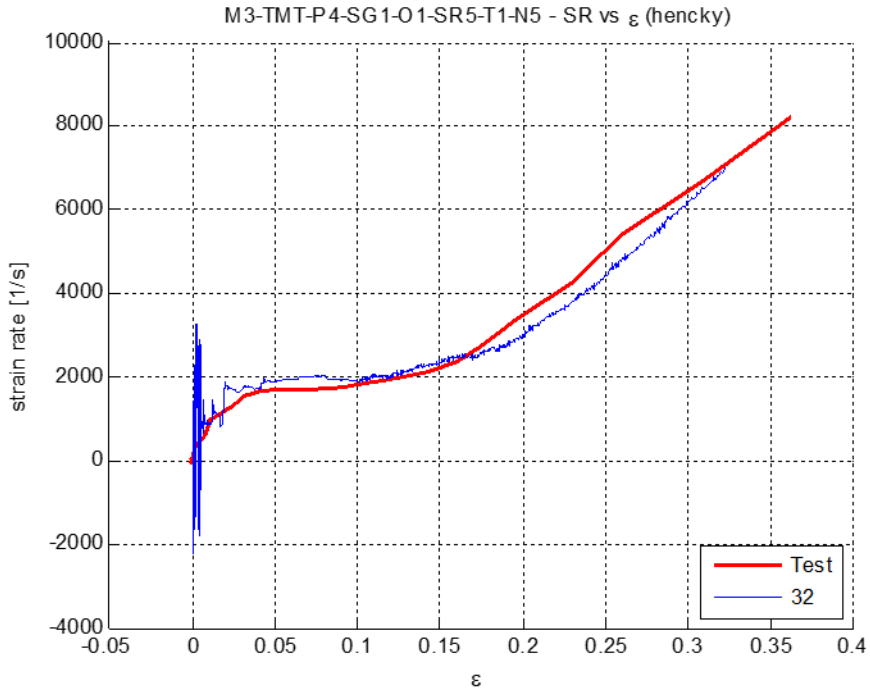
Figure 44. Strain Rate vs. strain (M3-TMT-P4-SG1-O1-SR5-T1-N5)

Figure 45. Strain contours (M3-TMT-P4-SG1-O1-SR5-T1-N5)

The total of six split-Hopkinson bar tests, with strain rates ranging from approximately 500 s^{-1} to 8000 s^{-1}, were successfully simulated using the presented stress strain table (labeled 32 in all the figures). This stress strain table was combined with a failure surface and failure scaling curves, which will be reported in Sections 4 and 5. When using this model to simulate the 0.5" Inconel-718 plate ballistic impact tests performed by NASA Glenn Research Center (Pereira, Revilock, & Ruggeri, 2020), the simulations were not producing the observed adiabatic shear bands. These initial simulations produced a non-physical crushing failure mechanism. An explanation for this incorrect prediction was sought, and the model's behavior at even higher strain rates was determined to be the cause.

The presented stress strain table produces accurate results up to the 8000 s^{-1} strain rate covered by the tests. However, in the ballistic impact tests strain rates can approach the order of 50,000 s^{-1}. Stress-strain curves covering this range were included in the presented stress strain table. The offset values used to synthesize them were based on extrapolating the rate sensitivity trend up to 8000 s^{-1}. It became apparent that this extrapolation did not match the actual rate sensitivity of the Inconel-718. Therefore, it was necessary to further assess Inconel-718 at the strain rates of between 8000 s^{-1} and 50,000 s^{-1}.

Two extrapolation assessment approaches were used. The first method created different extrapolations of rate sensitivity above 8000 s^{-1} and evaluated the results of the ballistic impact simulations. The second method used a hybrid explicit-implicit simulation to compute the static

34

indentation resulting from the unpenetrated Inconel-718 ballistic impact tests. The calculated indentations were compared to geometric profile scans of each unpenetrated test. This approach has previously been fully documented (Dolci, 2022). The extrapolation labeled NEW in Figure 46 was considered the best match to the complete set of test data, and is subsequently used in the Inconel-718 stress-strain rate sensitivity table. The previously presented extrapolation is labeled OLD in Figure 46, which matches the curve labeled 32 in Figure 27.
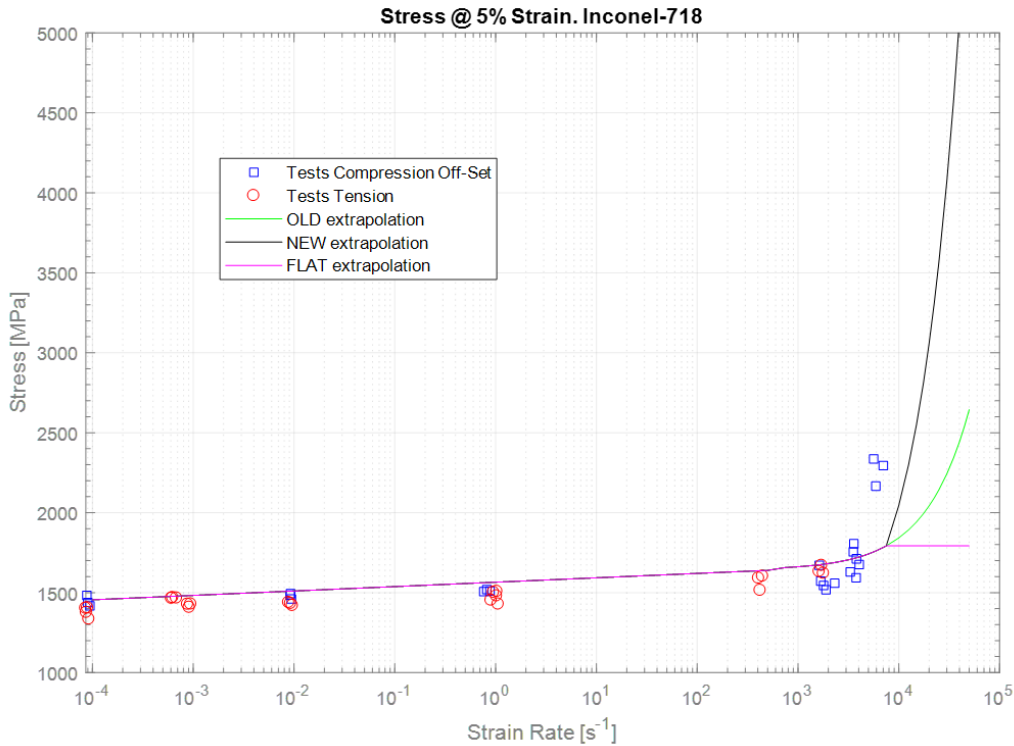
Figure 46. Stress at 5% strain with varying extrapolations

4 Methodology for failure surface model creation

In *MAT_224, the modeling of fracture most commonly uses element erosion. The element erosion criterion of effective plastic strain is dependent on several parameters, most notably the state of stress. This section describes the methodology for generating the stress state dependent, effective plastic strain failure surface for element erosion. The failure surface generation is explained, as well as the thermal, rate, and element size scaling of that surface.

With *MAT_224, there is an alternate to element erosion for the modeling of fracture. Adjacent elements can have separate nodes tied with constraints. When the *MAT_224 fracture criterion

is reached, the tied nodes can be released using *CONSTRAINED_TIED_NODES_FAILURE input. That alternate was not used in this modeling effort, but it is available.

4.1 Failure surface overview

Element erosion in *MAT_224 can be made dependent on four different curves or tables. The first table (LCF) defines the effective plastic failure strain as a function of the state of stress, and is referred to as the failure surface. For solid elements, the stress state is characterized by two parameters, the triaxiality, and the Lode parameter. For shell elements, a single load curve defining element erosion as a function of triaxiality can be used. The second input (LCG) is a load curve that scales the effective plastic strain at fracture as a function of the element strain rate. The third input (LCH) is a load curve that scales the effective plastic strain at fracture as a function of the element temperature. The last input (LCI) scales the effective plastic strain as a function of element size (as a curve), which in turn can also be made a function of triaxiality (as a table), or triaxiality and Lode parameter (as a 3D table).

Triaxiality, τ, is defined by the equation:

$$\tau = \frac{p}{\sigma_{vm}} \qquad 8$$

where p is the pressure and σ_{vm} is the von Mises stress. The Lode parameter, θ_L, is defined by the equation:

$$\theta_L = \frac{27s_1s_2s_3}{2\sigma_{vm}^3} \qquad 9$$

where s_1, s_2, and s_3 are the principal deviatoric stresses and σ_{vm} is the von Mises stress. Overall, the net effective plastic strain at fracture, ε_n, is defined by:

$$\varepsilon_n = \varepsilon_f(\tau, \theta_L) g(\dot{\varepsilon}_p) h(T) i(l_c, \tau, \theta_L) \qquad 10$$

where ε_f is the effective plastic strain at fracture from the LCF table, $\dot{\varepsilon}_p$ is the plastic strain rate, T is the temperature, and l_c is the element size. Therefore, the net effective plastic strain, which is the element erosion criteria, is the stress-state fracture strain multiplied by the product of the three scale factors.

For each element, the stress state, strain rate, and temperature are continually changing. So, a parameter must be defined to consider an element's history. A damage parameter is defined and

the accumulated damage for each element is calculated. The element erosion criterion in *MAT_224 is based on this accumulated damage parameter. When the damage parameter is greater than or equal to one in an integration point, the element is eroded. The damage parameter is defined by:

$$D = \int \frac{\dot{\varepsilon}_p}{\varepsilon_n} dt \qquad 11$$

To create a failure surface, many types of test specimens with varying geometries were created. Each test specimen geometry has a unique triaxiality and Lode parameter, which defines the fracture strain at a specific point on the surface. To generate an accurate and complete failure surface, there should be as many specimen geometries as possible. However, there will not be enough test specimens to fully define a failure surface. Interpolating between fracture strains at known triaxialities and Lode parameters is required to create a full failure surface, and unfortunately extrapolation is also often necessary.

After the LCF failure surface is generated, the scaling factor curves and tables are created. By observing how the fracture strain is affected by strain rate and temperature, the same strain rate and temperature test series described in Section 3 can be used to create the LCG and the LCF curves. Finally, by simulating selected tests in the fracture series with varying mesh densities, a 3D LCI table can be created that accounts for the changes in fracture strain as a function of the element size, and which in turn is a function of the stress state.

4.2   Failure surface generation

It is possible to interpolate and extrapolate the fracture strains from the tests with the varying triaxialities and Lode parameters, and to create a failure surface manually. However, automating the process is also possible using a failure surface generation tool. Such a tool was developed using MathWorks' MATLAB software environment.

OSU's Inconel-718 material testing program yielded 23 different fracture tests, with stress states as a function of triaxiality and Lode parameter presented in Figure 47p. In most of these specimens the state of stress is not a constant, and the plotted values are the average triaxiality and Lode parameter over the course of the loading. The fracture testing families identified in Figure 47 will be fully described in Section 5.1. Even though the 23 separate test specimens demonstrate a broad testing program, there remains regions where there is little or no test data. In addition, outside the bounds of the figure, where triaxiality is greater than 0.4 and less than -1.0, there is no test data. (Note that triaxiality can vary from $-\infty$ in hydrostatic tension to $+\infty$ in hydrostatic compression, while the Lode parameter can only vary between -1 and 1.)
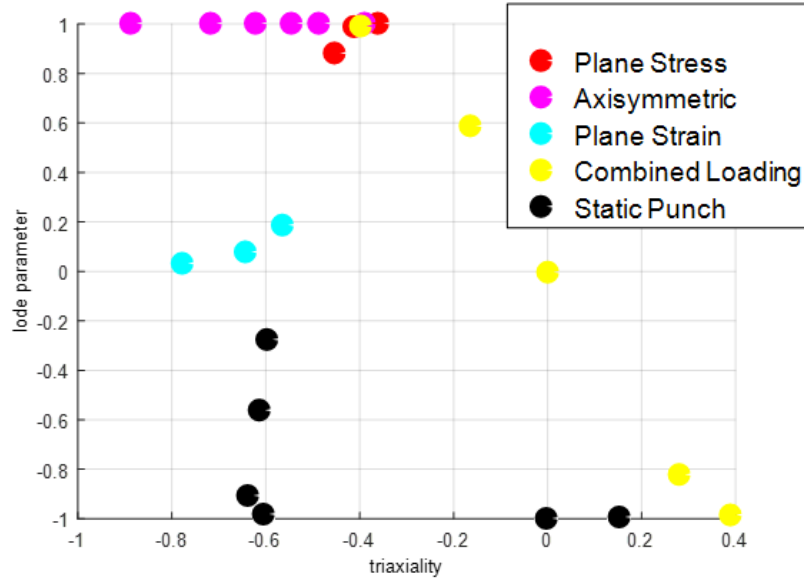
Figure 47. Example stress states of different material tests

In the first step of the Inconel-718 failure surface generation, three-dimensional splines between commonly defined states of stress were created. These commonly defined states of stress are given in the legend of Figure 48. Each three-dimensional spline of fracture strain is created by curve fitting to test data points close to these defining stress sets. In other words, the points that are close to the theoretical curves define the spline.

Four splines were created using the points belonging to the four primary, solid-line curves shown in Figure 48. Note that the test stress states are not precisely plane stress, plane strain, axisymmetric tension, or axisymmetric compression, and so in Figure 49 the points do not fall exactly on these lines. On the right side of Figure 49, in the 3D image the fracture strain is also plotted, and so an outline of the failure surface is discernable.
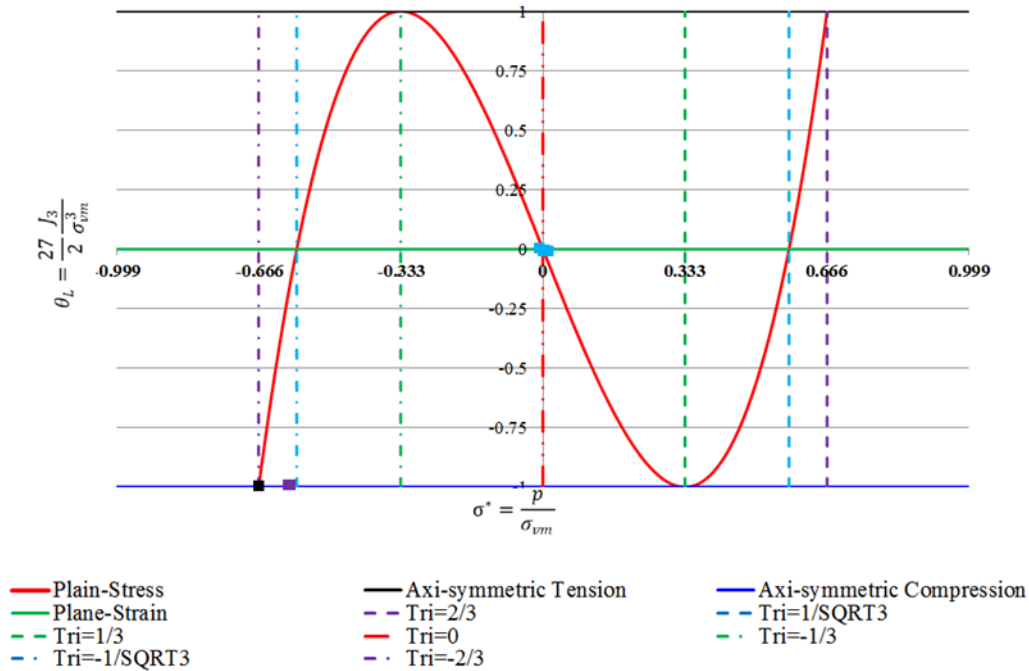
Figure 48. Commonly defined stress states
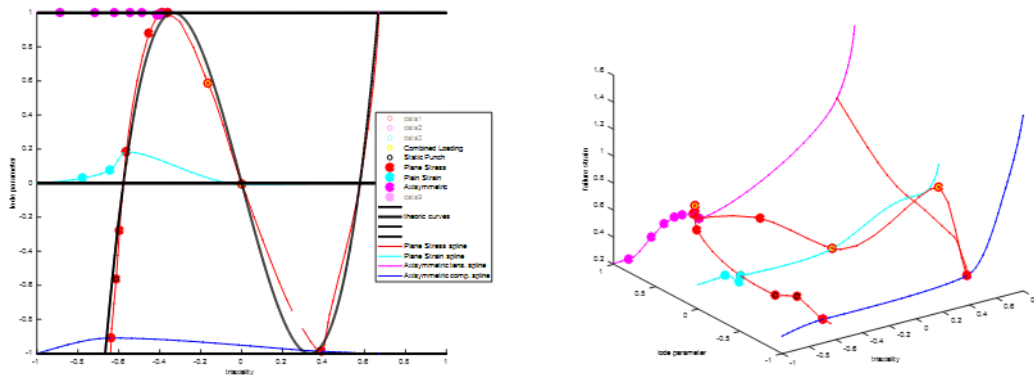
Figure 49. Three-dimensional splines control points and splines

Additional points are created along these three-dimensional splines. In the example shown in Figure 50, there are 234 totals control points where the fracture strains are defined. Mathematically, three one-dimensional vectors are created defining: 1) the triaxiality of the 234 control points 2) the Lode parameter of the 234 control points and 3) the failure strain for each of the 234 control points.

39
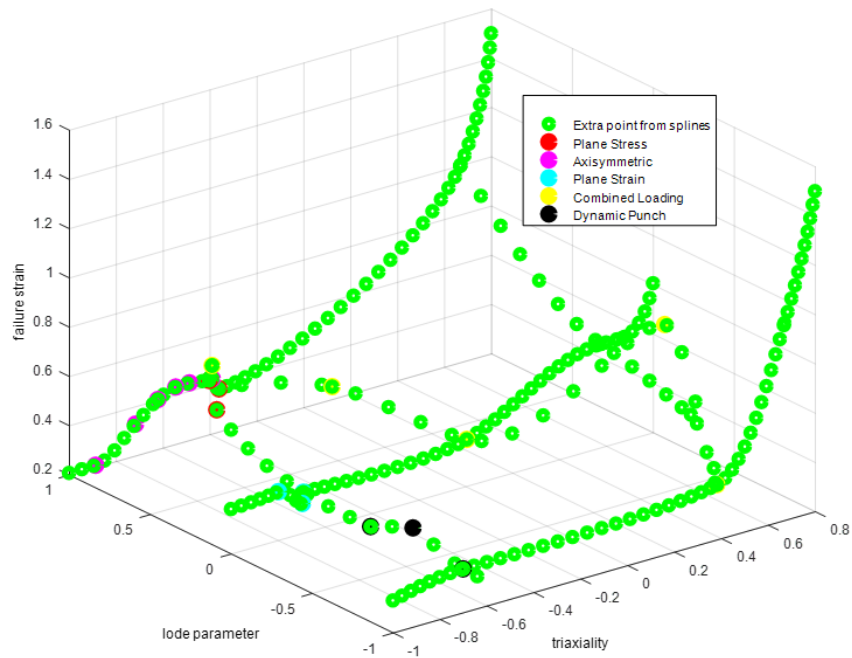
Figure 50. Additional control points created from the 3d splines

The next step in the failure surface creation uses a MATLAB subroutine that was implemented using the Curve Fitting Toolbox. This subroutine passes the three one-dimensional vectors of 234 control points, interpolates it over a uniform grid, and a surface fit to these splines is returned. The subroutine uses a 'v4' interpolation routine (MATLAB 4 grid data method) to generate the 3-dimensional surface. Plots of the surface are shown in Figure 51.
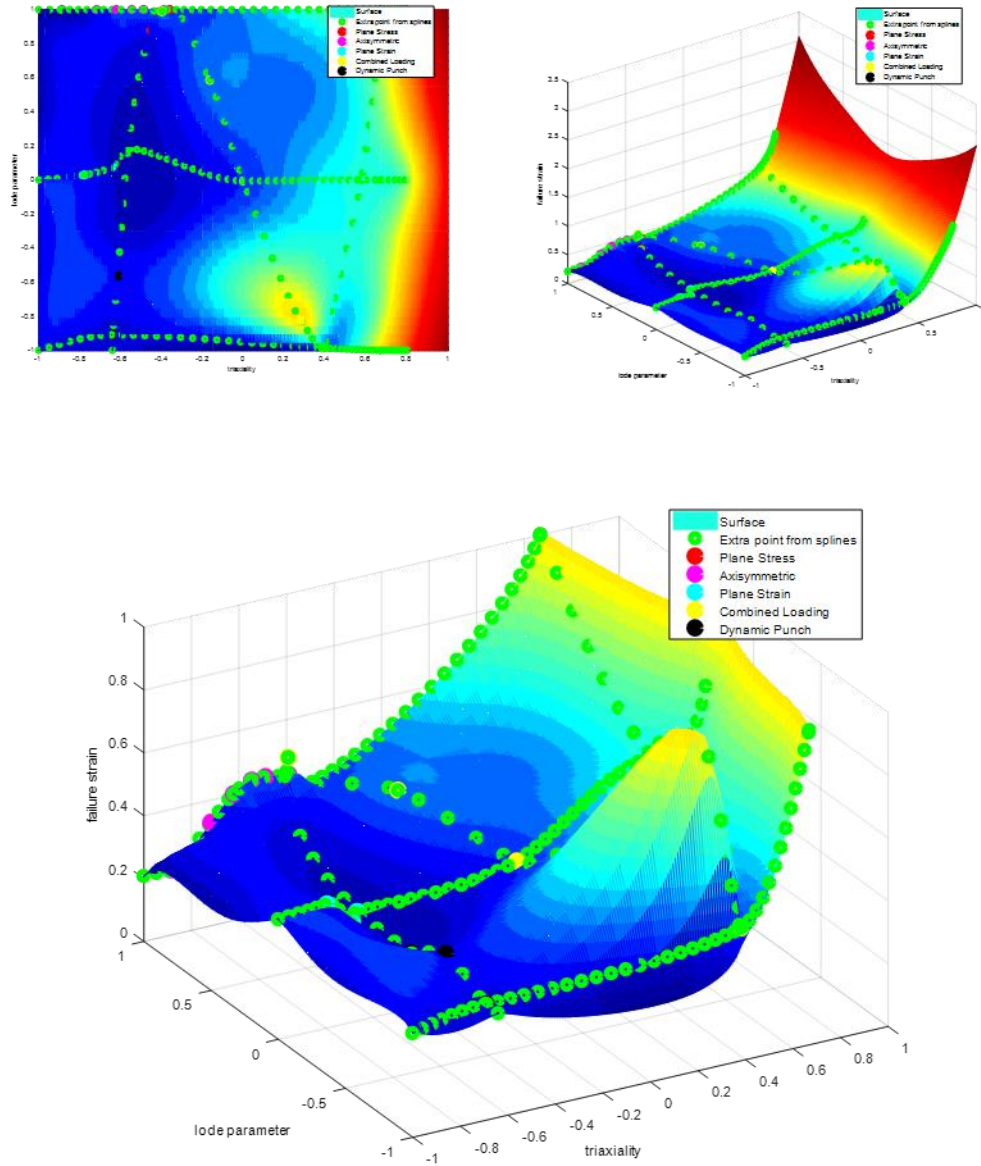
Figure 51. Failure surface generated by MATLAB subroutine

The next step of the failure surface generation discretizes the three-dimensional surface into individual data points. The three-dimensional surface is defined by 202 triaxiality values and 41 Lode parameter values, making a total of 8282 discrete points. The discretization of the three-dimensional surface is shown in Figure 52.
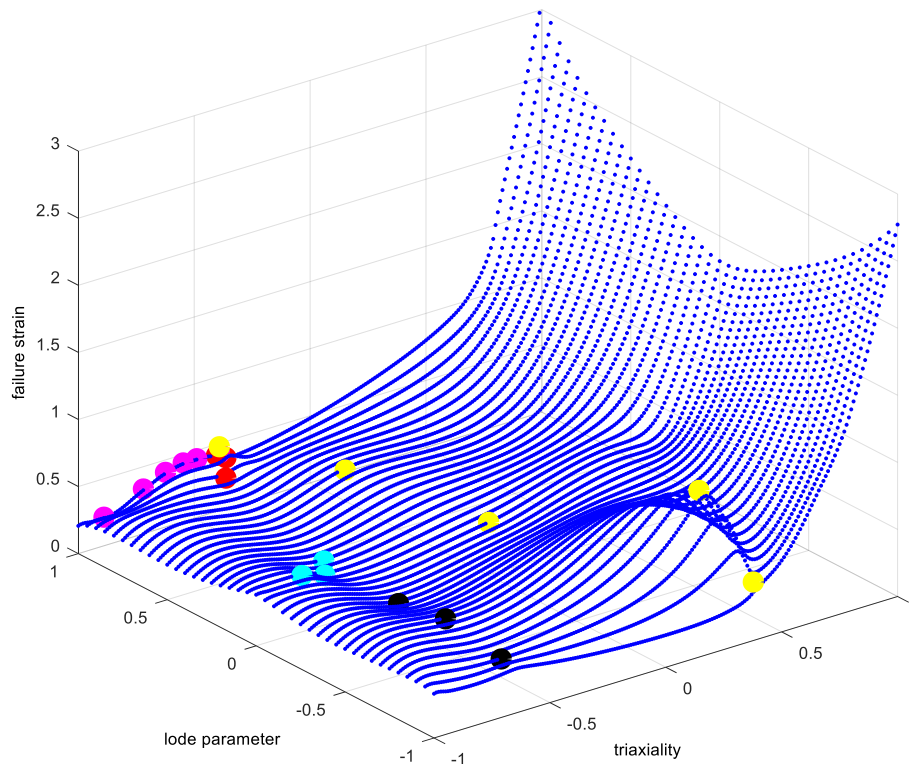
Figure 52. Discretized 3D failure surface

The final step in the failure surface generation is to generate the keyword input file that will be referenced by the *MAT_224 LCF parameter. This file includes a *DEFINE_TABLE that has 41 values ranging from -1 to 1, which represent the Lode parameter discretization. The triaxiality discretization is defined by 41 *DEFINE_CURVE keywords; each one having 202 fracture strain values. This keyword file can then be directly included into the simulation input.

After each test specimen described in Section 5 is simulated, the displacement at fracture is compared to the experimental test result. If the simulation reaches the failure criteria too late and so the failure strain is too high, or if it reaches the failure criteria too early and so the failure strain is too low, the control points near that specimen's state of stress can be adjusted and the surface can be immediately regenerated.

5 Failure model creation by simulation of mechanical property tests

In real-world loading applications, states of stress will vary drastically. And the fracture strain in stress states that are commonly tested, such as uniaxial tension, can be completely unrelated to the fracture strain in the stress state where a part ruptures. Therefore, as many different states of stress should be tested as possible. To create a reliable failure surface, these many different tests should vary both in triaxiality and in Lode parameter, as presented in Section 4.

The mechanical property tests were performed by OSU. The data provided included the specimen geometry, forces, displacements, strains, and DIC images. In total, 25 different specimens were used to determine the Inconel-718 failure. Several repeat tests were performed using each specimen. The 25 specimens are listed below (with abbreviations):

1. SG1: Plane stress specimen (uniaxial tension)

2. SG2: Plane stress specimen

3. SG3: Plane stress specimen

4. SG4: Plane stress specimen

5. SG5: Axisymmetric specimen (uniaxial tension)

6. SG6: Axisymmetric specimen

7. SG7: Axisymmetric specimen

8. SG8: Axisymmetric specimen

9. SG9: Axisymmetric specimen

10. SG10: Axisymmetric specimen

11. SG11: Plane strain specimen

12. SG12: Plane strain specimen

13. SG13: Plane strain specimen

14. LR1: Combined (tension/torsion) specimen

15. LR2: Combined (tension/torsion) specimen

16. LR3: Torsion specimen

17. LR4: Combined (compression/torsion) specimen

18. LR5: Combined (compression/torsion) specimen

19. Punch1: Large diameter punch specimen

20. Punch2: Large diameter punch specimen

21. Punch3: Large diameter punch specimen

22. Compression: Uniaxial (cylindrical) compression specimen

23. Punch4: Unbacked

24. Punch5: Thick back plate sequential

25. Punch6: Thin back plate sequential

Here, the terms 'plane stress' and 'plane strain' identify specimen design families. Only test specimen SG1 creates plane stress, and SG2, SG3, and SG4 include varying notches that create varying stress states. Likewise, only SG11 creates plane strain, and SG12 and SG13 include two different notches, which also create varying stress states. The final three tests in the above list (23-25) are additions to the previously existing fracture test series. Punch4, Punch5, and Punch6 were designed to have fractures at previously untested states of stress. These small diameter punch tests, two with backing plates, produce triaxialities along the Lode parameter = -1 contour, which is important in creating a failure surface for ballistic impact (Spulak, et al., 2020; Spulak, 2022).

Each test specimen and its associated finite element model will be more thoroughly described in the following sections. Figure 53 shows the states of stress of the listed OSU tests, in terms of triaxiality and Lode parameter.
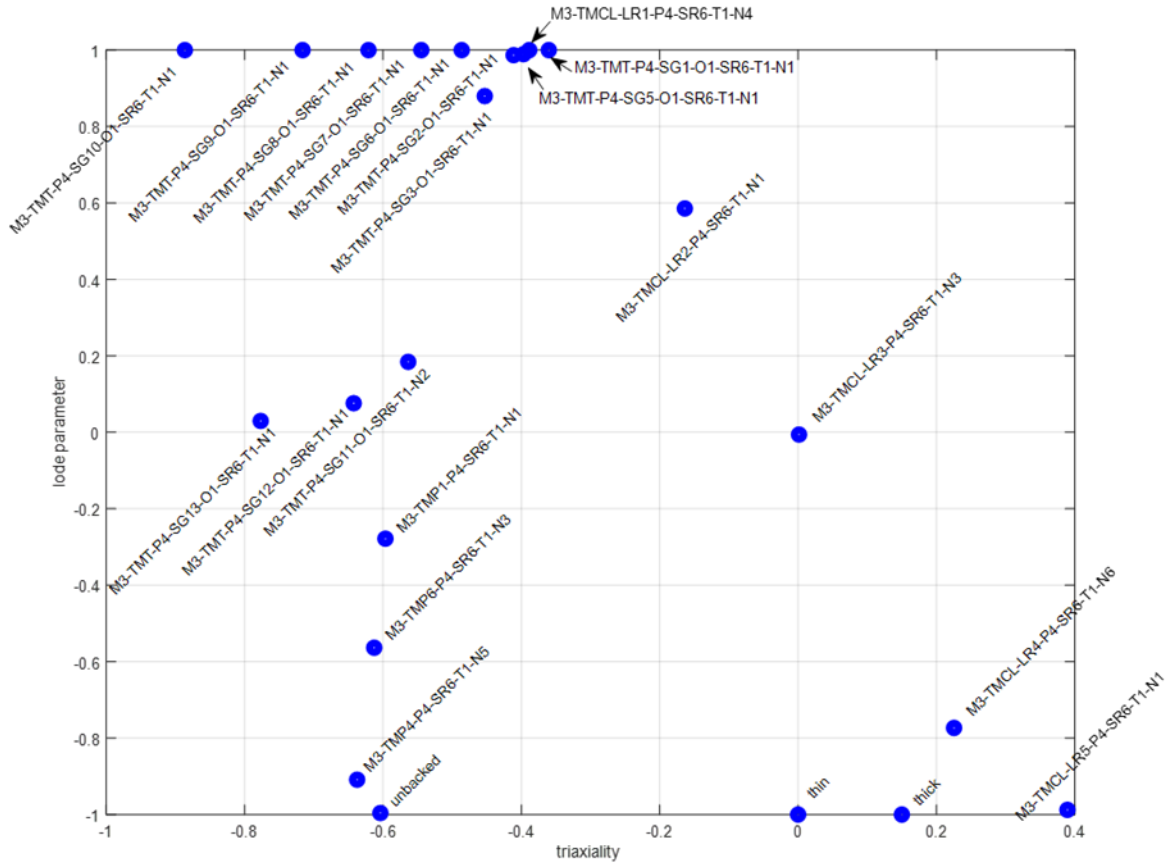
Figure 53. Tests triaxiality vs Lode parameter of OSU tests

5.1 Test specimen descriptions

A finite element mesh of each test specimen was created using a uniform approach. As previously stated, the units used are mm, ms, kg, and kN, and so the presented test specimen dimensions are in mm. The dimensions shown in the specimen diagrams are nominal. The actual test specimen dimensions will generally differ slightly from specimen to specimen. The mesh used in each simulation is adjusted to precisely match the actual test specimen dimensions.

5.1.1 SG1 – Plane stress specimen (uniaxial tension)

SG1 is a plane stress, uniaxial tension specimen that was also used to determine the stress strain relationships described in Section 3. The dimensions of the SG1 specimen are given in Figure 54.
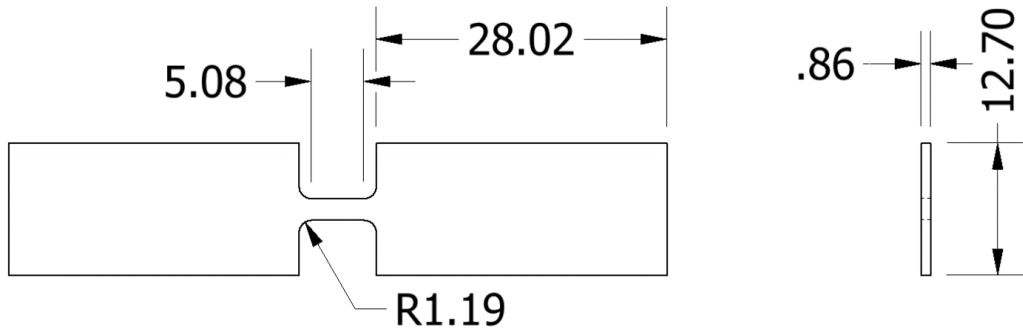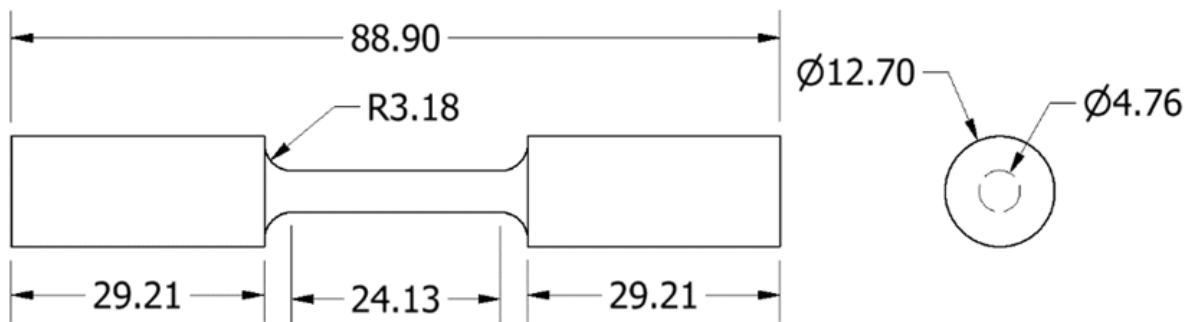
Figure 54. Geometry of the SG1 specimen

The specimen was meshed using solid elements with an average element dimension was 0.13 mm. The mesh of the SG1 specimen is shown in Figure 55. The finite element mesh of this specimen contains a total of about 240,000 solid elements. In the region of the Instron mechanical grips, the elements were defined as rigid. Of the 240,000 total elements, approximately 235,000 of them were defined as rigid. Figure 55 shows the rigid solid elements in grey and the flexible Inconel-718 elements in white.
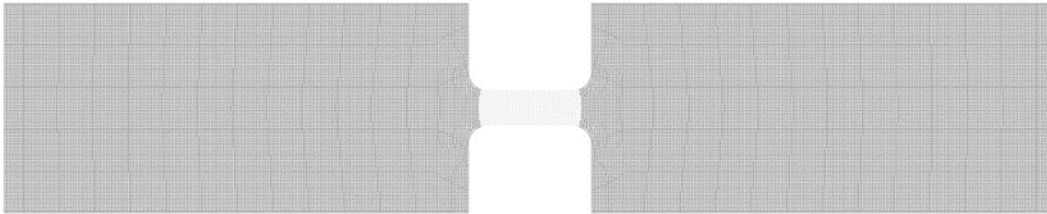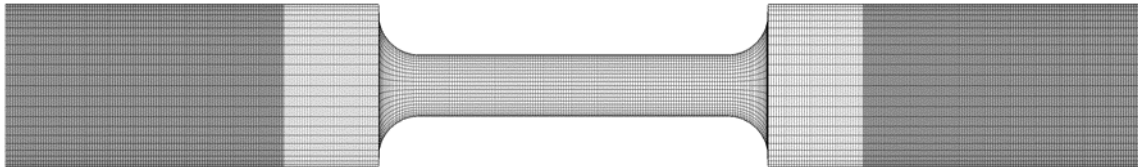

Figure 55. SG1 finite element mesh with grey rigid and white Inconel elements

5.1.2 SG2 – Plane stress specimen

SG2 is a variation of the plane stress specimen that has a specifically chosen center geometry, or notch, that will produce a unique triaxiality and Lode parameter. The specimen dimensions are shown in Figure 56.
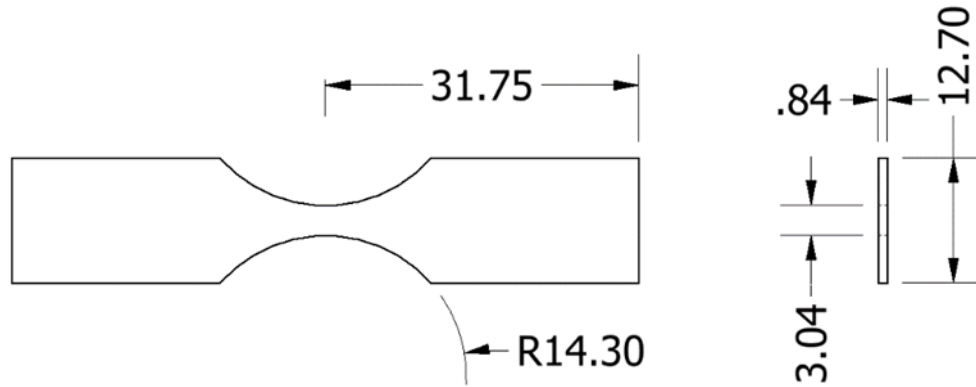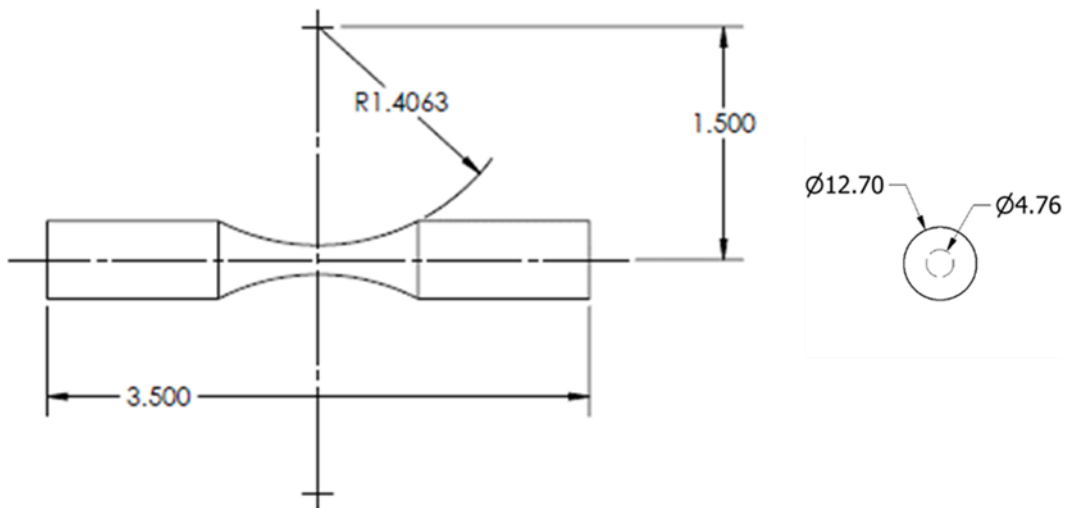
Figure 56. Geometry of the SG2 specimen

The specimen was meshed using solid elements with an average element size of 0.2 mm. The mesh of the SG2 specimen is shown in Figure 57. An enlargement of the test section is also shown. The mesh for this specimen contains a total of about 22,000 solid elements. In the Instron mechanical grip sections the elements were defined as rigid. Of the 22,000 elements, about 12,000 of them were defined as rigid. Figure 57 shows the rigid elements in grey, and the Inconel modeled elements in white.
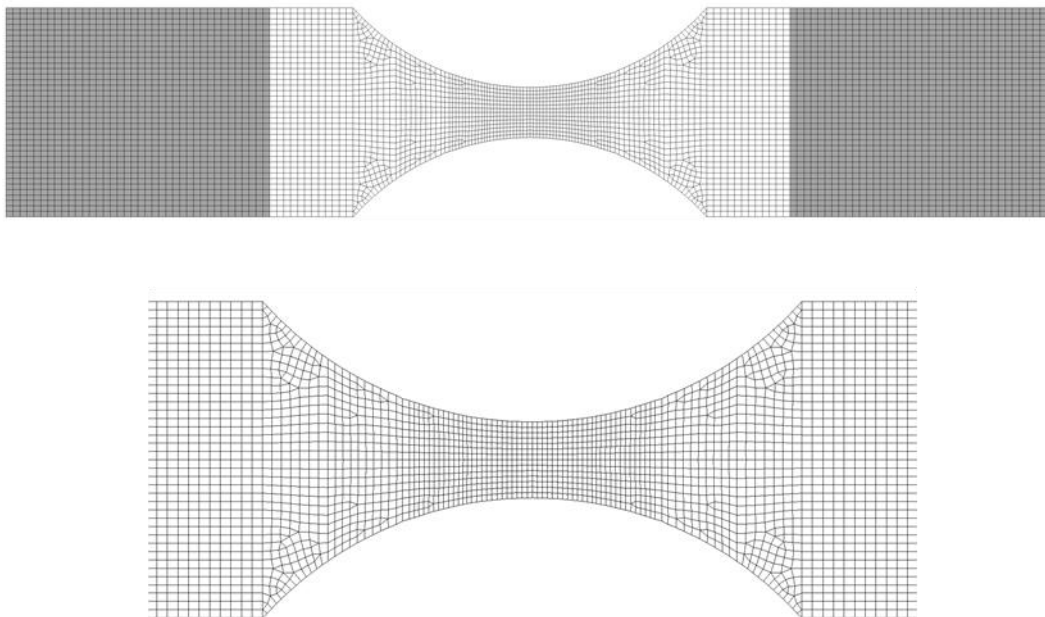

Figure 57. SG2 finite element mesh with grey rigid and white Inconel elements

5.1.3 SG3 – Plane stress specimen

SG3 is a variation of the plane stress specimen that has a specifically chosen center geometry, or notch, that will produce a unique triaxiality and Lode parameter. The dimensions of the specimen are shown in Figure 58.
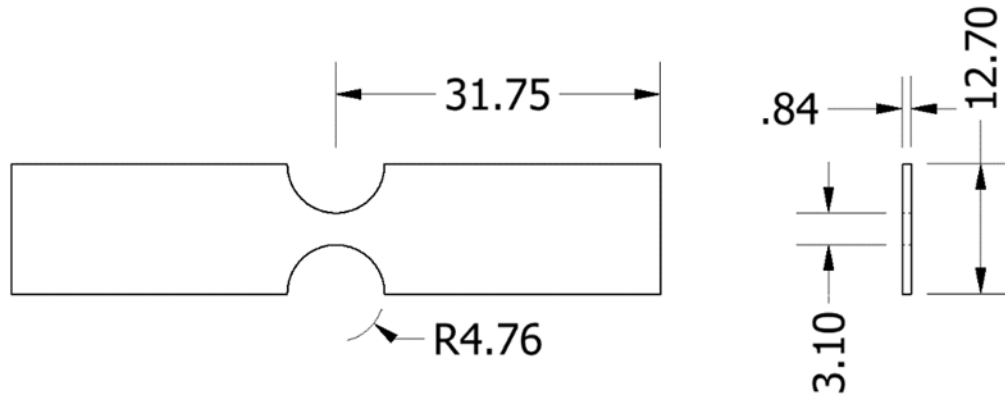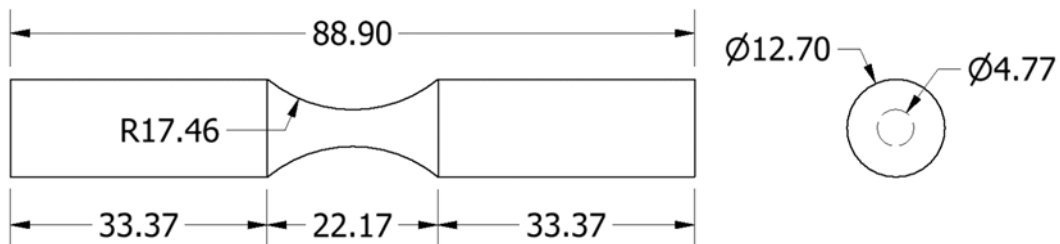

Figure 58. Geometry of specimen SG3

The specimen was meshed using solid elements with an average element size of 0.2 mm. The mesh of the SG3 specimen is shown in Figure 59. An enlargement of the test section is also shown. The mesh for this specimen contains a total of about 20,000 solid elements. In the Instron mechanical grip sections the elements were defined as rigid. Of the 20,000 elements, about 14,000 of them were defined as rigid. Figure 59 shows the rigid elements in grey, and the Inconel modeled elements in white.
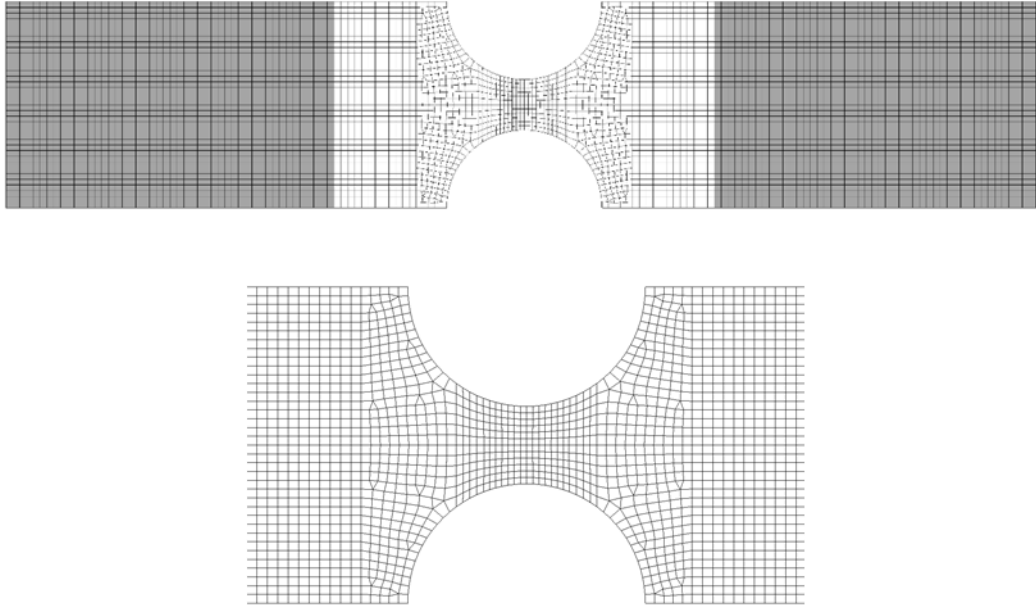
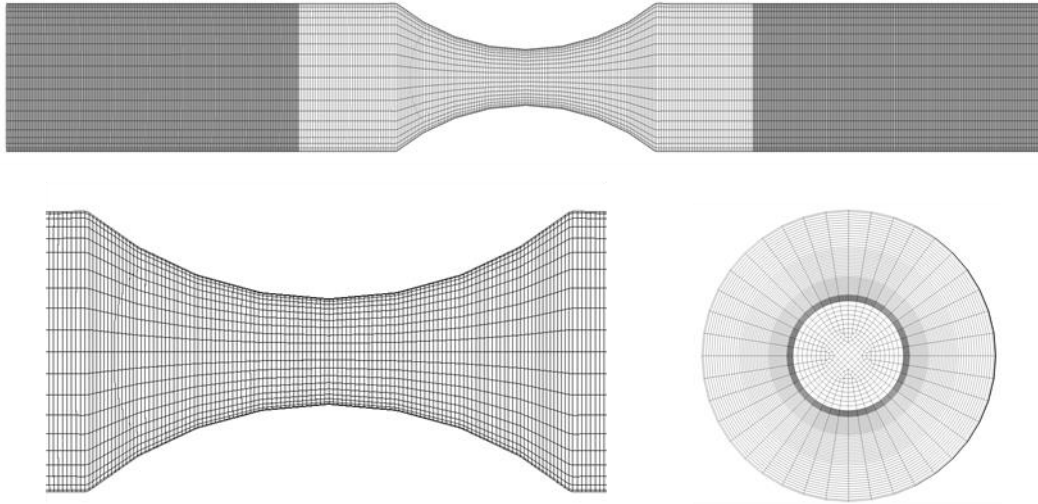Figure 59. SG3 finite element mesh with grey rigid and white Inconel elements

5.1.4 SG4 – Plane stress specimen

SG4 is a variation of the plane stress specimen that has a specifically chosen center geometry, or notch, that will produce a unique triaxiality and Lode parameter. The dimensions of the specimen are shown in Figure 60.
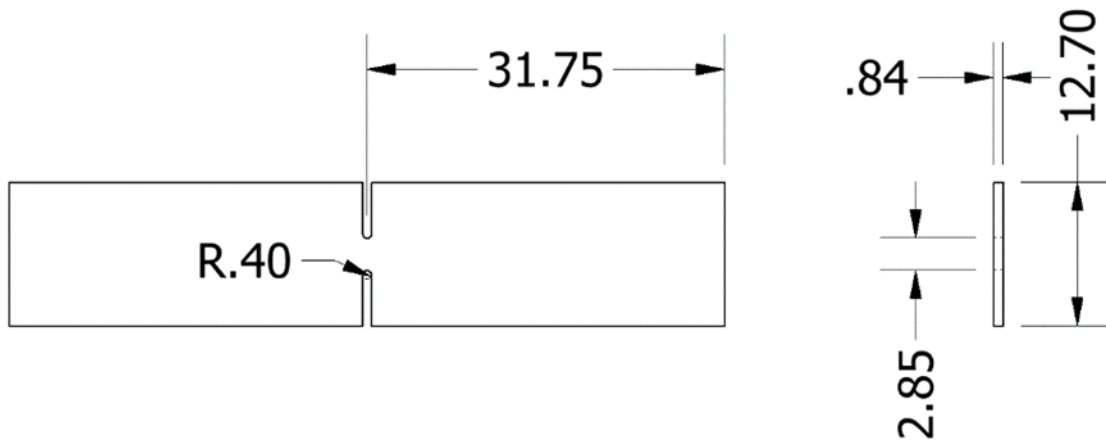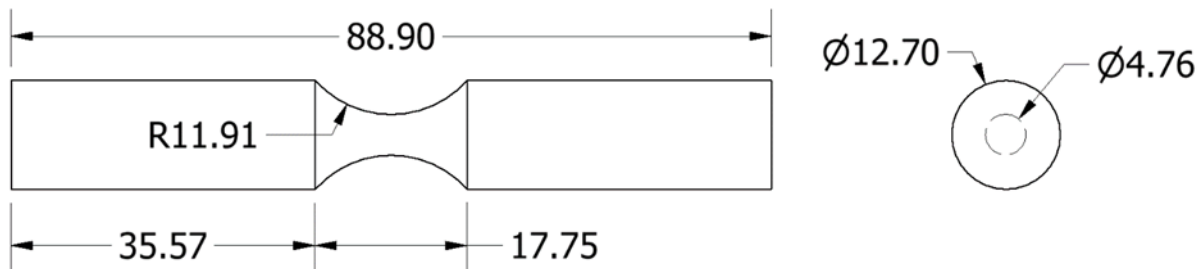

Figure 60. Geometry of the SG4 specimen

The specimen was meshed using solid elements with an average element size of 0.2 mm. The mesh of the SG4 specimen is shown in Figure 61. An enlargement of the test section is also

shown. The mesh for this specimen contains a total of about 41,000 solid elements. In the Instron mechanical grip sections, the elements were defined as rigid. Of the 41,000 elements, about 30,000 of them were defined as rigid. Figure 61 shows the rigid elements in grey, and the Inconel modeled elements in white.
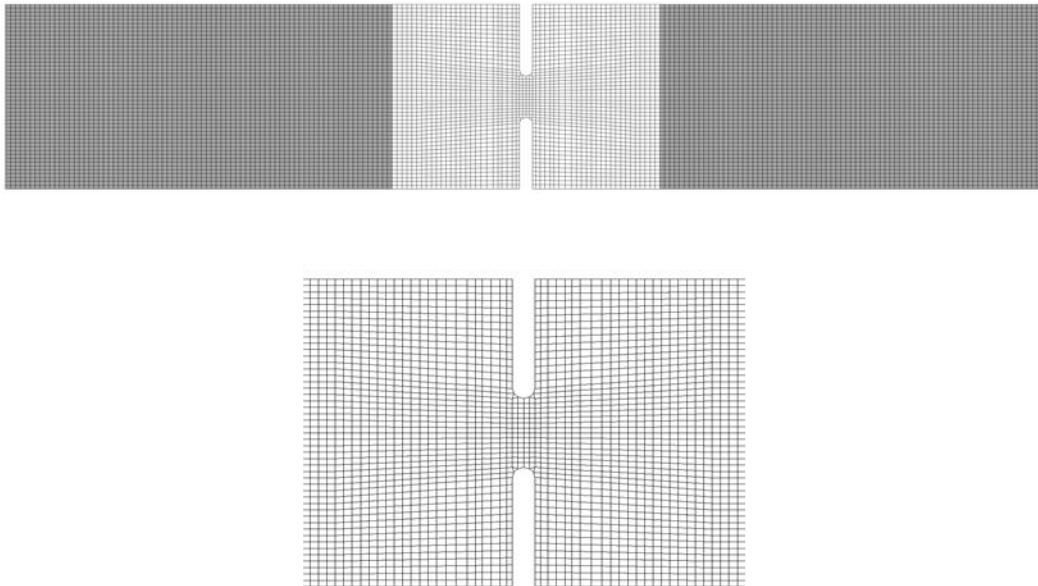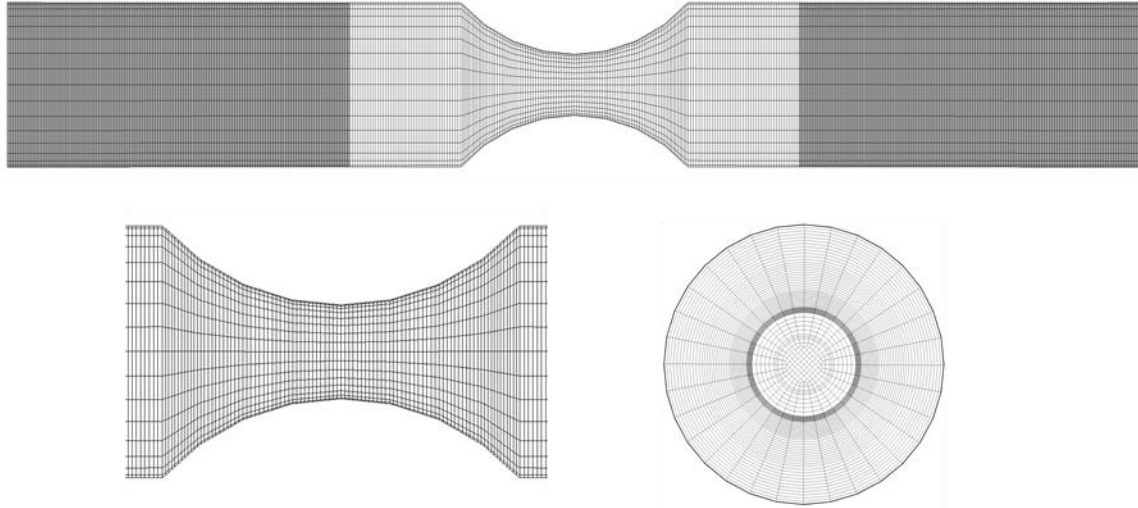

Figure 61. SG4 finite element mesh with grey rigid and white Inconel elements

5.1.5 SG5 – Axisymmetric specimen (uniaxial tension)

SG5 is an axisymmetric (cylindrical) specimen that has a center section that is under uniaxial tension. The dimensions of the specimen are shown in Figure 62.

Figure 62. Geometry of specimen SG5

The specimen was meshed using solid elements with an average element size of 0.2 mm. The mesh of the SG5 specimen is shown in Figure 63. The mesh for this specimen contains a total of about 471,000 solid elements. In the Instron mechanical grip sections the elements were defined as rigid. Of the 471,000 elements, about 300,000 of them were defined as rigid. Figure 63 shows the rigid elements in grey, and the Inconel modeled elements in white.
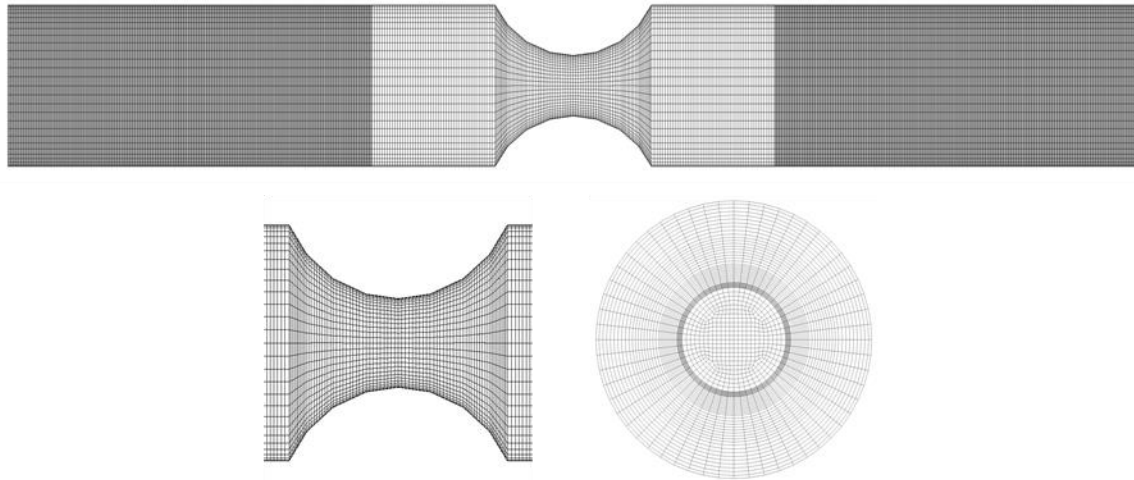

Figure 63. SG5 finite element mesh with grey rigid and white Inconel elements

5.1.6 SG6 – Axisymmetric specimen

SG6 is a variation of the axisymmetric specimen that has a specifically chosen center geometry, or notch, that will produce a unique triaxiality and Lode parameter. The dimensions of the specimen are shown in Figure 64.
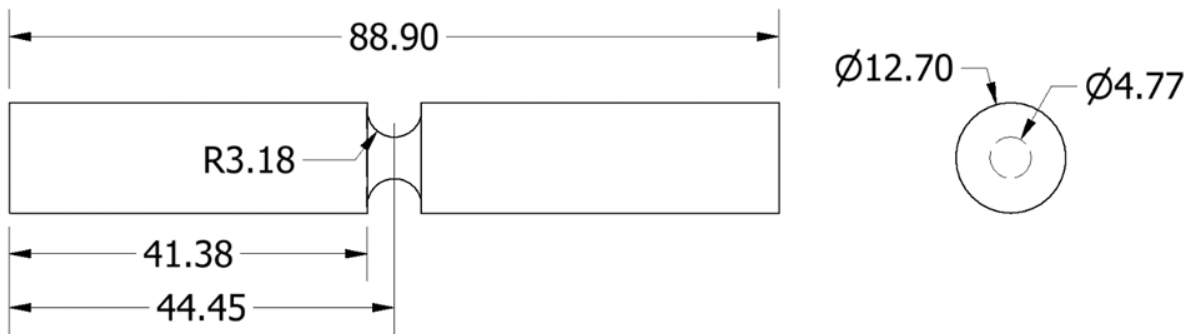

Figure 64. Geometry of the SG6 specimen

The specimen was meshed using solid elements with an average element size of 0.2 mm. A closeup of the mesh of the SG6 specimen is shown in Figure 65. The mesh for this specimen contains a total of about 430,000 solid elements. In the Instron mechanical grip sections, the elements were defined as rigid. Of the 430,000 elements, about 250,000 of them were defined as rigid. Figure 65 only shows the test section Inconel elements.
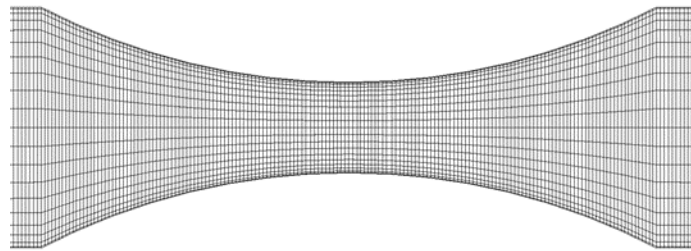
Figure 65. The SG5 Finite Element Mesh Test Section Elements

5.1.7 SG7 – Axisymmetric specimen

SG7 is a variation of the axisymmetric specimen that has a specifically chosen center geometry, or notch, that will produce a unique triaxiality and Lode parameter. The dimensions of the specimen are shown in Figure 66.

Figure 66. Geometry of the SG7 specimen

The specimen was meshed using solid elements with an average element size of 0.2 mm. The mesh of the SG7 specimen is shown in Figure 67. An enlargement of the test section is also shown. The mesh for this specimen contains a total of about 457,000 solid elements. In the Instron mechanical grip sections the elements were defined as rigid. Of the 457,000 elements, about 294,000 of them were defined as rigid. Figure 67 shows the rigid elements in grey, and the Inconel modeled elements in white.
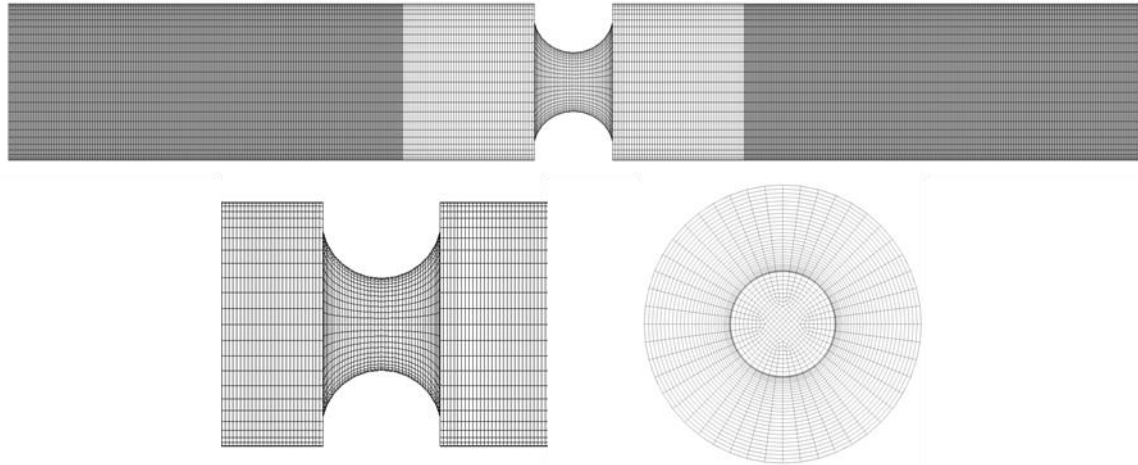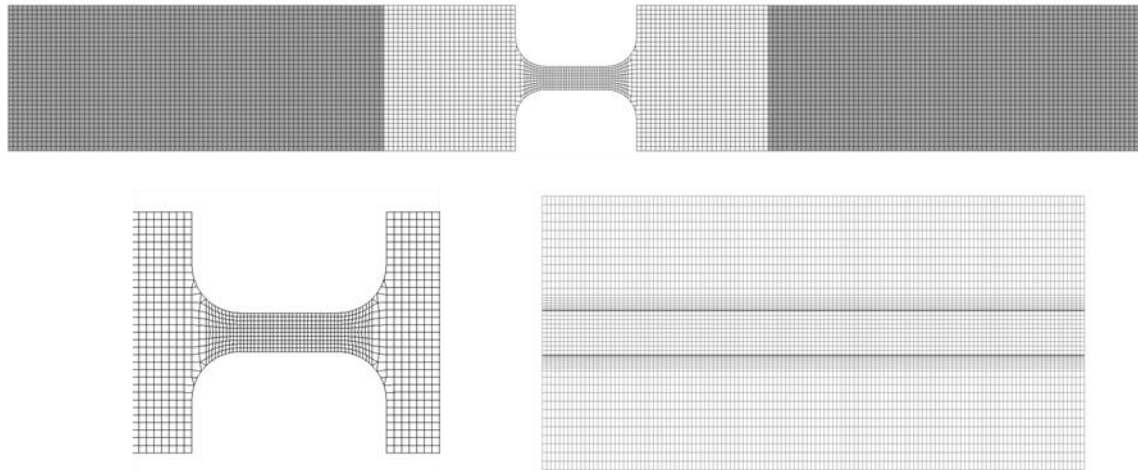
Figure 67. SG7 finite element mesh with grey rigid and white Inconel elements

5.1.8 SG8 – Axisymmetric specimen

SG8 is a variation of the axisymmetric specimen that has a specifically chosen center geometry, or notch, that will produce a unique triaxiality and Lode parameter. The dimensions of the specimen are shown in Figure 68.
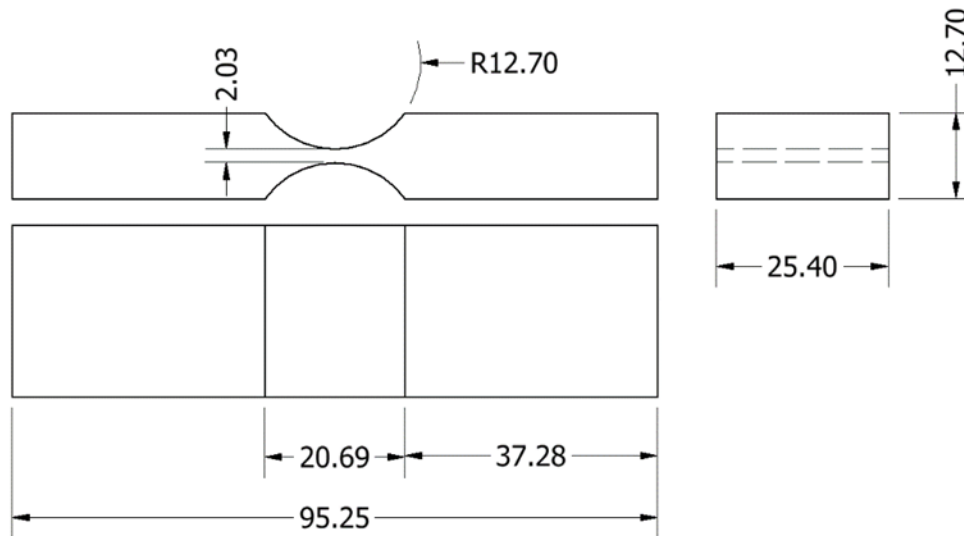

Figure 68. Geometry of the SG8 specimen

The specimen was meshed using solid elements with an average element size of 0.2 mm. The mesh of the SG8 specimen is shown in Figure 69. An enlargement of the test section is also shown. The mesh for this specimen contains a total of about 385,000 solid elements. In the Instron mechanical grip sections the elements were defined as rigid. Of the 385,000 elements, about 256,000 of them were defined as rigid. Figure 69 shows the rigid elements in grey, and the Inconel modeled elements in white.
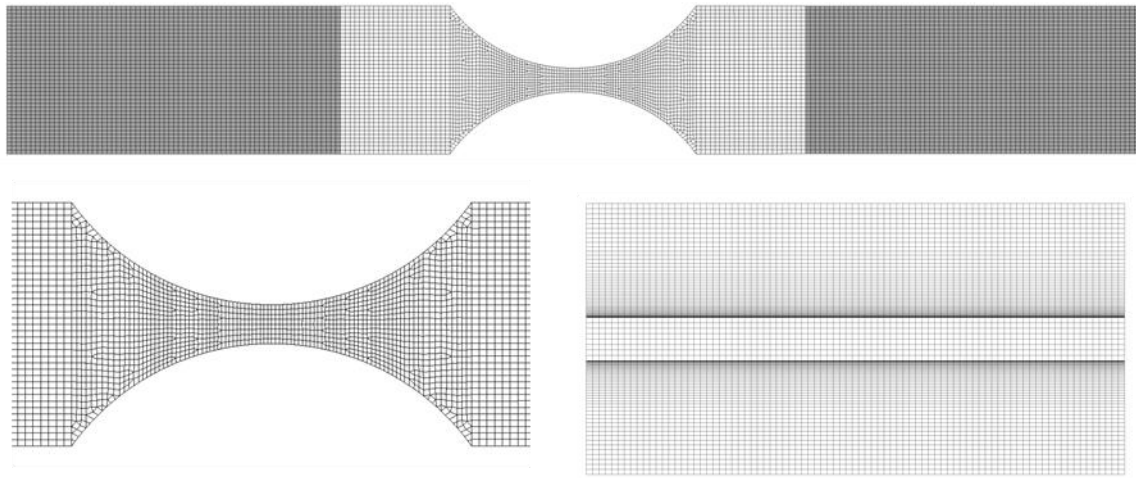
Figure 69. SG8 Finite element mesh with grey rigid and white Inconel elements

5.1.9 SG9 – Axisymmetric specimen

SG9 is a variation of the axisymmetric specimen that has a specifically chosen center geometry, or notch, that will produce a unique triaxiality and Lode parameter. The dimensions of the specimen are shown in Figure 70.
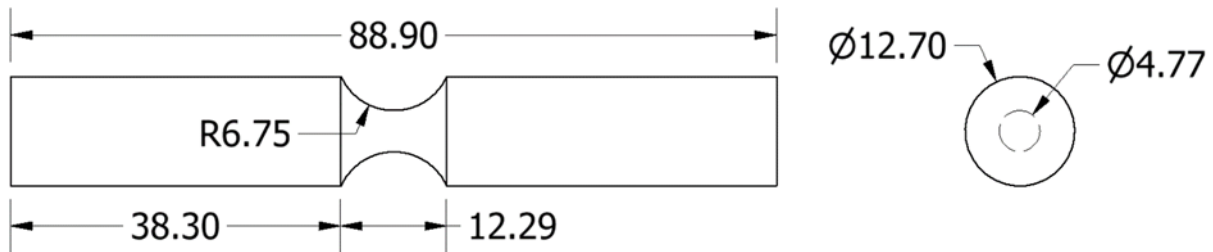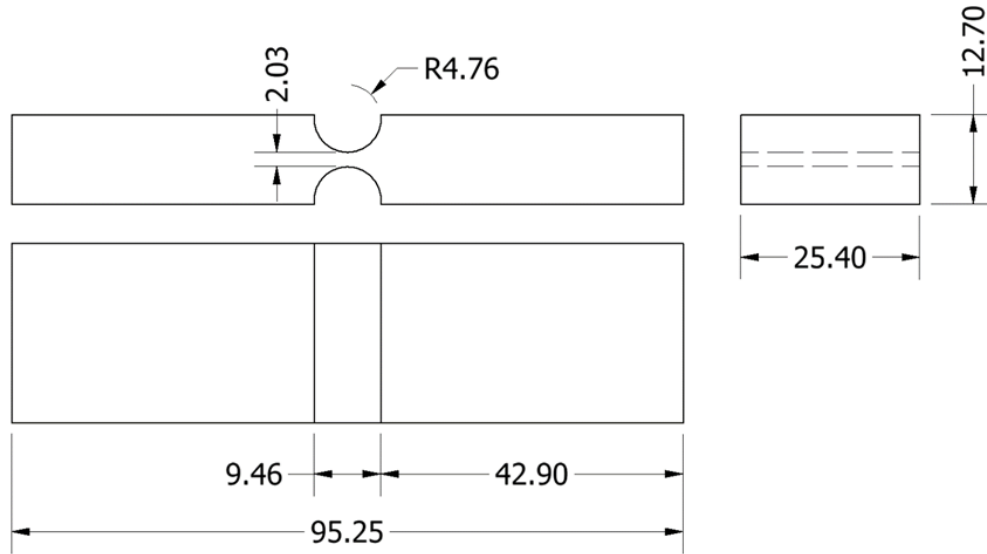

Figure 70. Geometry of specimen SG9

The specimen was meshed using solid elements with an average element size of 0.2 mm. The mesh of the SG9 specimen is shown in Figure 71. An enlargement of the test section is also shown. The mesh for this specimen contains a total of about 652,000 solid elements. In the Instron mechanical grip sections the elements were defined as rigid. Of the 652,000 elements, about 452,000 of them were defined as rigid. Figure 71 shows the rigid elements in grey, and the Inconel modeled elements in white.
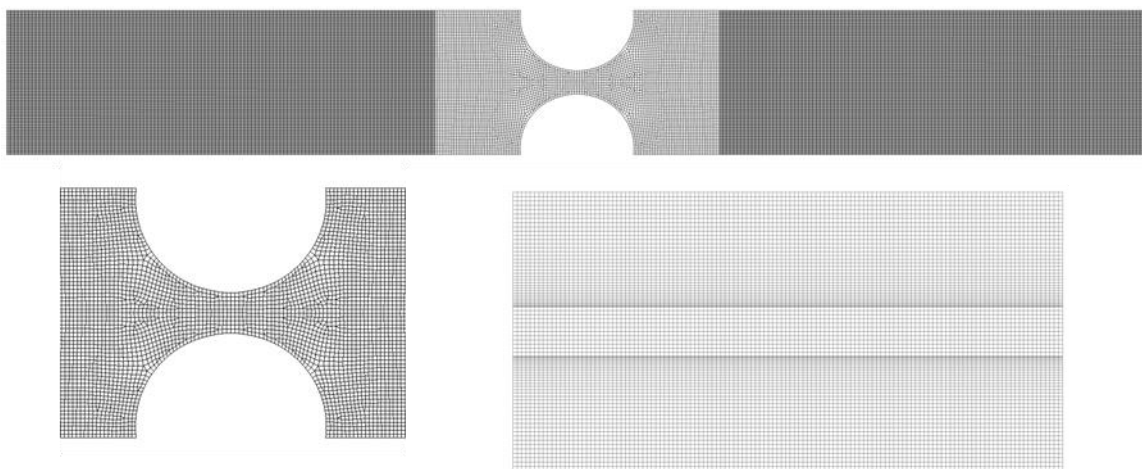
Figure 71. SG9 Finite element mesh with grey rigid and white Inconel elements

5.1.10 SG10 – Axisymmetric specimen

SG10 is a variation of the axisymmetric specimen that has a specifically chosen center geometry, or notch, that will produce a unique triaxiality and Lode parameter. The dimensions of the specimen are shown in Figure 72.
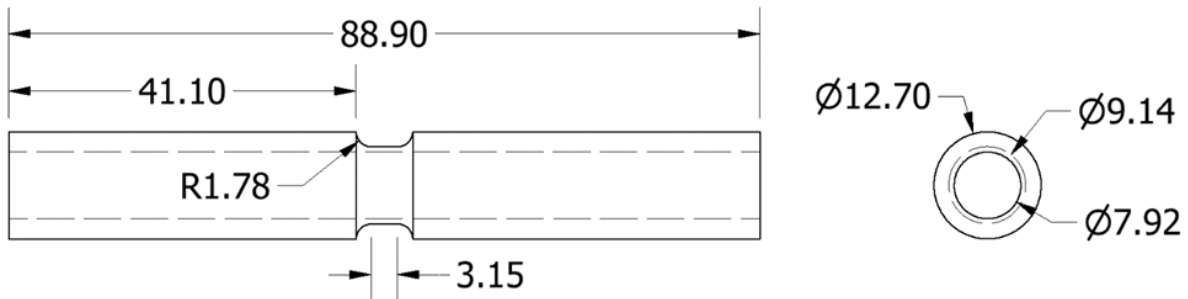

Figure 72. Geometry of the SG10 specimen

The specimen was meshed using solid elements with an average element size was 0.2 mm. The mesh of the SG10 specimen is shown in Figure 73. An enlargement of the test section is also shown. The mesh for this specimen contains a total of about 593,000 solid elements. In the Instron mechanical grip sections the elements were defined as rigid. Of the 593,000 elements, about 432,000 of them were defined as rigid. Figure 73 shows the rigid elements in grey, and the Inconel modeled elements in white.

Figure 73. SG10 finite element mesh with grey rigid and white Inconel elements

5.1.11 SG11 – Plane strain specimen

SG11 is a plane strain specimen that has a specifically chosen center geometry that is under pure tension. The dimensions of the specimen are shown in Figure 74.
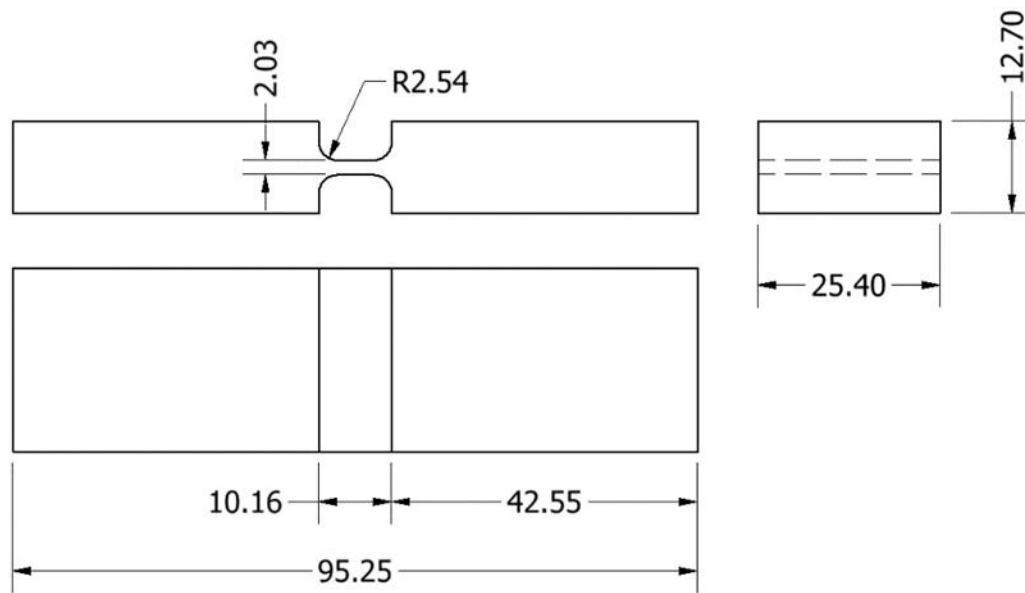
Figure 74. Geometry of the SG11 specimen

The specimen was meshed using solid elements with an average element size was 0.2 mm. The mesh of the SG11 specimen is shown in Figure 75. An enlargement of the test section is also shown. The mesh for this specimen contains a total of about 935,000 solid elements. In the

Instron mechanical grip sections the elements were defined as rigid. Of the 935,000 elements, about 642,000 of them were defined as rigid. Figure 75 shows the rigid elements in grey, and the Inconel modeled elements in white.

Figure 75. SG11 Finite element mesh with grey rigid and white Inconel elements

5.1.12 SG12 – Plane strain specimen

SG12 is a variation of the plane strain specimen that has a specifically chosen center geometry, or notch, that will produce a unique triaxiality and Lode parameter. The dimensions of the specimen are shown in Figure 76.

Figure 76. Geometry of the SG12 specimen

The specimen was meshed using solid elements with an average element size was 0.2 mm. The mesh of the SG12 specimen is shown in Figure 77. An enlargement of the test section is also shown. The mesh for this specimen contains a total of about 740,000 solid elements. In the Instron mechanical grip sections the elements were defined as rigid. Of the 740,000 elements, about 452,000 of them were defined as rigid. Figure 77 shows the rigid elements in grey, and the Inconel modeled elements in white.

Figure 77. SG12 Finite element mesh with grey rigid and white Inconel elements

5.1.13 SG13 – Plane strain specimen

SG13 is a variation of the plane strain specimen that has a specifically chosen center geometry, or notch, that will produce a unique triaxiality and Lode parameter. The dimensions of the specimen are shown in Figure 78.
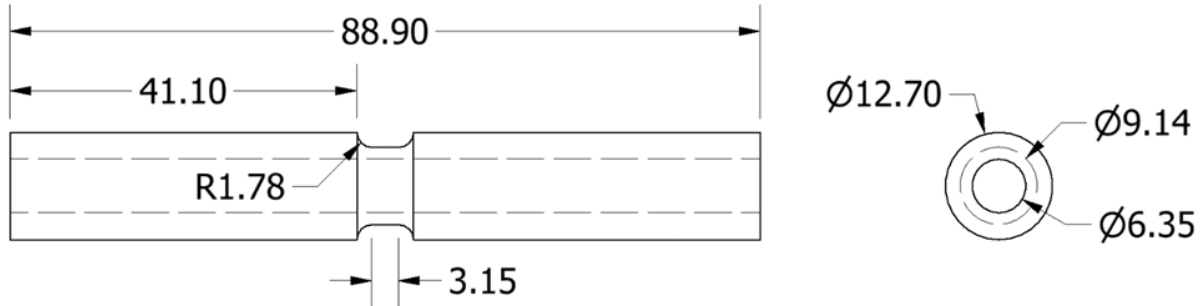
Figure 78. Geometry of the SG13 specimen

The specimen was meshed using solid elements with an average element size was 0.2 mm. The mesh of the SG13 specimen is shown in Figure 79. An enlargement of the test section is also shown. The mesh for this specimen contains a total of about 2,639,000 solid elements. In the Instron mechanical grip sections the elements were defined as rigid. Of the 2,639,000 elements, about 1,924,000 of them were defined as rigid. Figure 79 shows the rigid elements in grey, and the Inconel modeled elements in white.


Figure 79. SG13 Finite element mesh with grey rigid and white Inconel elements

5.1.14 LR1 – Combined (tension/torsion) specimen

LR1 is a combined loading specimen in which the ratio of tensile and torsional stress is adjusted so that the area of localization will result in a desired triaxiality and Lode parameter. LR1, LR2, and LR3 use the same specimen and mesh, but the ratio of the tension and the torsion differs. The dimensions of the tension/torsion specimen are shown in Figure 80.

Figure 80. Geometry of the LR1, LR2, and LR3 specimen

The specimen was meshed using solid elements with an average element size was 0.2 mm. The mesh of the LR1, LR2, and LR3 specimen is shown in Figure 81. An enlargement of the test section is also shown. The mesh for this specimen contains a total of about 814,000 solid elements. In the Instron mechanical grip sections the elements were defined as rigid. Of the 814,000 elements, about 442,000 of them were defined as rigid. Figure 81 shows the rigid elements in grey, and the Inconel modeled elements in white.
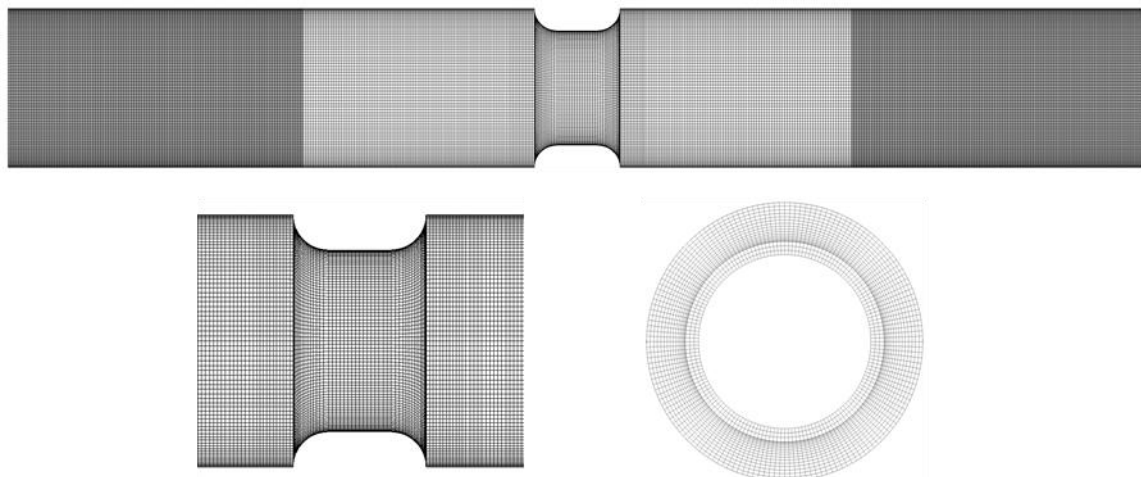
Figure 81. Tension/torsion combined finite element mesh

In the combined loading tests, the ratio of the applied force and torque determines the state of stress. In the simulations that ratio must precisely match the ratio of the tests. For these combined loading tests, the motion of the grips was controlled by an applied tension force and torque as defined by two input curves using a *LOAD_RIGID_BODY keyword. These two input curves were generated using data from the LR1 tests.

5.1.15 LR2 – Combined (tension/torsion) specimen

LR2 is a combined loading specimen in which the ratio of tensile and torsional stress is adjusted so that the area of localization will result in a unique triaxiality and Lode parameter. Because it is the tension and torque ratio that controls the stress state, the test specimen geometry is approximately the same as the LR1 specimen described in Section 5.1.14. As always, the mesh was adjusted slightly to precisely match the actual test specimen dimensions. The tension and torque curves were generated using data from the LR2 tests, and were applied using the *LOAD_RIGID_BODY keyword input.

5.1.16 LR3 – Torsion specimen

LR3 is a pure torsion test specimen that has the same geometry as the LR1 and LR2 specimen described in Section 5.1.14. Unlike the LR1 and LR2 combined loading tests, the LR3 test does not include an applied tension load. The mesh shown in Figure 81 and mechanical grip positions for the LR3 simulations were the same as for LR1 and LR2. The tension curve was generated using data from the LR3 tests, and was applied using the *LOAD_RIGID_BODY keyword input.

5.1.17 LR4 – Combined (compression/torsion) specimen

LR4 is a combined loading specimen in which the ratio of compressive and torsional stress is adjusted so that the area of localization will result in a desired triaxiality and Lode parameter. LR4 and LR5 use the same specimen and mesh, but the ratio of the compression and the torsion differs. The dimensions of the compression/torsion specimen are shown in Figure 82.

Figure 82. Geometry of the LR4 and LR5 specimen

The specimen was meshed using solid elements with an average element size was 0.2 mm. The mesh of the LR4 and LR5 specimen is shown in Figure 83. An enlargement of the test section is also shown. The mesh for this specimen contains a total of about 1,093,000 solid elements. In the Instron mechanical grip sections the elements were defined as rigid. Of the 1,093,000 elements, about 742,000 of them were defined as rigid. Figure 83 shows the rigid elements in grey, and the Inconel modeled elements in white.
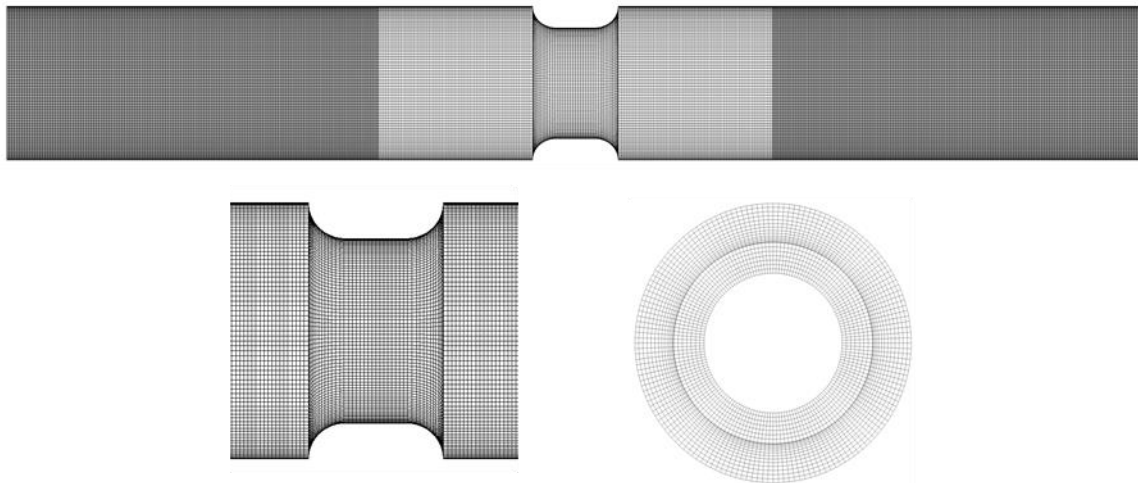
Figure 83. Compression/torsion combined finite element mesh

For these combined loading tests, the motion of the grips was controlled by an applied compression force and torque as defined by two input curves using a *LOAD_RIGID_BODY keyword. These two input curves were generated using data from the LR4 tests.

5.1.18 LR5 – Combined (compression/torsion) specimen

LR5 is a combined loading specimen in which the ratio of compression and torsional stress is adjusted so that the area of localization will result in a unique triaxiality and Lode parameter. Because it is the compression and torque ratio that controls the stress state, the test specimen geometry is approximately the same as the LR4 specimen described in Section 5.1.17. As always, the mesh was adjusted slightly to precisely match the actual test specimen dimensions. The compression and torque curves were generated using data from the LR5 tests, and were applied using the *LOAD_RIGID_BODY keyword input.

5.1.19 Punch1 – Large diameter punch specimen

Punch1 is a quasi-static test where a punch is forced through the center of an Inconel cylindrical plate until fracture occurs. The punch geometry was designed to produce a unique triaxiality and Lode parameter, on the opposite side of where the punch contacts the Inconel plate, and where the fracture occurs. The geometry and dimensions for Punch1 are shown in the Figure 84.
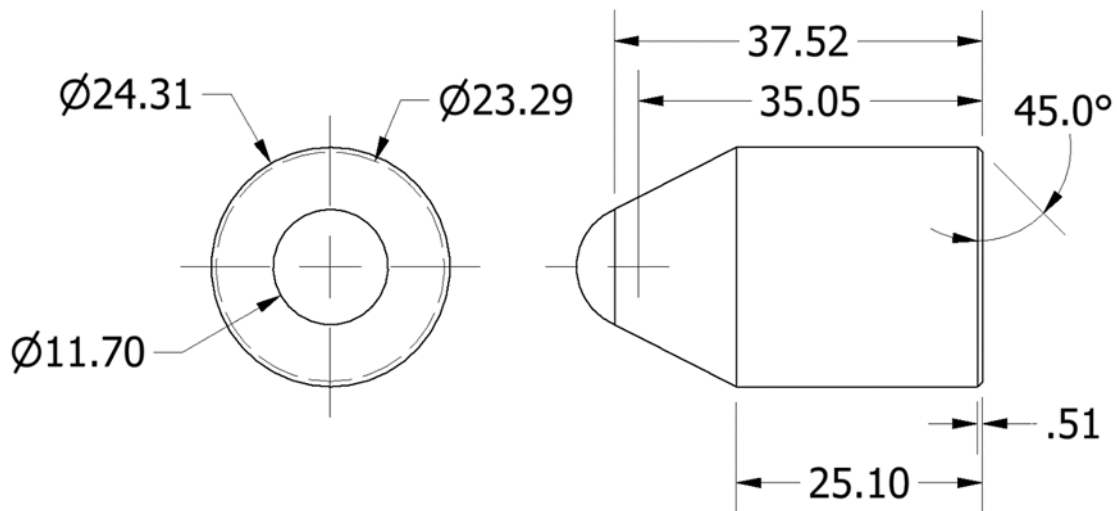
Figure 84. Geometry of the punch1 specimen

In the test simulation, the punch was modeled using rigid shell elements. The nominal size for each element was approximately 0.2 mm. The mesh has about 50,000 rigid shell elements (Figure 85).
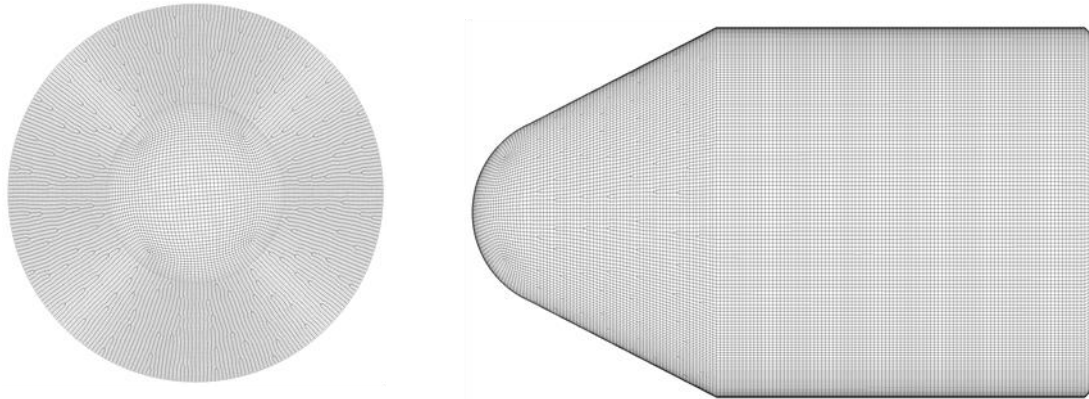
Figure 85. Meshed model of punch1

The Inconel plate is a cylinder with a 50.0 mm diameter and a 5.08 mm thickness. The outside of the cylindrical plate has fixed boundary conditions, and the plate's outer elements are modeled as rigid (shown in grey). The flexible elements are represented using the Inconel material model (shown in white). The mesh of the Inconel plate (Figure 86) contains about 420,000 elements. Of the total 420,000 elements, 164,000 are defined as rigid.
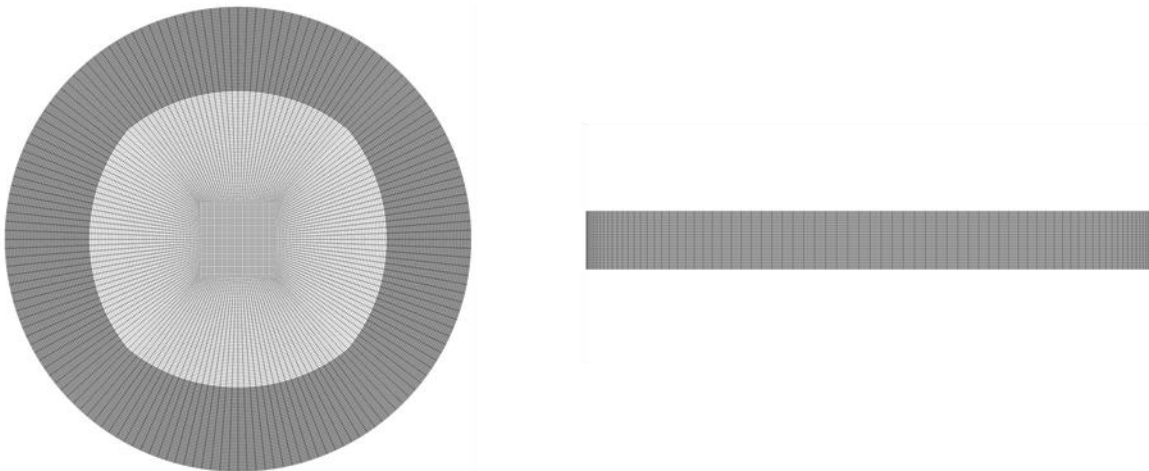
Figure 86. Meshed Inconel plate model for punch1, punch 2, and punch3

5.1.20 Punch2 – Large diameter punch specimen

Punch2 is a quasi-static test where a punch is forced through the center of an Inconel cylindrical plate until fracture occurs. The punch geometry was designed to produce a unique triaxiality and Lode parameter, on the opposite side of where the punch contacts the Inconel plate, and where the fracture occurs. The geometry and dimensions for Punch2 are shown in the Figure 87.
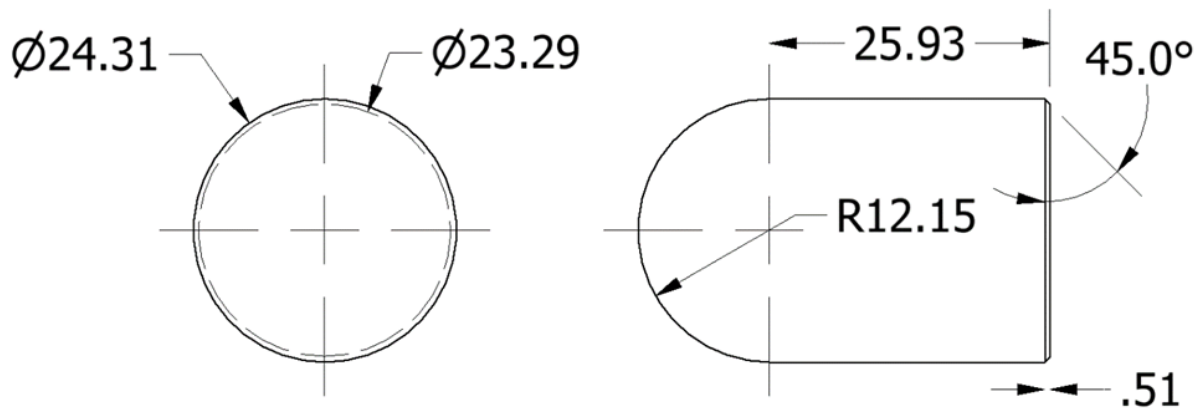
Figure 87. Geometry of punch2

In the test simulation, the punch was modeled using rigid shell elements. The nominal size for each element was approximately 0.2 mm. The mesh has about 58,000 rigid shell elements (see Figure 88).
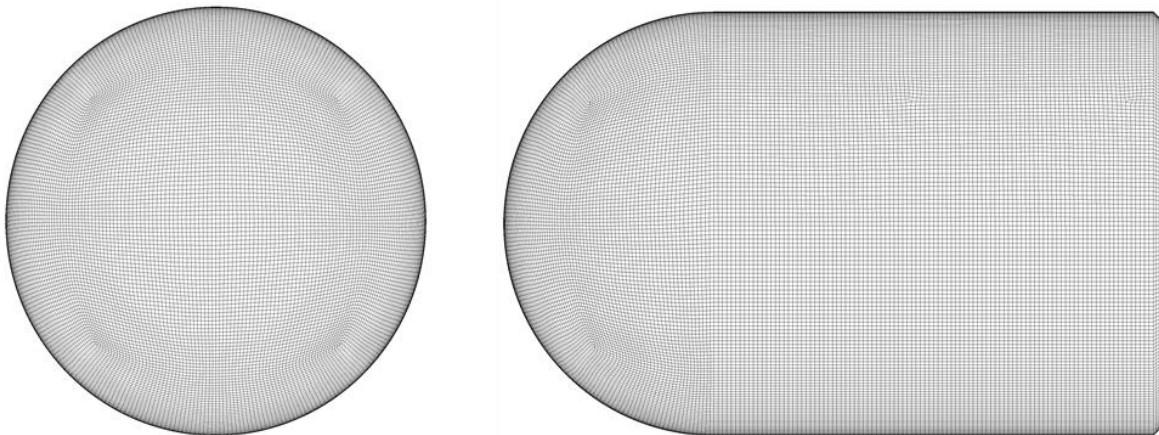
Figure 88. Meshed model of punch2

The Inconel plate used in the Punch2 test is identical to the Punch1 plate specimen. Therefore, the exact same dimensions and mesh described in the section above was used for this simulation (Figure 86).

5.1.21 Punch3 – Flat punch specimen

Punch3 is a quasi-static test where a punch is forced into the center of an Inconel cylindrical plate until fracture occurs. The punch geometry was designed to produce a unique triaxiality and Lode parameter, on the opposite side of where the punch contacts the Inconel plate, and where the fracture occurs. The geometry and dimensions for Punch3 are shown in the Figure 89.
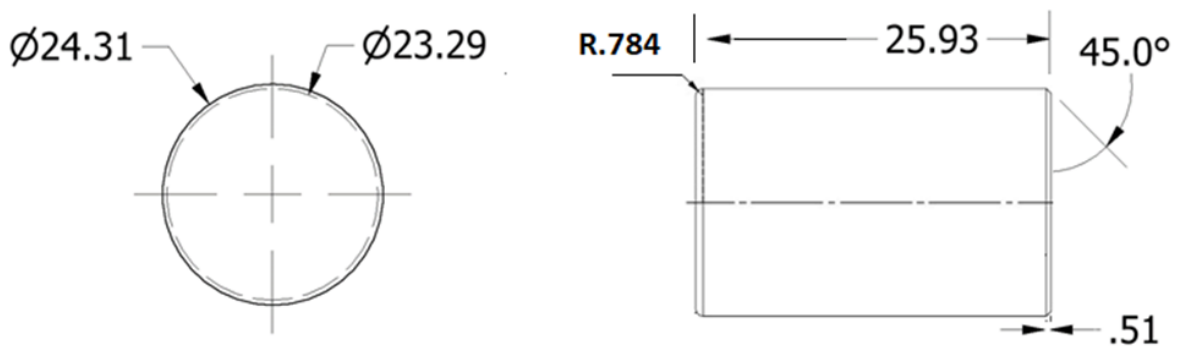
Figure 89. Geometry of specimen punch3

In the test simulation, the punch was modeled using rigid shell elements. The nominal size for each element was approximately 0.2 mm. The mesh has about 58,000 rigid shell elements (see Figure 90).
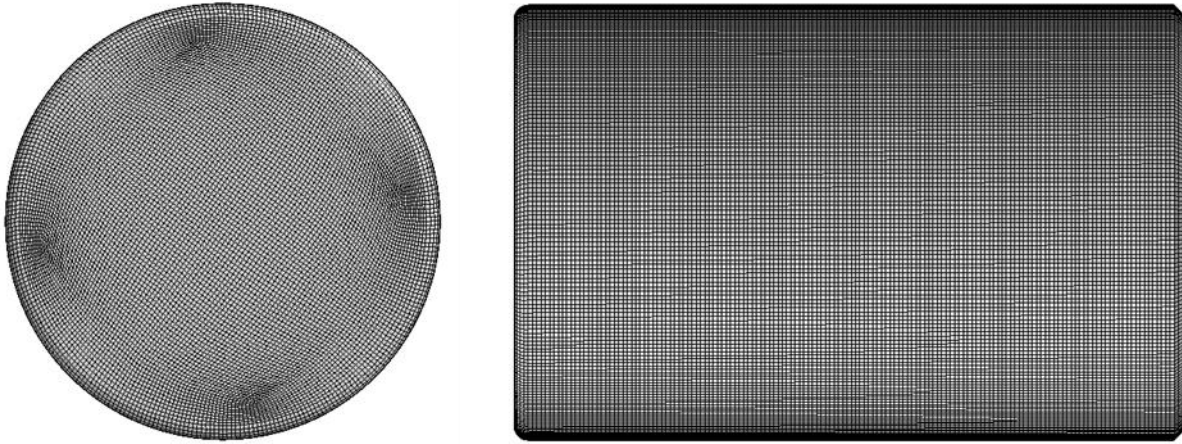
Figure 90. Meshed model of specimen punch3

The Inconel plate used in the Punch3 test is identical to the Punch1 plate specimen. Therefore, the exact same dimensions and mesh described in the section above was used for this simulation (Figure 86).

5.1.22 Compression –cylindrical specimen (uniaxial compression)

The compression test specimen is a small Inconel-718 cylinder. The cylinder has a diameter of 3.82 mm and a height of 3.73 mm. The finite element mesh has a nominal element size of 0.2 mm (Figure 91). Rigid walls are also modeled at the cylinder's two ends, simulating the plates of the Instron. One rigid wall is held fixed and the other displaces, compressing the cylinder, while allowing lateral expansion. The model of the compressive test specimen contains about 2,000 solid elements.
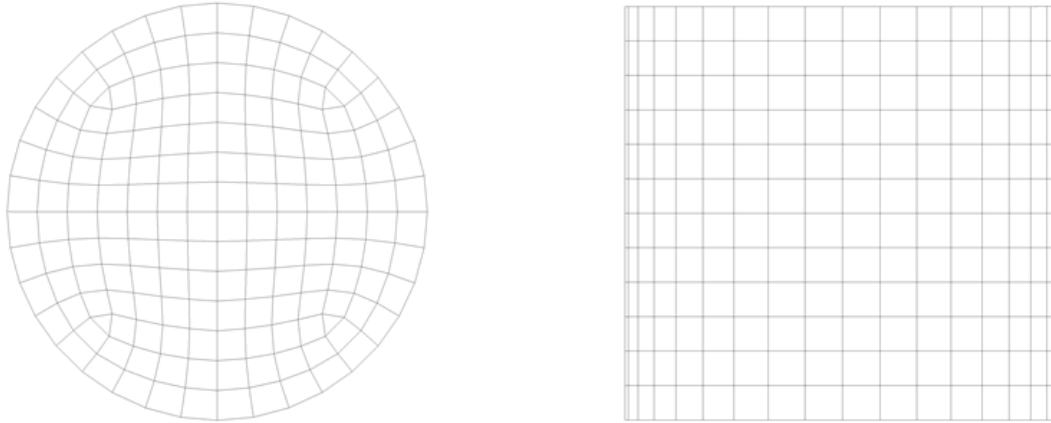
Figure 91. Meshed model of cylindrical compression specimen

Fractures did not occur during the uniaxial compression tests. Since no failure occurred in these tests, this specimen will essentially be used only to set a lower bound on the fracture strain. The failure surface at this stress state must be high enough that element erosion does not occur in the simulation of the test, and a specific value cannot be derived from this test.

5.1.23 Punch4: Unbacked

Punch4 is a test where a small diameter punch is forced into the center of an Inconel cylindrical plate until fracture occurs. The smaller punch head creates a stress state close to biaxial tension on the Inconel plate's side opposite from the punch, where the fracture occurs. The dimensions for Punch4 test, including both the punch and the Inconel plate, are shown in Table 4.

Table 4. Punch4 dimensions

Specimen Thickness (mm):	0.635
Clamp Diameter (mm):	25.4
Punch Diameter (mm):	2.2987
Punch Length (mm):	6.15

The nominal size for the elements in the Punch4 finite element mesh was approximately 0.15 mm. The simulation took advantage of the test's symmetry, using a ¼ axisymmetric mesh of both the plate and punch (Figure 92). The finite element mesh had a total 150,022 elements. There were 9,120 shell elements and 140,902 solids elements, of which 294 were rigid, and

149,728 were deformable. Because the tungsten carbide punch exhibited compressive elastic deformation in the test, the punch needed to be modeled as elastic.
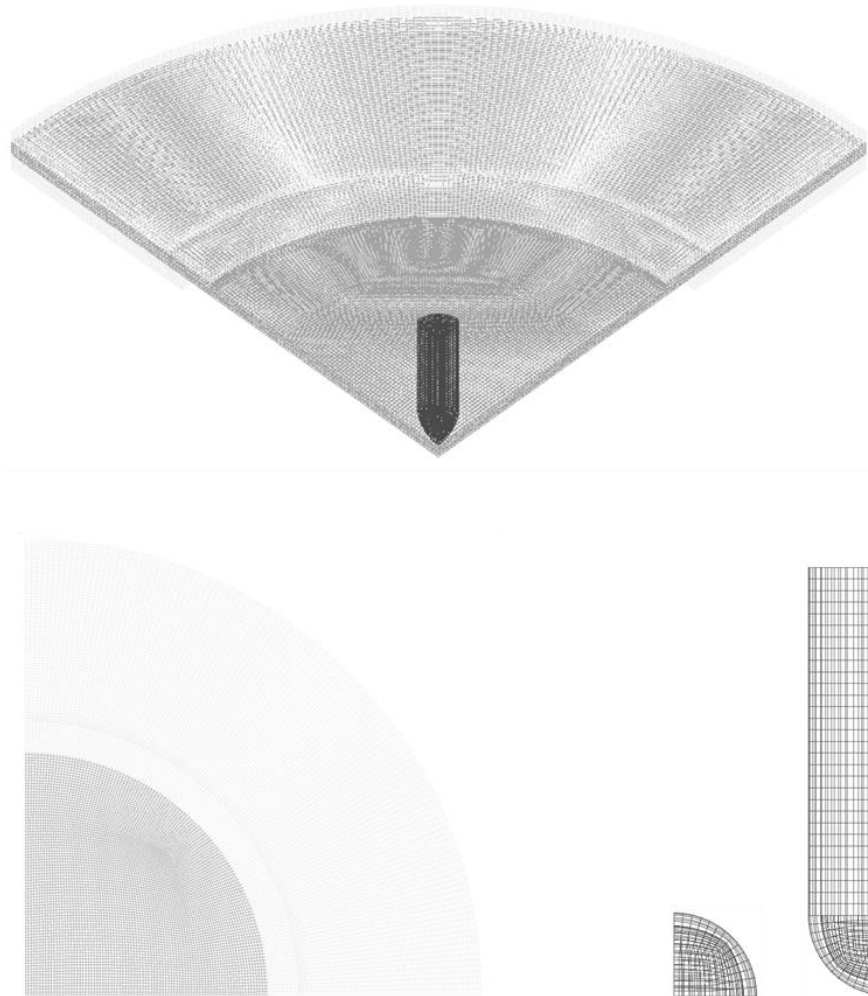
Figure 92. Punch4 test mesh, unbacked plate (left), and punch (right)

5.1.24 Punch5: Thick back plate

Punch5 is a test where a small diameter punch is forced into the center of an Inconel cylindrical plate until fracture occurs. Opposite of the punch side, there is a thick Copper backing plate behind the Inconel plate. This backing plate creates compression in the Inconel plate, and a Lode parameter of -1. The fracture occurs on the Inconel plate's surface where that plate contacts the backing plate. Because this location is not visible, the test must be conducted sequentially, with intermittent disassembles and inspections for fractures. The dimensions for the Punch5 test, including the punch, the Inconel plate, and the Copper backing plate are shown in Table 5.

Table 5. Punch5 dimension

Specimen Thickness (mm):	0.67056
Clamp Diameter (mm):	25.4
Punch Diameter (mm):	1.6129
Punch Length (mm):	66.8
Backing Plate Thickness (mm):	2.73304

The nominal size for the elements in the Punch5 finite element mesh was approximately 0.15 mm. The simulation took advantage of the test's symmetry, using a ¼ axisymmetric mesh of both the plate and punch (Figure 93). The finite element mesh had a total 398,761 elements. There were 11,040 shell elements and 387,715 solids elements, of which 430 were rigid, and 398,331 were deformable. Because the tungsten carbide punch exhibited compressive elastic deformation in the test, the punch needed to be modeled as elastic.
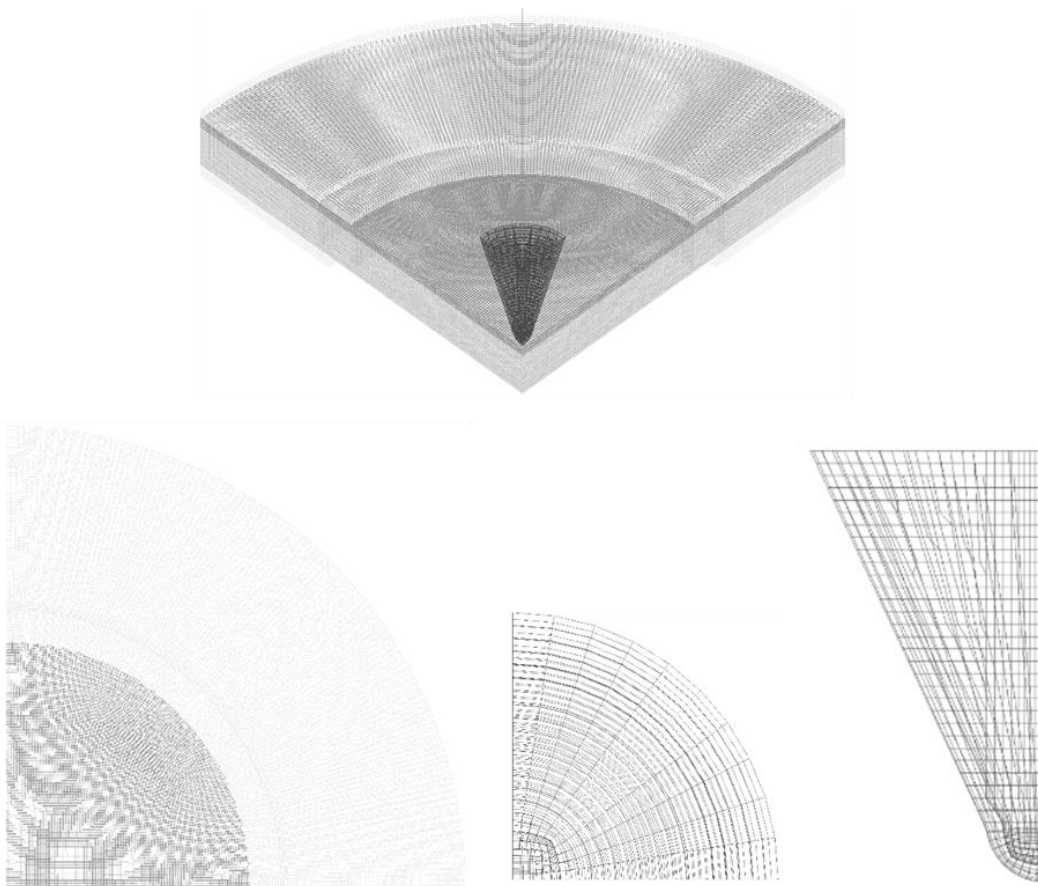
Figure 93. Punch5 test mesh, thick plate (left), and punch (right)

5.1.25 Punch6: Thin back plate

Punch6 is a test where a small diameter punch is forced into the center of an Inconel cylindrical plate until fracture occurs. Opposite of the punch side, there is a thin Copper backing plate behind the Inconel plate. This backing plate creates compression in the Inconel plate, and a Lode parameter of -1. The fracture occurs on the Inconel plate's surface where that plate contacts the backing plate. Because this location is not visible, the test must be conducted sequentially, with intermittent disassembles and inspections for fractures. The dimensions for the Punch6 test, including the punch, the Inconel plate, and the Copper backing plate are shown in Table 6.

Table 6. Punch6 dimensions

Specimen Thickness (mm):	0.6604
Clamp Diameter (mm):	25.4
Punch Diameter (mm):	1.6129
Punch Length (mm):	66.8
Backing Plate Thickness (mm):	1.83896

The nominal size for the elements in the Punch6 finite element mesh was approximately 0.15 mm. The simulation took advantage of the test's symmetry, using a ¼ axisymmetric mesh of both the plate and punch (Figure 94). The finite element mesh had a total 398,761 elements. There were 11,040 shell elements and 387,715 solids elements, of which 430 were rigid, and 398,331 were deformable. Because the tungsten carbide punch exhibited compressive elastic deformation in the test, the punch needed to be modeled as elastic.
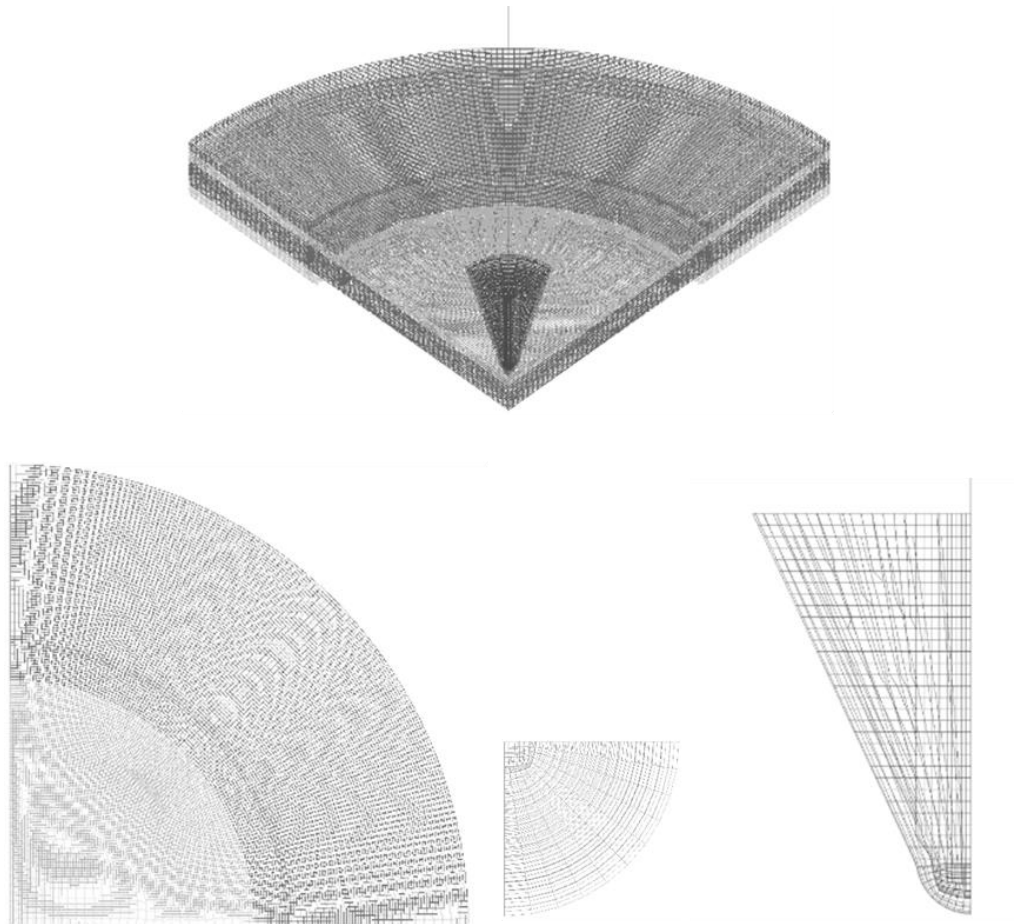
Figure 94. Punch6 test mesh, thin plate (left), and punch (right)

5.2   Simulation results of mechanical property tests

A single representative test from the several repeated tests of each specimen design series was selected. The selected test was simulated using the precise geometry of that specimen, and without a failure surface. The simulated force versus displacement predictions from each selected test was compared to the complete set of test repeats. In the combined loading tests, the torque versus twist angles were also compared. The full field strains from the simulation contour plots and test DIC images are also compared. Once a satisfactory match between simulation and test is obtained, initial inputs to the failure surface creation are estimated from the results.

To ensure that the correct displacements were compared, the test extensometer locations were matched to nodes from each finite element mesh. The differences between the two nodal displacements are used in comparisons to the test results. For the combined loading simulations,

the angle of twist must be extracted from nodal displacements. The angle of twist can be calculated using the extensometer nodal displacements, as shown in Figure 95. The angle of twist was compared directly to a rotary variable differential transformer (RVDT) test measurement.
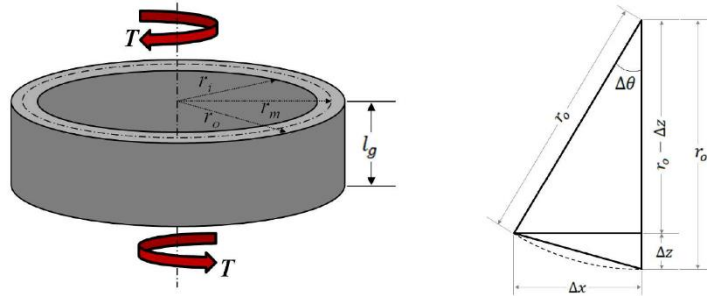
Figure 95. Measurement of twist angle

The geometry and dimensions shown in Figure 95 lead to the following equation for the angle of twist, $\Delta\theta$:

$$\Delta\theta = \arccos\left\{\frac{(r_0 - \Delta z)^2 + r_0^2 - \Delta x^2}{2[r_0 - (r_0 - \Delta z)]}\right\} \qquad 12$$

where r_0 is the outer radius of the cylinder, Δz is the displacement in the radial direction of the cylinder, and Δx is the displacement in the transverse lateral direction of the cylinder.

To obtain the forces, the *DATABASE_CROSS_SECTION_PLANE keyword input was defined at the center of the specimen. The normal vector of the cross-section was oriented to the direction of the loading. The force vs. displacement time history plots comparison for each specimen set is shown in Figure 96, a) thru x). Note that in the punch tests, fracture does not take place simultaneously with a sharp drop off in loading carrying capability. Rather, fracture takes place gradually.

The DIC virtual strain gauge length and element size of the simulation must be similar in order to accurately compare the strain contour images from the simulation and the test. Localization in the strain contour plots just prior to fracture, using the same normalization in both images, can be compared. The strain contour comparison for each specimen set is shown in Figure 97, a) thru v). No strain contour-comparison can be shown for Punch5 and Punch6 because the backing plates prevent the creation of DIC images.
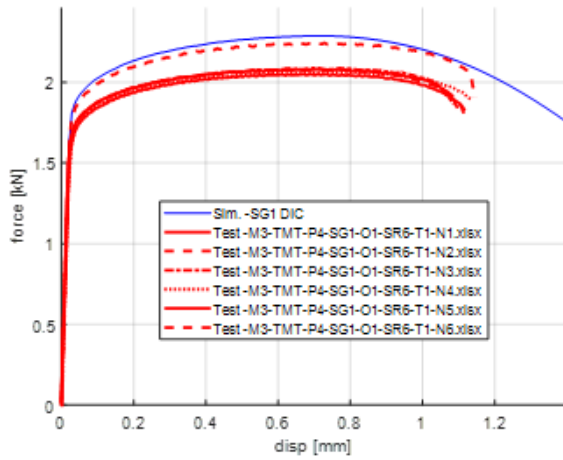
a) SG1
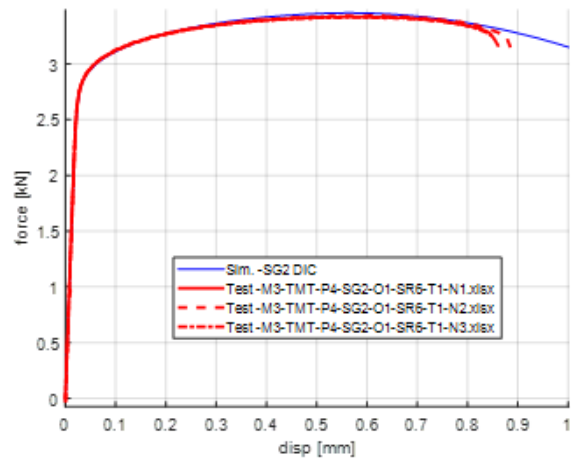
b) SG2
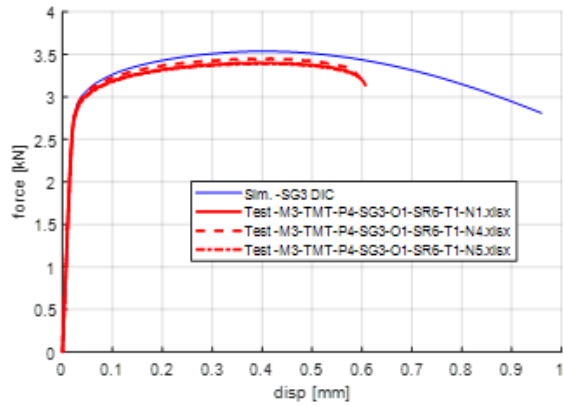
c) SG3
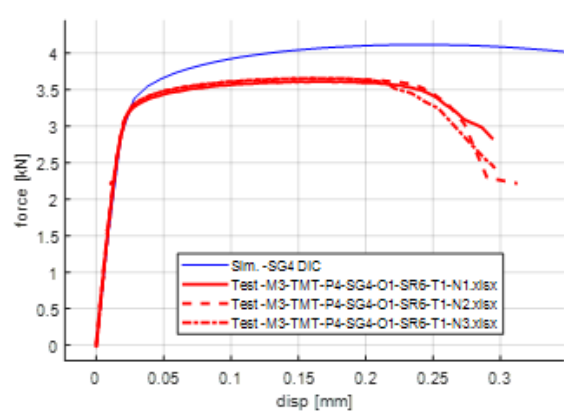
d) SG4
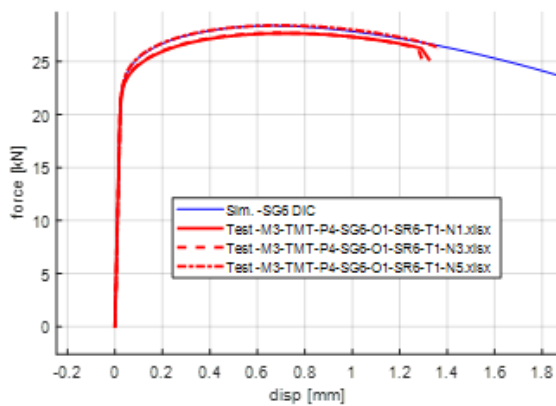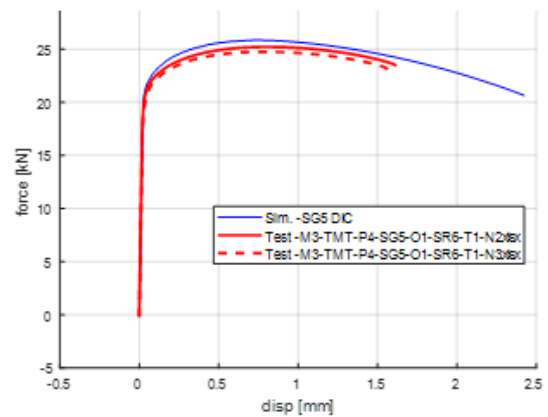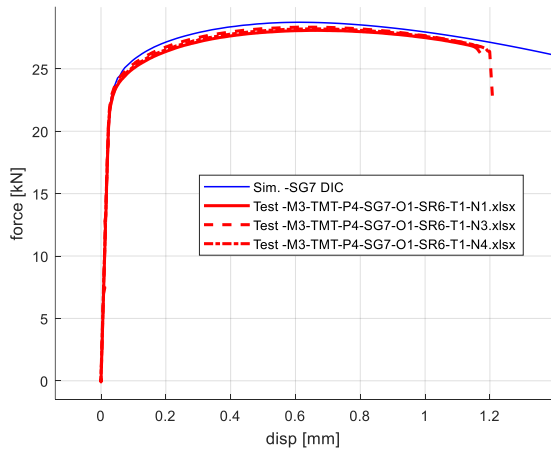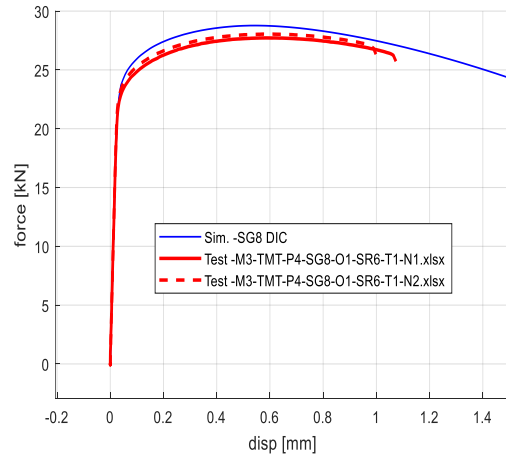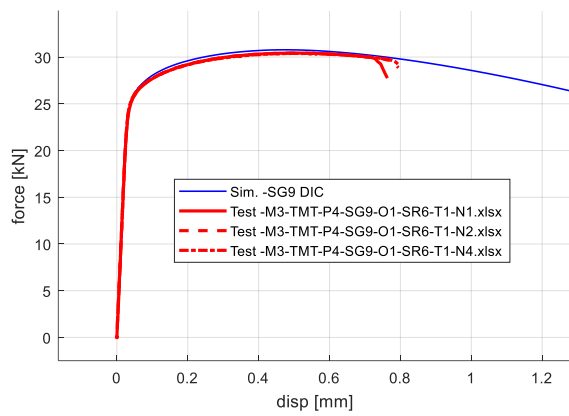
e) SG5
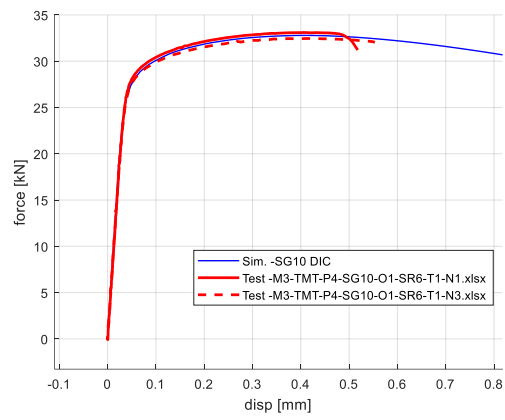
f) SG6

g) SG7
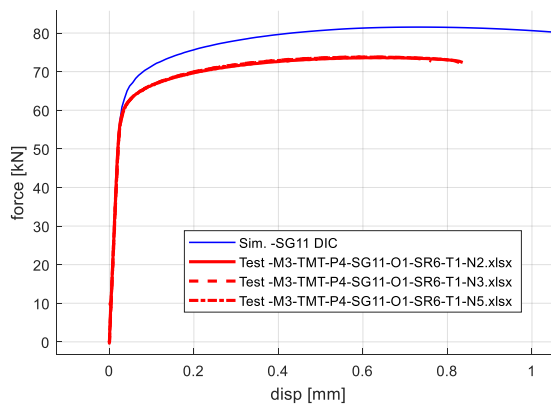
h) SG8
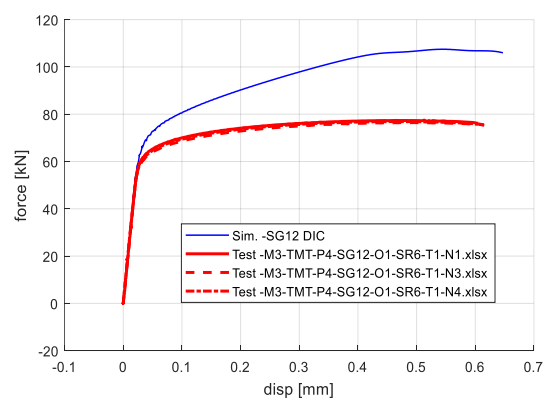
i) SG9
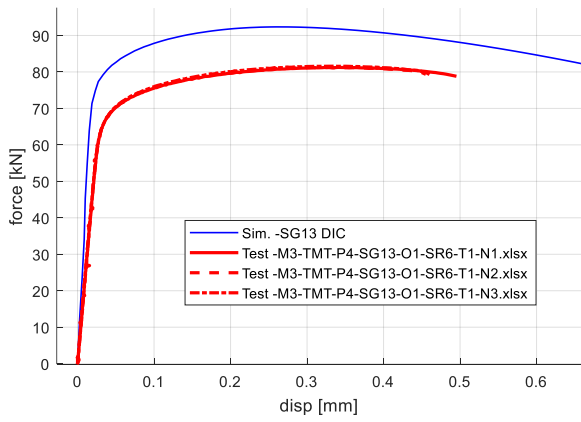
j) SG10
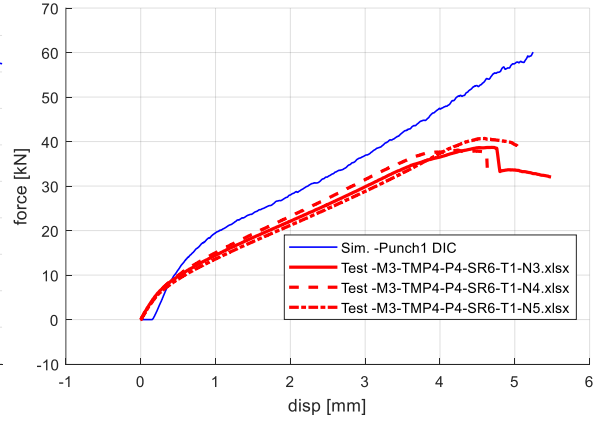
k) SG11

l) SG12

m) SG13

n) Punch1
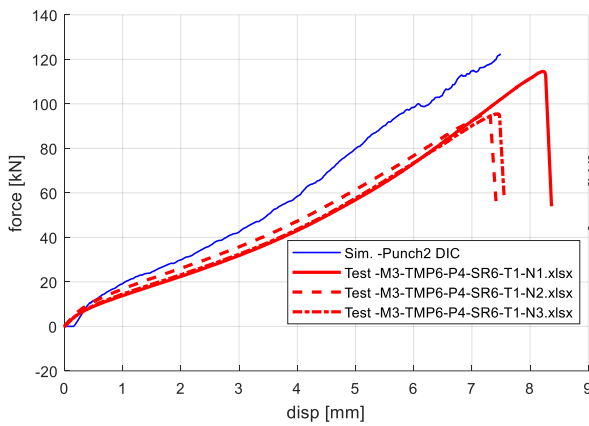
o) Punch2
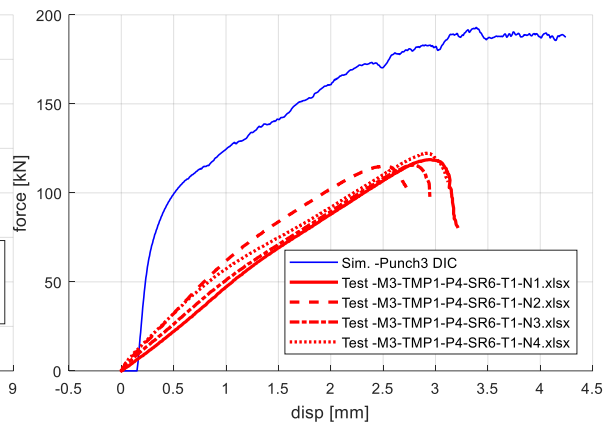
p) Punch3
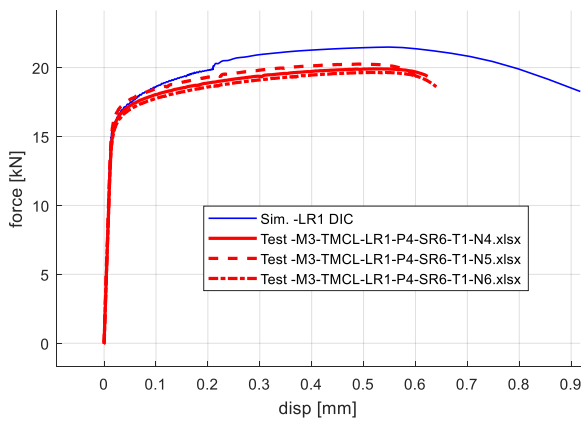
q) LR1
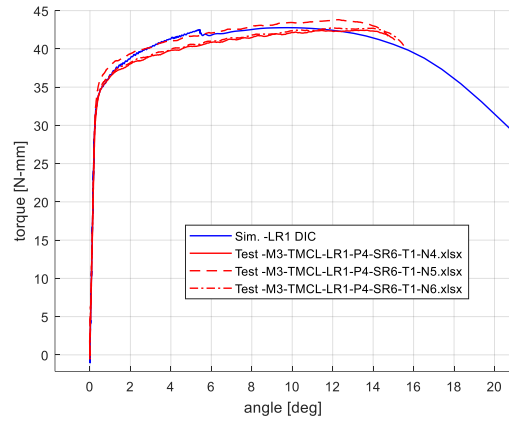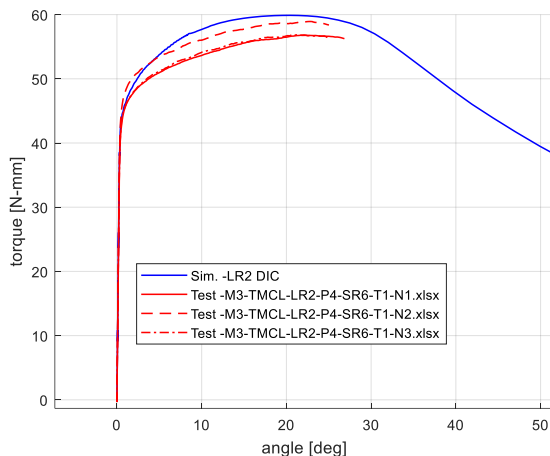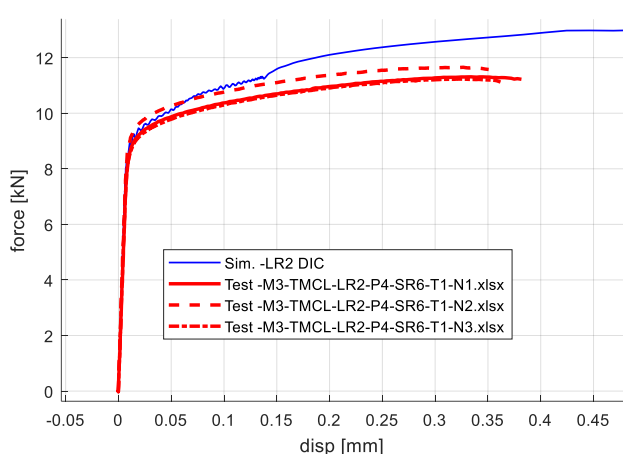
r) LR2
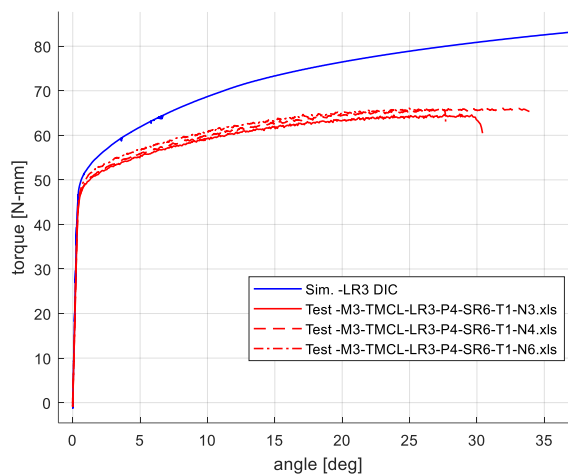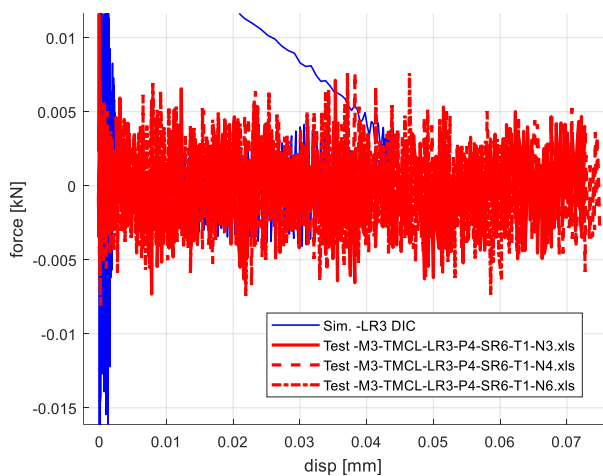
s) LR3
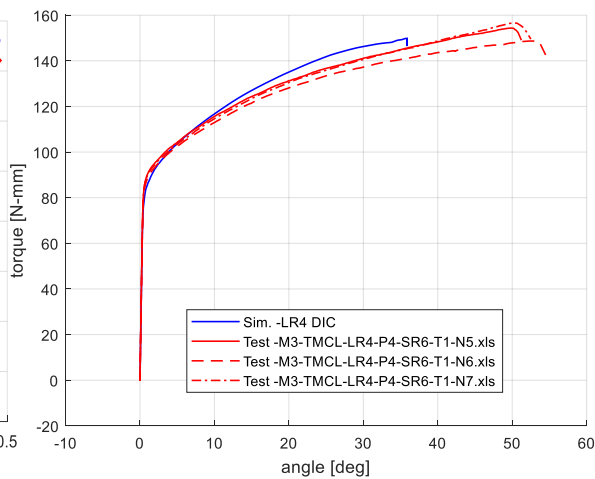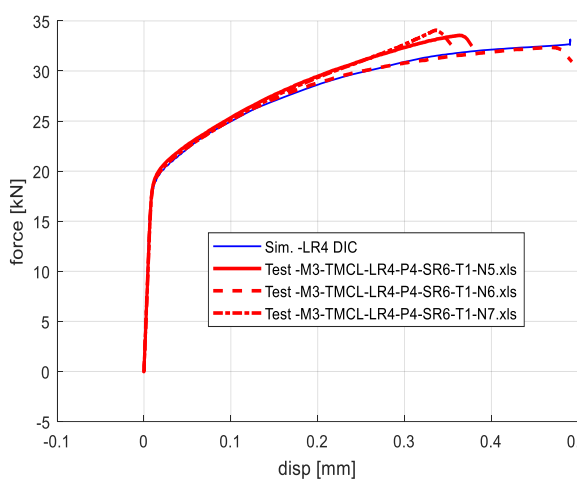
t) LR4
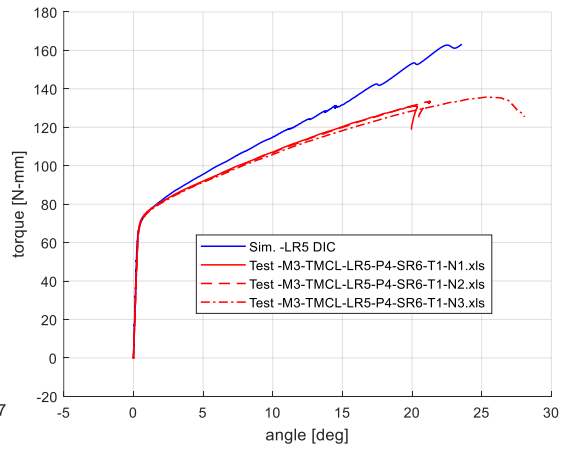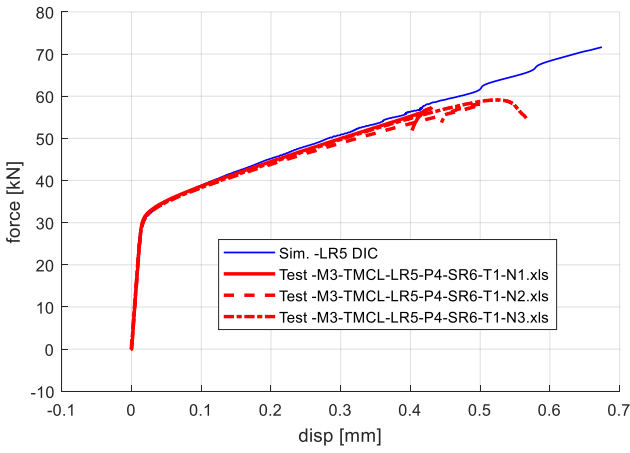
u) LR5
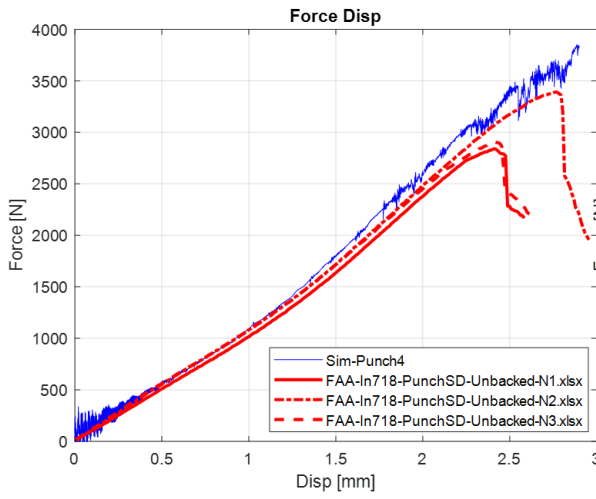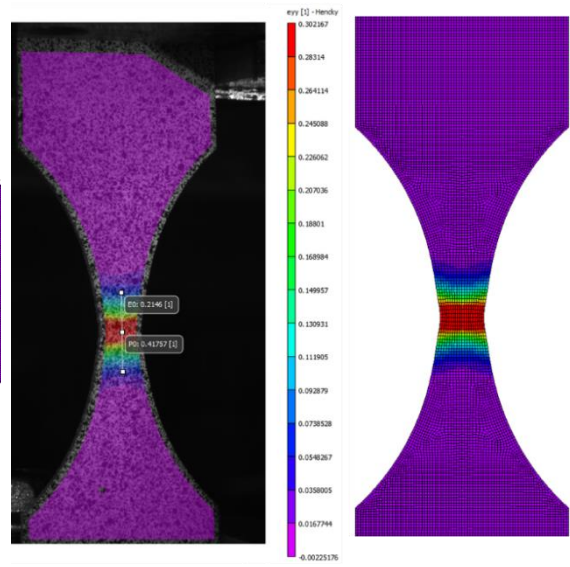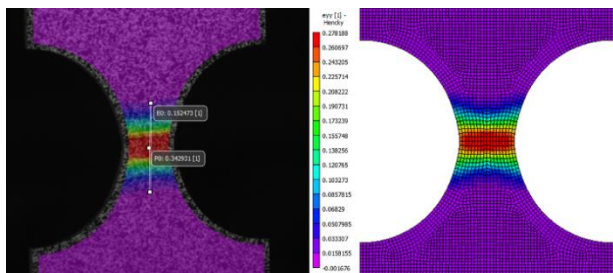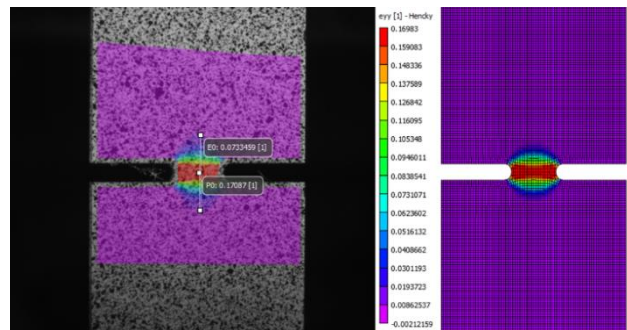

v) Punch4
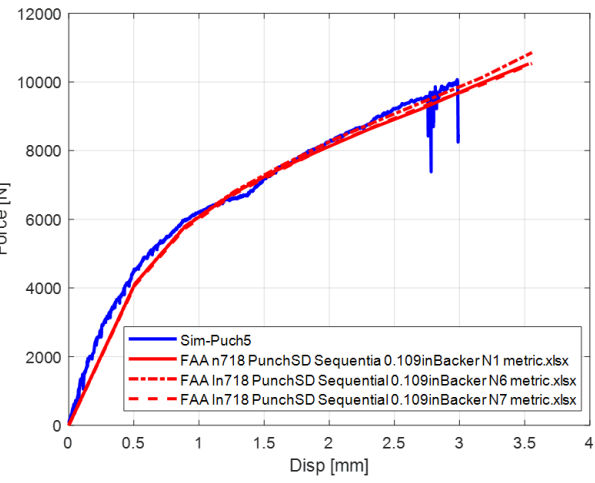
w) Punch5
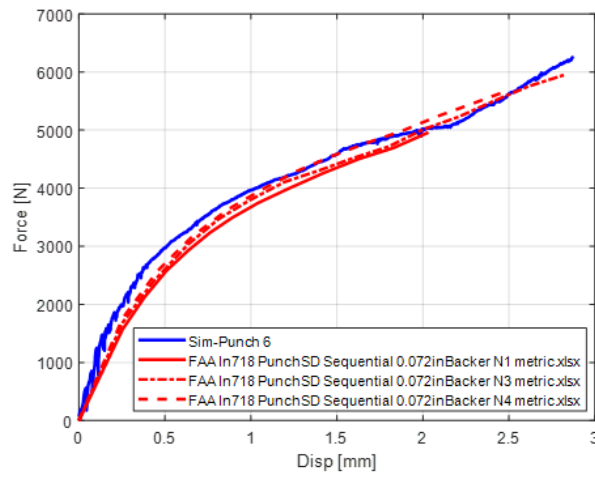
x) Punch6

Figure 96. Force vs. displacement comparison plot for each specimen set a) thru x)
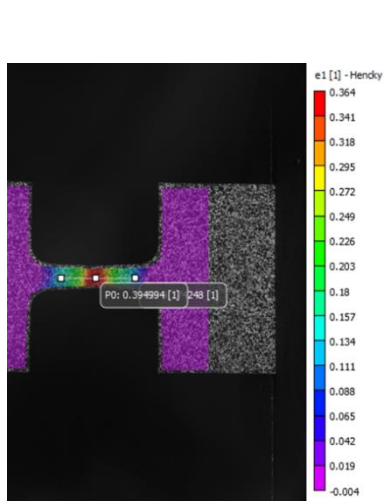
a) SG1

b) SG2

c) SG3

d) SG4
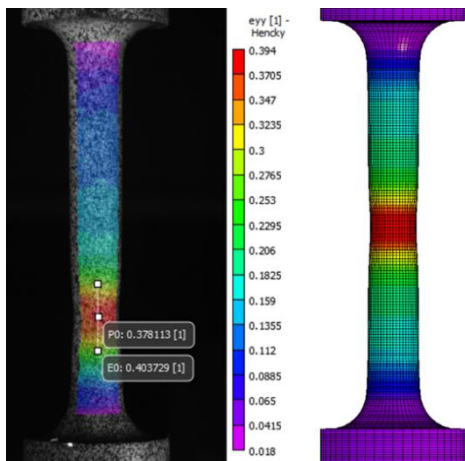
e) SG5
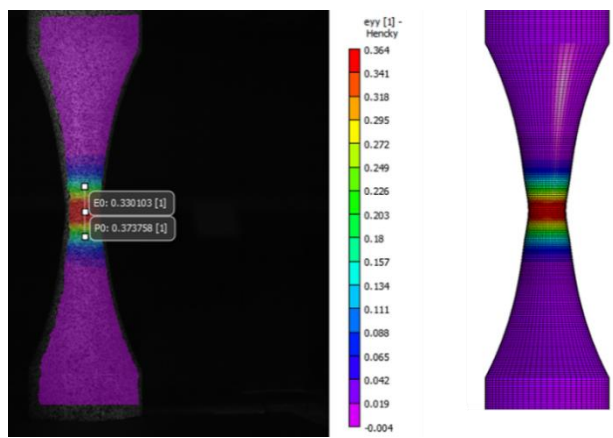
f) SG6

g) SG7
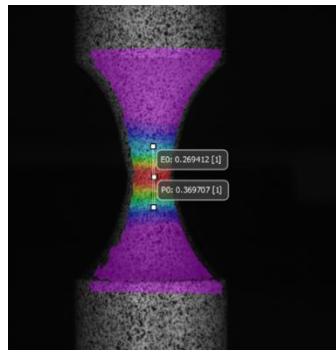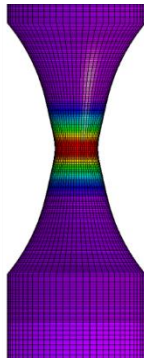
h) SG8
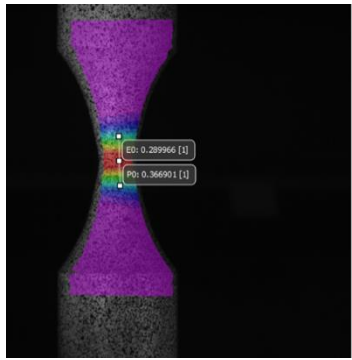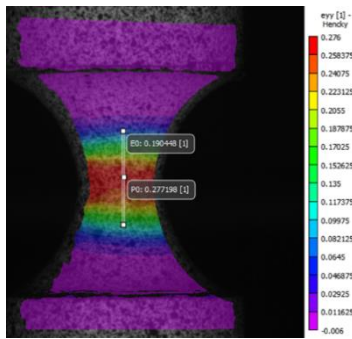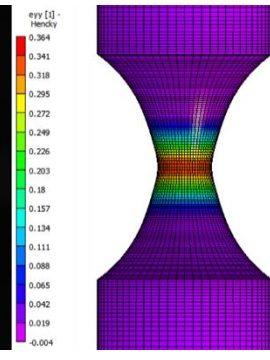

i) SG9
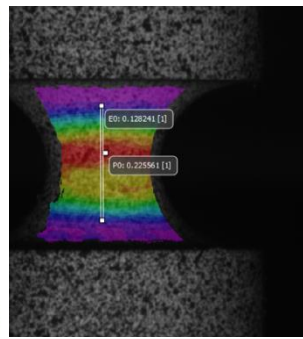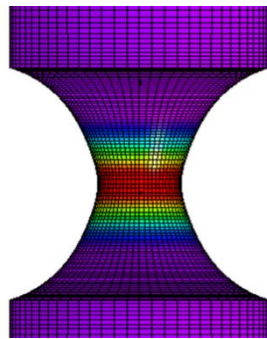
j) SG10
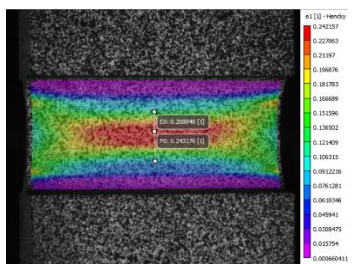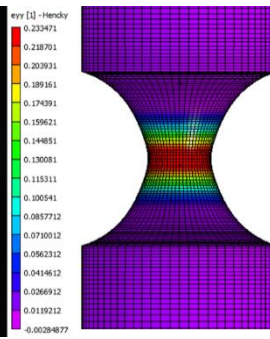
k) SG11
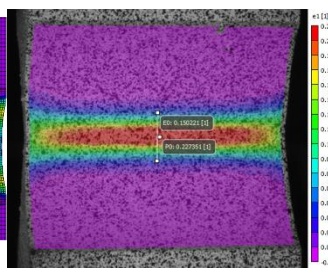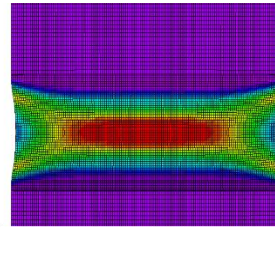
l) SG12
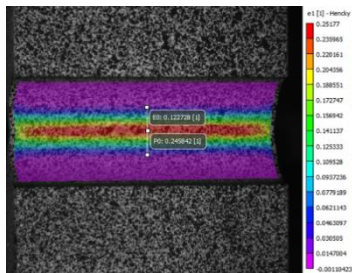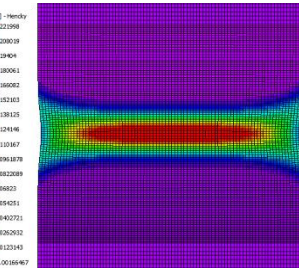
m) SG13
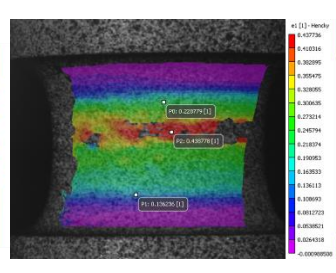
n) LR1
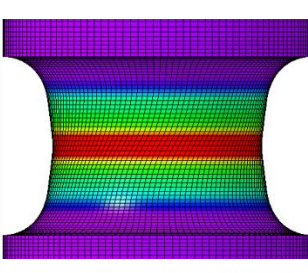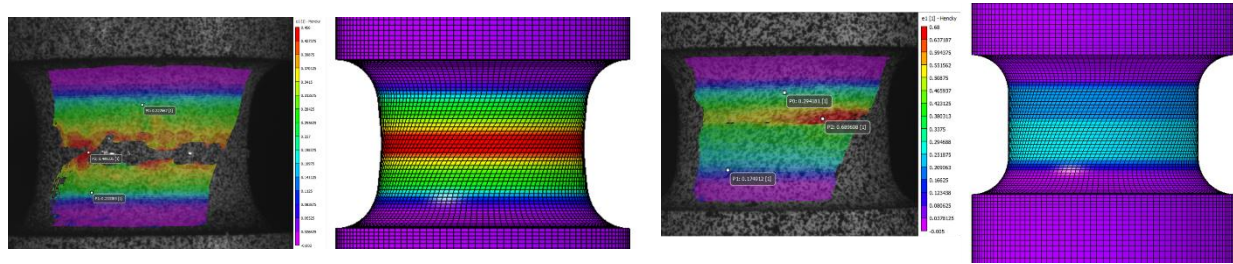
o) LR2

p) LR3
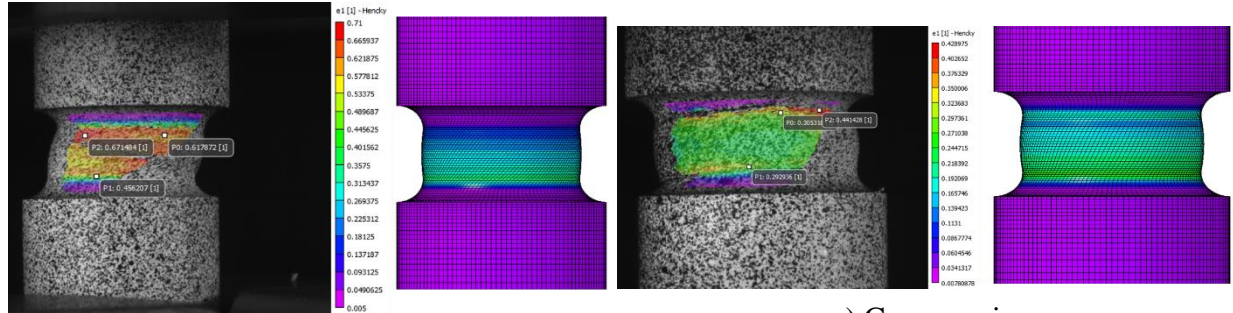
q) LR4

r) Compression
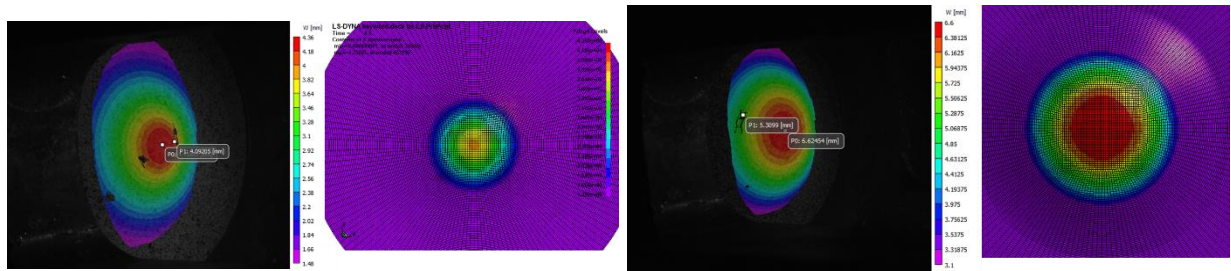
s) Punch1

t) Punch2
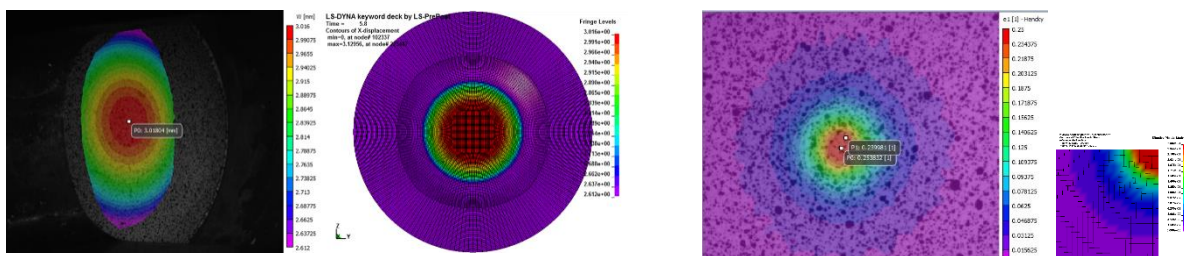
u) Punch3

v) Punch4

Figure 97. Strain contour comparison for each specimen set a) thru v)

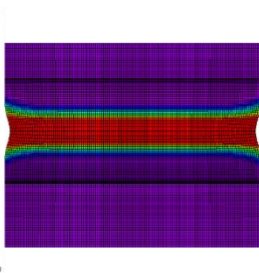The comparisons of the test and simulation results shown in Figure 96 and Figure 97 demonstrate acceptable agreement. Noticeable differences in SG11, SG12, SG13, and LR3's force versus displacement plots are thought to arise from Inconel-718 not precisely following J2 flow theory. Noticeable differences in the Punch1, Punch2, and Punch3 plots are thought to originate from the uncertain and difficult to model boundary conditions in these test setups. In both cases, these differences do not strongly affect the usage of these tests in failure surface creation.

The stress states of each test specimen are evaluated by examining the triaxiality and Lode parameters of a single element. An element where the fracture is likely to occur early, and located in the center of the specimen, is selected from each test set. Figure 98 a) thru x) shows the location of the selected element with a red spot, for each specimen.

a) SG1   b) SG2   c) SG3

d) SG4   e) SG5   f) SG6

g) SG7   h) SG8   i) SG9

j) SG10   k) SG11   l) SG12

m) SG13   n) LR1   o) LR2
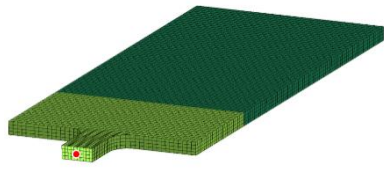
p) LR3   q) LR4   r) LR5

s) Punch 1   t) Punch2   u) Punch3

v) Punch4   w) Punch5   x) Punch6
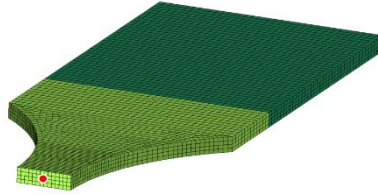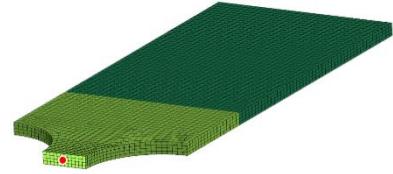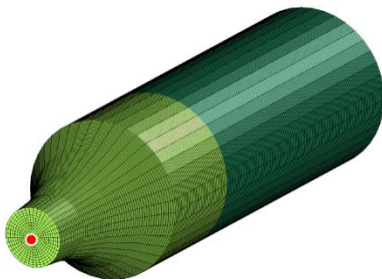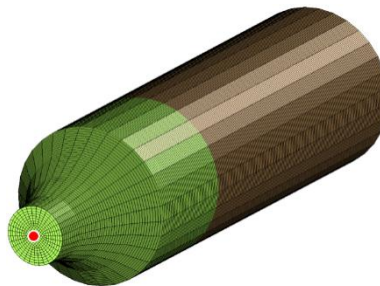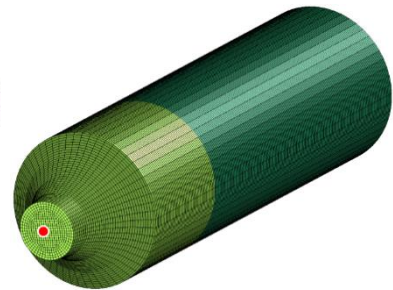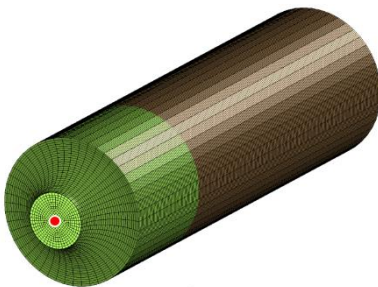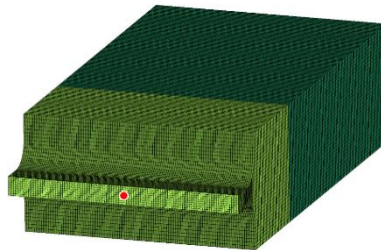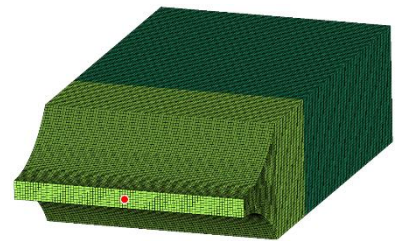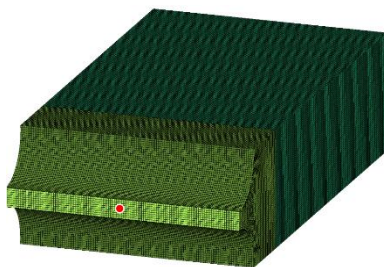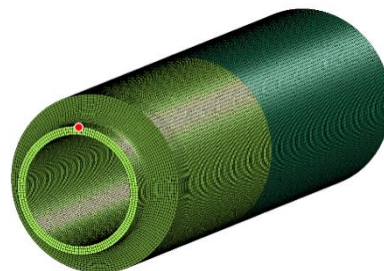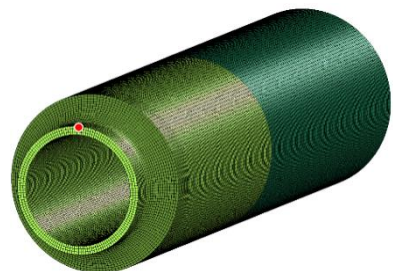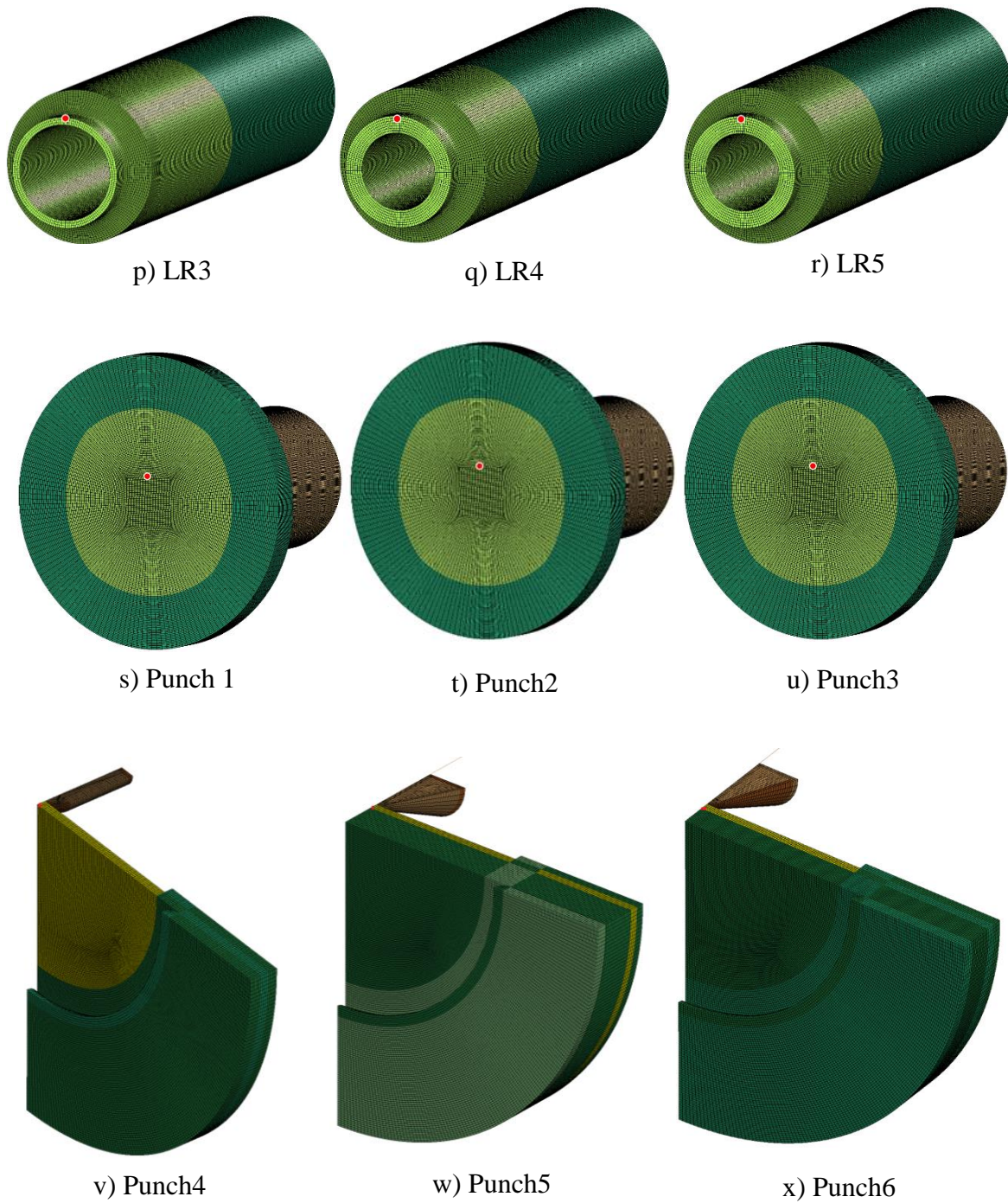
Figure 98. Red spot denoting selected elements for stress state evaluation a) thru x)

The triaxiality and Lode parameter time histories of the selected, likely to fracture elements are individually plotted as a function of the effective plastic strain in Figure 99 a) thru y).
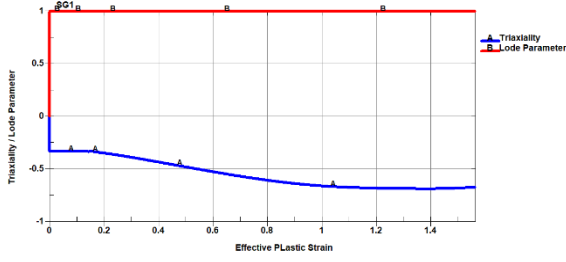
a) SG1
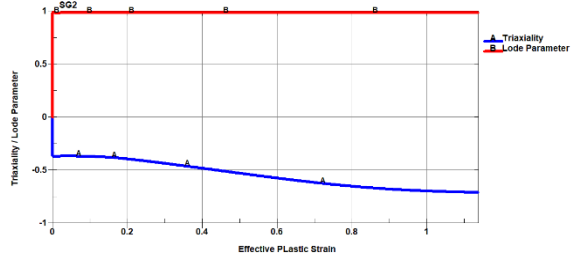
b) SG2
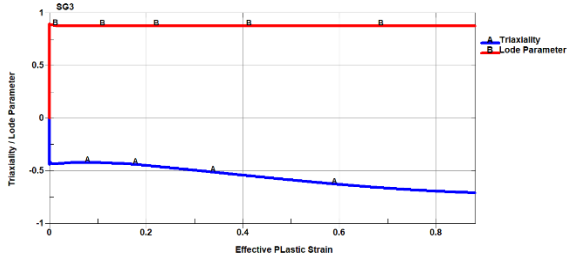
c) SG3
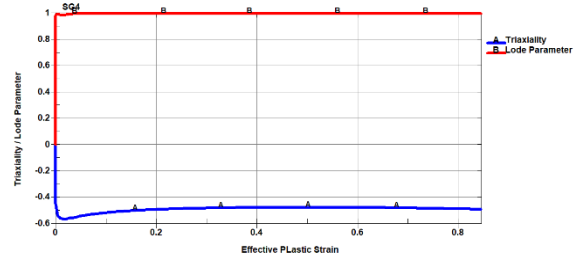
d) SG4
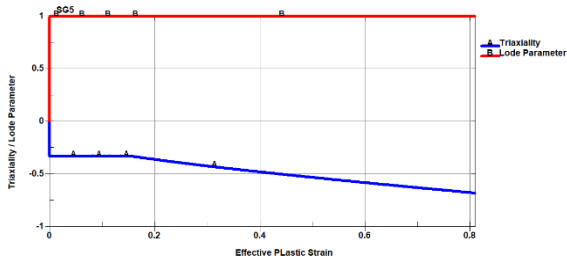
e) SG5
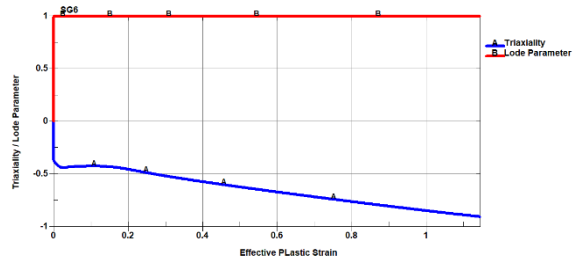
f) SG6
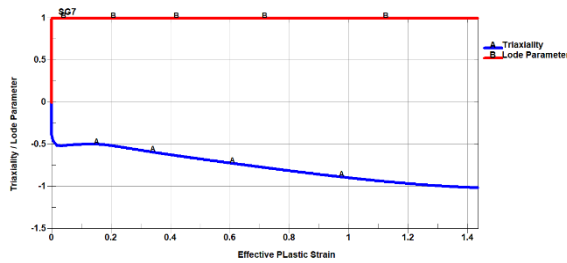
g) SG7
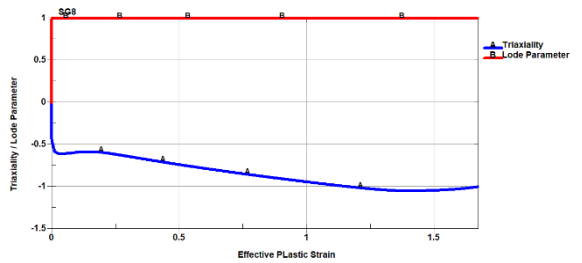
h) SG8
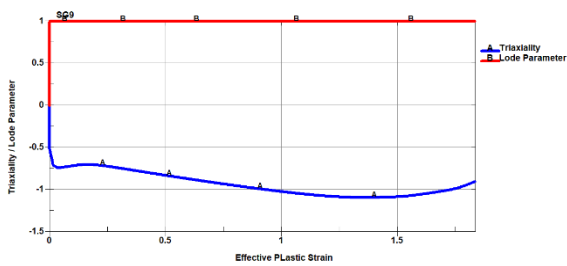
i) SG9
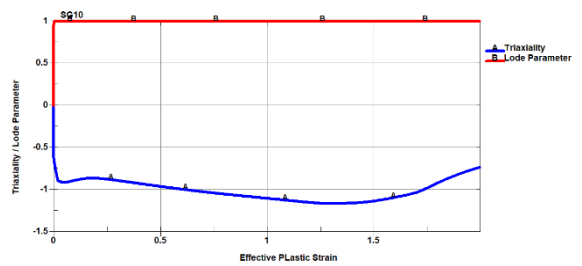
j) SG10
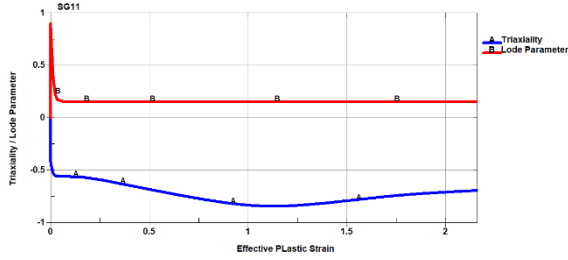
k) SG1
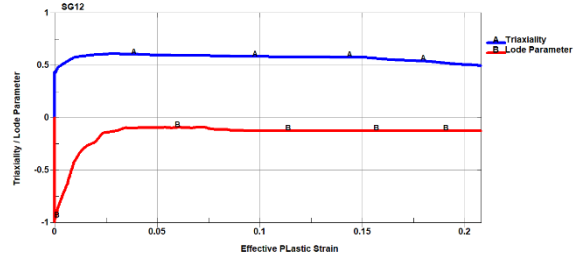
l) SG12
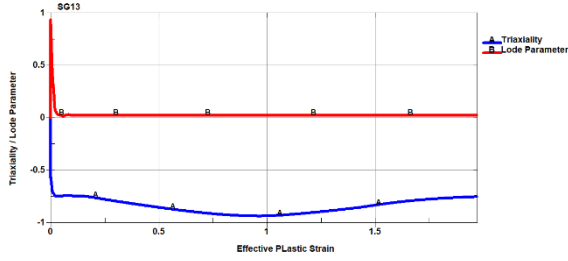
m) SG13
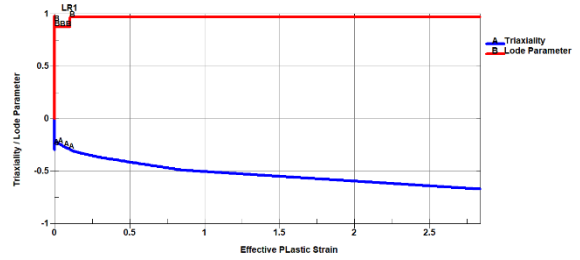
n) LR1
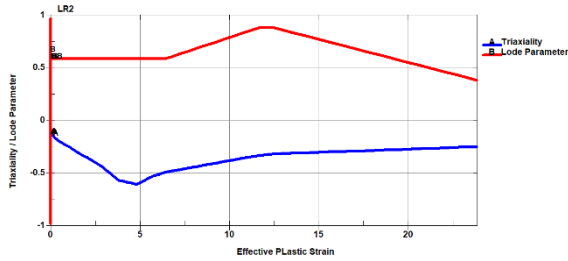
o) LR2
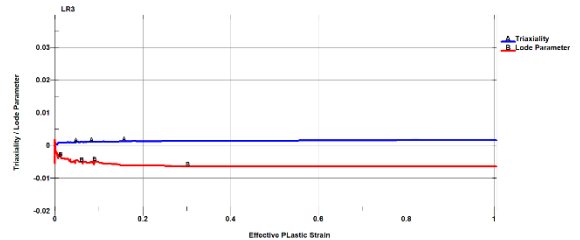
p) LR3
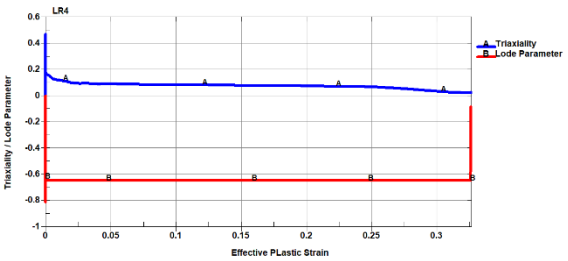
q) LR4
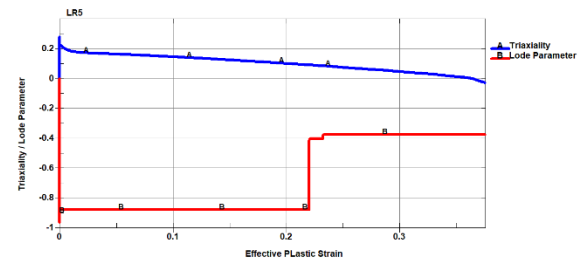
r) LR5
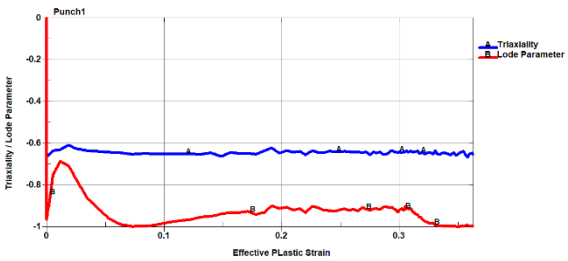
s) Punch1
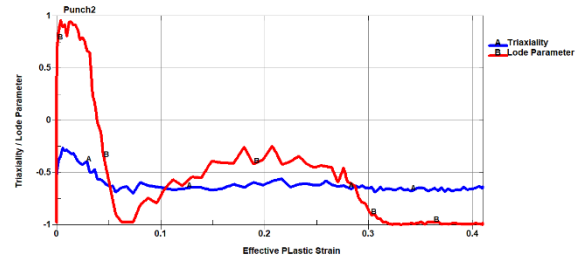
t) Punch2
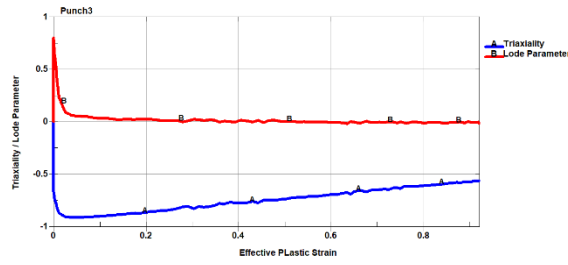
u) Punch3
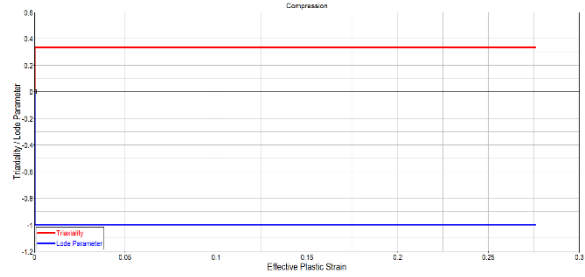
v) Compression
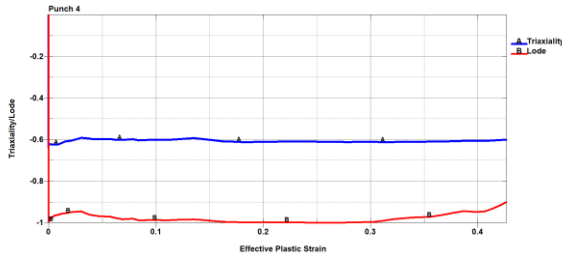
w) Punch4
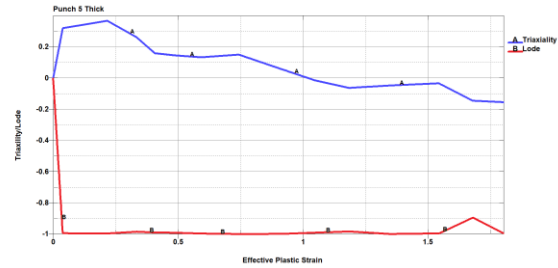
x) Punch5
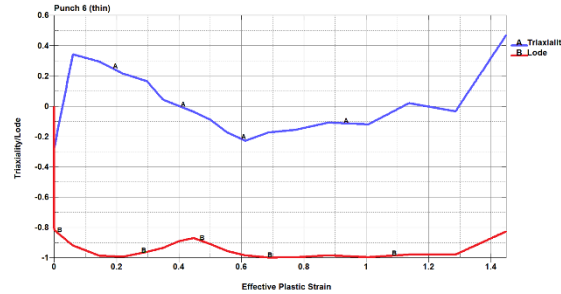
y) Punch6

Figure 99.) Triaxiality and lode parameter for each specimen's selected element a) thru y
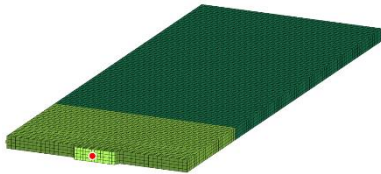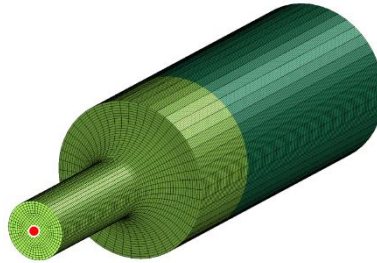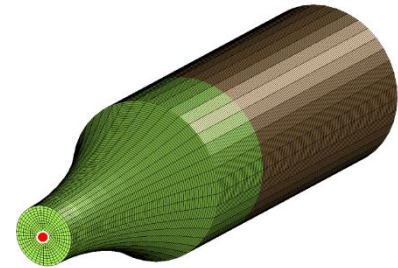
To determine an average triaxiality, τ_{avg}, and Lode parameter, θ_{Lavg}, for each specimen the following equations are used:

$$\tau_{avg} = \frac{\int_0^{\varepsilon_{pf}} \tau \ d\varepsilon_p}{\varepsilon_{pf}}$$

$$\theta_{Lavg} = \frac{\int_0^{\varepsilon_{pf}} \theta_L \ d\varepsilon_p}{\varepsilon_{pf}}$$

13

where τ is the triaxiality as a function of effective plastic strain (ε_p), θ_L is the Lode parameter as a function of effective plastic strain, and ε_{pf} is the final effective plastic strain. Note that in the simulations the triaxiality and Lode parameter are calculated and used in the damage parameter

calculation at each time step. The calculated average of triaxiality and Lode parameter are only used for characterization purposes, and for establishing the initial failure surface inputs.

The calculated averages of triaxiality and Lode parameter for test specimen are shown in Table 7. The simulation fracture strains were estimated by evaluating the effective plastic strain for the selected elements shown in Figure 98 a) thru x), by determining when the simulated nodal displacement matched the displacement where fracture occurred in the physical test. This estimated fracture strain is also shown in Table 7. Because of the lack of DIC data for the Punch5 and Punch6 tests, no initial fracture strain estimate was made for these tests.

Table 7. Triaxiality, Lode parameter and fracture strain simulation results

Test Number	Type	Simulation		
		Triaxiality	Lode Parameter	Fracture Strain
M3-TMT-P4-SG1-O1-SR6-T1-N1	PLANE STRESS	-0.360371775	0.999996903	0.373048
M3-TMT-P4-SG2-O1-SR6-T1-N1		-0.411197974	0.986821413	0.425239
M3-TMT-P4-SG3-O1-SR6-T1-N1		-0.452924851	0.879832338	0.351876
M3-TMT-P4-SG4-O1-SR6-T1-N1		-0.583850977	0.045760863	0.110749
M3-TMT-P4-SG5-O1-SR6-T1-N1	AXISYMMETRIC	-0.388683291	1	0.421788
M3-TMT-P4-SG6-O1-SR6-T1-N1		-0.486287228	1	0.431912
M3-TMT-P4-SG7-O1-SR6-T1-N1		-0.544672054	0.999999996	0.430983
M3-TMT-P4-SG8-O1-SR6-T1-N1		-0.620998954	0.999999992	0.40109
M3-TMT-P4-SG9-O1-SR6-T1-N1		-0.71633475	0.999999918	0.242366
M3-TMT-P4-SG10-O1-SR6-T1-N1		-0.886473301	0.999998852	0.172229
M3-TMT-P4-SG11-O1-SR6-T1-N2	PLANE STRAIN	-0.563583047	0.184349218	0.246002
M3-TMT-P4-SG12-O1-SR6-T1-N1		-0.64239929	0.076108857	0.280913
M3-TMT-P4-SG13-O1-SR6-T1-N1		-0.776842093	0.029777128	0.4478
M3-TMCL-LR1-P4-SR6-T1-N4	COMBINED	-0.396935213	0.989313044	0.481081
M3-TMCL-LR2-P4-SR6-T1-N1		-0.163694144	0.585690865	0.461228
M3-TMCL-LR3-P4-SR6-T1-N3		0.001339034	-0.005866648	0.46036
M3-TMCL-LR4-P4-SR6-T1-N6		0.225443615	-0.773368816	0.413095
M3-TMCL-LR5-P4-SR6-T1-N1		0.389326143	-0.98774337	0.30041
M3-TMP1-P4-SR6-T1-N1	PUNCH	-0.596541516	-0.278171678	0.288232
M3-TMP4-P4-SR6-T1-N5		-0.637466208	-0.908720122	0.329874
M3-TMP6-P4-SR6-T1-N3		-0.612773622	-0.563498889	0.378719
Unbacked-Punch4		-0.6038	-0.996	0.505
Thick backed-Punch5		0.15	-1	No Estimate
Thin Backed-Punch6		0	-1	No Estimate

5.2.1 Failure surface generation

The average triaxialities, average Lode parameters, and fracture strains shown in Table 7 are used as the input for the MATLAB failure surface generation routine. An initial failure surface is produced by the curve fitting as described in Section 4.2. Figure 100 shows the first failure surface using the initial data set.
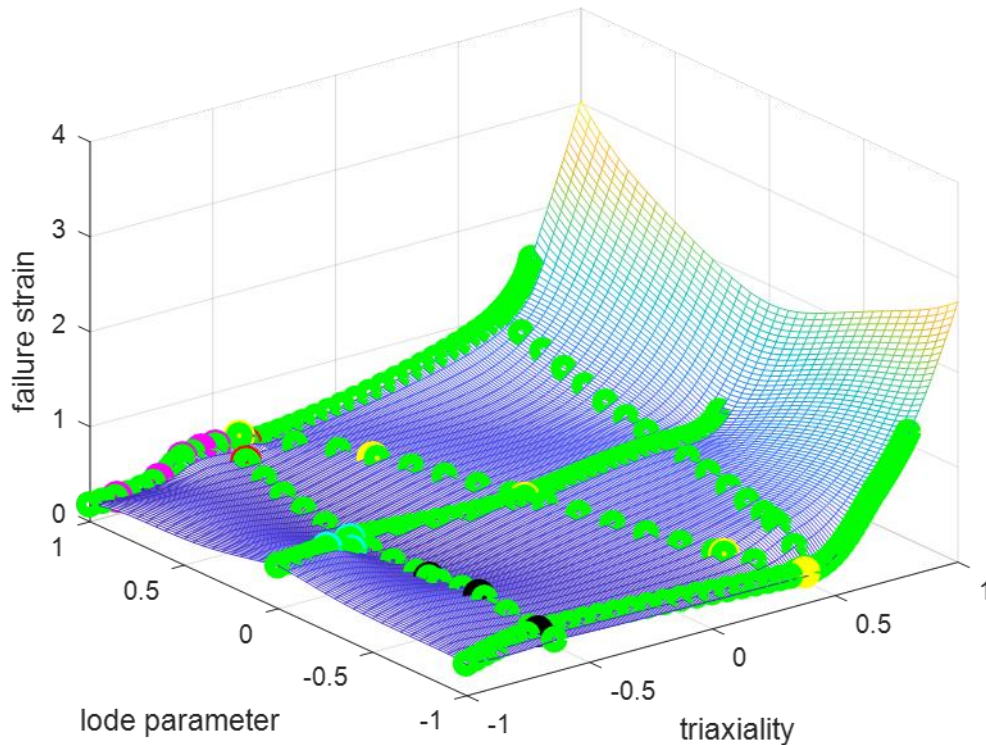
Figure 100. First failure surface generated using initial data set

Given that the initial input to failure surface was based upon stress states averages and fracture strain estimates, adjustments to the failure surface to obtain an acceptable test data match were expected. The input failure strains were manually adjusted until simulations, using the updated failure surface, fractured within the spread of the test fracture strains.

To reduce the iteration computational time, only a single stress-strain curve from the Inconel-718 plasticity model was used, and the simulations were performed at a synthetic higher loading speed. The selected stress-strain curve matched the strain rate that the loading speed of the test produced. The higher synthetic speed simulation was checked to ensure that there was no oscillatory or unstable response. Trial simulations were also performed at a lower synthetic speed to ensure that the simulation results were the same as at the higher synthetic loading speed.

Table 8 shows the test simulation fracture strains used to produce the final failure surface. The adjustment made to each specimen's fracture strain is also shown in terms of percentage. A 100% adjustment in the *Adjustment* column signifies that the final fracture strain input was 100% of the initial input, and that no adjustment was necessary for that test specimen's fracture strain.

Table 8. Control point iterations and adjustments for each specimen

Test Number	Type	Simulation			
		Triaxiality	Lode Parameter	Fracture Strain	Adjustment [%]
M3-TMT-P4-SG1-O1-SR6-T1-N1	PLANE STRESS	-0.360371775	0.999996903	0.373048	100
M3-TMT-P4-SG2-O1-SR6-T1-N1		-0.411197974	0.986821413	0.425239	100
M3-TMT-P4-SG3-O1-SR6-T1-N1		-0.452924851	0.879832338	0.351876	100
M3-TMT-P4-SG4-O1-SR6-T1-N1		-0.583850977	0.045760863	~~0.110749~~	REMOVED
M3-TMT-P4-SG5-O1-SR6-T1-N1	AXISYMMETRIC	-0.388683291	1	0.421788	100
M3-TMT-P4-SG6-O1-SR6-T1-N1		-0.486287228	1	0.431912	100
M3-TMT-P4-SG7-O1-SR6-T1-N1		-0.544672054	0.999999996	0.430983	100
M3-TMT-P4-SG8-O1-SR6-T1-N1		-0.620998954	0.999999992	0.40109	100
M3-TMT-P4-SG9-O1-SR6-T1-N1		-0.71633475	0.999999918	0.242366	135
M3-TMT-P4-SG10-O1-SR6-T1-N1		-0.886473301	0.999998852	0.172229	120
M3-TMT-P4-SG11-O1-SR6-T1-N2	PLANE STRAIN	-0.563583047	0.184349218	0.246002	110
M3-TMT-P4-SG12-O1-SR6-T1-N1		-0.64239929	0.076108857	0.280913	100
M3-TMT-P4-SG13-O1-SR6-T1-N1		-0.776842093	0.029777128	0.4478	85
M3-TMCL-LR1-P4-SR6-T1-N4	COMBINED	-0.396935213	0.989313044	0.481081	100
M3-TMCL-LR2-P4-SR6-T1-N1		-0.163694144	0.585690865	0.461228	100
M3-TMCL-LR3-P4-SR6-T1-N3		0.001339034	-0.005866648	0.46036	85
M3-TMCL-LR4-P4-SR6-T1-N6		0.28111199	-0.823624084	1.4	339
M3-TMCL-LR5-P4-SR6-T1-N1		0.390150742	-0.987271678	~~0.4160959~~	REMOVED
M3-TMP1-P4-SR6-T1-N1	PUNCH	-0.596541516	-0.278171678	0.288232	100
M3-TMP4-P4-SR6-T1-N5		-0.637466208	-0.908720122	0.329874	100
M3-TMP6-P4-SR6-T1-N3		-0.612773622	-0.563498889	0.378719	100
Unbacked-Punch4		-0.6038	-0.996	0.505	100
Thick backed-Punch5		0.15	-1	4	No Initial Estimate
Thin Backed-Punch6		0	-1	1	No Initial Estimate

After the adjustments to the input shown in Table 8, the failure surface generation tool produced the failure surface shown in Figure 101.
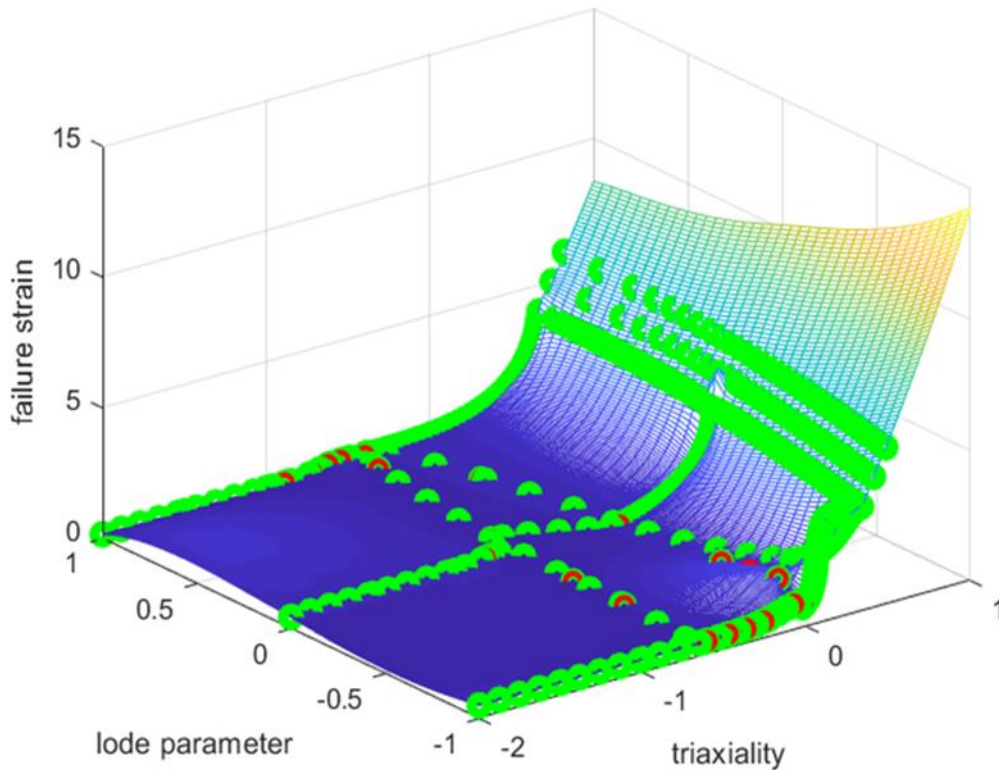
Figure 101. Failure surface generated after adjustments

Two test specimens were removed from the fracture series and as input to the final failure surface generation. The ~11% fracture strain of the SG4 test was much lower than the fracture strains of tests from the plane strain series, which had similar triaxialities and Lode parameters. The SG4 test specimen design has a narrow notch, and is sensitive to fabrication tolerances and finite element mesh density around the notch. It is uncertain why the SG4 simulation produced such a low fracture strain, but the plane strain specimens were judged to be easier to reliably both fabricate and model. Therefore, the plane strain series fracture strains were selected to take precedent, and the SG4 fracture strain was removed from consideration.

In the two compression/torsion combined loading specimens, LR4 and LR5, the specimens were not maintaining their longitudinal axis alignment in the loading direction. This was due to Inconel-718's high strength, which caused the test grips to deform, and the tests did not remain axisymmetric under the compression. Various techniques were adopted in attempts to recover the correct physical deformation patterns from the test. The most reasonable reconstruction of the

tests prescribes a lateral force component in the simulation to simulate the misalignment. The use of this estimated lateral force led to LR4 force-displacement and torque-angle results that appeared reasonably good. However, this technique was not successful with the LR5 test simulation. The estimated fracture strain was also inconsistent with the thick backed, Punch5 fracture strain. LR5 was also removed from the failure surface generation input.

5.2.2 Simulation results with failure surface

The failure surface described in the previous section, and shown in Figure 101, was used in simulations of each test specimen set. The force-displacement simulation time histories were compared to the physical test data. The force-displacement plots are shown in Figure 102 a) thru x). The failure displacements occurred within or close to the experimental test data spread. This was the first step in the failure surface verification.
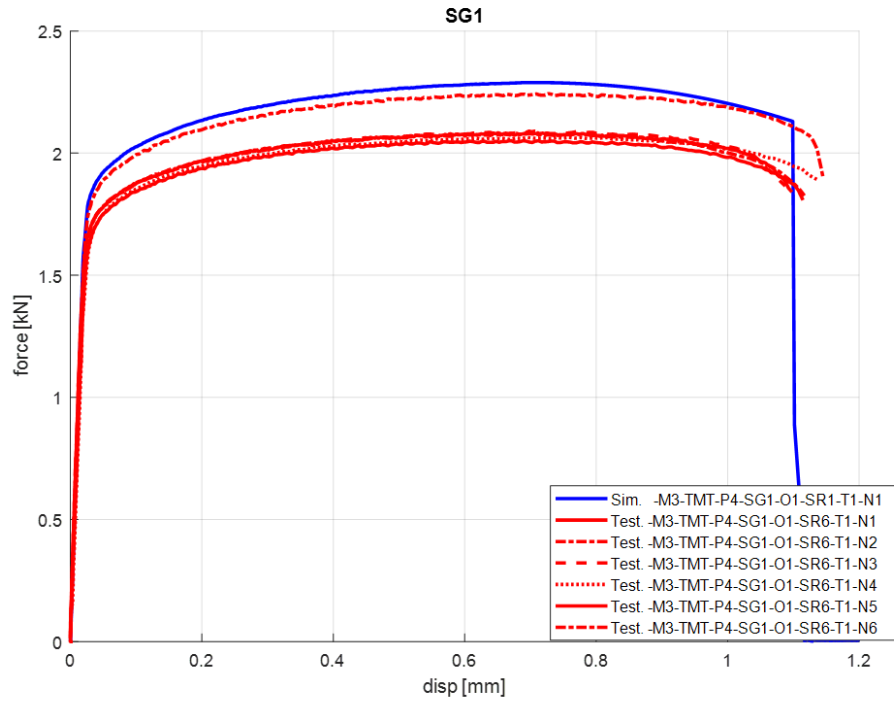
a) SG1
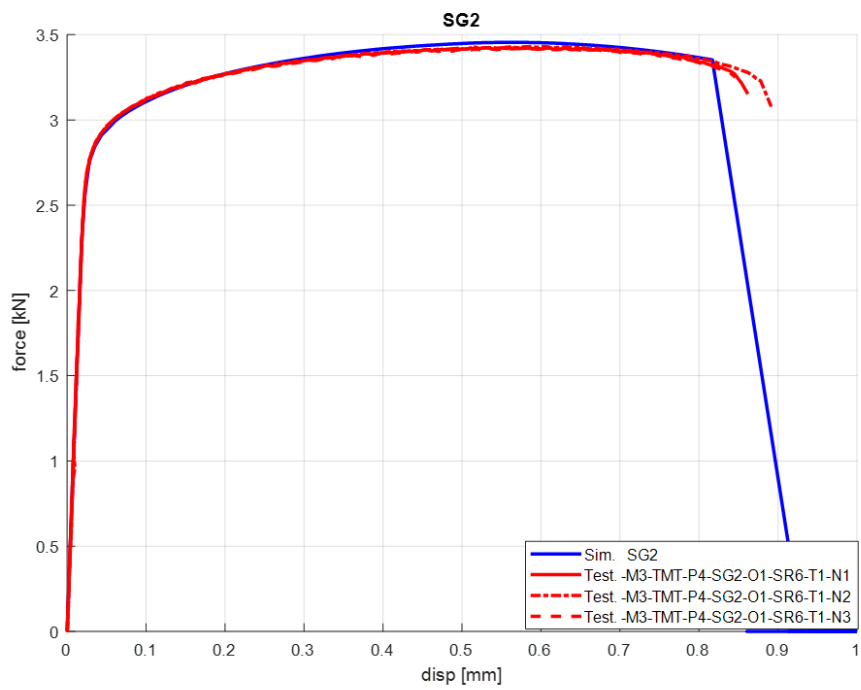
b) SG2
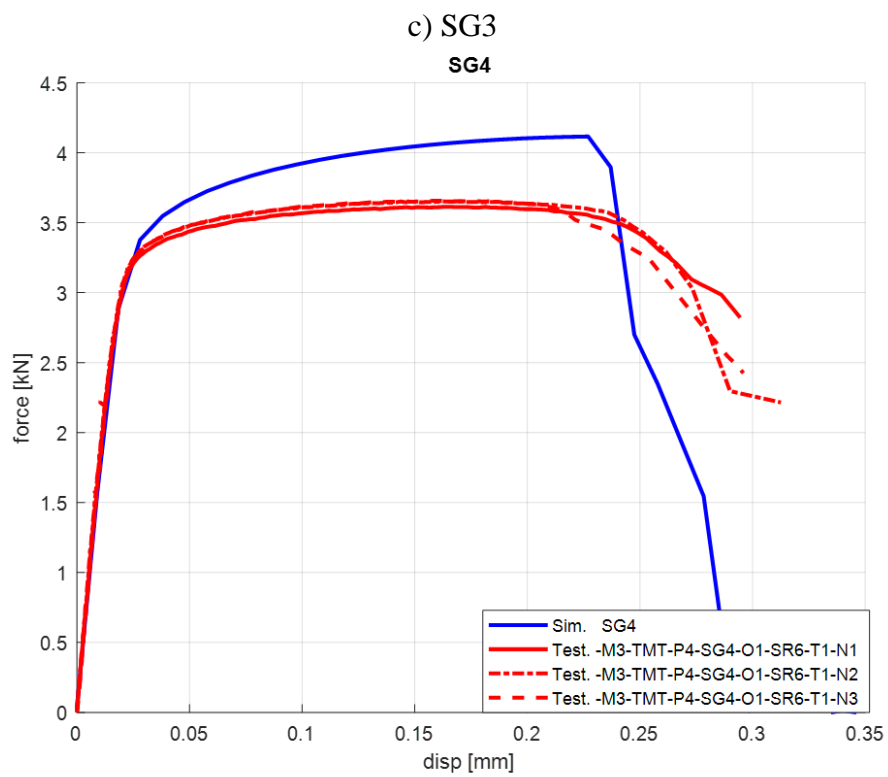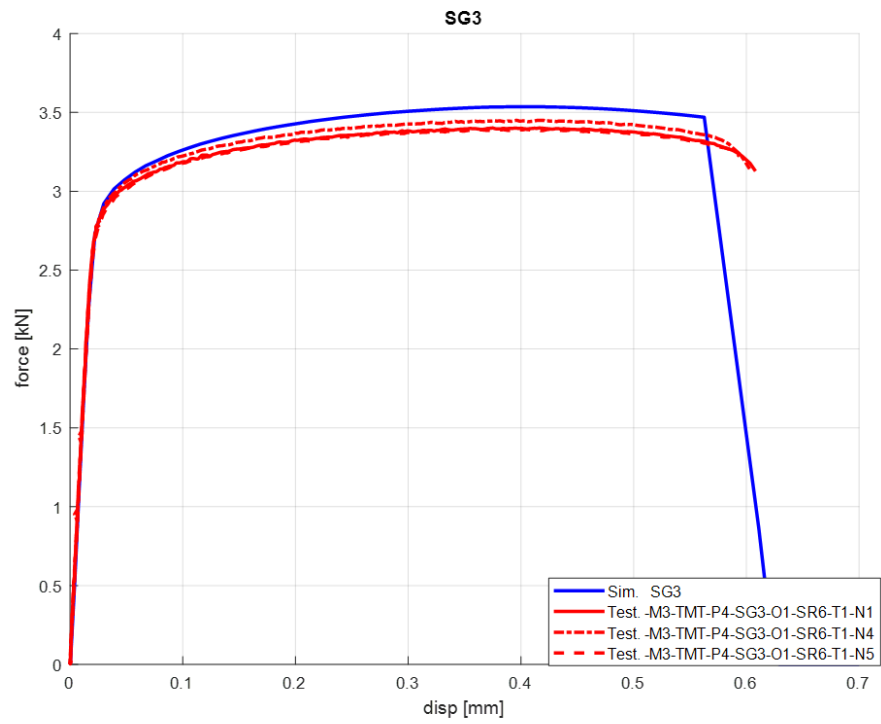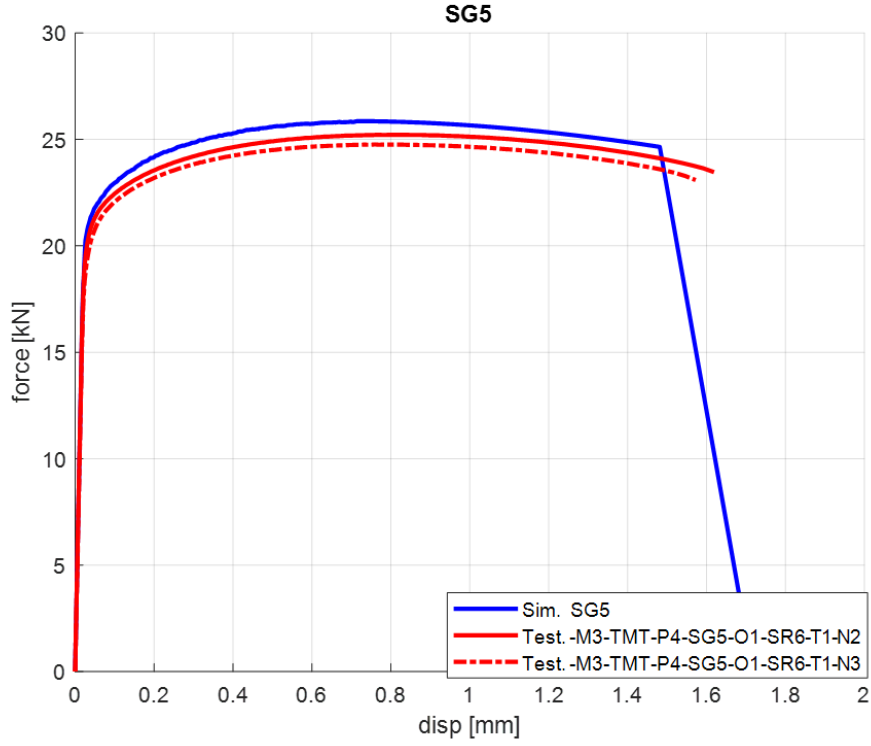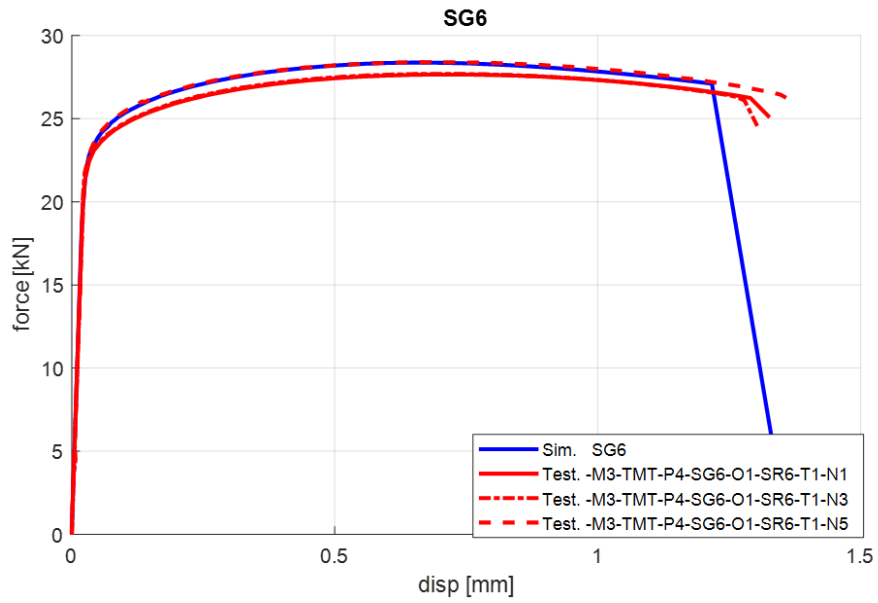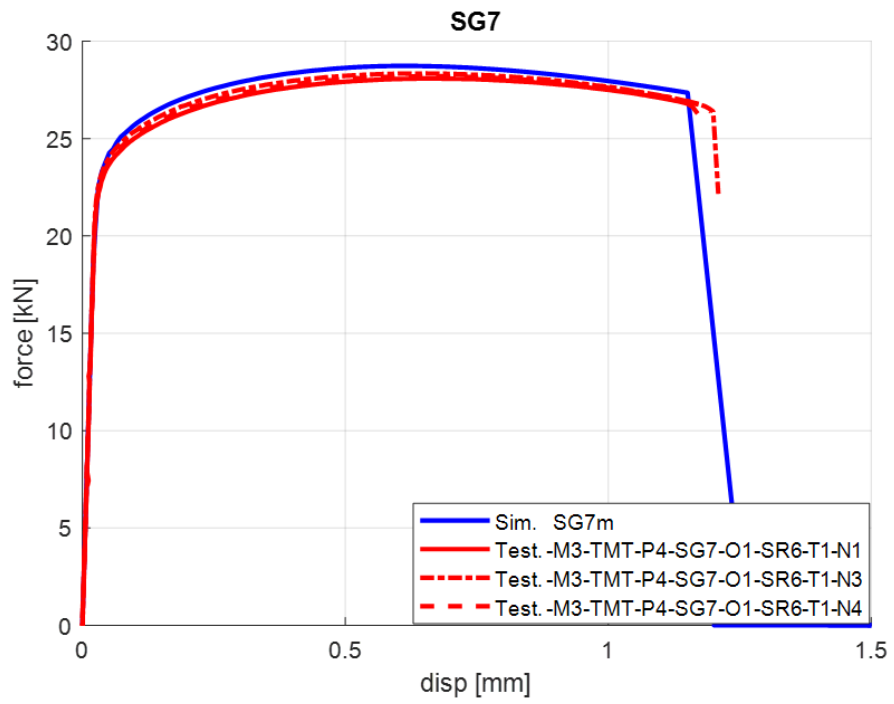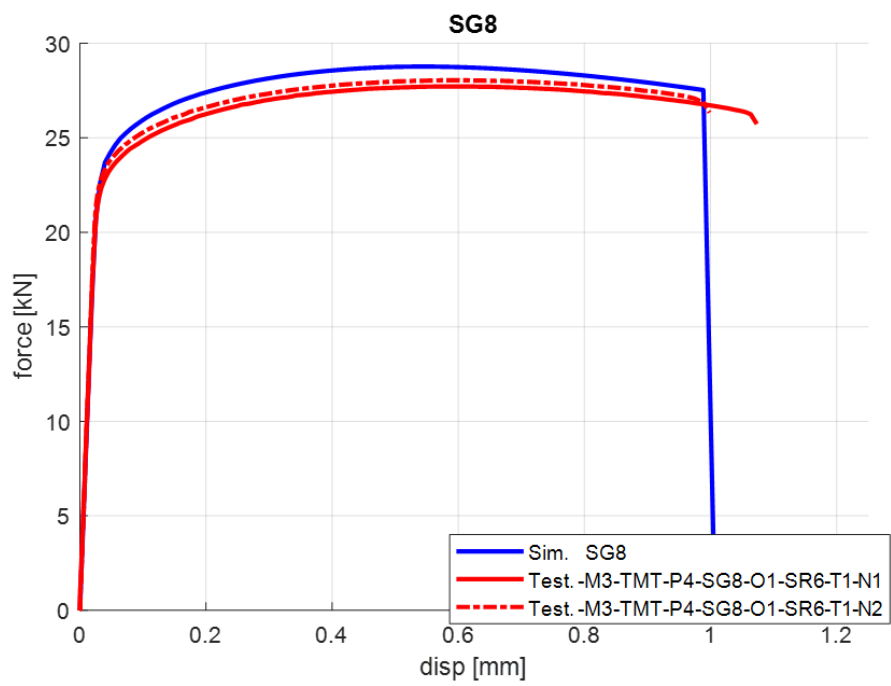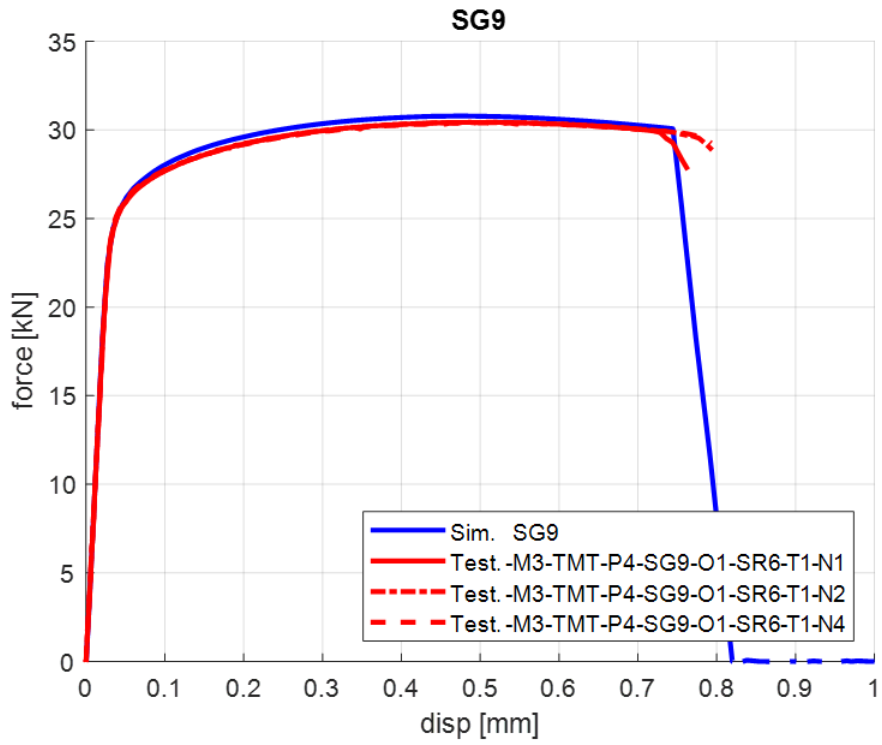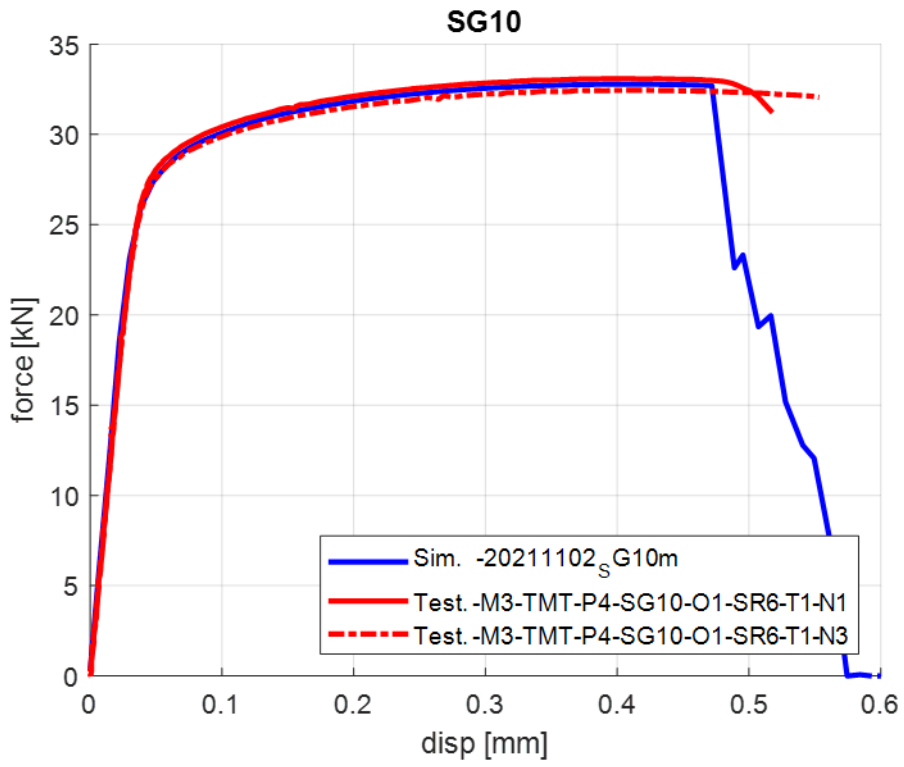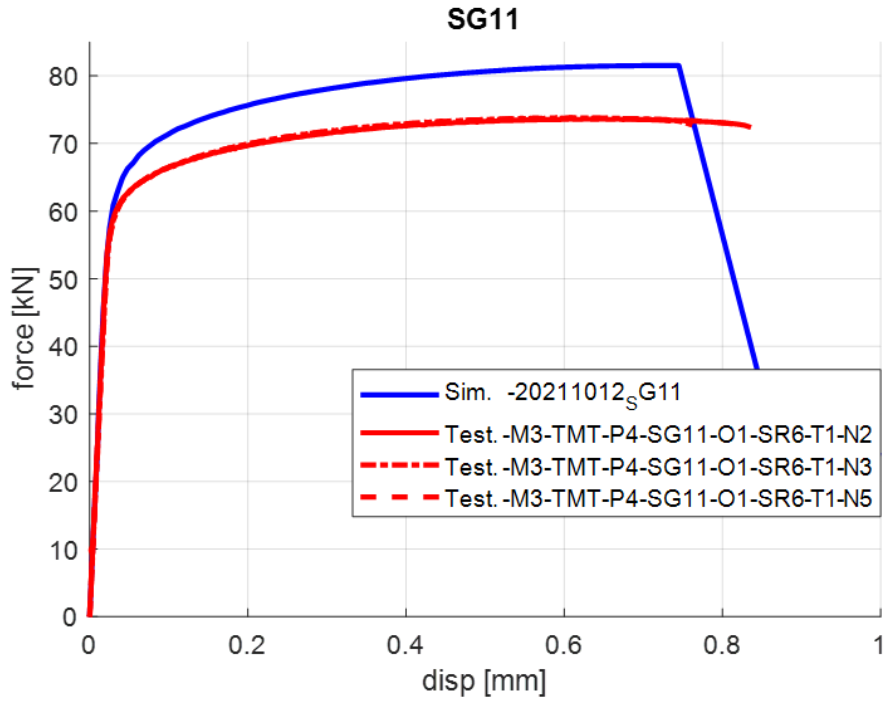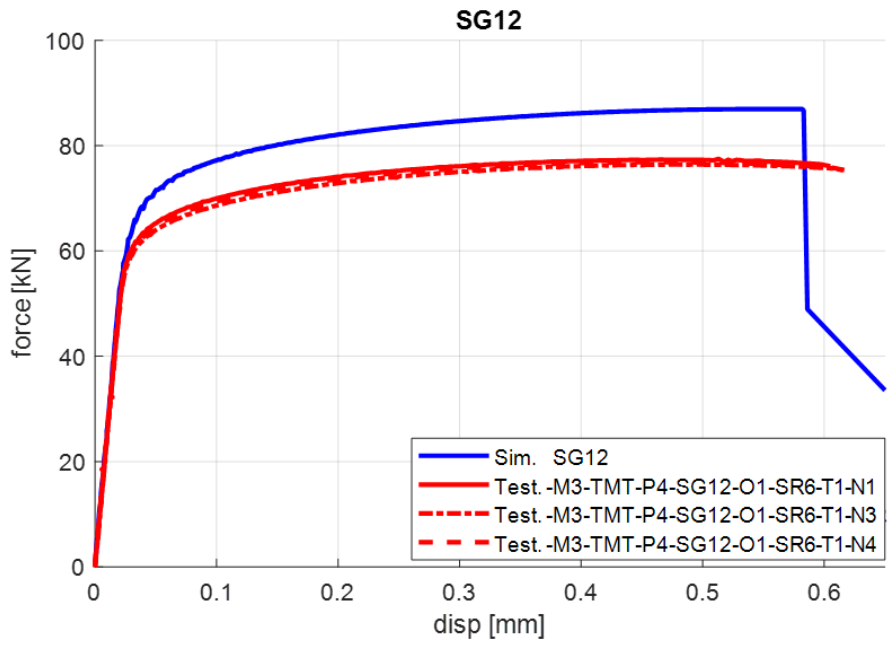
c) SG3

d) SG4

e) SG5

f) SG6

g) SG7

h) SG8

i) SG9

j) SG10

k) SG11

l) SG12
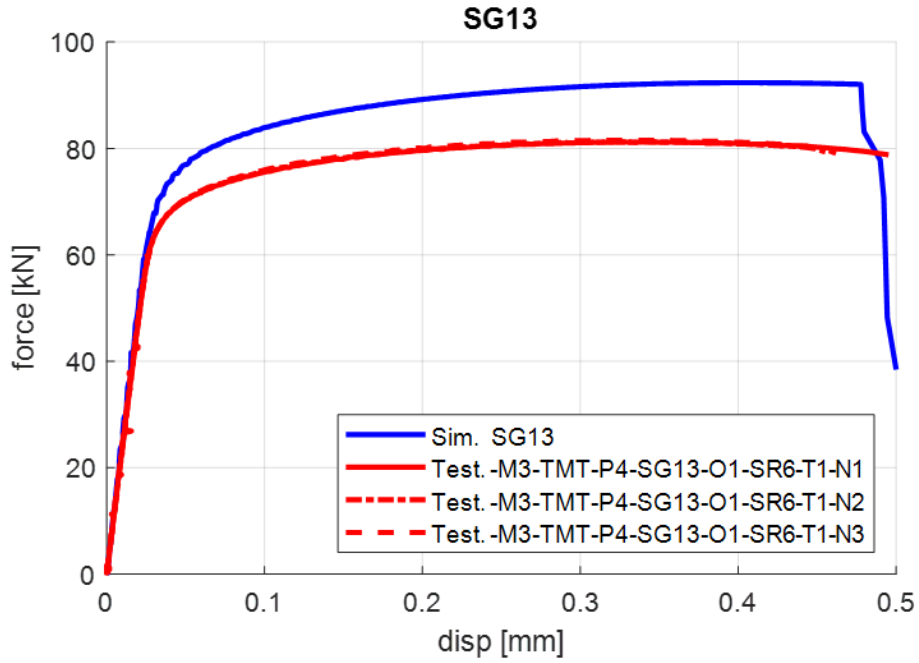
m) SG13
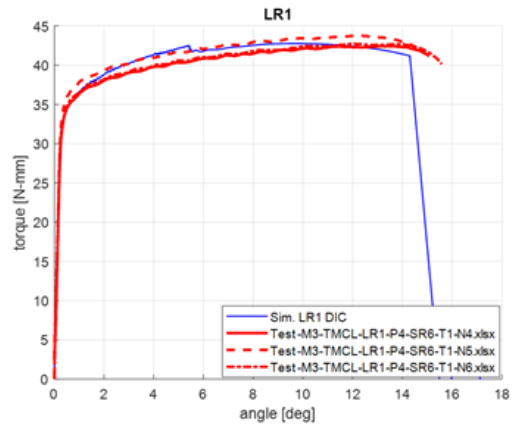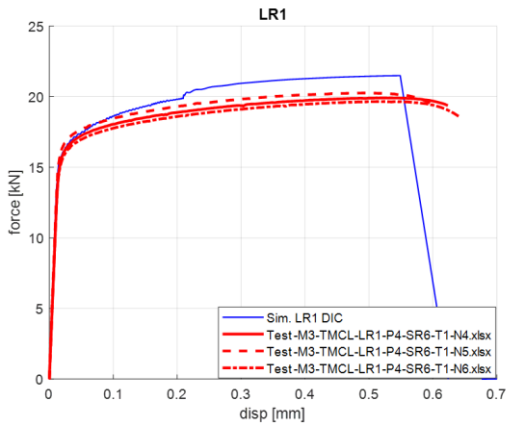
n) LR1
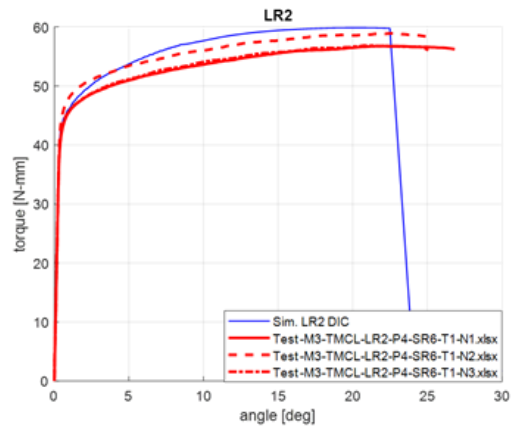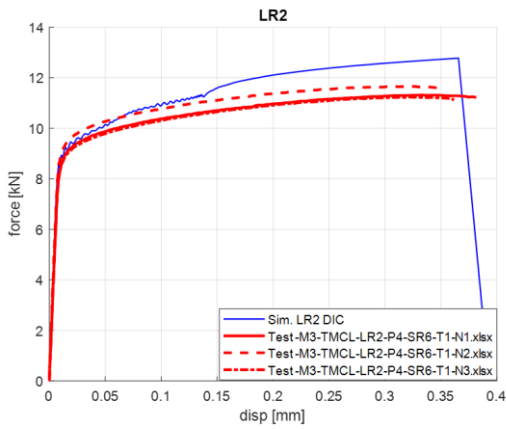
o) LR2
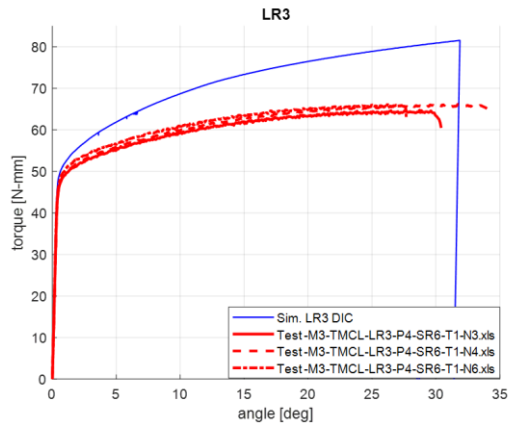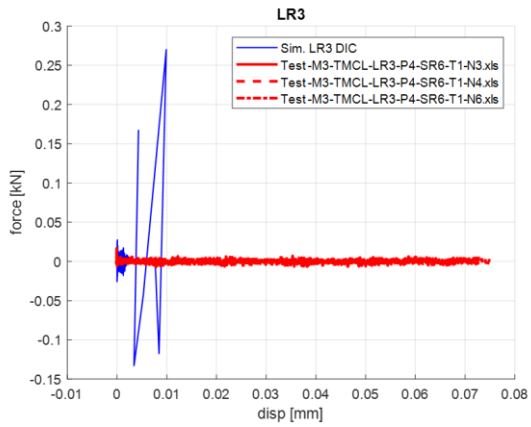
p) LR3
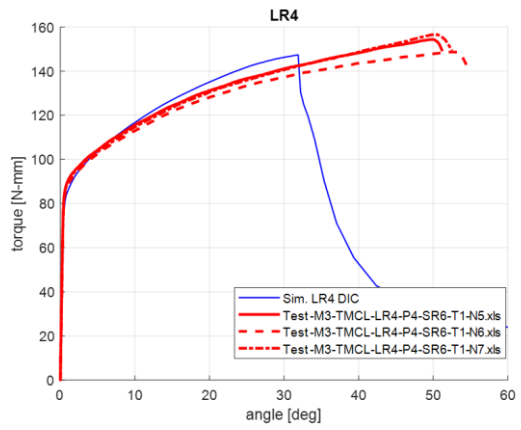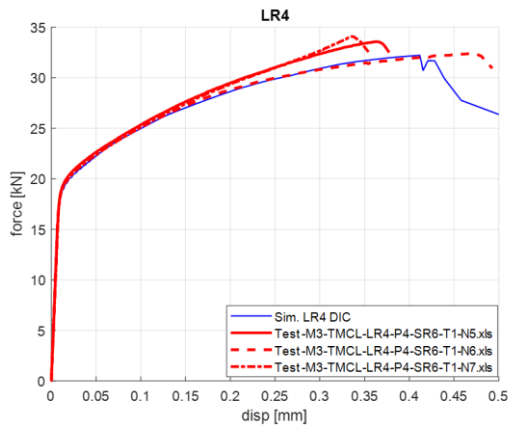
q) LR4
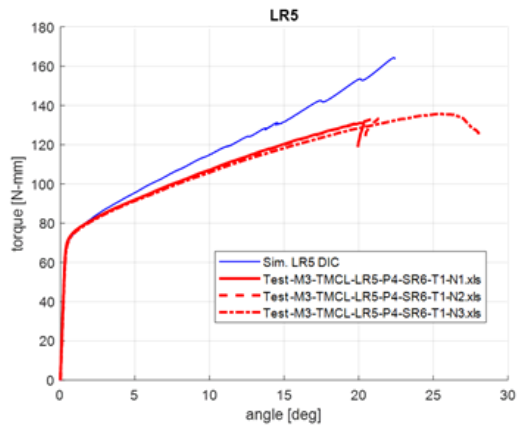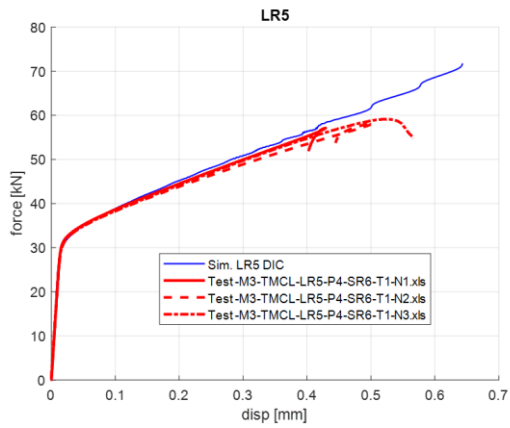
r) LR5
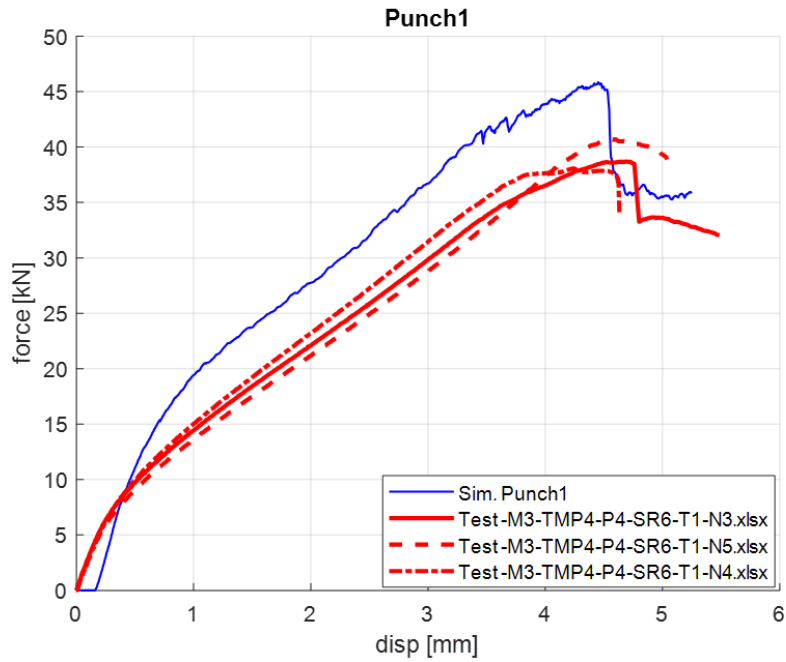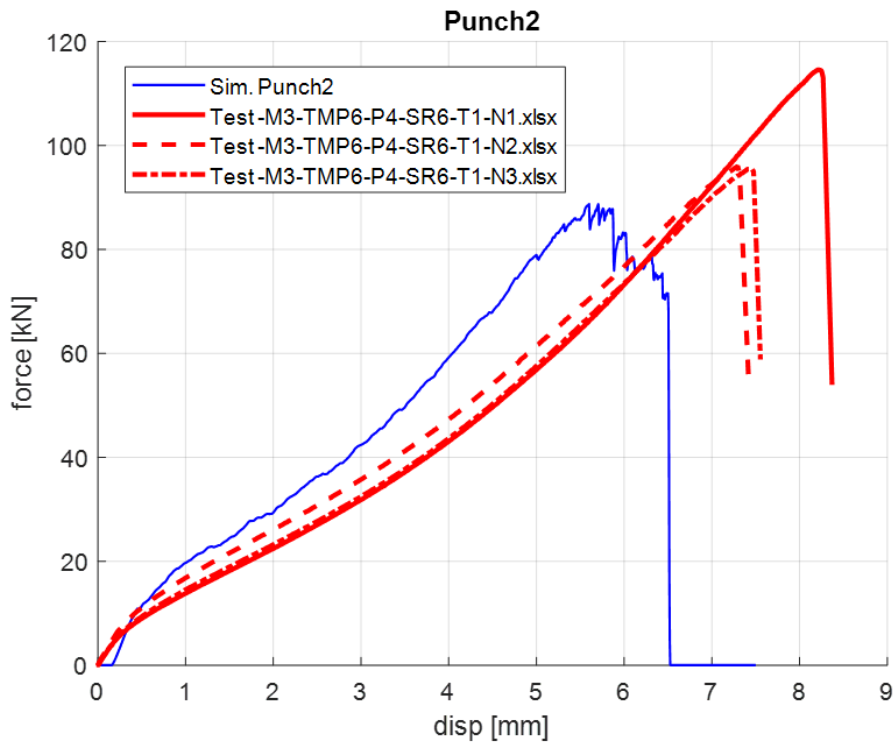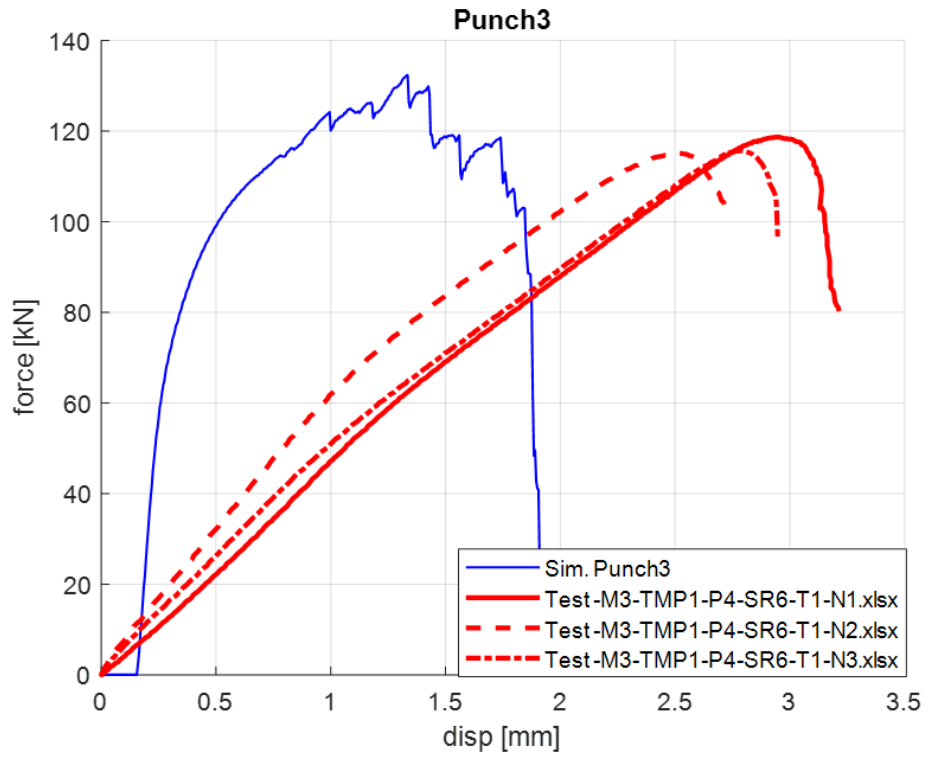
s) Punch1
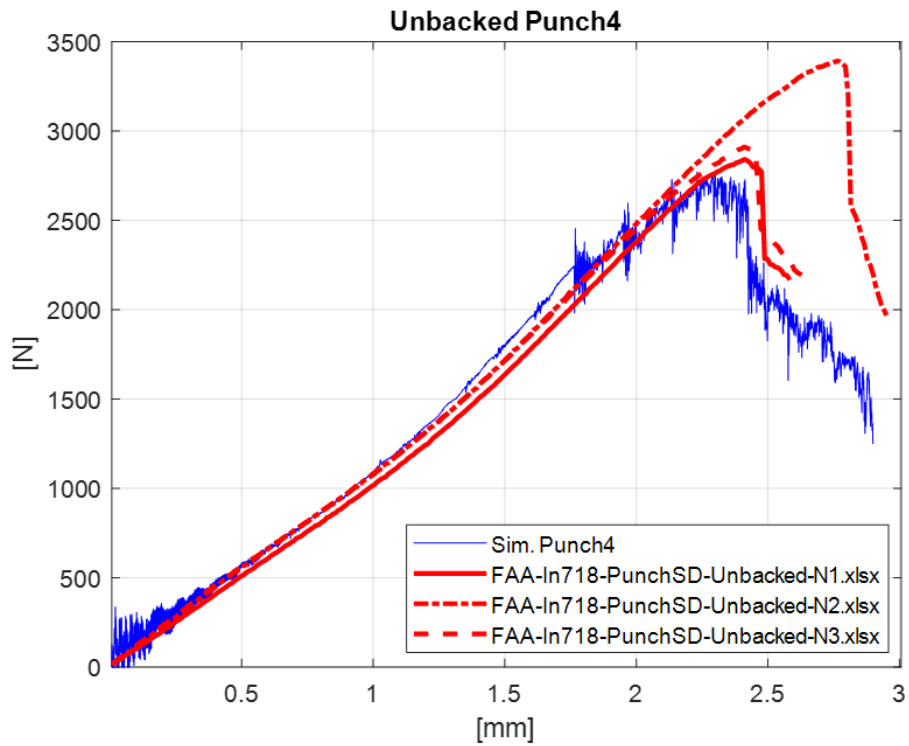
t) Punch2

u) Punch3

v) Punch4
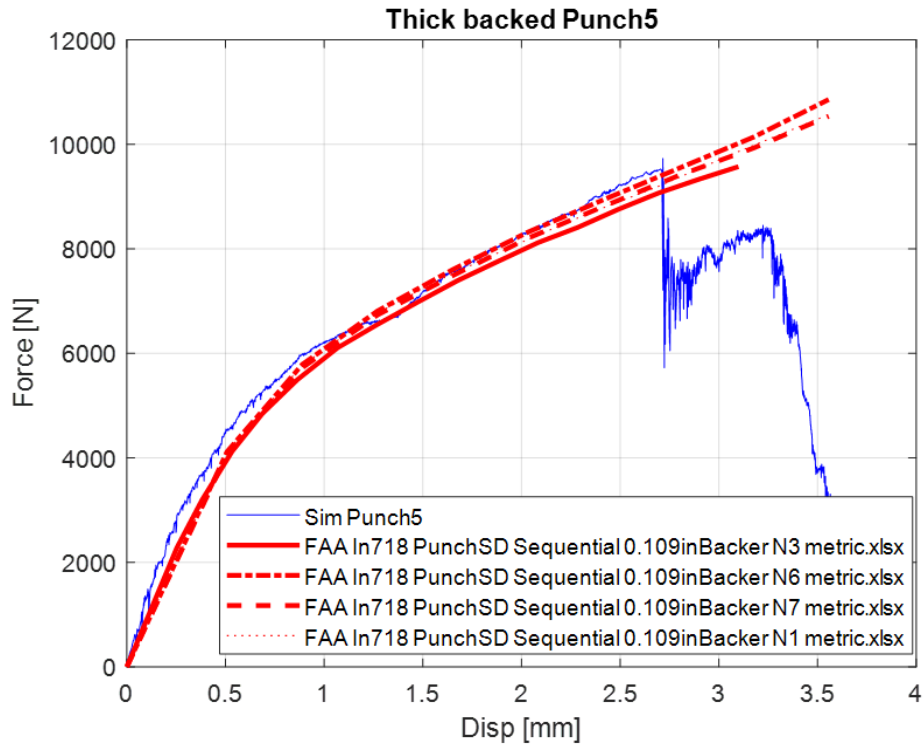
w) Punch5
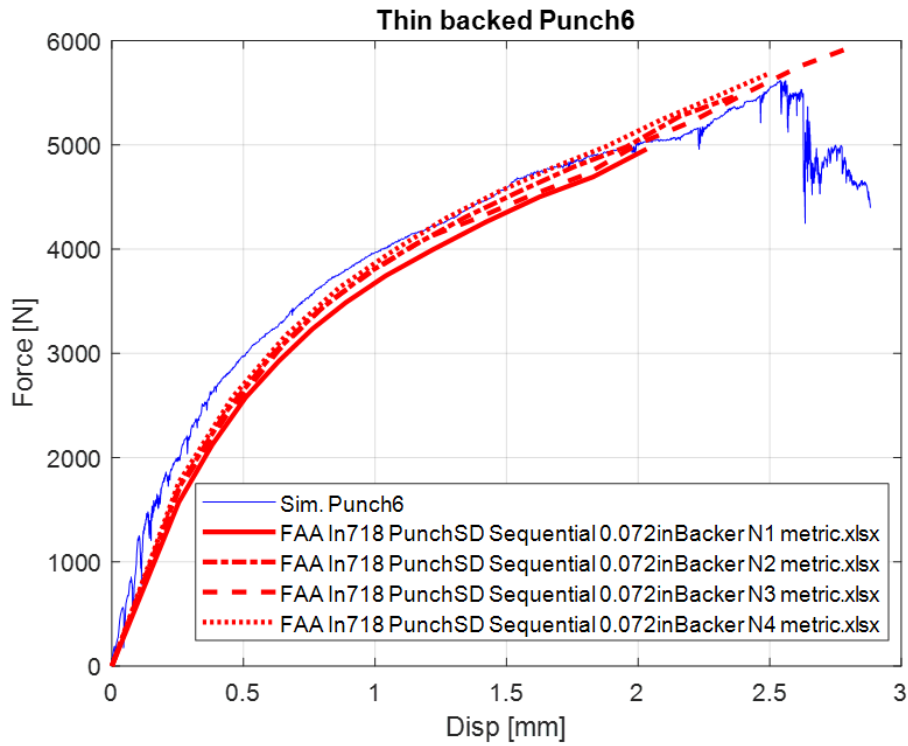
x) Punch6

Figure 102. Force-displacements for each test specimen a) thru x)

106

The Punch1, Punch2, and Punch3 test simulations did not predict force-displacement curves that were a good match to the physical tests. Because of the large diameter of these punches, the punch edges were close to the fixture. In addition, the Inconel-718 plates appeared to be overcoming friction and slightly pulling out of the fixture. So, it was difficult to determine the precise distribution of the boundary forces in these tests. Due to the difficulty of accurately modeling these boundary conditions, an exact match was not possible.

For reference, the simulation times for each test specimen have been tabulated in Table 9. All the simulations were performed with 16 processors using the LS-DYNA MPP configuration except the Punch4, Punch5, and Punch6 simulations; these were performed using 32 processors.

Table 9. Simulation statistics for each specimen

Specimen Number	Number of elements	Problem time (ms)	Problem cycles	Total CPU time (s)	Elapsed time (hh:mm:ss)
SG1	240528	2.00	132472	976	**00:15:26**
SG2	130760	1.50	119996	1699	**00:28:19**
SG3	143960	1.00	66684	598	**00:09:58**
SG4	157240	0.50	30198	219	**00:03:39**
SG5	471264	6.00	327363	27743	**07:42:23**
SG6	571136	3.00	213498	20675	**05:44:35**
SG7	376345	3.00	227366	13208	**03:40:08**
SG8	314240	3.00	238839	8474	**02:21:14**
SG9	291072	3.00	245063	7250	**02:00:50**
SG10	273664	3.00	211831	4263	**01:17:03**
SG11	934720	3.00	147660	11209	**03:06:49**
SG12	739840	1.00	40975	3323	**00:55:23**
SG13	2628900	2.00	107781	17503	**04:51:43**
LR1	235008	8.50	885534	14470	**04:01:10**
LR2	235008	3.00	184530	4093	**01:08:13**
LR3	235008	15.0	1436146	27648	**07:40:48**
LR4	325888	4.00	297519	10622	**02:57:02**
LR5	325888	6.50	488845	17309	**04:48:29**
Punch1	268356	10.5	776643	19643	**05:28:26**
Punch2	276535	15.0	721963	31194	**08:39:54**
Punch3	282898	8.50	421887	14559	**04:02:29**
Punch4	150022	3	1201906	16875	**04:41:27**
Punch5	398761	4	1576771	68756	**19:06:22**
Punch6	398761	3	1058997	62766	**17:26:28**

5.3   Creation of a temperature scaling function

The fracture strains of metals are dependent on their temperature. This dependence is in addition to a metal's stress-strain thermal dependence. The *MAT_224 failure model can scale the failure surface as a function of temperature. This thermal function scales the failure surface for each element, at each time step, enabling an accurate damage parameter calculation.

The same thermal testing series presented in Section 3.2 was utilized to create the thermal scaling function. The SG1 uniaxial tension plane stress-specimen was selected, which was also used to develop the temperature dependent stress-strain curves. Here, the failure strain values are used rather than the stress-strain data. A single yield curve, selecting the curve for the temperature that the test was conducted at, was used in each simulation. In Johnson-Cook models, it is assumed that the temperature scaling and strain rate scaling are decoupled. So, the temperature scaling is independent of strain rate. The force-displacement plots, including all the test repeats and the simulations, are shown in Figure 103 a) thru f).

As discussed in Section 3.2.1, two sets of temperature dependent stress-strain curves have been created, material sets V1.1 and V1.2. Two different temperature scaling function curves have created for these two material sets. These two scaling function curves are the same except for 1073K, the highest temperature. As shown in Figure 103 e) and f), the test data used for V1.1 requires a scale factor that will produce high temperature brittle behavior, while the test data used for V1.2 requires a scale factor that will produce high temperature ductile behavior.
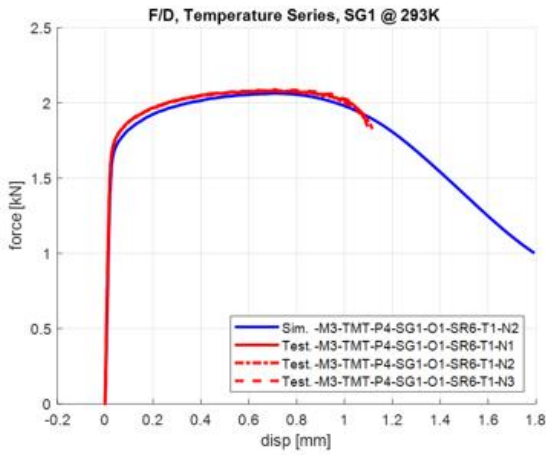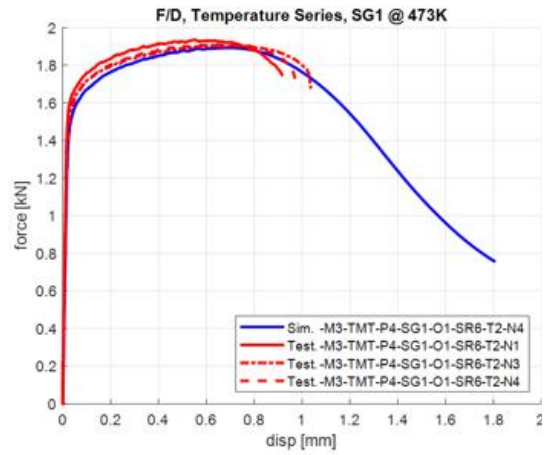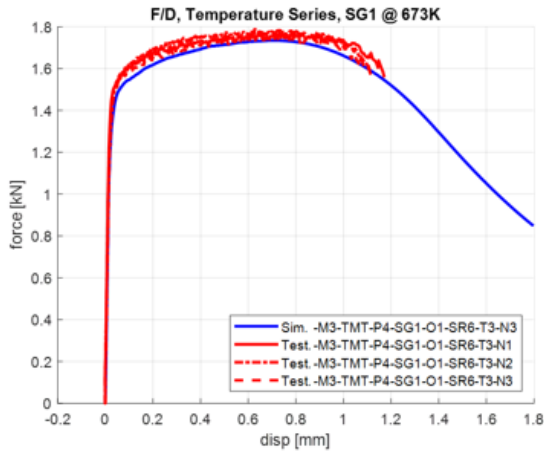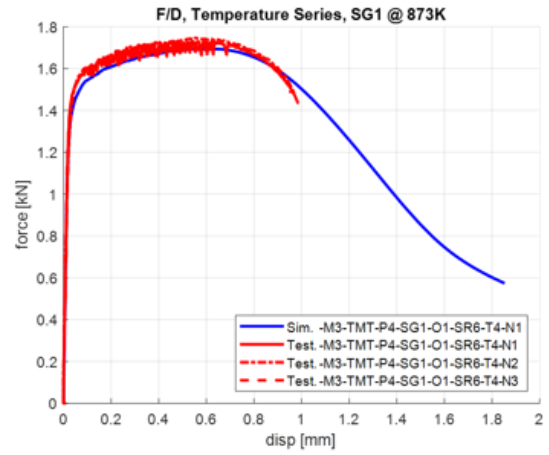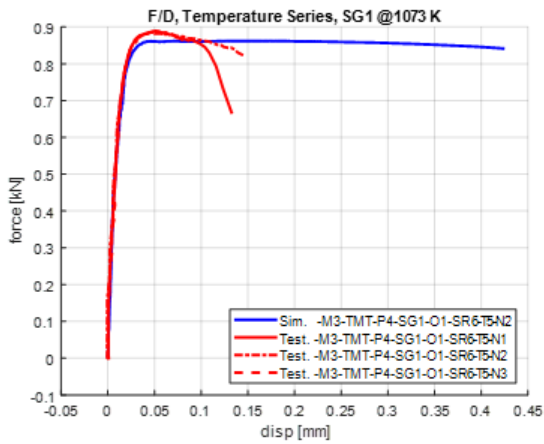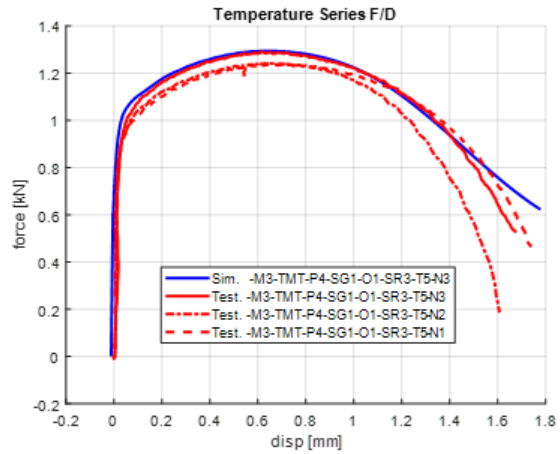
Figure 103. Force-displacement at each temperature a) thru f)

An initial scaling function is estimated by inspection of the test curves in Figure 103, and the following normalizing equation,

$$ScalingFactor = \frac{\varepsilon_{pf}}{\varepsilon_{pf_{RT}}}$$

14

where ε_{pf} is the fracture strain at each specific test, and $\varepsilon_{pf_{RT}}$ is the fracture strain at room temperature. The simulations were repeated using the failure surface and the initial thermal scaling curve. After several iterations of adjusting the scaling factors, each simulation failure displacement occurred within the experimental spread. For the stress-strain curves representing temperatures below and above those tested (discussed in Section 3.2.3), scale factors were also added. The same scale factors as those for the temperatures adjacent to the added curves were used, preventing non-physical scale factors due to extrapolation. Table 10 shows the final temperature scaling function.

Table 10. Scaling factors by temperature

Temp (K)	Scaling Factor V1.1	Scaling Factor V1.2
0	1.000	1.000
300	1.000	1.000
473	1.000	0.889
673	1.000	0.844
873	1.000	0.778
1073	0.100	1.444
2000	0.100	1.444

For V1.1, the scaling factors below 900K were set equal to one so that the curve would be monotonically decreasing, since the data used shows that Inconel becomes brittle at temperatures above 900K. It was later determined that the thermal scaling curve does not require monotonicity. As a result, the V1.2 curve decreases till 873K, and then increases above 900K.

Figure 104 a) thru f) shows the force-displacement plots from simulations including the failure surface and thermal scaling curves. Figure 104 e) shows the 1073K force-displacement plot using the V1.1 model. Figure 104 f) shows the 1073K force-displacement plot using the V1.2 model. It is a characteristic in the simulation of localization (in tension tests, necking) that once the adiabatic temperature rise causes significant material softening, adiabatic heating accelerates and fracture quickly occurs. As a result, the differences in the scaling between V1.1 and V1.2 at

473K, 673K, and 873K do not cause significant differences in the fracture displacement. So, only a single set of results is shown for these temperatures.

a) 293K

b) 473K

c) 673K

d) 873K

e) 1073K

f) 1073K V1.2
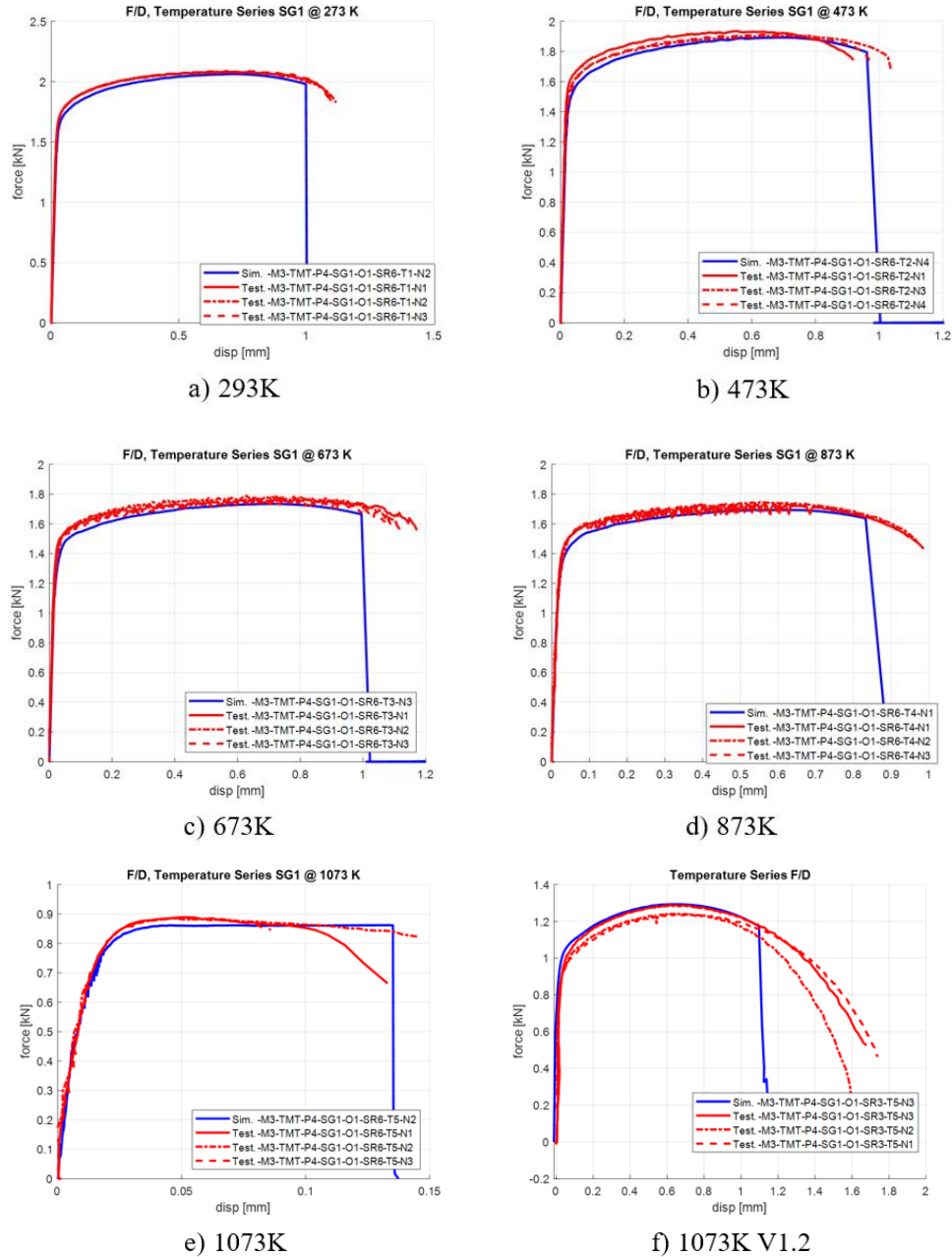
Figure 104. Force-displacement with a scaling function for each temperature a) thru f)

5.4   Creation of a strain rate scaling function

In addition to the thermal dependence presented in the discussed Section 5.3, the fracture strains of most metals are also dependent on the strain rate of the loading. This usual dependence is in addition to a metal's stress-strain rate dependency. Inconel-718 is an exception to this general rule, but *MAT_224 capabilities and typical practice will be briefly described. The *MAT_224 failure model can scale the failure surface as a function of strain rate, just as it can as a function of temperature. This strain rate function scales the failure surface for each element, at each time step.

The same strain rate testing series presented in Section 3.4 was utilized to create a strain rate scaling function. The SG1 uniaxial tension plane stress-specimen was selected, which was also used to develop the strain rate dependent stress-strain curves. Again, as in the thermal scaling development, the failure strain values are used here rather than the stress-strain data. As previously presented, in Johnson-Cook models the strain rate scaling is independent of temperature.

The SG1 tests at the varying strain rate tests were simulated using the full material model, with strain rate curves, temperature curves, failure surface, and the temperature scaling curve. Therefore, the rate and thermal effects occurring in these tests are modeled. Somewhat unusual for metals, Inconel-718 fracture strains displays little or no rate sensitivity, unlike the rate sensitivity its plasticity behavior displays. Table 11 shows the final strain rate scaling values.

Table 11. Scaling factors by strain rate

Strain Rate	Scaling Factor
0 s^{-1}	1.000
0.0001 s^{-1}	1.000
3000 s^{-1}	1.000
8000 s^{-1}	1.000
50000 s^{-1}	1.000
100000 s^{-1}	1.000

The Table 11 strain rate scaling function is essentially the failure surface without scaling. The failure surface, the temperature scaling presented in Section 5.3, and the strain rate scaling function were used in simulations. Because of the varying temperatures and rates occurring in these tests, the SR4 (500 s^{-1}) and SR5 (2000 s^{-1}) tests were simulated. Comparisons of the force-displacement and strain rate-strain results to the test data are shown in Figure 105 a) and b) for SR4, and Figure 105 c) and d) for SR5, demonstrating the lack of fracture rate sensitivity.
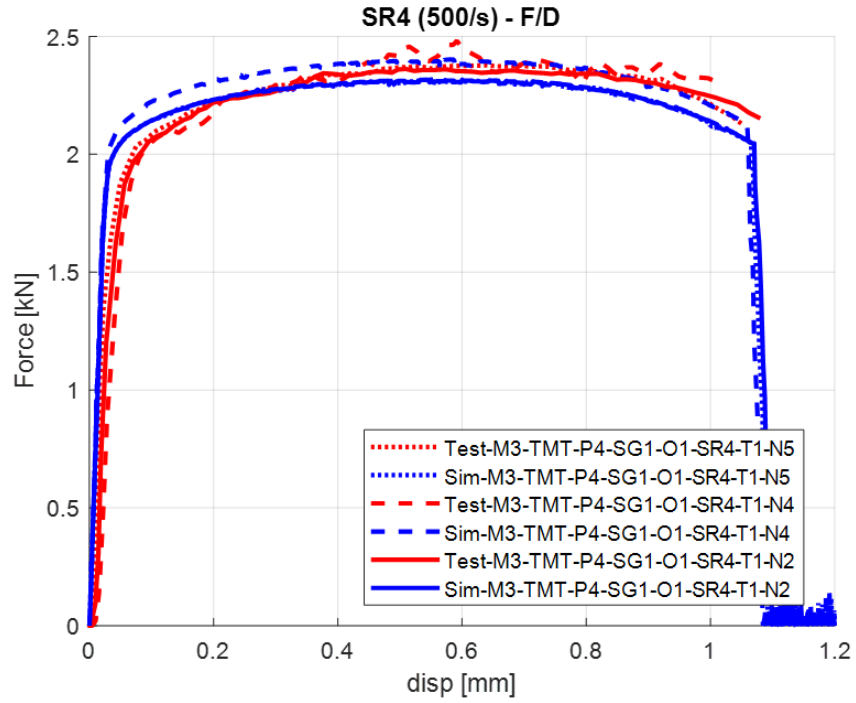
a) SR4 Force vs. Displacement
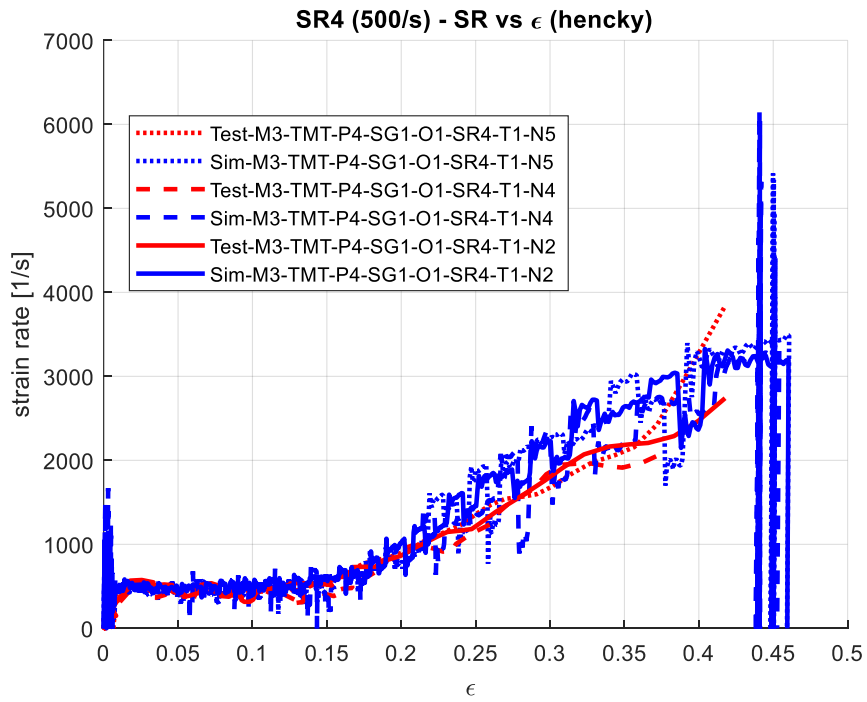
b) SR4 Strain Rate vs. Strain
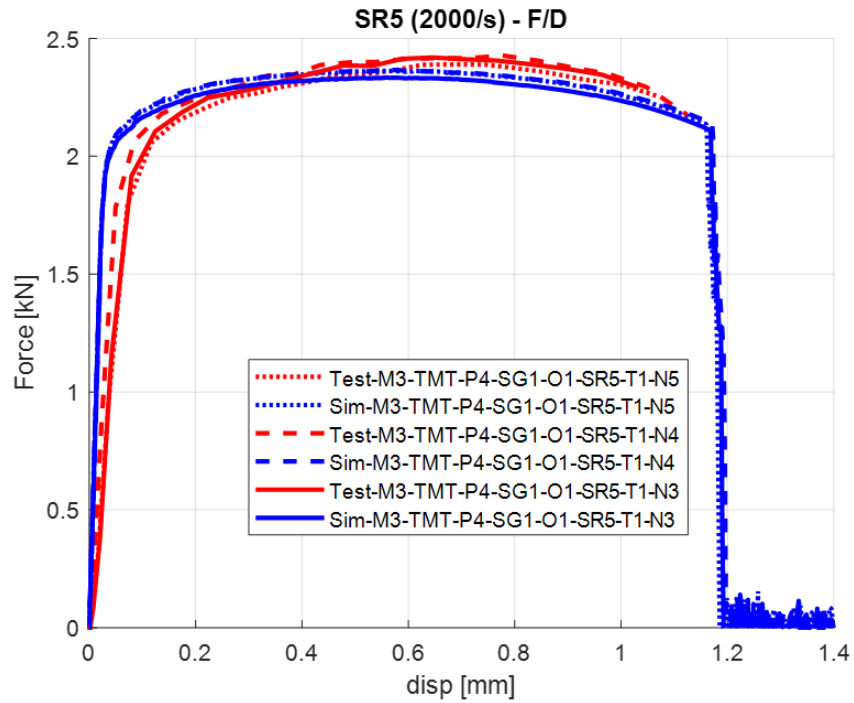
c) SR5 Force vs. Displacement
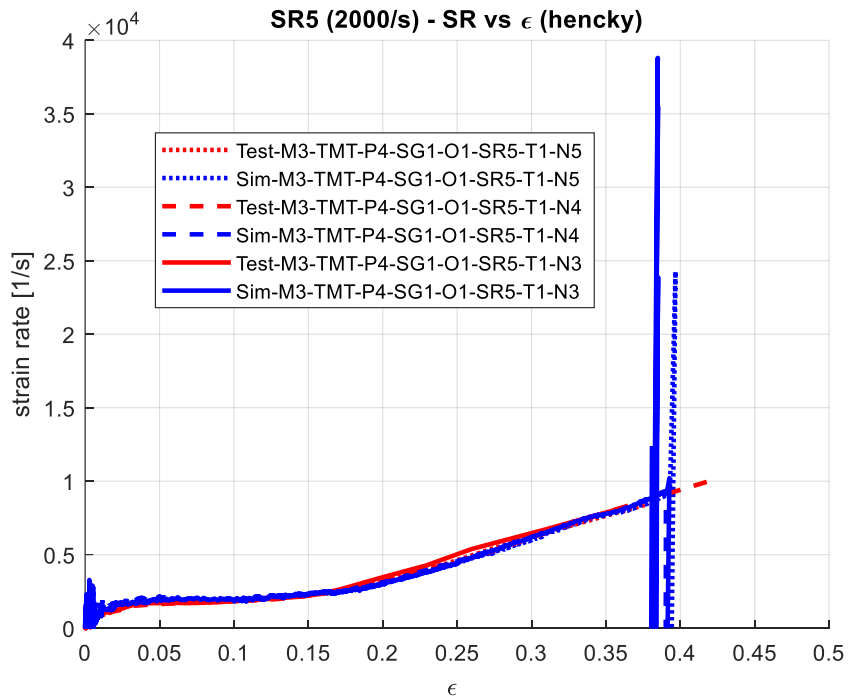
d) SR5 Strain Rate vs. Strain

Figure 105. Force-displacement and strain rate-strain comparisons for specimens SR4 and SR5

5.5 Creation of an element size fracture regularization curve

The modeling of fracture using element erosion is dependent on the element size in the finite element mesh. Unlike stresses, element erosion values do not converge to a fracture strain as the mesh size is reduced (LS-DYNA Aerospace Working Group (AWG), 2023). In *MAT_224, the failure surface can be scaled by element size, regularizing simulation results and for varying element sizes, produce the same failure displacements. As most practical finite element meshes contain elements of varying sizes, mesh size regularization capability is critical to produce accurate simulations.

The regularization load curve scales the failure surface as a function of the element size. The solid element size is calculated by the square root of the volume divided by the maximum area. The Inconel-718 regularization curve was developed by simulating the uniaxial tension (SG1) specimen with varying elements sizes. The previously presented simulations used a nominal element size of 0.2 mm. The SG1 test specimen was re-meshed with 0.1 mm and 0.4 mm element sizes. The element configuration for each element size is shown in Figure 106 a) thru c).

a) 0.10 mm mesh (582,248 elements)

b) 0.20 mm mesh (240,528 elements)

c) 0.40 mm mesh (9,184 elements)
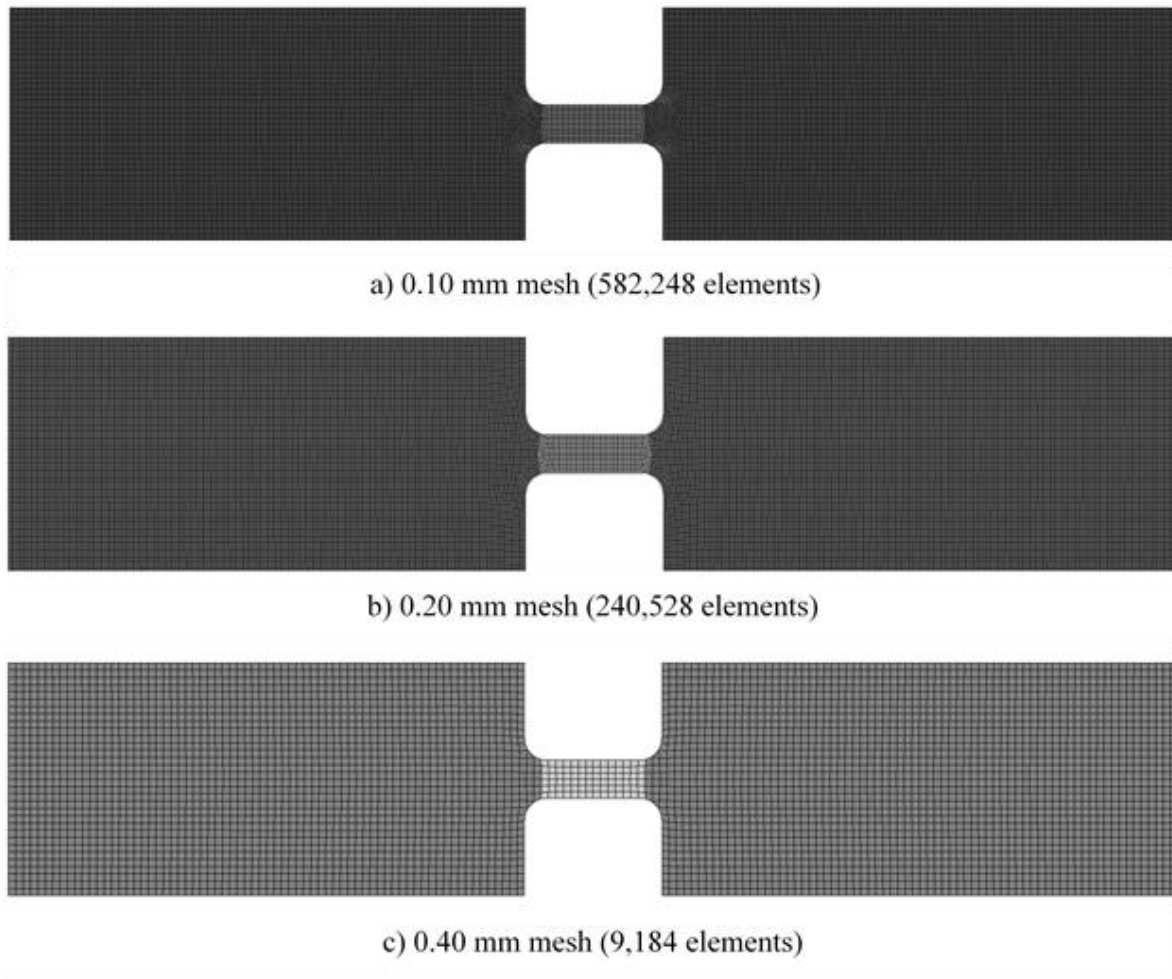
Figure 106. SG1 meshes using different element sizes, a) thru c)

The simulations with the three different meshes used a single load curve and the failure surface; the temperature and strain rate scaling factors were not included. Since the failure surface was developed with a 0.2 mm nominal element size mesh, the scale factor for this value is 1.0. The scale factors for the 0.1 mm and 0.4 mm element size meshes were varied until the simulated fracture displacements produced an acceptable match to the tests. Additional scale factor inputs were created so that there would be no non-physical extrapolations at very small and very large element sizes. The final regularization scaling curve can be seen in Table 12.

Table 12. Scaling factors by mesh size

Mesh Size	Scaling Factor
0.01 mm	1.5
0.10 mm	1.5
0.16 mm	1.000
0.20 mm	1.000
0.40 mm	0.75
1.00 mm	0.75

It is recommended that material model users who are using nominal element sizes smaller than 0.1 mm, or greater than 0.4 mm, should extend this scaling curve to their nominal element size. This requires performing additional simulations of tests with their nominal element size, and calculating a scale factor that will provide an acceptable match to the test data.

The force-displacement plots from simulations using the 0.10 mm, 0.20 mm and 0.40 element size meshes are shown in Figure 107. Using the scaling factors shown in Table 12, all three of the simulations predict an acceptable match to the test fracture displacements.
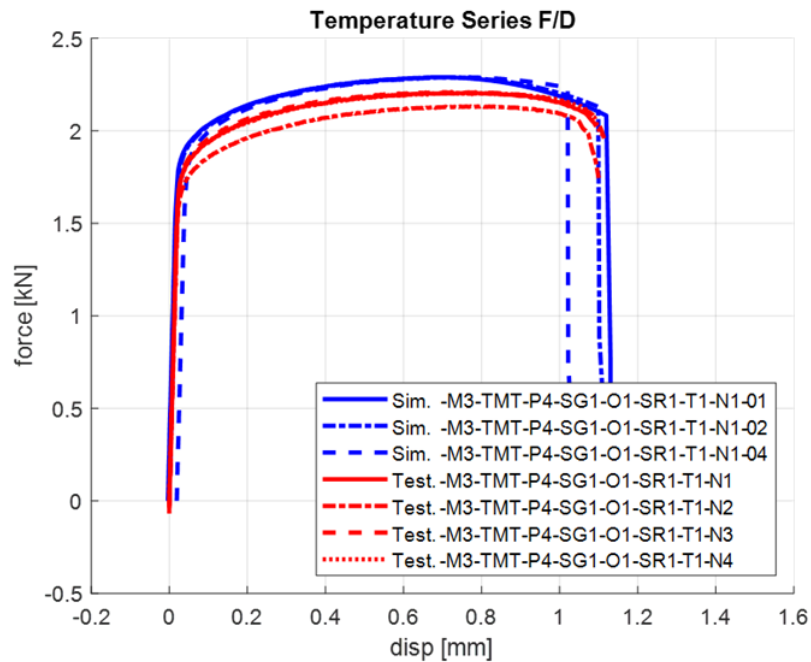
Figure 107. Force-displacement comparisons using varying element sizes

119

6 Validation of Inconel-718 material model

Validation of the Inconel-718 material model was achieved by comparing analytical predictions to ballistic impact tests. The ballistic impact tests that were used in the validation were performed at NASA Glenn Research Center (GRC) (Pereira, Revilock, & Ruggeri, 2020). The tests featured cylindrical tool steel projectiles impacting 12.7mm (0.5 inch) Inconel-718 plates. The Inconel-718 plasticity and failure model development described in Section 3 and Section 5 used an approach that had previously been successful in creating validated models multiple times (Haight, Wang, Du Bois, Carney, & Kan, 2016; Park, Carney, Du Bois, Cordasco, & Kan, 2020). However, this initial Inconel model did not predict any fracture or rupture at velocities at or near the test-established ballistic limit. The velocities at which the simulations predicted rupture where significantly higher than any velocity in this series of tests.

It was determined by test specimen inspection that the failure modes in the ballistic impact tests were ASBs. ASBs could be predicted using extremely small, nano-scale element sizes using the existing *MAT_224. However, for prediction of ASBs using practical element sizes, a new *MAT_224 capability was required. This new capability was developed and added to *MAT_224, and is described in detail (Dolci, 2022; Dolci, et al., 2023). A brief summary follows here.

The new capability raises the TQC, β, in elements where a high shear strain and a high strain rate are characteristic of an ASB formation. When the extremely small element sizes are used, the shear strain and strain rate is concentrated, raising temperatures sufficiently to cause rapid failure, matching ASB conditions. In a practical size mesh, this shear and rate concentration did not occur, preventing an ASB-like temperature rise from occurring.

In *MAT_224, the TQC, β, can now be defined as a function of an ASB characteristic shear strain, an ASB characteristic strain rate, and the element size. These independent functions can be specified precisely using multi-dimensional table input. Using the tabular β, a new material model was created that can successfully predict both the appearance of ASB and the validation test ballistic limit, using a variety of practical element sizes. A full description of the V1.0 Inconel-718 material input parameter set validation, including utilization of the new capability, has previously been reported (Dolci, 2022).

The initial validation effort was successful in showing that the new material model can simulate ASBs, accurately and robustly. This initial Inconel-718 input parameter set was released internally, and informally designated as V1.0. Adjustments and refinements were made to the V1.0 model, producing the V1.1 and V1.2 material input parameter sets presented in this

document. A summary of the testing and the validation simulation results is presented in the following sections.

6.1 Ballistic impact tests

The target was a square Inconel-718 plate with a 381.0 mm edge length and a nominal 12.7 mm (0.5") thickness. A fixture held the target plate rigidly between two steel plates with a 254.0 mm diameter circular opening. The two steel plates were connected with bolts, as shown in Figure 108 (Buyuk, 2013).
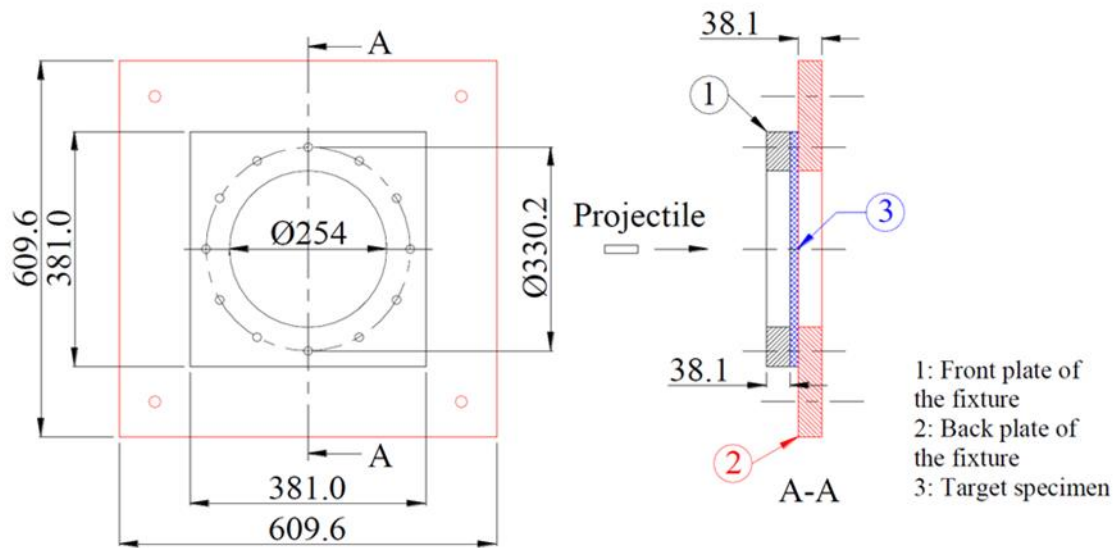
Figure 108. Specimen and fixture geometry

6.1.1 Projectile geometry

The projectiles were made of A2 tool steel and had a cylindrical geometry. The geometry and dimensions of the projectile are shown in Table 13, and Figure 109 (Pereira, Revilock, & Ruggeri, 2020; Buyuk M. , 2013).
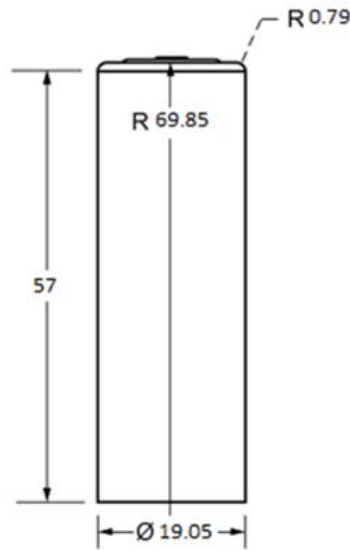
Figure 109. Projectile geometry (dimensions in mm)

Table 13. Projectile geometry

Panel Thickness [mm]	Projectile Material	Projectile Length [mm]	Projectile Diameter [mm]	Average Projectile Mass [g]
12.7	A2 Tool Steel	57.0	19.05	126.4

6.1.2 Ballistic impact tests apparatus

A helium-propelled pressurized gas gun was the accelerator of a polycarbonate sabot within a 50.8 mm diameter barrel as shown in Figure 110 (Pereira, Revilock, & Ruggeri, 2020). The pressure vessel had a total volume of $1.116 \cdot 10^7$ mm^3. The gun barrel had a length of 3.65 m and a bore of 50.8 mm. (The image shows a 76.2mm (3. inch) diameter gun barrel. An image with 50.8 mm diameter barrel is not available.) The A2 tool steel projectiles were carried by polycarbonate sabots. The sabot was stopped at the end of the gun barrel by a stopper plate. To minimize disturbances the target plate was held in a vacuum. The gun barrel protruded into the vacuum chamber, which also supported the fixture holding the Inconel plate. (Pereira, Revilock, & Ruggeri, 2020).

Figure 110. Large vacuum gas gun

6.1.3 Ballistic impact test results

The results of the ballistic impact tests are summarized in Table 14 (Pereira, Revilock, & Ruggeri, 2020). Only 2 of the tests showed a full penetration and the containment trend was not fully consistent with increasing impact velocity, further adding difficulties in identifying a precise ballistic limit. The inconsistent trend was likely due to slightly different impact angles, and to the natural expected variability of experimental test results.

Table 14. Panel impact test results from Pereira, Revilock & Ruggeri (2020)

Test	Impact velocity [m/s]	Exit velocity [m/s]	Penetration	Comments
DB266	203.8	52.5	yes	Plug exit velocity 65.8m/s
DB267	161.0	0.0	no	Created a dent but no visible crack
DB268	190.8	54.6	yes	Plug exit velocity 67m/s
DB269	180.4	0.0	no	No visible crack
DB270	183.8	0.0	no	No visible crack
DB271	189.1	0.0	no	No visible crack
DB272	195.7	0.0	no	No visible crack

6.2 Ballistic impact test simulations

In order to demonstrate the improved predictive capability of the new *MAT_224 capability, the simulations of the Inconel-718 ballistic tests will be presented using the initial model, without the ASB, and the enhanced *MAT_224 constitutive model. The results of the simulations will be compared to the test results, and model validation will be demonstrated.

6.2.1 Numerical models of the ballistic impact

The enhanced *MAT_224 ASB capability was utilized by the V1.0, V1.1, and V1.2 Inconel-718 material input parameter sets. Each of the material input parameter sets were used in simulations of the NASA GRC ballistic impact tests. All the simulations used the same finite element meshes, as shown in Table 15. Each simulation was initialized by defining the projectile impact velocity and orientation angles that were measured with high-speed cameras during the tests.

Table 15. Ballistic impact simulation mesh characteristics

Number of elements	2582604	
Element size [mm]	0.2	
Plate material model	*MAT_TABULATED_JOHNSON_COOK (*MAT_224, with ASB capability)	
Projectile material model	V1.0 - *MAT_ELASTIC V1.1 - *MAT_224 V1.2 - *MAT_224	

The V1.0 and V1.1 material models have the same input parameters, with the important exception of the TQC tabulated function. V1.0 was characterized using the brittle high temperature behavior, which was retained in V1.1. The V1.0 input parameter set was calibrated using simulations that included an elastic material model for the projectile, and the nominal plate thickness of 12.7 mm.

The TQC tabulated function of the V1.1 model was calibrated using simulations that included a plastic A2 tool steel projectile model. This *MAT_224 tool steel model approximated the plastic

deformation observed in the tested projectiles. In addition, the measured plate thickness of 13.46 mm (0.53") was used in the simulations, instead of the nominal thickness of 12.7 mm (0.5"). As presented in Section 3.2.1, the V1.1 model included high temperature brittleness.

The V1.2 model also included the plastic projectile material model and the 13.46 mm measured plate thickness, as used in V1.1. But as previously presented, the thermal stress-strain curves of V1.2 did not include the brittle high temperature behavior. Therefore, V1.2 has different thermal stress-strain curves at the highest temperatures, as presented in Section 3.2, and a different, corresponding temperature failure scaling function, as presented in Section 5.3. These differences resulted in a third calibrated TQC tabulated function.

A plot of the ASB transition maximum shear strain versus element size for all three models is shown in Figure 111. The figure also shows a plot of β versus element size, for after an ASB has been initiated. The 50,000 s^{-1} transition strain rate, which is also required to prompt a simulated ASB, is consistent in the V1.0, V1.1, and V1.2 Inconel-718 material input parameter sets.
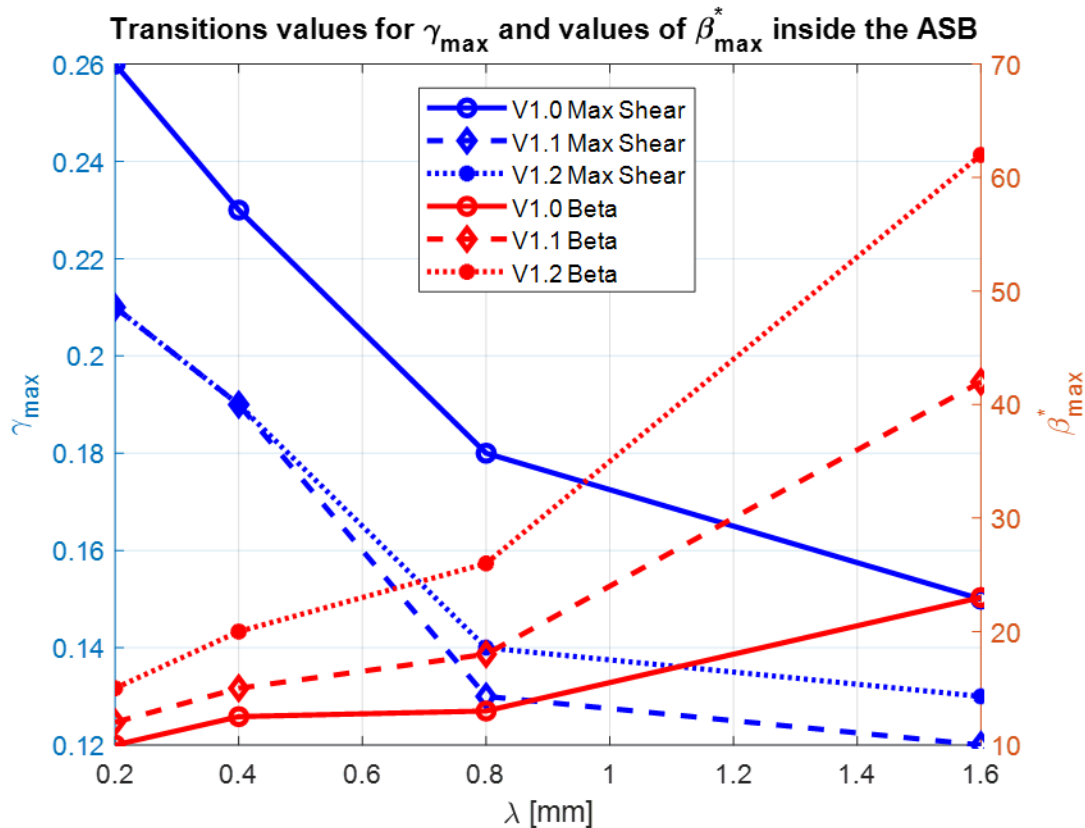
Figure 111. Transition values of the V1.0, V1.1 and V1.2 TQC tables

Note that β shows a monotonically increasing trend with increasing element size in all three input parameter sets. This trend is consistent with expectations and with the observation that a constant β of .8 produces ASBs using very small element sizes. Also note the monotonically decreasing maximum shear strain trend as a function of element size in all three input parameter sets. This trend is consistent with the observation that finer meshes typically produce higher strain concentration maximums. These consistent trends and the success of ballistic impact predictions using all three models, which will be presented in the next section, demonstrates the reliability and robustness of the new ASB simulation capability.

6.2.2   Simulation results

A plot of exit velocities as a function of impact velocity, comparing the tests and the simulations, is shown in Figure 112. Results from all three Inconel-718 material models and varying element sizes are shown. The predicted ballistic limits using the V1.0, V1.1, and V1.2 material models are shown to be within the test data variation for all element sizes. Figure 113 shows a lateral view of the highest impact velocity test of 203.8 m/s, DB266, simulated using the V1.0 input parameter set. A physically realistic plug formation can be seen. Table 16 reports the temperature contour time-sequence from the same V1.0 DB266 test simulation. Table 17 shows a comparison between the temperature contours sequence of DB266 test simulations using V1.1 and V1.2 material models, and varying element sizes.
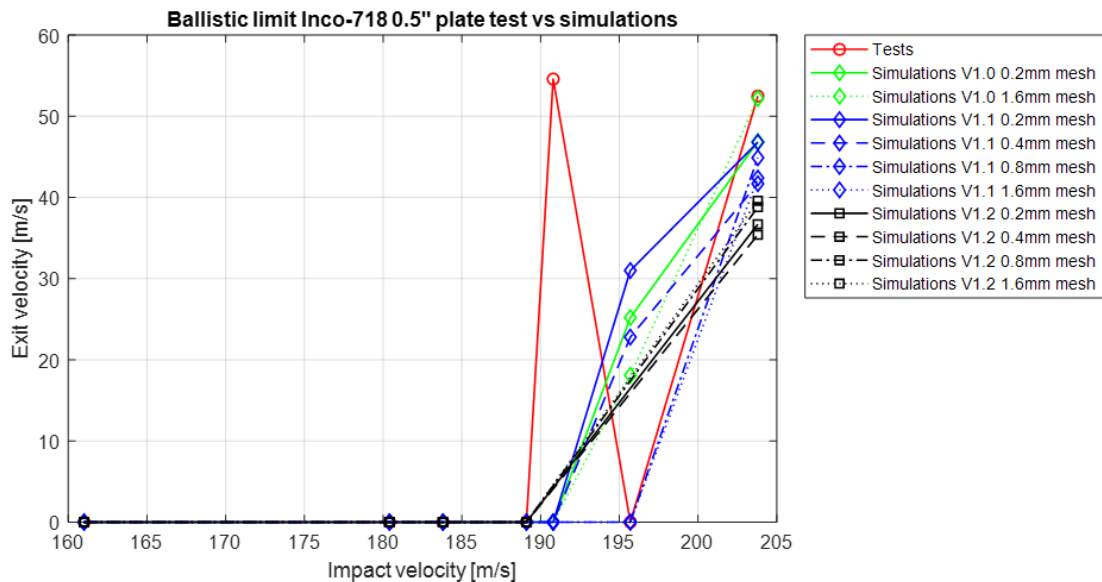
Figure 112. Exit velocities comparing test and V1.0, V1.1 and V1.2 simulations

1) Time 0 ms

2) Time 0.050499 ms

3) Time 0.095948 ms

4) Time 0.146145 ms

5) Time 0.19695 ms

6) Time 0.24745 ms

7) Time 0.29795 ms

8) Time 0.34845 ms

9) Time 0.39895 ms

10) Time 0.5 ms
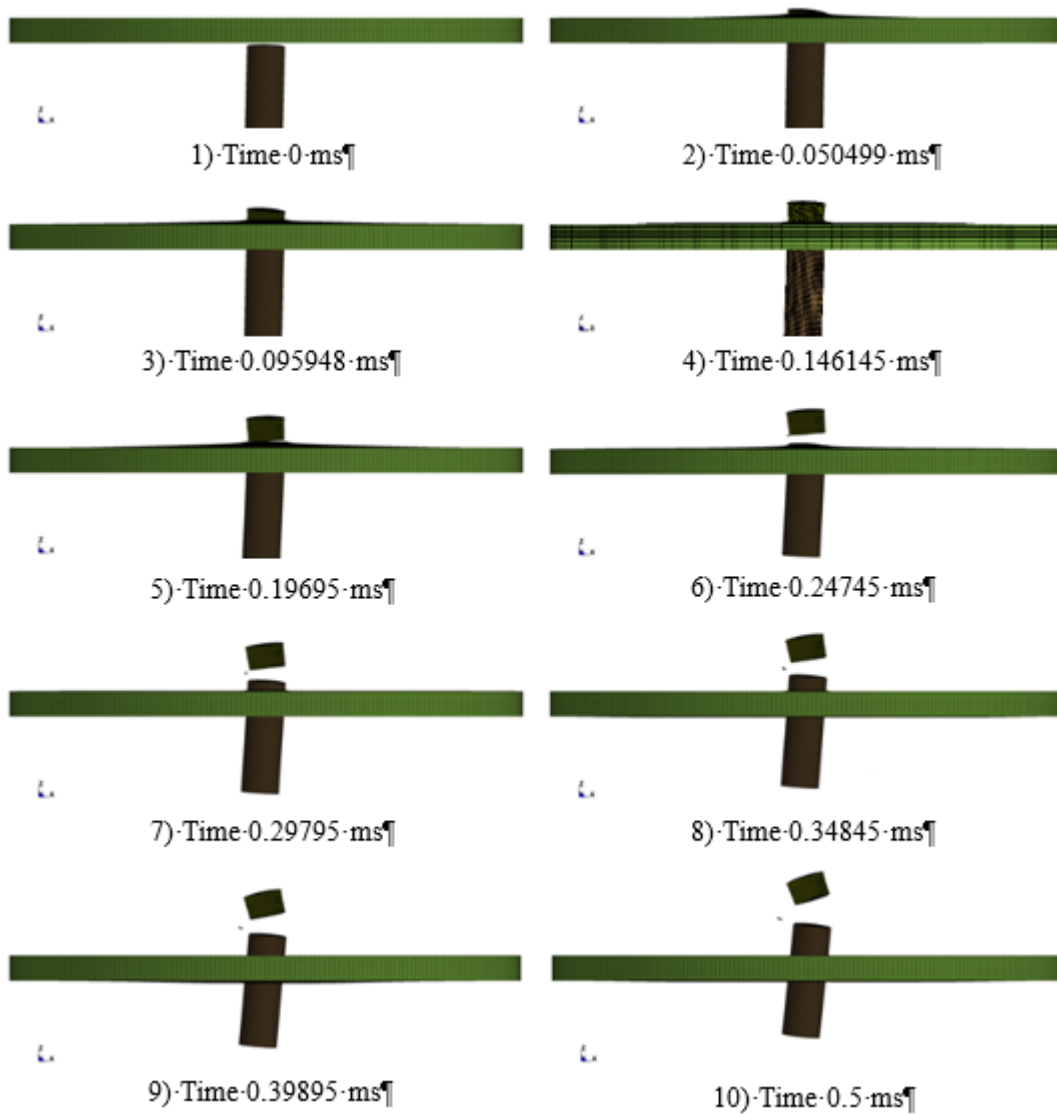
Figure 113. Sequence from DB266 (203.8 m/s) simulation using the V1.0 material model

Table 16. Temperature contour sequence from the V1.0 DB266 simulation

1) Time 0ms	**2) Time 0.015ms**
3) Time 0.020ms	**4) Time 0.025ms**
5) Time 0.030ms	**6) Time 0.035ms**

7) Time 0.040ms	**8) Time 0.045ms**
9) Time 0.050ms	**10) Time 0.090ms**
11) Time 0.200ms	**12) Time 0.250ms**
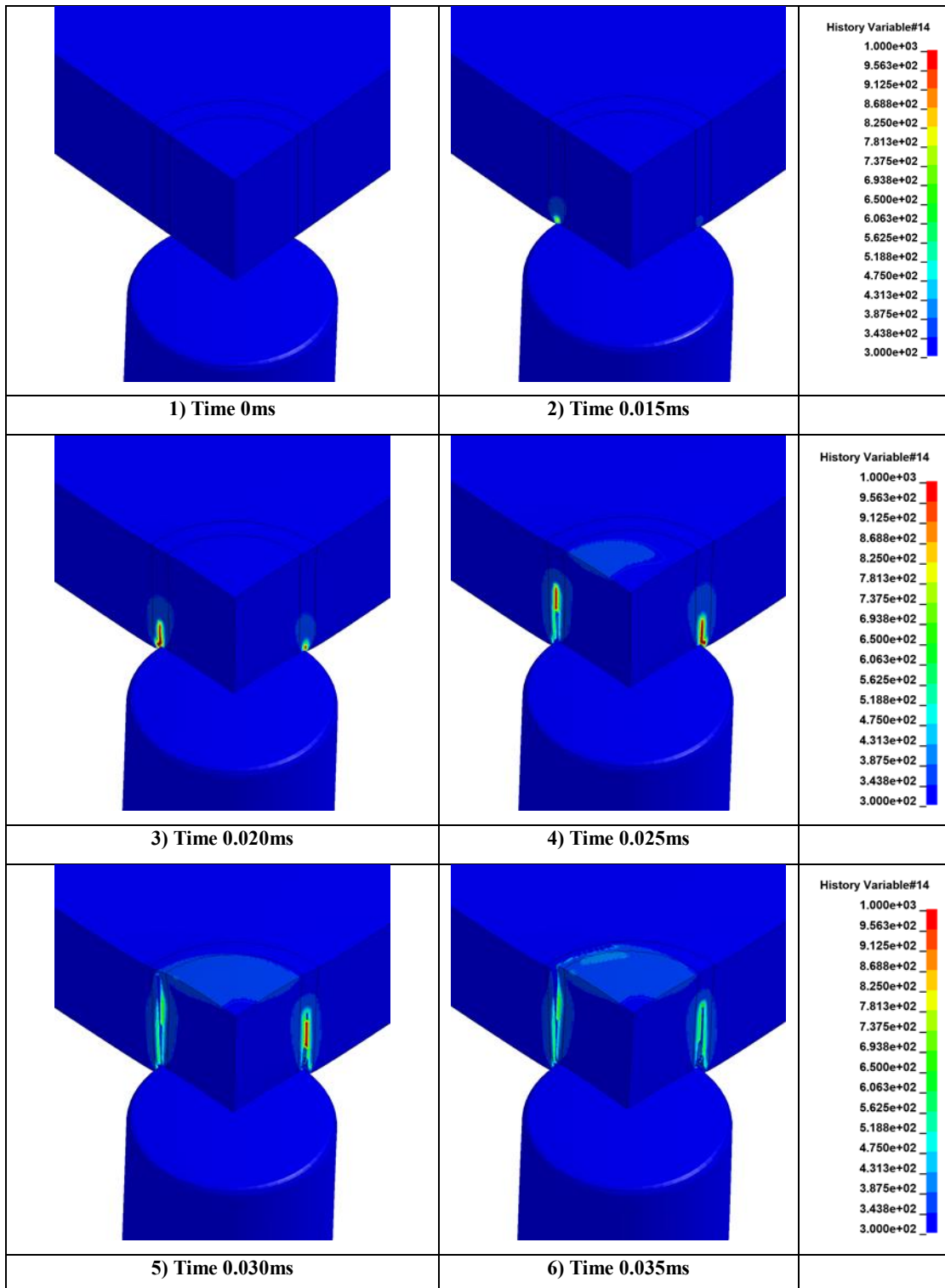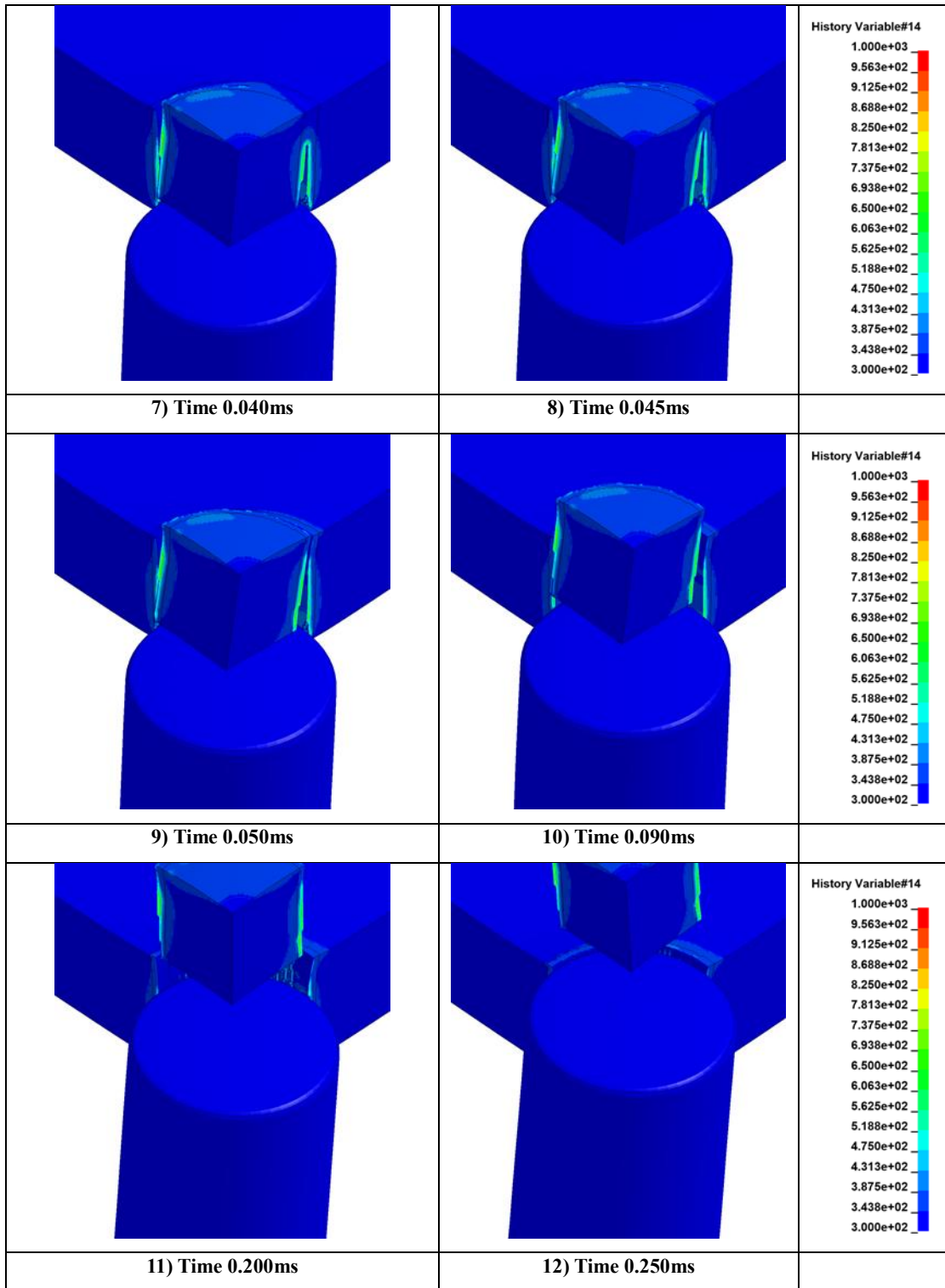
Table 17. DB266 V1.1 and V1.2 temperature contours using varying element sizes

V1.1 0.2mm	**V1.2 0.2mm**
V1.1 0.4mm	**V1.2 0.4mm**
V1.1 0.8mm	**V1.2 0.8mm**

V1.1 1.6mm	V1.2 1.6mm
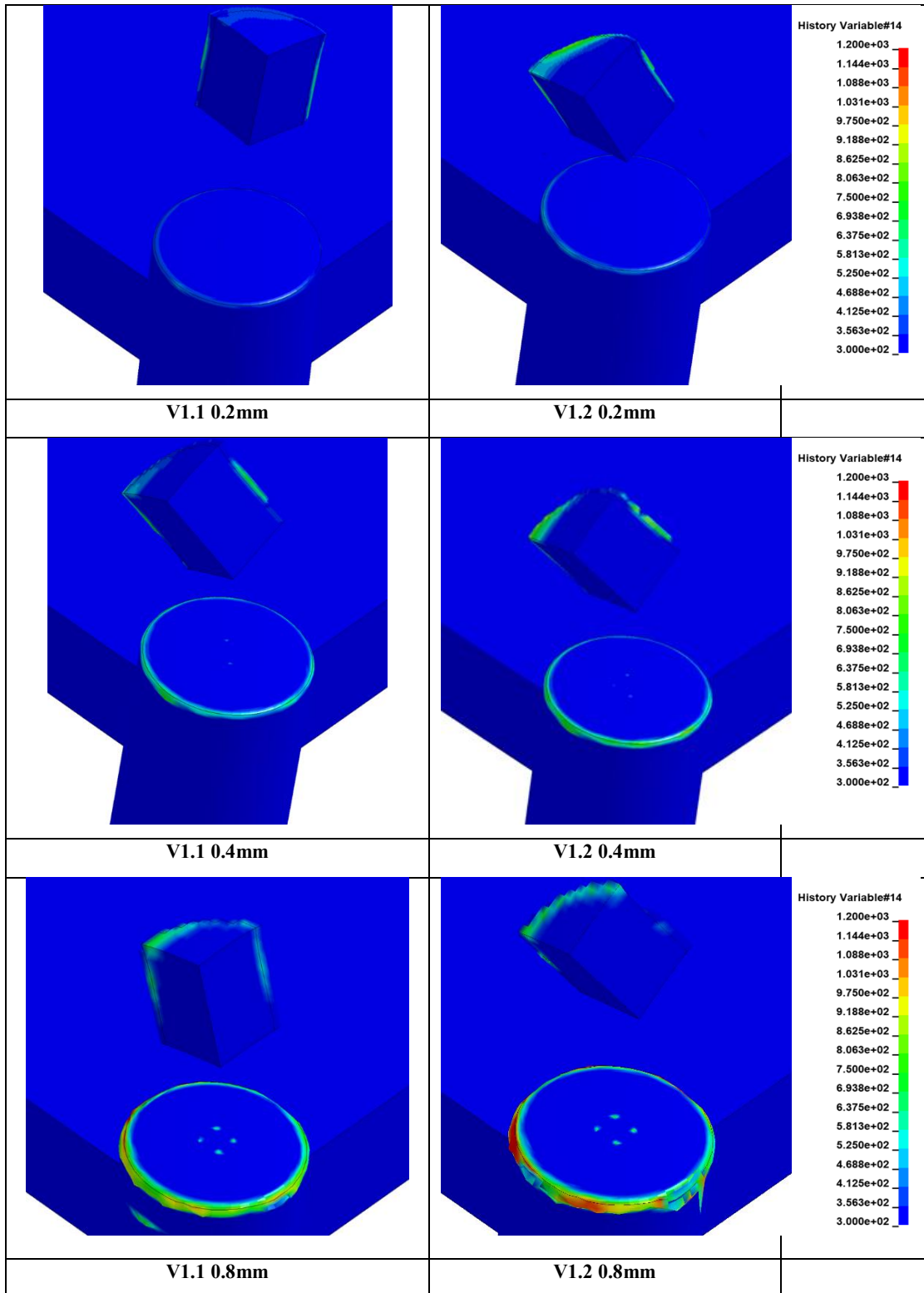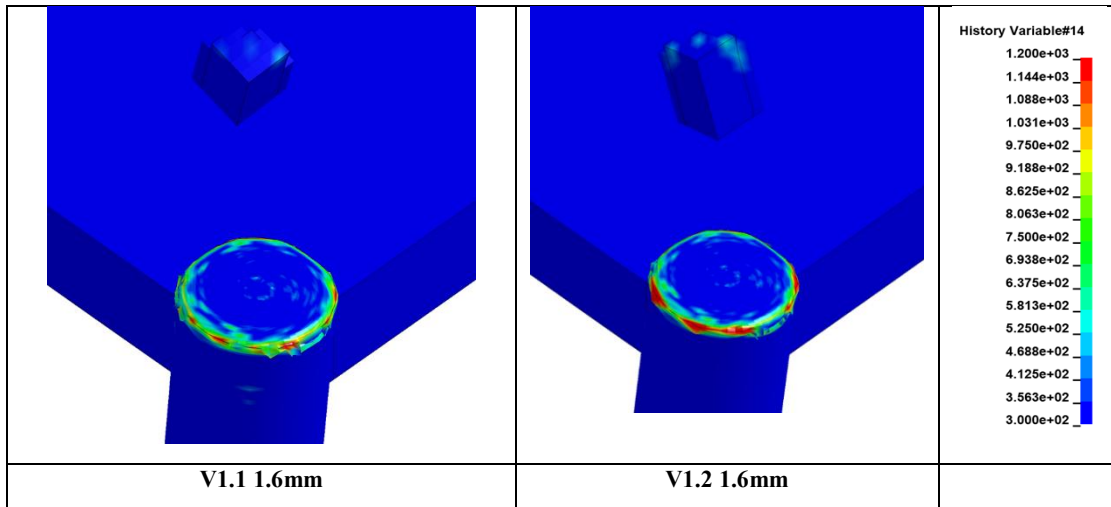
6.3   Discussion

The material model demonstrates a good prediction capability of the Inconel-718 impact physics, using all three input parameter sets; V1.0, V1.1, and V1.2. The plugging ASB failure morphology, along with the associated high strain rates, high crack propagation velocity, and narrow and high thermal bands are all predicted. As a result, accurate ballistic limits are also predicted. For the higher impact velocities, the temperatures inside the ASB simulation reaches values above 1200K, 227K beyond the temperature that makes Inconel brittle in static conditions. The average simulated crack propagation speed through the total thickness was approximately 1200m/s, with a local ASB propagation speed of about 4000m/s, which is consistent with values found in the literature. Moreover, the width of the ASB was of only one element, consistent with the very narrow shear bands observed in Inconel-718 failures. The results from the V1.2 simulations also demonstrate that the enhanced *MAT_224 ASB capability is not dependent on high temperature brittleness. For more info on the ASB feature refer to Dolci (2022) and Dolci et al. (2023).

7   Conclusions

Two validated material input parameter sets for Inconel-718 have been presented. Complete models simulating both the plasticity, conventional fracture, and ASB failure in Inconel-718 were produced. In order to successfully predict the ballistic impact tests, the new ASB capability was required. This new capability was created and added to *MAT_224. The validated material models are designed for use with the enhanced *MAT_224.

The complete Inconel-718 input parameter sets are available on the LS-DYNA Aerospace Working Group website (LS-DYNA Aerospace Working Group (AWG), 2023). In addition to the input parameter set units presented in this report (millimeter, millisecond, kilogram, kilonewton), the models are also available there in SI units (meter, second, kilogram, newton) and in English units (inch, second, lbf/s^2, lbf).

ASB formation has been observed in ballistic impact tests on Inconel-718 plates with other thicknesses. The presented models should be tested for their prediction capabilities of these impacts. The use of the enhanced ASB prediction capabilities should not be limited to Inconel-718. However, successful ASB predictions using other materials have not yet been demonstrated.

8 References

Ansys LS-DYNA. (2023). *LS-DYNA Keyword manual Vol II.* Retrieved from
https://lsdyna.ansys.com/manuals/

Buyuk, M. (2013). Development of a tabulated thermo-viscoplastic material model with
regularized failure for dynamic ductile failure prediction of structures under impact
loading. *Doctoral Dissertation.* The George Washington University.

Buyuk, M., Loikkanen, M., & Kan, C.-D. (. (2008). *Explicit finite element analysis of 2024-
T3/T351 aluminum material under impact loading for airplane engine containment and
fragment shielding.* Washington, D.C.: U.S. Department of Transportation, Federal
Aviation Administration. Retrieved from
https://www.tc.faa.gov/its/worldpac/techrpt/ar0836.pdf

Carney, K., Pereira, J., Revilock, D., & Matheny, P. (2009). Jet engine fan blade containment
using an alternate geometry. *Int. J. Impact Eng*, 720–728.

Dolci, S. (2022). *The influence of strain rate, temperature effects, and instabilities in failure
modeling for metal alloys.* Federal Aviation Administration. DOT/FAA/TCTT-22-21.

Dolci, S., Carney, K., Du Bois, P., Revilock, D., Ruggeri, C., & Kan, C. (2023). Novel method in
the modeling of adibatic shear band in ballisitic impact: an application on Inconel 718
Alloy. *International Journal of Impact Engineering*.

Emmerling, W., Altobelli, D., Carney, K., & Pereira, M. (2014). *Development of a new metal
material model in LS-DYNA, Part 1: FAA, NASA, and industry collaboration
background.* Technical Report, Federal Aviation Administration, U.S. Department of
Transportation. Retrieved from https://www.tc.faa.gov/its/worldpac/techrpt/tc13-25-
p1.pdf

Haight, S., Wang, L., Du Bois, P., Carney, K., & Kan, C. (2016). *Development of a titanium
alloy Ti-6Al-4V material model used in LS-DYNA.* Federal Aviation Administration.
DOT/FAA/TC-15/23.

Kay, G. (2003). *Failure modeling of Titanium 6Al-4V and Aluminum 2024-T3 with the Johnson-
Cook material model.* U.S. Department of Transportation, Federal Aviation
Administration. Retrieved from https://www.tc.faa.gov/its/worldpac/techrpt/AR03-57.pdf

Liutkus, T. (2014). Digital image correlation in dynamic punch testing and plastic deformation
behavior of Inconel 718. *Master Thesis.* The Ohio State University.

LS-DYNA Aerospace Working Group (AWG). (2023). *LS-DYNA material parameter sets*. Retrieved from LS-DYNA Aerospace Working Group: https://awg.ansys.com/Material+Parameter+Sets

LS-DYNA Aerospace Working Group (AWG). (2023). *Modeling guidelines document*. Retrieved from LS-DYNA Aerospace Working Group: https://awg.ansys.com/Resources

Moretti, M. D. (2022). Correction to: high strain rate deformation behavior and recrystallization of Alloy 718. *Metall Mater Trans A 53*.

Park, C., Carney, K., Du Bois, P., Cordasco, D., & Kan, C. (2020). *Aluminum 2024-T351 input parameters for *MAT_224 in LS-DYNA*. Federal Aviation Administration. DOT/FAA/TC-19/41, P1.

Pereira, J., Revilock, D., & Ruggeri, C. (2020). *Impact testing of Inconel 718 for material impact model development (NASA/TM-2020-220451, DOT/FAA/TC-19/40)).* Cleveland, Ohio: NASA, Glenn Research Center.

Ressa, A. M. (2015). Plastic deformation and ductile fracture behavior of Inconel 718. *M.S. Thesis*. The Ohio State University.

Ressa, A., Liutkus, T., Seidt, J., Gilat, A., & Cordasco, D. (2023). *Experimental testing to characterize plastic deformation, dynamic response, and ductile fracture of Inconel 718 under various loading conditions.* Washington, D.C.: U.S. Department of Transportation, Federal Aviation Administration. Retrieved from https://www.tc.faa.gov/its/worldpac/techrpt/tc23-52.pdf

Special metals INCONEL Alloy 718. (n.d.). Retrieved from MatWeb: http://www.matweb.com/search/DataSheet.aspx?MatGUID=94950a2d209040a09b89952d45086134&ckck=1

Spulak, N. (2022). *Investigations into ductile fracture and deformation of metals under combined qusi-static loading and under extemely high-rate compressive impact loading.* Federal Aviation Administration. DOT/FAA/TCTT-22/23.

Spulak, N., Lowe, R., Seidt, J., Gilat, A., Park, C., & Carney, K. (2020). Ductile fracture under in-plane biaxial tension and out-of-plane compression. *International Journal of Structures and Solids*, 234-242.